Title
Shake Table Testing and Analytical Modeling of a Full-Scale, Four-Story Unbonded Post-Tensioned Concrete Wall Building

Permalink
https://escholarship.org/uc/item/9db2s5cp

Author
Gavridou, Sofia

Publication Date
2015

UNIVERSITY OF CALIFORNIA

Los Angeles

Shake Table Testing and Analytical Modeling of a Full-Scale, Four-Story Unbonded Post-Tensioned Concrete Wall Building

A dissertation submitted in partial satisfaction of the
requirements for the degree Doctor of Philosophy
in Civil Engineering

by

Sofia Gavridou

2015

ABSTRACT OF THE DISSERTATION

Shake Table Testing and Analytical Modeling of a Full-Scale, Four-Story Unbonded Post-Tensioned Concrete Wall Building

by

Sofia Gavridou

Doctor of Philosophy in Civil Engineering

University of California, Los Angeles, 2015

Professor John Wright Wallace, Chair

The level of structural damage and the associated economic impact caused by recent earthquakes worldwide have spurred an increased interest in high performance seismic resisting systems that can sustain severe earthquakes with minimal damage. A particularly efficient high performance wall system consists of precast concrete panels vertically post-tensioned to the foundation with unbonded post-tensioning steel. The system relies on the vertical unbonded post-tensioning steel for flexural strength and re-centering, while mild bonded steel bars provide energy dissipation and additional flexural strength. Under lateral loading, the traditional plastic hinge mechanism, associated with structural damage and the potential for large residual deformation, is replaced by a controlled rocking mechanism at the wall-to-foundation interface that allows the system to undergo large nonlinear displacements with minimal damage and minor residual deformations.

This thesis presents experimental results from a dynamic test on a full-scale, four-story precast concrete building that utilized unbonded post-tensioned (UPT) walls in one principal direction of response and bonded post-tensioned concrete frames in the orthogonal direction. The building was subjected to simultaneous three-dimensional shaking using recorded ground motions from the 1995 Kobe earthquake. The excellent performance of the test building in the wall direction of response, exhibiting minimal damage and no residual deformations, confirms that UPT walls are a viable alternative to conventional reinforced concrete (RC) structural walls.

In addition to providing experimental evidence of seismic performance of UPT walls incorporated into a building system, the tests provided valuable insight into issues typically not addressed in component-level experimental studies, such as the role of the floor diaphragm, influence of component interactions, and contributions of three-dimensional responses and torsion. As evidenced by the E-Defense test building, these effects need to be considered to obtain realistic estimates of lateral resistance and displacement demands.

The tests also provided a wealth of data against which design methodologies and analytical models for UPT systems can be benchmarked. Based on a detailed assessment of the E-Defense UPT walls in accordance with ACI ITG-5.2 (2009), and the performance of the UPT walls in the tests, design implications were identified and some revisions to ACI ITG-5.2 were suggested. Finally, an analytical model of the building in the wall direction was developed. Experimental results in this direction were used to assess the ability of the model to capture the dynamic responses and interactions of unbonded post-tensioned structural systems. Correlations between analytical and experimental results were satisfactory for a range of global and local responses, and key aspects of the interaction between components such as framing action and beam elongation effects were adequately reflected in the model.

The dissertation of Sofia Gavridou is approved.

Henry V. Burton

Stanley B. Dong

Christopher S. Lynch

John Wright Wallace, Committee Chair

University of California, Los Angeles
2015

To my parents, Konstantinos and Barbara

Στους γονείς μου, Κωνσταντίνο και Βαρβάρα

TABLE OF CONTENTS

LIST OF FIGURES

LIST OF TABLES

ACKNOWLEDGMENTS

The test of the PT building that formed the basis of this research work was conducted by the National Research Institute for Earth Science and Disaster Prevention (NIED) at the E-Defense facility in Miki City, Japan. Funding for US participation in the pre-test planning and analytical studies was provided by U.S. National Science Foundation under award CMMI-1000268 (PI John Wallace), while funding for NEES@UCLA instrumentation was provided under award CMMI-1110860 (PI John Wallace).

The efforts of the combined Japan-US team are gratefully acknowledged, as the work presented here would not have been possible otherwise. In particular, the contribution of Dr. Takuya Nagae, formerly with E-Defense, and now Associate Professor at Nagoya University, in filling in gaps and providing additional documentation related to the testing whenever needed, is greatly appreciated. Dr. A. Salamanca of the NEES@UCLA, Dr. S. Sritharan of Iowa State University, and Professor T. Kabeyasawa at the Earthquake Research Institute at the University of Tokyo are acknowledged for providing additional instrumentation for the test buildings, and Dr. Richard Sause and his PhD Student, Wesley Keller, at Lehigh University for conducting the pre-test studies on the PT building. Special thanks are extended to Dr Zeynep Tuna for her collaboration on the E-Defense studies and her friendship ever since. Dr. Felipe Perez is also gratefully acknowledged for providing data from the UPT wall tests performed at Lehigh University. Opinions, findings, conclusions, and recommendations in this dissertation are those of the author and do not necessarily represent those of the sponsors or other individuals mentioned here.

Appreciation is extended to the members of the Doctoral Committee, Professors Henry Burton, Stanley Dong, Christopher Lynch and Thomas Sabol for their time and interest in this work.

To Prof. Wallace I express my sincere gratitude for entrusting me with this project, for his constant encouragement, immense patience and deep insight into all things concrete.

To my family in Greece my warmest thanks for their endless love and inexhaustible support. And to Jorge, for asking me to embark on this journey five years ago and being there for me ever since.

VITA

2004	B.S., Structural Engineering Department of Civil Engineering Aristotle University of Thessaloniki Greece
2006	M.S., Earthquake Engineering Center for Post-Graduate Training and Research in Earthquake Engineering University of Pavia (ROSE School) Italy
2006-2010	Project Engineer METE SYSM Consulting Engineers Thessaloniki, Greece
2011-2014	Graduate Student Researcher Department of Civil and Environmental Engineering University of California, Los Angeles
2011-2014	Teaching Assistant Department of Civil and Environmental Engineering University of California, Los Angeles

PUBLICATIONS

Gavridou, S., Wallace, J.W. and Nagae T. (2015). "Shake table test of a full-scale four-story post-tensioned precast concrete building - Part I: Overview and experimental results." *ASCE Journal of Structural Engineering* (submitted for publication).

Gavridou, S., Wallace, J.W. and Nagae T. (2015). "Shake table test of a full-scale four-story post-tensioned precast concrete building - Part II: Analytical studies." *ASCE Journal of Structural Engineering* (submitted for publication).

Gavridou, S., Melek, M., Wallace, J. W. (2014). "Conventional and unbonded post- tensioned lateral force resisting systems – A comparative assessment of expected performance and losses." *Proc. 10th National Conf. in Earthquake Eng.*, Earthquake Eng. Research Institute, Anchorage, AK.

Gavridou, S., Wallace, J. W. (2014). "Comparative study of seismic performance of unbonded post-tensioned rocking wall systems" *Proc. 2014 Annual LATBSDC Conference*, Los Angeles Tall Buildings Structural Design Council, Los Angeles, CA.

Tuna, Z., Gavridou, S., Wallace, J.W., Nagae, T., and Matsumori, T. (2014). "2010 E-Defense four-story reinforced concrete and post-tensioned buildings - comparative study of experimental and analytical results." *Proc. 10th National Conf. in Earthquake Eng.*, Earthquake Eng. Research Institute, Anchorage, AK.

Gavridou, S., Pinho, R., Crowley, H., Calvi, G.M., Montaldo, V, Meletti, C. and Stucchi M. (2007). "Preliminary study on the impact of the introduction of an updated seismic hazard model for Italy." *Journal of Earthquake Engineering*, 2007, Volume 11, Sup. 1, 89-118.

Chapter 1 Introduction

1.1 General

In response to the need for improved seismic performance of buildings, there has been a growing body of research on self-centering structural systems that can sustain severe earthquake shaking with minimal damage and no (or limited) residual deformations. Unbonded post-tensioned (UPT) precast concrete walls are part of this family of self-centering systems. Similar technologies have been developed for precast concrete frames (Priestley and Tao 1993, Stanton et al. 1997, Bradley et al. 2008,) and have been extended to other construction materials such as masonry, wood and steel (Toranzo 2002, Palermo et al. 2006, Eatherton et al. 2014).

The design objectives for these high-performance systems are to limit structural damage by better controlling where nonlinear deformations occur (typically at critical rocking interfaces) and to ensure self-centering response by providing a reliable restoring force (typically through post-tensioning steel). In UPT precast concrete walls, nonlinear deformations are concentrated at the wall-to-foundation interface, and the restoring force is provided by unbonded post-tensioning steel that is designed to remain elastic under the design earthquake. In this way, the traditional plastic hinge mechanism of conventional RC walls, associated with structural damage and the potential for large post-earthquake residual deformation, is replaced by a controlled rocking mechanism at the wall-foundation interface that allows the wall to undergo large nonlinear displacements with minimal damage and minor residual deformations.

Research on precast seismic systems initiated in the early 1990s with the PRESSS (Precast Seismic Structural Systems) project that culminated with the pseudo-dynamic testing of a 0.60-scale five-story precast building (Priestley et al. 1999). The PRESSS building utilized coupled UPT walls in one direction and precast frames with different types of beam-column connections in the orthogonal direction. Subsequent experimental research related to UPT walls mainly focused on behavior of individual uncoupled walls, including UPT walls without energy dissipators (Perez et al. 2004, Henry et al. 2012, Nazari et al. 2014), with energy dissipators in the form of mild bonded reinforcement (Holden et al. 2003, Restrepo and Rahman 2007, Smith and Kurama 2012), and with alternative dissipative solutions (Marriott et al. 2008).

ACI 318-11 permits use of precast concrete structural systems only if experimental results and analysis demonstrate that the proposed precast system has "strength and toughness" at least equal to those of a comparable monolithic (cast-in-place) reinforced concrete system (21.1.1.8). ACI ITG-5.1 (2007), adopted since 2008 by ACI 318, defines the minimum experimental evidence required to satisfy 21.1.1.8 to permit use of UPT walls as special RC structural walls. ACI ITG-5.2 (2009), now referenced in ACI 318-11 (R21.10.3), provides design requirements for a specific type of unbonded post-tensioned precast wall system, coupled or uncoupled. These ACI Standards constitute a significant step in codifying UPT precast concrete systems and incorporating them into ACI 318.

Despite the advances outlined in the preceding paragraphs, relatively few new buildings utilize these higher-performance technologies, in part because of the lack of field and laboratory experience with full- or large-scale three-dimensional buildings subjected to dynamic loading and the lack of detailed modeling recommendations comparable to those available for conventional structural systems. The test program documented in this work addresses the former issue, while the analytical studies presented contribute to the latter.

The work presented here adds to the growing body of research aimed at experimental validation of UPT structural systems and provides unprecedented experimental evidence of seismic performance of UPT walls incorporated into an entire building system. The experiment was conducted in 2010 at the E-Defense shake table facility in Japan and included dynamic testing of a full-scale, four-story precast concrete building. The building utilized UPT walls coupled to corner columns by UPT beams in one principal direction of building response, and bonded post-tensioned concrete frames in the orthogonal direction. This work provides an overview of the test program and experimental results in the wall direction of response. Given that the majority of prior UPT wall tests involved two-dimensional, moderate-scale structures tested under quasi-static cyclic loading, the three-dimensional, full-scale dynamic tests presented herein provide unique data to assess behavior of UPT walls under multi-directional dynamic loading and to investigate system interactions (e.g. wall with UPT beams and slab). In addition, the E-Defense tests added a wealth of data against which design methodologies and analytical models of UPT walls can be validated.

1.2 Scope

While prior research on unbonded post-tensioned structural systems has demonstrated the advantages of these systems, namely their ability to achieve large nonlinear deformations expected in strong earthquake shaking with minimal structural damage and minor residual deformations, their use in practice is still limited. In order to move UPT systems into wider practice it is necessary that experimental evidence of their seismic performance be accompanied with design and analysis tools suited for design office application.

The work presented herein is aimed at further advancing knowledge on unbonded post-tensioned concrete structural systems and promoting their wider use by: (i) providing experimental evidence of their seismic performance, including data to address system interactions and, (ii) validating design methodologies and analysis tools that are ultimately required to move these systems into practice.

1.3 Organization

The dissertation is divided into seven chapters. Following the introductory Chapter 1, Chapter 2 highlights the main features of unbonded post-tensioned precast concrete walls and provides an overview of previous experimental and analytical research on UPT walls.

Analytical component-level studies that were conducted to establish modeling approaches for UPT precast concrete components are summarized in Chapter 3. More specifically, analytical models of cantilevered UPT walls and UPT beam-column sub-assemblages are developed and validated through comparisons of analytical results with published experimental data.

Chapter 4 provides an overview of the full-scale, four-story, precast post-tensioned building that was tested on the E-Defense shake table in 2010. Information provided includes design details, material properties, test sequence, and instrumentation. A detailed assessment of the design of the E-Defense UPT walls based on ACI ITG-5.2 (2009) is provided at the end of the Chapter. Results from this assessment provide a useful context for interpreting the experimental results presented in the next Chapter and identifying design implications.

Chapter 5 presents experimental results for a range of responses in the wall direction of the four-story, precast post-tensioned building that was tested on the E-Defense shake table in 2010. Results presented include global force-displacement relations, response envelopes and local responses, with an emphasis on performance of the two UPT walls in the test building. Design aspects of UPT walls with reference to ACI ITG-5.2 are also discussed. In addition to wall responses, experimental results related to the UPT beams in the building and the slab are also presented. The experimental results provide valuable insight into aspects typically not addressed by two-dimensional component tests, such as system interactions, torsional response, and effect of out-of-plane responses on UPT wall performance.

Building on the information presented in the previous chapters, Chapter 6 describes the development and experimental verification of a nonlinear analytical model in the wall direction of the E-Defense PT building. The modeling approaches validated through component studies presented in Chapter 3, are implemented in the analytical model of the E-Defense PT building, with additional considerations to account for system interactions. Comparisons between analytical and experimental results are presented for a range of global and local responses including story lateral displacements, story shear forces and moments, and gap opening due to rocking at the wall base. In addition to validating the proposed computational model, the analyses allow system interactions such as framing action resulting from coupling of the UPT walls to the corner columns through the UPT beams, and interactions of the UPT beams with the floor system to be quantified. Together with the experimental results, the analyses provide valuable insight into the dynamic responses and interactions of a full-scale, three-dimensional UPT building.

Finally, a summary and conclusions of the study are presented in Chapter 7 together with recommendations for future work and improvements.

Chapter 2 Literature review

Following an introductory section on the main features of unbonded post-tensioned precast concrete (UPT) walls, this chapter provides an overview of previous experimental and analytical research on UPT walls and available design guidelines for these systems. The role of residual displacements sustained by structures after an earthquake is discussed at the end of the chapter.

2.1 Main features of UPT walls

The main features of unbonded post-tensioned precast concrete walls considered in this study are shown in Figure 2-1. The UPT wall consists of precast concrete panels vertically post-tensioned to the foundation with high-strength post-tensioning (PT) steel. Under lateral load, the wall is intended to rock against the foundation in essentially a rigid body motion.

The PT steel is placed inside ducts and is unbonded from an anchor at the top of the wall to an anchor in the foundation. Note that the distributed (bonded) mild steel reinforcement within the base wall panel does not extend across the wall-to-foundation joint. As shown in Figure 2-1, in addition to the post-tensioning steel, the only reinforcement crossing the wall-to-foundation joint and providing moment strength at the base of the wall, are energy dissipating (ED) reinforcing bars. These ED bars are symmetrically located about the vertical centerline of the wall, adequately anchored inside the foundation, and deliberately debonded for a short length above the base to prevent low-cycle fatigue fracture under the high strains that are expected to develop at the base section during rocking. It is noted that, in place of the energy dissipating reinforcing bars at the base of the wall considered herein, other types of energy dissipating devices have also been proposed for use in UPT walls and have been studied both analytically and experimentally. These include external tension-compression yielding steel dampers, viscous fluid dampers (Marriott et al. 2008, 2009) and hysteretic or friction dampers along vertical joints of coupled UPT walls (Priestley et al. 1999, Kurama 2001).

As shown in Figure 2-1, non-shrink grout is placed at the horizontal joints between individual precast wall panels and at the wall-to-foundation interface. Fiber reinforced grout (with steel or polyethylene fibers) is typically used at the base joint to ensure that it remains intact under the large compressive strains that develop during rocking. The end regions of the bottom panel (shown by the shaded regions in Figure 2-1) are confined with transverse reinforcement so that the concrete can also sustain the large compressive strains that are expected to develop at the wall toes. As will be discussed in detail in the following chapters, the region of inelastic deformations (nonlinear concrete strains) in UPT walls is expected to be limited to a short height above the base, generally smaller than the plastic hinge length of a conventional (monolithic) reinforced concrete wall, and performance of UPT walls is largely governed by their ability to develop large compressive stains in a ductile manner within this critical region. In addition to transverse confining reinforcement at the ends of the base wall panel, and fiber reinforced grout at the wall-to-foundation interface grout, other means to ensure that inelastic action due to high compressive forces can develop in a ductile manner at the critical base joint include: use of fiber reinforcement in the concrete mix of the base panel, use of local armor such as steel plates at the base of the wall, or placement of the grout inside a trough below the wall (Priestley et al. 1999, Holden et al. 2003, Marriot et al 2008).

Under lateral load, behavior of the UPT wall is governed by a gap opening at the wall-to-foundation interface. The gap opening reduces the stiffness of the wall and results in non-linear response. Note that other possible deformation modes (e.g., sliding along the base joint, sliding along horizontal joints between wall panels, or uplift at horizontal joints between panels) are prevented by proper design and detailing, e.g., embedment of the wall in a slotted foundation to prevent sliding, or inclusion of mild steel reinforcement extending across the horizontal joints between wall panels to prevent uplift from occurring at upper joints. The post-tensioning steel is designed to remain elastic so that upon unloading it provides (together with gravity loads acting on the wall) an elastic restoring force that returns the wall to its initial position and closes the gap at the base. The ED bars are designed to yield in tension and compression during the gap opening-closing behavior and thus provide energy dissipation to the system.

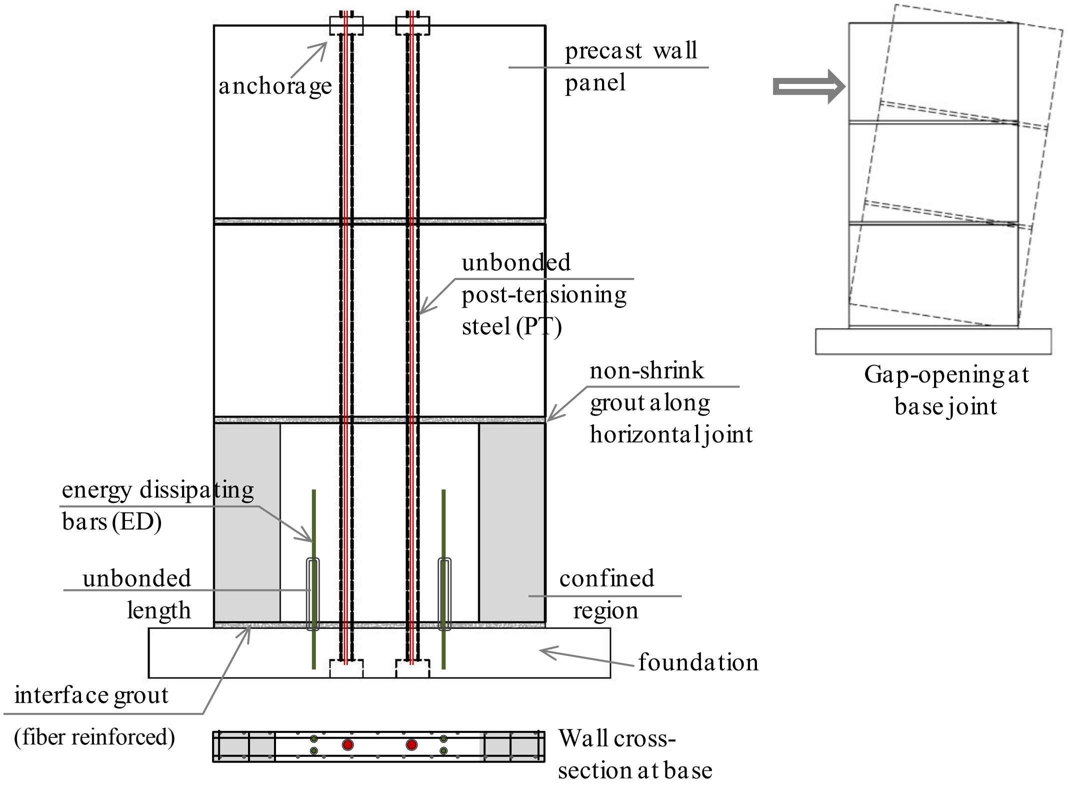

Figure 2-1 Main features of Unbonded Post-Tensioned (UPT) precast concrete wall

Note that in the absence of the ED bars at the base, the UPT wall would display an essentially nonlinear elastic behavior under lateral load, which ensures self-centering response but also results in no energy dissipation. When ED bars are provided at the base of the wall to enhance the energy dissipating characteristics of the system, in order for re-centering to be achieved, the prestressing force in the PT steel (together with the axial load on the wall) should be sufficient to cause yielding in compression of the ED bars and overcome the permanent elongations that this reinforcement develops as it yields in tension. With an appropriate selection of the relative contribution of the energy-dissipating (ED) and self-centering (PT) components, under lateral load, a UPT wall exhibits a controlled rocking behavior characterized by a flag-shaped hysteretic response. This is fundamentally different from the response of a conventional RC wall, as illustrated in Figure 2-2.

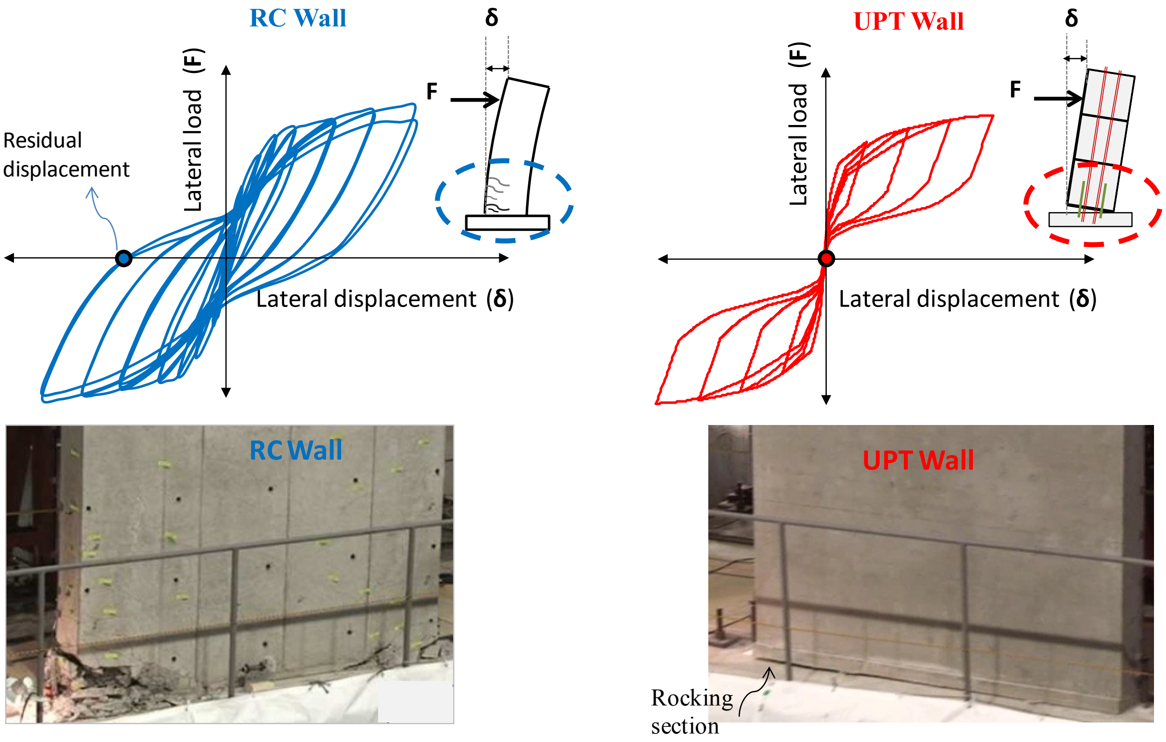

Figure 2-2 Conventional RC structural walls versus UPT walls

Nonlinear behavior in the RC wall is governed by the formation of a plastic hinge at the base of the wall and is associated with structural damage and the potential for large residual deformations upon unloading from a large nonlinear displacement. In the UPT wall, nonlinear behavior is associated with gap opening and is accommodated at the wall-to-foundation interface, resulting in minimal structural damage to the wall panels and no residual deformations, even after large nonlinear displacements. In effect, an essentially damage-free, self-centering structural system can be obtained by:

(i) ensuring that the critical base joint of a UPT wall can sustain large local compressive strains in a ductile manner, without significant degradation in the concrete or grout (through transverse reinforcement, fiber reinforced grout, and other means discussed previously),

(ii) selecting that the PT steel remains within the elastic range and the force in it is sufficient to cause compressive yielding in the ED bars to overcome any permanent elongations that they develop as they yield in tension (through appropriate selection of initial prestress and location of PT steel), and

(iii) controlling the magnitude of strains in the ED bars (through appropriate selection of their unbonded lengths and their location in the section).

As will be discussed in the following section, this innovative technological solution and the associated conceptual design philosophy was developed in the 1990s during the PRESSS Program (PREcast Seismic Structural System) coordinated by the University of California, San Diego (Priestley et al. 1999). However, the concept and implementation of rocking sections can be traced back to classical Greece, where many temples utilized a similar type of segmental construction with marble blocks rocking on top of each other under lateral sway (Buchanan et al. 2011).

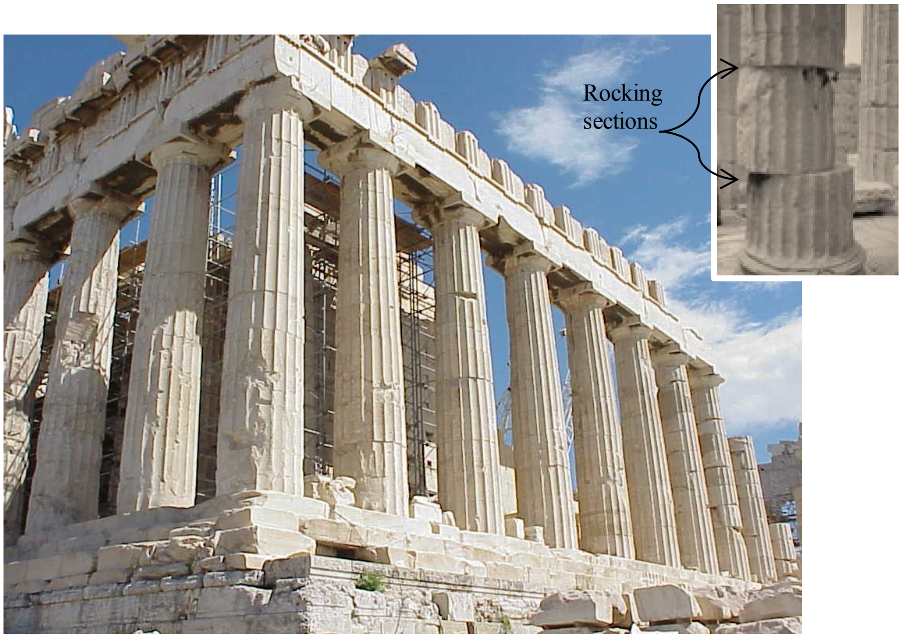

Figure 2-3 Implementation of rocking sections in ancient Greek temples (Parthenon, Athens)

2.2 Experimental research

2.2.1 The PRESSS research program

In recognition of the limited use of precast concrete construction in regions of high seismicity despite its apparent advantages (high quality control, speed of construction, cost effectiveness) and in the absence of prescriptive seismic design recommendations for precast concrete structures, the PRESSS (PREcast Seismic Structural Systems) research program was initiated in 1990 with the objective of developing precast structural systems suitable for use in seismic regions and formulating design guidelines to achieve them in practice (Priestley et al. 1999, Stanton and Nakaki 2002). Both frame and wall precast structures were considered and emphasis was placed on jointed connections that utilize unbonded PT steel rather than the more traditional reinforced concrete emulation approaches that rely on cast-in-place techniques to provide equivalent monolithic connections.

Phases I and II of the program included analytical studies, component tests and tests of precast beam-to-column joint subassemblies to investigate different types of connections. In the final phase of the 10-year program a 60%-scale five-story precast concrete building was tested under pseudo-dynamic loading. A typical floor plan of the building is shown in Figure 2-4(a). Lateral resistance was provided by two perimeter frames in the north-south direction (with different types of UPT connections) and by a central spine wall in the east-west direction. The structural wall consisted of four precast panels, each two and a half stories tall (Figure 2-4b). The panels were vertically connected to each other and to the foundation by unbonded post-tensioning steel located at the center of each panel. Hysteretic damping was provided through connection devices (U-shaped flexure plates) located at the vertical joints between the wall panels. An overview of the test building is provided in Nakaki et al. (1999) while experimental results are presented in Priestley et al. (1999).

The response of the structure under simulated seismic loading was extremely satisfactory (Priestley et al. 1999). Damage in the wall direction was minimal despite being subjected to seismic intensities 50% above the design level (Seismic Zone 4, UBC 1997). The wall was essentially uncracked except at the base connection to the foundation and minor, easily repairable, crushing of concrete developed at the compression ends of the wall base over a height of about 150 mm. Also, as anticipated, the residual drift after the design level excitation was very low (0.06%) and corresponded to only 3% of the peak drift (1.85%) during the tests. Following the successful testing of the PRESSS building, a number of component-level tests, some of them presented in the following sections, further explored the advantages of UPT wall systems.

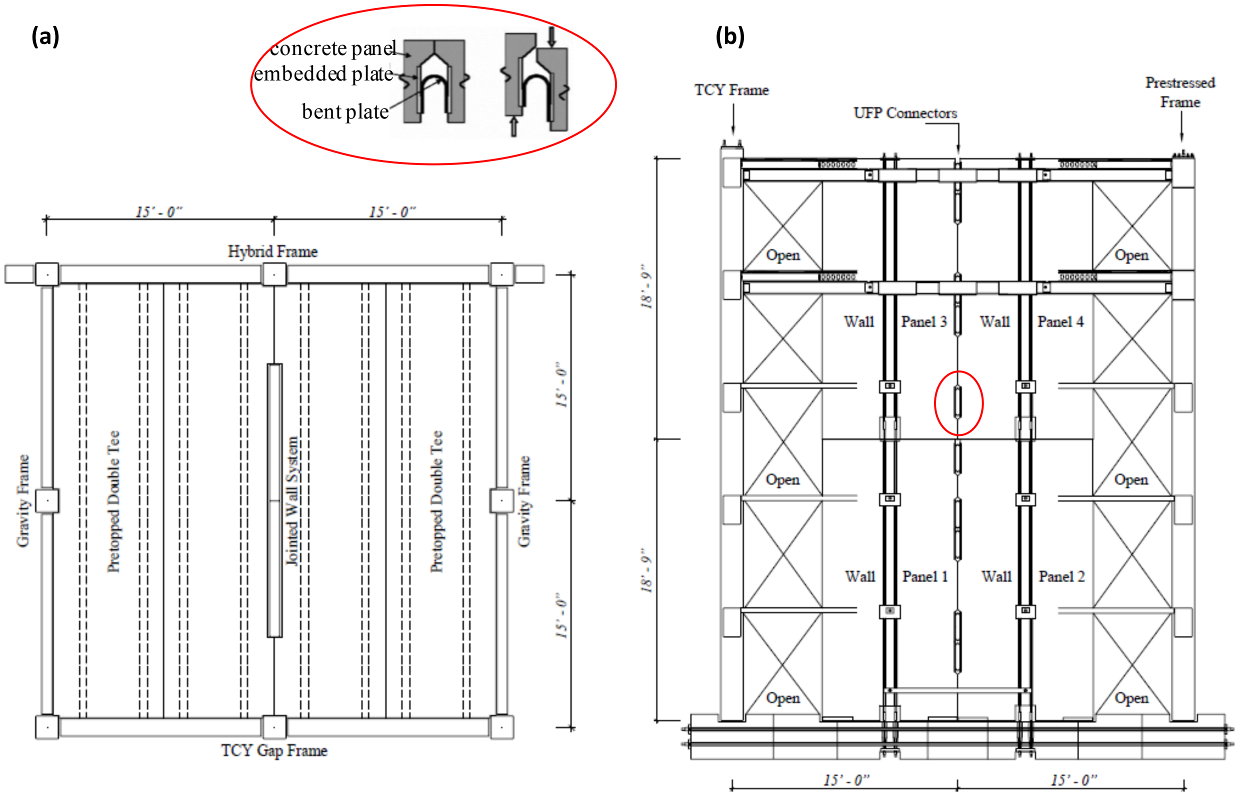

Figure 2-4 – PRESSS test building; (a) plan view and (b) wall elevation (from Priestley et al. 1999)

2.2.2 Quasi-static tests by Rahman and Restrepo (2000) and Holden et al. (2003)

Rahman and Restrepo (2000) tested three half-scale precast concrete walls under quasi-static reversed cyclic loading. The walls were post-tensioned with unbonded tendons and were designed to achieve a drift ratio of 2.5% before yielding of the tendons. All specimens were 4.0 m high, 1.35 m long by 125 mm thick. Units 2R and 3R incorporated energy dissipators at the base (in the form of longitudinal mild steel reinforcement crossing the wall-foundation interface) while Unit 1R was post-tensioned only. The geometry and the lateral load versus lateral drift response of Unit 3R are shown in Figure 2-5. Response of Unit 3R was very stable, showing excellent self-centering characteristics and no strength degradation up to 3% drift. Significant energy was dissipated by yielding of the mild steel bars connecting the precast unit and the foundation beam. Damage to the precast concrete unit was minimal and limited to concrete spalling at the compression ends of the wall base as illustrated in Figure 2-5.

Holden et al. (2003) tested two half-scale precast concrete wall units with dimensions identical to those tested by Rahman and Restrepo (2000). One unit (1H) was a conventionally reinforced specimen designed to emulate a ductile cast-in-place concrete wall whereas the other one (2H) incorporated unbonded post –tensioning and energy dissipators in the form of tapered longitudinal reinforcement. Unit 2H was similar to Unit 3R tested by Rahman and Restrepo (2000), except that the wall in Unit 2H was cast using steel-fiber reinforced concrete and was post-tensioned using carbon fiber tendons.

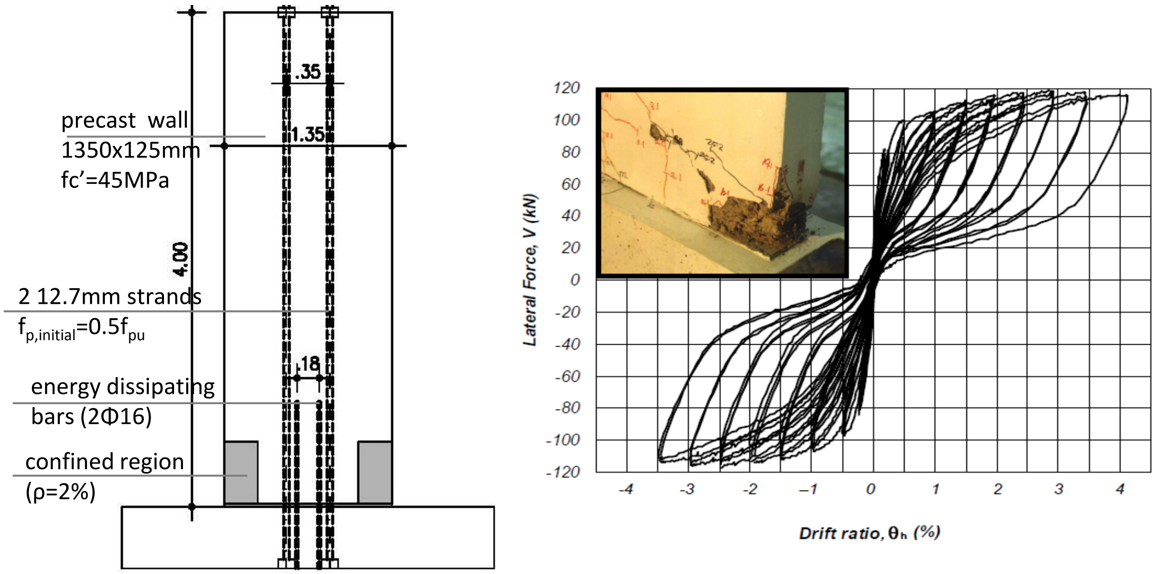

Figure 2-5 – Geometry and lateral force-drift response of Unit 3R (from Restrepo and Rahman 2007)

Both units (1H, 2H) showed satisfactory behavior (Figure 2-6). Behavior of Unit 1H was typical of a monolithic reinforced cast-in-place structural wall. Significant energy was dissipated through yielding of the longitudinal reinforcement in the plastic hinge region. Failure occurred by fracturing of the longitudinal reinforcing bars at a drift of 2.5%. Residual cracks up to 2 mm wide and significant permanent drifts were observed upon unloading. Unit 2H performed very well, sustaining no visible damage to the wall panel even past the 2.5% design level drift; however, due to a design fault, a push-out failure of the dissipator bars resulted in limited energy dissipation. Nevertheless, the lateral load capacity was not significantly affected by this failure and the unit sustained a drift in excess of 6% before the tendons ruptured.

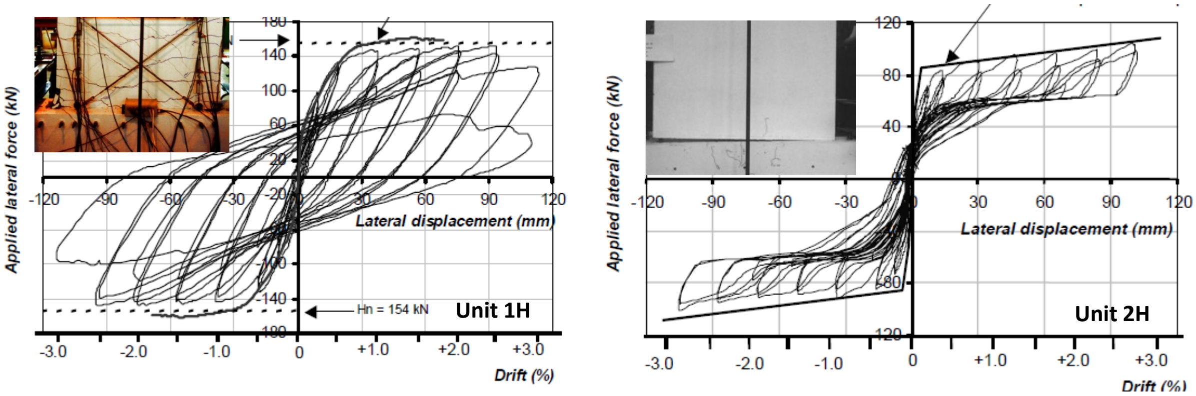

Figure 2-6- Lateral force-drift response of Units 1H and 2H (from Holden et al. 2003)

2.2.3 Quasi-static tests of UPT walls by Perez et al. (2004, 2013)

An experimental investigation of the behavior of multistory UPT walls under quasi-static monotonic and cyclic lateral loads was carried out at the ATLSS Center at Lehigh University (Perez et al. 2004, 2013). Five half-scale walls were tested; one wall subjected to monotonic lateral loading (TW1) and four walls tested under reversed cyclic lateral loading (TW2-TW5) The objective of the tests was to investigate the effect of different parameters on the lateral load behavior of the walls. The parameters considered included: the total area and location of PT steel, the initial stress in the PT steel, and the confining reinforcement details at the base of the wall. A typical test wall, together with a summary of the test variables, is shown in Figure 2-7.

The behavior of all test walls was governed by gap opening along the base joint. All walls sustained large drifts with minimal damage and displayed excellent self-centering characteristics. The largest residual drift in any test wall prior to failure was 0.1%. With the exception of test wall TW2, where a sudden buckling failure of the confined region of the base panel occurred, failure generally occurred when the confining steel at the base of the wall fractured. As no additional energy dissipating mechanism was provided in these test walls, the primary source of energy dissipation was the nonlinear behavior of the confined concrete at the ends of the wall and yielding of the post-tensioning steel. Significant prestress losses were observed under cyclic loading, with TW5 losing its entire prestress. Stiffness degradation due to nonlinear behavior of the confined concrete was observed for all test walls under cyclic loading with TW2 and TW4 displaying 50% reductions in their lateral stiffness, whereas TW3 and TW5 experienced 72% reductions.

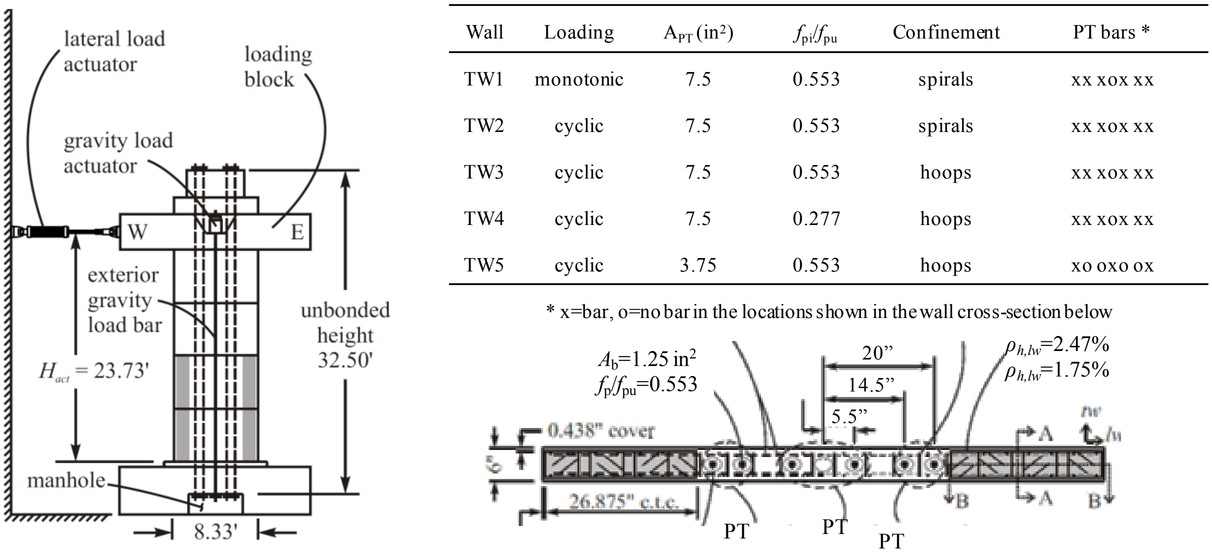

Wall	Loading	A_{PT} (in^2)	f_{pi}/f_{pu}	Confinement	PT bars *
TW1	monotonic	7.5	0.553	spirals	xx xox xx
TW2	cyclic	7.5	0.553	spirals	xx xox xx
TW3	cyclic	7.5	0.553	hoops	xx xox xx
TW4	cyclic	7.5	0.277	hoops	xx xox xx
TW5	cyclic	3.75	0.553	hoops	xo oxo ox

* x=bar, o=no bar in the locations shown in the wall cross-section below

Figure 2-7 – Lehigh typical test wall configuration and test wall variables (from Perez et al. 2004)

Comparisons between responses of TW4 and TW3 (Figure 2-8) show that reducing the initial stress in the concrete by reducing the initial prestress in the PT steel (f_{pi}), while maintaining the total area of PT steel (A_p) constant, resulted in a wall that softened earlier (smaller range of linear elastic behavior), but achieved the same strength and failed at a larger lateral drift than a wall with the same A_p, but with a higher f_{pi}. Comparison between responses of

TW3 and TW5 (Figure 2-8) show that reducing A_p while keeping f_{pi} constant, thus reducing the initial stress in the concrete, resulted in a wall that softened earlier, had reduced strength, but had over twice the lateral drift capacity of a wall with the same f_{pi} but with a larger A_p.

The Lehigh test results showed that the lateral load behavior of unbonded post-tensioned precast concrete walls can be effectively controlled through appropriate selection of the critical design parameters and provided a wealth of data for validation of analytical models. In Chapter 3 the Lehigh test walls are used to validate the analytical models developed in this study. However, it should be noted that, as no additional energy dissipation mechanism was provided in the Lehigh test walls, they did not satisfy ACI ITG-5.2 (2009) requirements.

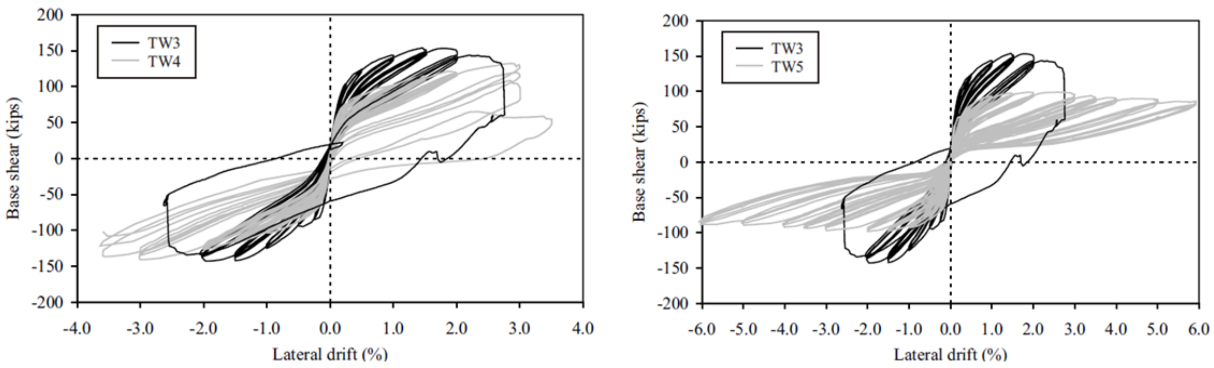

Figure 2-8 – ATLSS experimental results for test walls TW3, TW4 and TW5 (from Perez et al. 2004)

2.2.4 Quasi static tests of UPT walls by Smith and Kurama (2012)

A research project at the University of Notre-Dame investigated lateral load behavior of precast concrete wall structures that use a combination of mild steel reinforcing bars and unbonded post-tensioning steel (Smith et al. 2012, Smith and Kurama 2012). As part of the experimental program, a total of six 0.4-scale precast concrete wall specimens were tested under quasi-static reversed cyclic lateral loading. Five specimens (HW1-HW5) utilized hybrid reinforcement details (ED mild reinforcement and PT steel) and one emulative control wall (EW) utilized only mild steel reinforcement. The primary experimental variables included relative amounts of mild steel and PT steel, concrete confinement details at the base panel, and presence of perforations within the wall panels. The specimens were 2.43 m (l_w) long by 159 mm (t_w) thick. As shown in Figure 2-9, the lateral load was applied at 3.66 m from the wall base, resulting in a relatively low wall base moment to shear ratio: $M/(Vl_w) = 1.5$.

A primary focus of the project was code approval of UPT precast concrete walls as special reinforced concrete structural walls according to ACI ITG-5.1 (2007). The ACI ITG-5.1 Standard provides the minimum required experimental evidence and acceptance criteria for Special Unbonded Post-Tensioned Precast Structural Walls. For the given wall dimensions, the prescribed validation-level drift (or maximum drift) per ACI ITG-5.1 was $\Delta_w = 2.3\%$.

Specimen HW1 sustained a premature failure at a lateral drift of 1.9% due to smaller than specified concrete compressive strength (f_c') and misplaced boundary transverse (confinement) reinforcement. With these issues addressed, Specimen HW2 was ultimately subjected to three fully-reversed cycles to the validation-level drift of 2.3%. However, during the 1.5% cycles, the ED bars pulled out from the (ACI 318 Type II) mechanical splice connectors placed inside the foundation, which resulted in strength loss and reduced energy dissipation in HW2. In Specimen HW3, the full development length inside the foundation was provided for the ED bars, instead of the Type II mechanical splice connectors. As shown in Figure 2-9, HW3 sustained two fully-reversed drift cycles to 2.3% followed by a cycle to 3.0%. The total strength loss in HW3, from the peak base shear during the test to the peak resistance during the 3.0% cycle, was 20% and was associated with concrete crushing that was observed at the wall toes, and extended vertically approximately 355 mm ($\approx 2.2t_w$) from the base. Specimen HW4 was essentially identical to HW3, except for perforations within the wall panels and modifications to the confining reinforcement of the base panel to reduce concrete damage observed in HW3. As shown in Figure 2-9, HW4 exhibited excellent re-centering, considerable energy dissipation and smaller strength degradation than HW3. Finally, failure in Specimen HW5, which included larger perforations than HW4 and reduced ratio of PT steel to ED steel, occurred during the first cycle to 2.3%. Due to the reduced ratio of PT to ED steel, upon unloading of the wall after significant tensile yielding of the ED bars, the restoring force was not sufficient to yield the bars back in compression. Therefore, a residual gap along the base joint developed and ultimately, upon unloading from the first cycle to -2.3%, the wall failed through large out-of-plane displacements at the base, and buckling of the ED bars in compression (Smith et al. 2012). In the emulative specimen (EW) test, a residual gap also developed along the entire length of the base joint due to insufficient restoring force, which, in this case, was provided only by the axial load. This behavior caused excessive horizontal slip and large strength and stiffness degradation that ultimately led to failure of the emulative specimen at a small drift (3rd cycle at 1.15%).

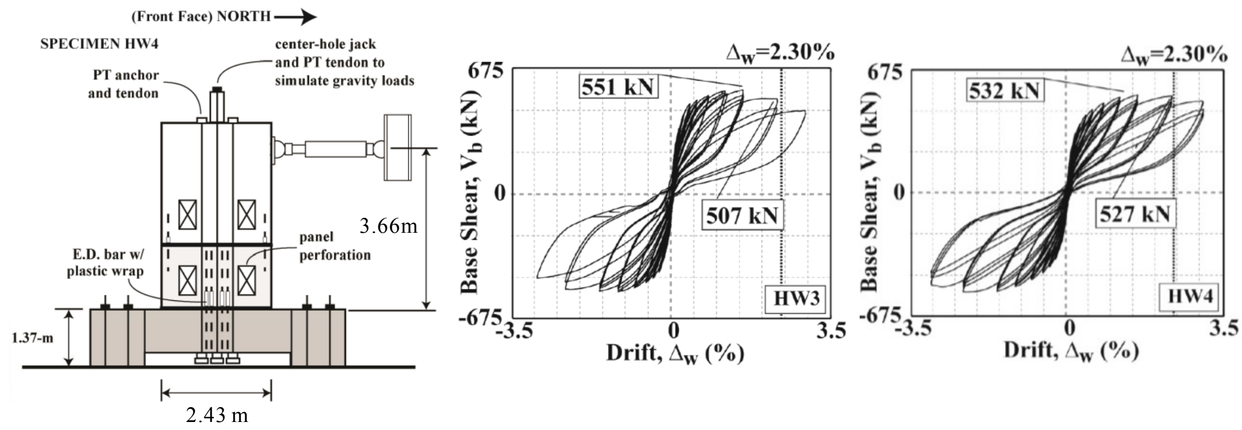

Figure 2-9 Test setup and response of specimens HW3 and HW4 (from Smith et al. 2012)

2.2.5 Monotonic tests on UPT precast wall panels by Henry et al. (2012)

Henry et al. (2012) conducted a series of 32 tests on UPT precast wall panels. The wall panels in this study had no special confinement reinforcement at the wall toes and no energy dissipating bars were included at the wall-to-foundation joint. This type of UPT wall was intended for applications in low- or non-seismic regions. The wall panels were tested under monotonic only loading with the objective of investigating the magnitude of axial compressive strains that develop in the toe region of UPT walls. Based on the experimental results, it was recommended that a strain of 0.005 be used for defining the nominal moment capacity of UPT concrete walls, as opposed to the 0.003 concrete compressive strain that is used for conventional RC structural walls.

The study also pointed out the challenges in obtaining reliable experimental concrete strain measurements in the toe region of UPT walls. It was argued that, due to the single crack that develops at the wall-to-foundation interface, the strain at the extreme compression fiber of a UPT wall increases significantly near the base of the wall. In comparison, inelastic deformations in conventional RC walls are assumed to be distributed over a larger height, so that concrete strains at the extreme compression fiber change less severely along the height of the wall near the base. Due to the steep strain gradient at the base of the UPT walls, obtaining accurate measurements proved challenging despite employing various techniques such as displacement gauges, strain gauges, and photogrammetry (Henry 2011, Henry et al. 2012).

2.2.6 Dynamic tests on UPT walls by Marriot et al. (2008)

Marriot et al (2008) performed shake-table tests on UPT precast concrete walls at the University of Canterbury in New Zealand. A total of five post-tensioned walls with alternative energy dissipating solutions, including mild steel (hysteretic) tension-compression yielding devices

(TCY devices), viscous dampers, combinations of the above, and finally a UPT wall that relied on contact damping alone, were tested. Experimental results showed that all performance objectives were generally achieved, with peak lateral displacements below the targets for design level and maximum considered earthquake excitation, except for the wall that relied only on contact damping. Damage to the wall specimens upon completion of the tests was minor for all wall specimens.

2.2.7 DSDM shake table test on a three-story half-scale precast concrete building

Finally, with respect to dynamic testing of UPT walls, it should be noted that as part of a four-year-long research project on development of a diaphragm seismic design methodology (DSDM) for precast concrete buildings, a three-story, half-scale, precast concrete structure, which utilized UPT walls in one direction of response, was tested in 2008 on the shake-table at San Diego. Although the main objective of the test was to examine the diaphragm response and connections, the performance of the UPT walls is also documented in Schoettler et al. (2009).

Figure 2-10 Half-scale, three-story, precast building on shake table at University of California, San Diego

While the UPT walls in the test building generally performed as intended, under the design-level excitation (peak wall roof drift ratio of 1.90%) one of the energy dissipating bars at the base of one of the walls fractured. This resulted in increased demands and reduced flexural capacity under the subsequent MCE-level excitation. The increased force demands in the PT steel exceeded the design level limit and tendon failures at the anchor wedges occurred under the MCE test. Schoettler et al. (2009) report that tendon failure occurred at an average strand stress of $0.45f_{\mathrm{pu}}$. Noting that the ten strands in each wall had been simultaneously seated with hollow-core jacks rather than each strand being individually seated, Schoettler et al. (2009) argue that the tendon failure was likely influenced by uneven force distribution among the strands.

2.3 Analytical research

Prior analytical studies related to UPT concrete systems range from simplified methods to characterize their monotonic response (Pampmanin et al. 2001, Aaaleti and Sritharan 2009) to lumped plasticity and multi-spring models (Palermo et al. 2006, Pennucci et al. 2009), fiber element models (Kurama et al. 1996, Perez et al. 2007, Smith et al. 2012) and more detailed continuum finite element models (Henry et al. 2012). Given the limited experimental data on dynamic responses and interactions of full scale, three-dimensional UPT structural systems subjected to dynamic loading, the aforementioned models have been primarily validated against quasi-static cyclic tests of individual components.

2.4 Existing code and design guidelines for UPT precast concrete walls

2.4.1 ACI ITG-5.1 and ACI ITG-5.2 Standards for UPT walls

Available experimental research and analytical studies on UPT precast concrete walls have demonstrated that these systems are suitable for use in regions of high seismicity (Seismic Design Categories D through F) as they have the potential for reducing damage and permanent deformations after a major seismic event. Despite their improved seismic performance compared to conventional reinforced concrete systems, these types of jointed systems do not satisfy the prescriptive requirements of Chapter 21 of ACI 318-11 for structural walls of monolithic construction and are currently permitted by ACI 318 (Section 21.1.1.8) only if experimental evidence and analysis demonstrate that the strength and toughness of the proposed system equals or exceeds that provided by a comparable monolithic reinforced concrete system that satisfies the prescriptive requirements of Chapter 21. This limitation is attributed to the fact that the proportioning and detailing requirements of Chapter 21 in ACI 318 were primarily based on field and laboratory experience with monolithic reinforced concrete structures or precast concrete structures designed and detailed to behave like monolithic structures (referred to as reinforced concrete emulation).

In precast structures that are designed according to the reinforced concrete emulation approaches, inelastic demand is spread over a plastic hinge length, similar to monolithic reinforced concrete structures. Under the design earthquake, these structures can suffer significant cracking and concrete crushing in the plastic hinge regions. In contrast, in jointed precast systems such as UPT walls, the precast members are maintained essentially in the elastic range as inelastic demand is accommodated within the connection through the opening and closing of the joint at the interface between the precast walls and the foundation. While reinforced concrete emulation systems generally rely on bonded mild steel reinforcement for strength and ductility, jointed precast systems such as UPT walls rely on unbonded post-tensioning steel for flexural strength and re-centering, while mild bonded steel bars (or external dissipative devices) provide energy dissipation and additional flexural strength.

As previously mentioned, ACI 318 does not allow direct extrapolation of the requirements for monolithic concrete structures to jointed precast structures and requires testing and analysis results to demonstrate their equivalence. ACI ITG-5.1 (2007) gives the minimum required experimental evidence and acceptance criteria for Special Unbonded Post-Tensioned Precast Structural Walls. Specific requirements are given with regards to the tested wall roof drift, measured wall lateral strength to predicted strength ratio, stresses and strains in the post-tensioning steel, amount of energy dissipation, strength degradation, and shear slip along the horizontal joints. Similar information for Special Precast Hybrid Moment Frames is provided in ACI 374.1-05. A step towards accommodating unbonded post-tensioned precast wall systems within the ACI 318 design context without the requirement for expensive and time-consuming testing was achieved with ACI ITG-5.2 (2009). This Standard defines procedures that can be used to design Special Unbonded Post-Tensioned Precast Shear Walls that satisfy ACI ITG-5.1.

ACI ITG-5.2 defines design requirements for a certain class of unbonded post-tensioned precast concrete walls that can be used as special reinforced concrete structural walls for Bearing Wall and Building Frame Special Reinforced Concrete Shear Wall Systems, as defined in ASCE/SEI 7. The characteristic wall configurations that are covered in this Standard are: Individual (uncoupled) or coupled walls composed of precast panels, one story or more in height, vertically post-tensioned with tendons that are unbonded from an anchor in the foundation to an anchor at the top of the wall. The walls should have essentially planar proportions in the vertical direction, with no significant discontinuities in plan, or in vertical configuration, and are designed to have a single critical section at the base of the wall.

The walls covered in this standard should have tendons placed either in a single duct at the centroid of the wall or in two or more ducts symmetrically positioned about the centroid and within 10% of the wall length from that centroid. For uncoupled walls, energy dissipation should be provided by two sets of vertical reinforcing bars (energy dissipating bars) crossing the wall-foundation interface and designed to yield over a specified unbonded length. The energy dissipating bars should be positioned symmetrically about the centroid of the wall. In coupled walls, energy dissipation is provided by coupling mechanical devices connecting the vertical boundaries of adjacent wall panels. The coupling devices should be distributed uniformly along the height of the panel with at least two devices at each connected vertical boundary of every precast panel.

ACI ITG-5.2 contains the minimum requirements for ensuring that the types of uncoupled and coupled precast walls covered by this Standard are able to sustain a series of oscillations in the inelastic range without significant loss of strength or excessive story drifts. The walls designed to this Standard should exhibit minimal or no damage to the precast wall and minimal or no residual deformations under the design earthquake.

2.4.2 PRESSS Design guidelines for precast concrete seismic structural systems

As part of the PRESSS research program, briefly described in Section 2.1.1, a set of design guidelines was developed (Stanton and Nakaki, 2002) for the precast systems that were utilized in the five-story test building. It is noted that the precast wall system utilized in the PRESSS program consisted of coupled walls with shear connectors at the vertical joints between the precast panels. More recently, a newer set of design guidelines, the "PRESSS design handbook" has been published by the New Zealand Concrete Society (NZCS, 2010).

2.4.3 Appendix B of the New Zealand Concrete Structures Standard

The New Zealand Concrete Structures Standards (NZS 3101:2006) includes a normative Appendix with special provisions for the seismic design of ductile jointed precast concrete structural systems. This document is more general than the ACI ITG-5.2 Standard as it applies to a broader category of jointed precast concrete structures (structural walls, moment resisting frames and dual systems) consisting of precast concrete elements assembled by post-tensioning techniques with or without the presence of non-prestressed steel reinforcement or other energy dissipating devices.

The general design approach adopted in the New Zealand Standard is similar to that of the ACI ITG-5.2 Standard. The main objective is to achieve self-centering response and minimal damage under the design earthquake. The condition for full re-centering response is expressed in the NZ Standard by an upper limit on the moment contribution ratio, λ:

$$\lambda = \frac{M_{\mathrm{PT}} + M_{\mathrm{N}}}{\mathrm{M_s}} \geq \alpha_0 \qquad \text{Equation 2-1}$$

where M_{PT}, M_{N} and M_{s} are the flexural strength contributions of the post-tensioning tendons, the axial load and the non-prestressed steel reinforcement or energy dissipating devices calculated with respect to the centroid of the concrete compression resultant of the section. The factor α_0 (≥ 1.15) is the overstrength factor of the non-prestressed steel reinforcement or the energy dissipating devices.

The NZ Standard includes an important provision related to drift limits, which are typically set to recognize the correspondence between observed damage and displacement demand (and ultimately material strains). As jointed precast concrete systems are expected to have reduced (structural and non-structural) damage compared to equivalent monolithic systems, the NZ Standard allows higher drift limits to be used for jointed precast concrete systems. In particular, the drift limits corresponding to a damage control limit state are permitted to be 50% higher than corresponding values for equivalent monolithic structures.

2.5 Residual displacements

The inherent advantage of unbonded post-tensioned precast concrete systems over conventional monolithic structures is their ability to re-center after an earthquake. This section discusses the role of residual displacements in performance of structures and presents previous research on the development of performance-based methodologies that incorporate residual displacements into the design or assessment process.

Large residual deformations after an earthquake can result in increased cost of repair or replacement of non-structural elements, and may even render a structure unusable or irreparable given the difficulty of straightening a leaning building. Moreover, excessive residual deformations can make a building appear unsafe to its occupants or undermine its performance in subsequent earthquakes. Reports from earthquake reconnaissance observations have highlighted the importance of residual deformations. In the 1995 Kobe earthquake, several low-rise reinforced concrete buildings sustained large residual deformations despite suffering relatively low structural damage (Okada et al. 2000) and about 100 reinforced concrete bridge piers had to be demolished and rebuilt after the earthquake due to residual drifts exceeding 1.75% (Kawashima et al. 1998). Ruiz-Garcia and Miranda (2006) also report that several reinforced concrete buildings in Mexico City were demolished after the 1985 earthquake due to the technical difficulties associated with straightening and repairing buildings with large permanent deformations.

These examples indicate the need for consideration of residual displacements in the seismic design or assessment process. If structural performance is evaluated based on maximum response only (without consideration of residual deformations), as typically done in current codes, then expected economic losses are likely to be underestimated for structures that sustain large residual deformations while the enhanced characteristics of inherently self-centering systems cannot be captured. As use of Performance-Based Seismic Design approaches that aim at realistically assessing building performance and expected losses at various levels of seismic intensity become more common, it is essential that residual deformations are evaluated and incorporated in the design or assessment process.

In Performance-Based Design, performance design objectives are defined by coupling different performance levels with different levels of seismic intensities. The performance levels represent the maximum acceptable extent of structural and non-structural damage for a given intensity of seismic input and are thus associated with losses and repair costs. Although, typically, the performance levels are expressed using structural response indices related to the maximum deformation (such as the maximum interstory drift), recently the residual deformations sustained by a structure after an earthquake have been highlighted as an additional damage indicator for quantifying the performance level of the structure (Christopoulos et al. 2004, Ruiz-Garcia and Miranda 2006, Pettinga et al. 2007) and methods for including residual local and global deformations in Performance-Based Design and Assessment approaches have been proposed and implemented (e.g., LATBSDC 2008). Pampanin et al. 2003 proposed a 3-dimesional performance domain where for a given seismic intensity, the performance level of a structure is evaluated using a combination of maximum and residual drift. Application of such a framework requires an estimate of the expected levels of permanent deformations in structures and the level of uncertainty involved in the estimation procedures.

Previous studies on the magnitude of residual deformations range from parametric studies on residual displacements of elastoplastic single-of-freedom systems to probabilistic assessment of residual drift demands on multi-degree-of-freedom systems. Early analytical studies mainly focused on identifying the parameters that control the magnitude of residual displacements of single-degree-of-freedom (SDOF) systems. The hysteresis loop shape was identified as a controlling factor. MacRae and Kawashima (1997) studied the response of several elastoplastic SDOF oscillators and found that the residual displacement ratio, which is defined as the residual displacement divided by the maximum possible residual displacement (obtained by unloading from the peak displacement), was almost totally dependent on the stiffness ratio of the bilinear curve (post-elastic stiffness to initial stiffness), with negative stiffness ratios resulting in larger residual displacements. In a subsequent study Kawashima et al. (1998) verified the dependence of residual displacements of elastoplastic SDOF systems on the stiffness ratio and calculated residual displacement spectra as a function of the stiffness ratio.

Christopoulos et al. (2003) conducted response history analyses of SDOF systems using three different hysteretic models (elastoplastic, Takeda degrading stiffness model and flag-shaped) and found residual displacements to be influenced by hysteretic characteristics, post-yield stiffness and maximum ductility. The elastoplastic hysteretic rule was found to result in higher residual displacements especially for cases of negative post-yielding stiffness (as could be induced by significant P-Δ effects). The Takeda systems exhibited almost constant residual/maximum displacement ratios for all effective periods while the elastoplastic systems exhibited a linear increase for longer effective periods. The superior performance of the self-centering systems which exhibited zero residual displacements while reaching similar levels of ductility as the other systems was emphasized and it was noted that these systems were less sensitive to decreasing values of post-yield stiffness and thus possibly less affected by P-Δ effects. In a companion paper (Pampanin et al. 2003) the authors extended the results to multi-degree-of-freedom (MDOF) systems by starting from the effective residual drift of an equivalent

SDOF system and introducing amplification factors to account for higher-mode effects and P-Δ effects.

It is worth noting that all the above referenced studies recognized that the scatter in residual deformations about the mean was considerable and generally larger than the scatter in peak displacements. In their study, Ruiz-Garcia and Miranda (2010) incorporated the uncertainty (record-to-record variability) in the estimation of residual drift demands by using a probabilistic procedure to compute residual drift demand hazard curves.

FEMA P-58 also recognizes that residual drifts predicted by nonlinear analysis are highly sensitive to component modeling assumptions related to post-yield hardening/softening slope and unloading response, and suggests that accurate statistical simulation of residual drift requires the use of advanced component models, careful attention to cyclic hysteretic response, and a large number of ground motion pairs.

Table 2-1 Damage states for residual story drift ratio (from FEMA P-58)

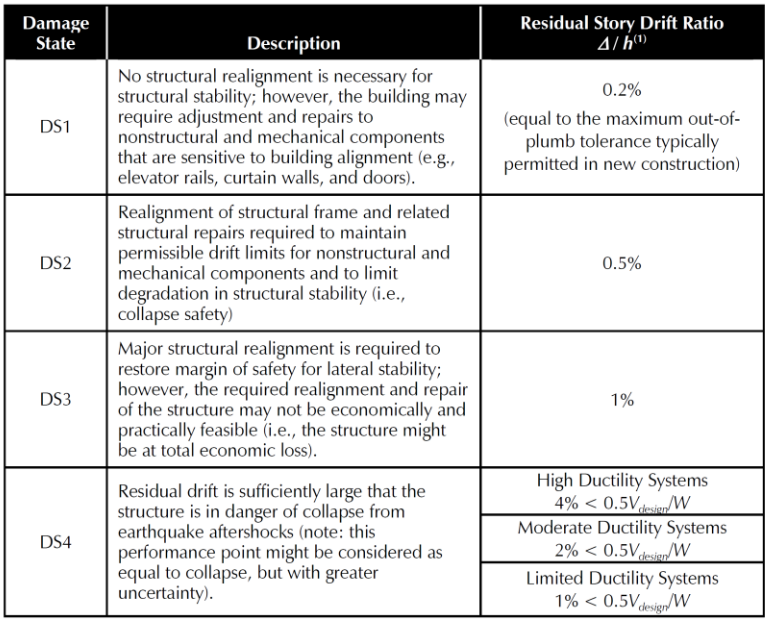

Damage State	Description	Residual Story Drift Ratio $\Delta / h^{(1)}$
DS1	No structural realignment is necessary for structural stability; however, the building may require adjustment and repairs to nonstructural and mechanical components that are sensitive to building alignment (e.g., elevator rails, curtain walls, and doors).	0.2% (equal to the maximum out-of-plumb tolerance typically permitted in new construction)
DS2	Realignment of structural frame and related structural repairs required to maintain permissible drift limits for nonstructural and mechanical components and to limit degradation in structural stability (i.e., collapse safety)	0.5%
DS3	Major structural realignment is required to restore margin of safety for lateral stability; however, the required realignment and repair of the structure may not be economically and practically feasible (i.e., the structure might be at total economic loss).	1%
DS4	Residual drift is sufficiently large that the structure is in danger of collapse from earthquake aftershocks (note: this performance point might be considered as equal to collapse, but with greater uncertainty).	High Ductility Systems 4% < $0.5V_{design}/W$
		Moderate Ductility Systems 2% < $0.5V_{design}/W$
		Limited Ductility Systems 1% < $0.5V_{design}/W$

Given that these requirements are computationally demanding, FEMA P-58 provides estimates of median residual drifts (Δ_r) as a function of the peak transient drift, based on results of previous analytical studies: $\Delta_r = 0$ for $\Delta \leq \Delta_y$, $\Delta_r = 0.3(\Delta - \Delta_y)$ for $\Delta_y < \Delta < 4\Delta_y$ and $\Delta_r = \Delta - 3\Delta_y$ for $\Delta \geq 4\Delta_y$. In the above expressions, Δ is the peak (median) story drift calculated by analysis and Δ_y is the median story drift at yield. Finally, Appendix C of FEMA P-58 relates predicted residual drift ratios to expected damage in the structure by identifying damage states associated with different values of residual drift. These damage states range from onset of damage to nonstructural components to near-collapse of the structure and are summarized in Table C-1 of FEMA P-58, reproduced here as Table 2-1.

2.6 Summary

Following the successful testing of the five-story PRESSS precast concrete building, a number of experimental studies have demonstrated the advantages of UPT walls, namely, the ability to recenter even after large nonlinear displacements and, the minimal damage to the structural elements as inelastic demand is accommodated at the wall-to-foundation interface through the gap opening behavior. The majority of these experimental studies on UPT walls involved two-dimensional, moderate-scale structures tested under quasi-static cyclic loading. Similarly, prior analytical studies and design methodologies for UPT walls have been primarily validated against quasi-static cyclic tests of individual components.

The recent E-Defense shake table tests on a full-scale, four-story precast post-tensioned building that utilized UPT walls, added a wealth of data to the limited database on dynamic responses and interactions of UPT systems. The tests provided unique data to assess behavior of UPT walls under multi-directional dynamic loading and investigate system interactions (e.g., wall with UPT beams and slab). Following Chapter 3, which is devoted to analytical component-level studies, Chapter 4 provides an overview of the E-Defense precast post-tensioned test building and an assessment of the design of the E-Defense UPT walls based on ACI ITG-5.2. Chapter 5 presents detailed experimental results for a range of responses in the wall direction of the test building, with an emphasis on performance of the two UPT walls. Finally, Chapter 6 describes the development and experimental verification of a nonlinear analytical model in the wall direction of the E-Defense test building. Together with the experimental results and design aspects discussed in Chapters 4 and 5, the analyses provide valuable insight into the dynamic responses and interactions of a full-scale, three-dimensional UPT building.

Chapter 3 Modeling of unbonded post-tensioned components

Due to the jointed nature of UPT precast concrete structural systems, achieved through the use of unbonded post-tensioning steel, deformations primarily concentrate in the connections between the precast elements and damage along the member lengths is generally limited. As a result, modeling of the connections (e.g. wall-to-foundation in UPT walls, or beam-to-column in UPT frames) is critical in simulating the response of UPT structural systems.

The end goals of this work, as identified in Chapter 1, are to (i) document the shake table tests on a full-scale, four-story, precast post-tensioned building that was tested on the E-Defense shake table in 2010 and utilized UPT structural systems in one direction of response (UPT walls, UPT beams), (ii) assess interactions of full scale, three-dimensional UPT structural systems subjected to dynamic loading and (iii) develop an analytical model of the test building in the direction that utilized UPT systems that is able to capture the experimentally measured dynamic responses and observed interactions.

Prior to analyzing the complete test building, under the imposed dynamic loading, separate analytical component-level studies were conducted to establish and experimentally verify modeling approaches for UPT connections under static cyclic lateral loading conditions. More specifically, analytical models of cantilevered UPT walls, tested at Lehigh University by Perez et al. (2013), and UPT beam-column sub-assemblages tested at the National Institute of Standards and Technology (NIST) by Stone et al. (1995), were developed using the commercially available software Perform3D (CSI, 2011a). The models were validated through comparisons of analytical results with published experimental data from the tests. These component-level studies are documented in this chapter. In Chapter 6, the modeling approaches validated through the component studies presented herein will be implemented in the analytical model of the E-Defense PT building to examine how approaches suitable for component-level analyses can be extended to predict responses at the system-level, and capture interactions between individual components.

3.1 UPT wall model and experimental validation

Tests on UPT cantilever walls conducted at Lehigh University by Perez et al. (2004, 2013), served as the basis for the development of the analytical model for UPT walls described herein. A summary of the experimental program was provided in Section 2.2.3. Additional information is provided herein as it relates to the development of the analytical models.

3.1.1 UPT wall tests at the ATLSS Center at Lehigh University

A total of five unbonded post-tensioned precast concrete walls were tested by Perez et al. (2004, 2013); one of them under monotonic lateral loading (TW1) and four under reversed cyclic lateral loading (TW2-TW5). The 5/12-scale test walls consisted of four precast wall panels, each 65 in tall, 100 in (l_w) long and 6 in (t_w) thick. A loading block, and a filler and extension panel, were also provided resulting in an overall height of 360 in.

The precast panels were post-tensioned to the foundation with unbonded PT bars symmetrically located about the vertical wall centerline, with a total unbonded length, including length within the foundation and filler panel, of 390 in (Figure 3-1). Fiber-reinforced grout was provided at the wall-foundation interface and closely spaced transverse reinforcement or spirals confined the ends of the bottom two panels (Figure 3-2). The walls were tested under reversed cyclic lateral load applied at a height of 284 in from the base and constant axial load ($P/A_g f_c' \approx$ 0.036).

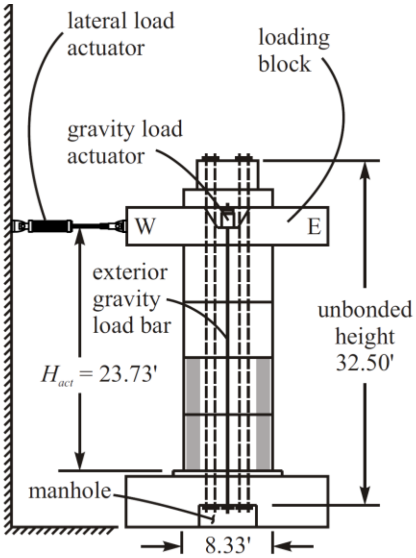

Figure 3-1 UPT walls tested at Lehigh University; test setup (from Perez et al. 2004)

Table 3-1 summarizes the parameters of the five test walls including the area of PT steel in the section (A_{PT}), the initial prestress as a percentage of the ultimate strength of the PT steel ($f_{\mathrm{pi}}/f_{\mathrm{pu}}$) the type of confinement (hoops or spirals) and the location of the PT bars. Typical cross-sections at the base of the hoop-confined and spiral confined wall panels are shown in Figure 3-2 and Figure 3-3, respectively.

Table 3-1 Test wall parameters (from Perez et al. 2004)

Wall	Loading	A_{PT} (in^2)	f_{pi}/f_{pu}	Confinement	PT bars *
TW1	monotonic	7.5	0.553	spirals	xx xox xx
TW2	cyclic	7.5	0.553	spirals	xx xox xx
TW3	cyclic	7.5	0.553	hoops	xx xox xx
TW4	cyclic	7.5	0.277	hoops	xx xox xx
TW5	cyclic	3.75	0.553	hoops	xo oxo ox

* x=bar, o=no bar in the locations shown in the wall cross-section below (Fig. 3.2)

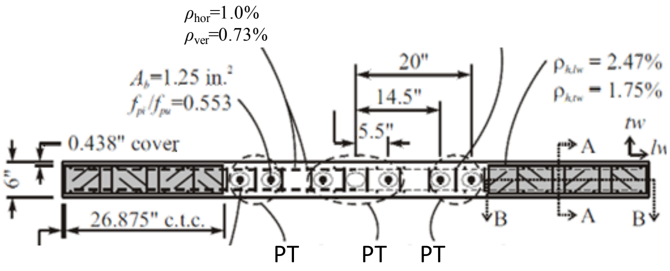

Figure 3-2 Typical wall cross section at base of hoop-confined wall panel (from Perez et al. 2004)

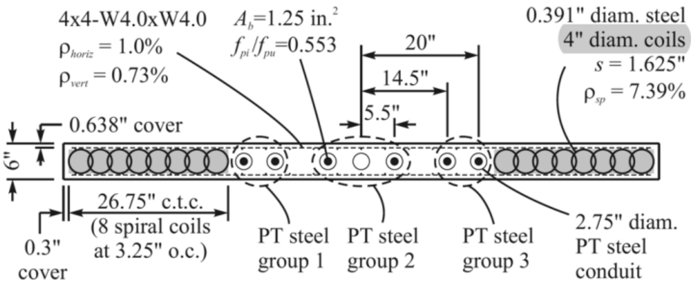

Figure 3-3 Typical wall cross section at base of spiral-confined wall panel (from Perez et al. 2004)

3.1.2 Development of analytical model of UPT walls

Analytical models of the five UPT walls which were tested at Lehigh University were developed in Perform-3D (CSI, 2011a). The UPT walls were modeled using a combination of inelastic "shear wall elements" and truss elements.

Shear wall elements in Perform3D are 4-node macro-elements organized in two primary layers acting in parallel: an axial-bending layer and a shear layer. The axial-bending properties parallel to the element axis, associated with vertical axial deformations and vertical bending, are captured by fiber sections consisting of concrete and steel fibers. Each fiber is characterized by its area and location along the section, and is assigned a uniaxial stress-strain relationship (elastic or inelastic). Axial strain and curvature are assumed to be constant along the element length (vertical axis). Thus, a shear wall element is a lower order element than a typical beam element, where the curvature varies linearly along the element length (CSI, 2011b).

Acting in parallel with the axial-bending layer, the shear layer only has shear stiffness and does not add any axial or bending stiffness. Similar to the axial-bending layer, it is defined by a shear material, described by an elastic or inelastic stress-strain relationship, and is based on the assumption of constant shear stress in the element. In addition to these deformation modes (vertical axial-bending and shear), the element also accounts for horizontal axial and bending deformations. However, these are assumed to be secondary and are defined using elastic properties (elastic transverse stiffness). Note that contrary to the "shear wall element" described herein, the "general wall element", also included in Perform3D's element library, allows horizontal axial-bending deformations to be defined using inelastic fiber sections.

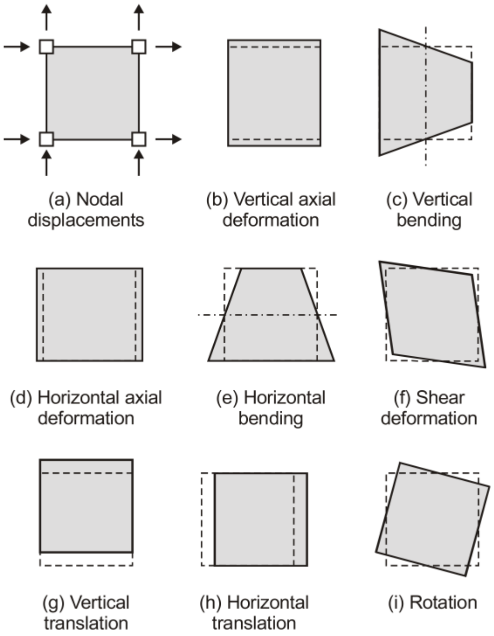

Figure 3-4 In-plane deformations of shear wall element in Perform3D (from CSI, 2011b)

Figure 3-4 shows the five in-plane deformation modes described above (vertical axial deformations, vertical bending, shear, horizontal axial deformations, and horizontal bending) and the three in-plane rigid body modes (vertical translation, horizontal translation and rotation) of the shear wall element. Note that similar to horizontal axial-bending deformations, out-of-plane deformations are assumed to be of secondary importance and are defined based on an elastic out-of-plane bending stiffness.

Finally, with respect to the shear wall element in Perform3D, it is noted that while axial-flexural interactions (e.g., effect of axial load on flexural strength, shifting of the neutral axis as concrete fibers crack and steel fibers yield) are adequately implemented within the fiber section, interactions between flexural and shear deformations are not captured. Although the axial-bending layer and shear layer interact, since they are connected at the element nodes, this interaction only models typical beam action (with the additional limitation that curvature is assumed to be constant along each wall element) and does not capture the actual shear-flexure interaction that occurs in concrete elements under multi-axial stress (combined axial load, shear and flexure). Experimental and analytical studies (Massone and Wallace 2004, Beyer et al. 2011, Tran 2012, Kolozvari et al. 2014) have shown that even for flexure-controlled RC walls, shear displacement-shear force relationships can be highly nonlinear, with inelastic shear deformations initiating simultaneously and increasing almost proportionally with inelastic flexural deformations. These types of interactions are not captured in the shear wall element in Perform3D, which does not consider multi-axial stress and instead separates the various aspects of behavior into uncoupled layers, with uniaxial stress in each layer, as described in the previous paragraphs. This limitation poses challenges in selecting an appropriate shear material behavior, e.g., selection of an effective shear stiffness when an elastic shear material is used, or definition of shear stress-shear strain backbone curves and cyclic degradation parameters when an inelastic shear material is used.

Despite the aforementioned limitation, shear wall elements in Perform-3D have been generally shown to predict reasonably well the behavior of conventional (monolithic) planar RC walls (PEER/ATC-72-1, Tuna 2012) and are commonly used in practice for nonlinear analysis of RC structural walls. However, when it comes to modeling of UPT walls, issues specific to the rocking behavior need to be addressed. Shear wall elements, as fiber elements, rely on the assumption that plane sections remain plane and there is no bond slip between concrete and steel. In UPT walls, the presence of unbonded reinforcement violates the strain compatibility assumption at the section level. Moreover, the assumption of plane sections remaining plane is generally not valid in the region close to the wall-foundation interface due to the separation gap. The following sections cover modeling issues of UPT walls including modeling of gap opening, meshing, and cyclic degradation.

3.1.2.1 Modeling of precast wall panels and gap opening

The precast concrete panels of the UPT walls were modeled in Perform3D using shear wall elements. The main features of shear wall elements were described in the previous section. Modeling issues specific to the behavior of UPT walls related to meshing, modeling of gap opening and material properties are discussed herein, with a focus on the modeling approaches used for the Lehigh test walls.

While in a conventional RC wall a single element for the entire wall length is generally adequate (Powell 2007), in a UPT wall where the critical section may not remain plane due to the separation gap, use of more elements per wall length is generally needed, especially when gap-bars are used to model uplift, as discussed in the following paragraph. It is noted that the "plane sections remain plane" assumption is still enforced within each shear wall element in Perform3D. A total of eight wall elements along the wall length were used in this study. This also allowed the base section to be discretized into an adequate number of fibers along the wall length. Note that there is a limit of sixteen fibers within the fiber section of each shear wall element in Perform3D.

A total of forty fibers along the wall length were used herein for the base section. A finer discretization (more fibers per element) is desirable near the ends of the wall at the base, in order to capture (i) the high concrete compressive strains that develop at these locations and (ii) the progression of concrete crushing into the section. As computational time increases with increasing number of inelastic fibers, coarser discretization can be used within the middle portion (web) of the base wall panel, which is expected to remain elastic. After concrete crushing initiates at the extreme fiber at the compressive toe of the wall, it progresses continuously into the cross section, resulting in the concrete compression area (and neutral axis depth) to progressively increase. In the idealized fiber section, concrete crushing occurs fiber by fiber and changes in concrete compression area are discontinuous (CSI, 2011b). In order to capture the progression of crushing into the section, and resulting degradation in lateral resistance of the wall, an adequate number of fibers need to be included within the estimated neutral axis depth of the wall at the base. A minimum of ten fibers within the estimated neutral axis depth were used in this study at each of the two ends of the base section.

Gap opening at the base of a UPT wall can be modeled using shear wall elements with concrete-only fibers (no-tensile strength) over a short distance (H_{cr}) from the base. In this way, gap opening under lateral load is simulated as elongation of the wall concrete fibers that go into tension (positive strain under zero stress, Figure 3-5a). Note that the base section consists only of concrete fibers as the mild steel reinforcement of the base panel does not cross the wall foundation-interface and the PT steel is modeled separately, outside the wall fiber section, as it is not bonded to the concrete (Section 3.1.2.2). Alternatively, the gap opening behavior can be modeled by connecting short nonlinear elastic "gap-hook bars" between the wall elements and a fixed base. The gap-hook bars have large compression stiffness to simulate the rigidity of the foundation but no tensile strength or stiffness. In this way, gap opening is simulated as uplift of the gap bars' top nodes as opposed to elongation of the wall concrete fibers above (Figure 3-5b). Note that, for this approach to be implemented as intended (elongation of gap bars as opposed to elongation of wall elements), a minimum tensile resistance needs to be provided to the wall elements (e.g. inclusion of concrete tensile strength).

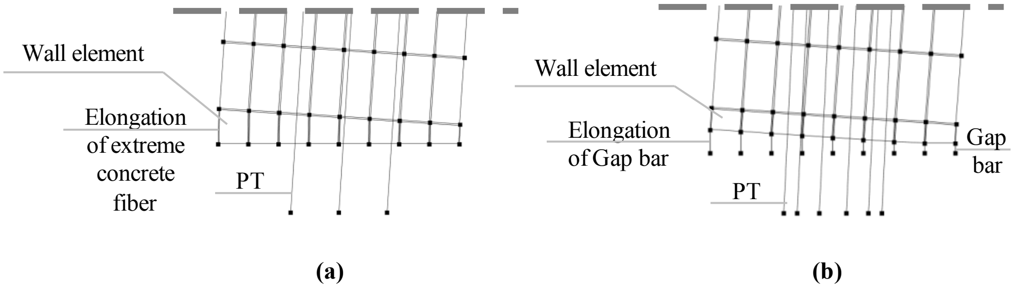

Figure 3-5 Modeling of gap opening at base of UPT wall as (a) elongation of wall element; (b) elongation of gap bar

Both approaches are able to capture the reduction in lateral stiffness associated with gap opening. By treating wall uplift separately from the concrete behavior, the latter approach (gap bars) better approximates the actual behavior at the wall-foundation joint but also requires a greater number of elements along the wall length to adequately capture the position of the neutral axis. When gap bars are used to model uplift it is recommended that at least one shear wall element is included within the estimated neutral axis depth at the critical base section (i.e. element size along wall length smaller than the neutral axis depth). In the present study, gap opening was modeled using shear wall elements with concrete-only fibers (no-tensile strength) over a critical height H_{cr} from the wall base. As shown in Figure 3-6, uplift is modeled as elongation of the extreme tensile fiber of the concrete section, as opposed to the actual separation gap that forms at the wall-foundation interface of the UPT wall.

It is noted that although the gap-opening displacements, calculated by integrating the concrete tensile strains over H_{cr}, are not that sensitive to the assumed value for H_{cr}, the calculated concrete compressive strains are dependent on the value of H_{cr}. Assuming a linear strain profile at the base of the wall and rotation, θ, occurring about the neutral axis (Figure 3-7), the concrete compressive strain at the wall toe can be approximated as $\varepsilon_c = \theta c/H_{cr}$, where c is the neutral axis depth of the wall. Note that when distributing the shortening of the extreme compression fiber (θc) over the element height H_{cr}, using the expression $\varepsilon_c = \theta c/H_{cr}$, it is assumed that the concrete strain is constant over a height H_{cr} at the base of the wall (Figure 3-8). This is consistent with the shear wall element in Perform3D, which assumes constant axial strain and curvature along the element length (H_{cr} in this case).

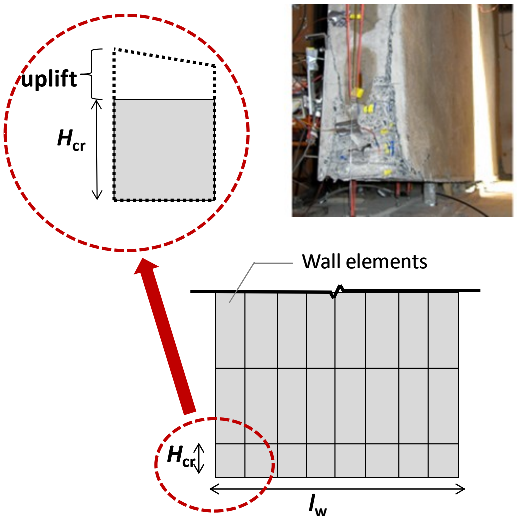

Figure 3-6 Modeling of gap opening at base of UPT wall

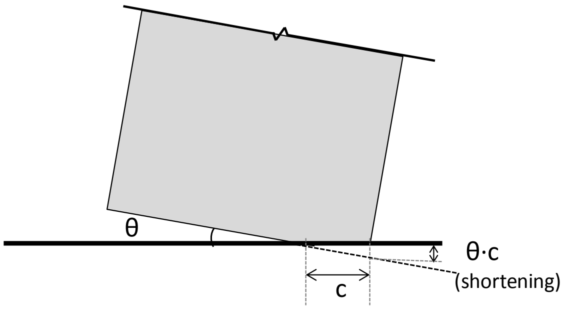

Figure 3-7 Axial shortening at wall toe assuming rotation about neutral axis and linear displacement profile

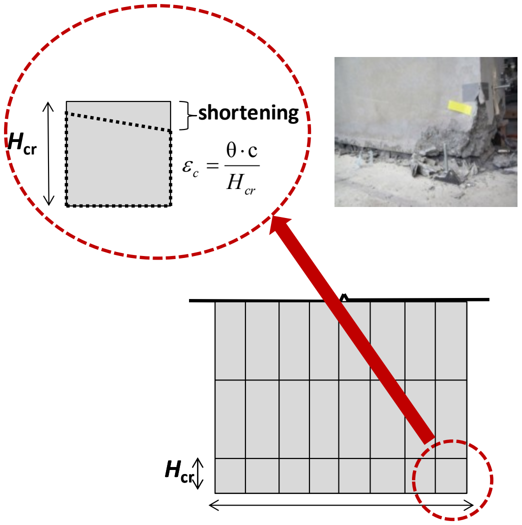

Figure 3-8 Concrete strain at extreme compressive fiber at wall toe

As mentioned in the previous paragraph, calculated concrete compressive strains are dependent on the value of H_{cr}, i.e., the height of the first row of wall elements. A short height for H_{cr} can lead to large concentrated deformations, nonlinear behavior of the concrete in compression, and early degradation in the moment-rotation behavior of the critical section. Accordingly, a longer height can underestimate peak concrete strains and overestimate moment strength at large rotations. Such dependence of calculated strains on element size is inherent in any fiber model and applies to both conventional RC and UPT precast concrete elements. However, selection of H_{cr} (height of fiber element closest to the base) should be based on different considerations for UPT walls compared to RC walls. As will be discussed in Chapter 5

(Section 5.3) with respect to observed damage to the UPT walls of the E-Defense PT building, performance of UPT walls is largely governed by the ability of the critical base joint to develop large compressive stains in a ductile manner without significant degradation in the concrete at the wall toes (or in the wall-to-foundation interface grout). In that respect, accurately predicting concrete strains is critical in design and analysis of UPT walls and selection of H_{cr} herein will be based on concrete strain considerations.

In a conventional RC wall, a height equal to the expected plastic hinge length is commonly used for the first wall fiber element. Available plastic hinge length expressions that are based on field and laboratory experience with monolithic RC walls (e.g., Priestley 2007) , are generally not applicable to UPT connections where nonlinear deformations are primarily concentrated at a critical interface, as opposed to distributed over a plastic hinge length. On that basis, H_{cr} for a UPT wall is expected to be smaller than the plastic hinge length of an equivalent RC wall. Note that in RC walls, the plastic hinge length (L_p, Figure 3-9) generally represents the height above the wall base over which the plastic curvature can be assumed constant (φ_p), and expressions for L_p have been calibrated against experimental data for RC walls. Using a similar approach for UPT walls, but considering the nonlinear concrete strains as the controlling parameter instead of the plastic curvature, H_{cr} is defined herein as the wall height above the base where nonlinear behavior of the concrete in compression is expected to extend. Note that curvature is not defined at the base joint of a UPT wall due to the separation gap that forms.

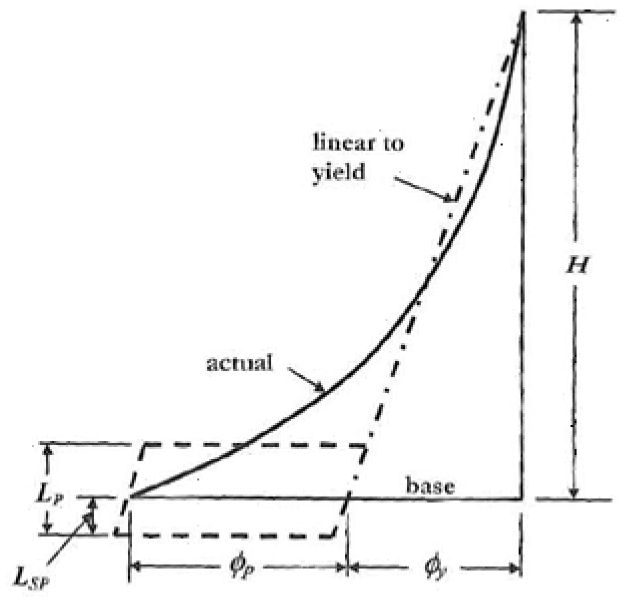

Figure 3-9 Plastic hinge length in conventional RC walls (from Priestley et al. 2007)

In order to define appropriate expressions for H_{cr}, available experimental results on UPT walls were examined. As previously noted and experimentally validated by Henry et al. (2012), concrete compressive strains in UPT walls are expected to be larger than concretes strains in RC walls and the region of inelastic deformations in UPT walls is expected to be limited to a shorter height compared to a traditional RC wall (Figure 3-10). A review of published experimental results of UPT walls (Priestley et al. 1999, Restrepo and Rahman 2007, Henry et al. 2012, Smith et al. 2012, Perez et al. 2013, and E-Defense UPT walls described in Chapter 5 herein) revealed that vertical extent of concrete spalling was generally confined to a short distance from the base, usually between 0.5-2.5t_w (where t_w is the wall thickness), with the larger values generally observed in specimens with larger c/l_w values (where c is the neutral axis depth and l_w the wall length).

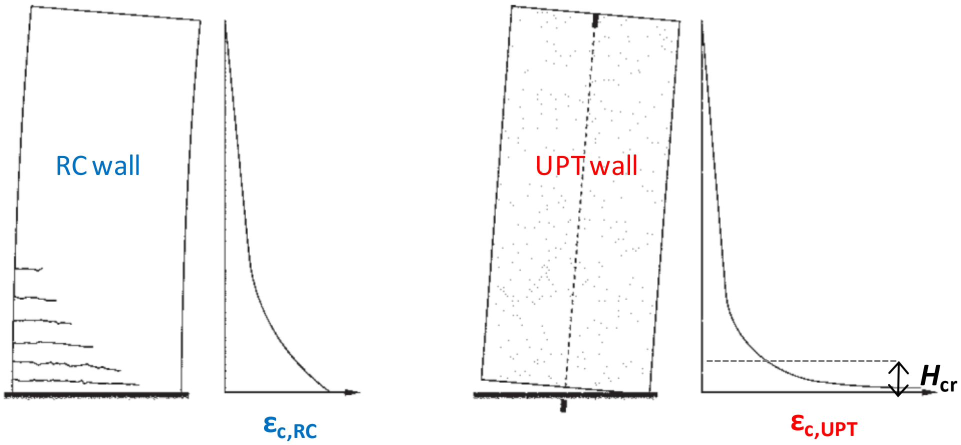

Figure 3-10 Strains at extreme compressive fibers of RC and UPT walls (adapted from Henry et al. 2012)

Based on these observations, it is recommended that $H_{cr} \leq (1.5t_w, c)$ be used for estimating strain demands on UPT walls. In their analytical study, Perez et al. (2007) use a similar expression: $H_{cr} = \min(2.0t_w'', 2.0c'')$ with t_w'' and c'' measured from the centerline of the confining reinforcement. Restrepo and Rahman (2007) also suggested using H_{cr} = c for estimating the maximum compressive strains in UPT walls.

It is worth noting here that for ultimate strain calculations ($\varepsilon_{c,max} = \theta c/L_p$) and design of confinement at the wall toes, ACI ITG-5.2 (2009) considers an effective plastic hinge length $L_p = 0.06H_w$, where H_w is the wall height. This recommendation, which appears more in line with conventional RC walls, generally predicts lower concrete strains for the Lehigh wall tests considered herein and the E-Defense building with UPT walls discussed in Chapter 5, than the H_{cr} values that were presented above. Table 3-2 summarizes the alternative values for H_{cr} that could be considered for the five Lehigh test walls, including the ACI ITG-5.2 recommendation of L_p=$0.06H_w$. Note that strains at a given rotation are inversely proportional to H_{cr}. The neutral axis depth values (c) included in Table 3-2 were estimated for the five walls at a rotation θ =

3.0%, based on recommendations in ACI ITG-5.2 and applicable conditions of equilibrium and compatibility of deformations.

Table 3-2 H_{cr} values for Lehigh test walls based on different recommendations

Wall	c (in)	$1.5t_w$ (in)	$2c''$ (in)	$2t_w''$ (in)	$0.06H_w$ (in)
TW1, TW2	20.1	9.0	40.0	8.0	21.7
TW3	20.0	9.0	39.7	9.5	21.7
TW4	17.4	9.0	34.5	9.5	21.7
TW5	11.8	9.0	23.3	9.5	21.7

Based on the recommendation $H_{cr} \leq (1.5t_w, c)$, and the values summarized in Table 3-2, a height $H_{cr} = 9.0$ in was selected and used as the height of the first wall element in the analytical models of the Lehigh UPT walls. Sensitivity of results to the value of H_{cr} will be discussed in the results section (Section 3.1.3).

As previously mentioned, the wall fiber sections over the height H_{cr} consist of concrete only fibers with no tensile strength. The mild bonded reinforcement of the precast wall panel (Figure 3-2) was not included in the base fiber sections as it did not cross the wall-foundation interface. Above the height H_{cr}, any reinforcement that was bonded and adequately developed was included in the wall fiber sections. Note that the vertical mild steel reinforcement of individual wall panels in the test building did not extend across the horizontal joints between panels, so that similar to the base joint, moment resistance at upper joints was solely provided by the unbonded PT steel crossing the joints. This behavior was implemented in the analytical model by introducing a series of wall elements with concrete-only fibers (no-tensile strength) over a height H_{cr} at the base of each panel, similar to modeling of gap opening at the base section. This allows uplift to occur at upper joints, if the decompression moment is exceeded.

However, no significant uplift was observed at upper joints in the analytical model and no uplift was reported by Perez et al. (2004, 2013) for the test walls.

The effect of transverse reinforcement was accounted for by using concrete fibers with different stress-strain relationships to model the well-confined ends of the base panel compared to the unconfined concrete within the middle portion (web) of the panel (Figure 3-2). The unconfined concrete stress-strain relationship was based on material characterization tests reported in Perez et al. (2004), while the confined concrete relationship was defined based on the Razvi and Saatcioglu (1999) model. It is noted that in defining the wall fiber sections of the confined ends of the wall panels, the entire wall thickness (6 in) was assigned the confined concrete properties, i.e. the (unconfined) cover concrete on either side of the well-confined boundary was assumed to behave as the confined core. Implications of this assumption are discussed in Section 3.1.3.1.

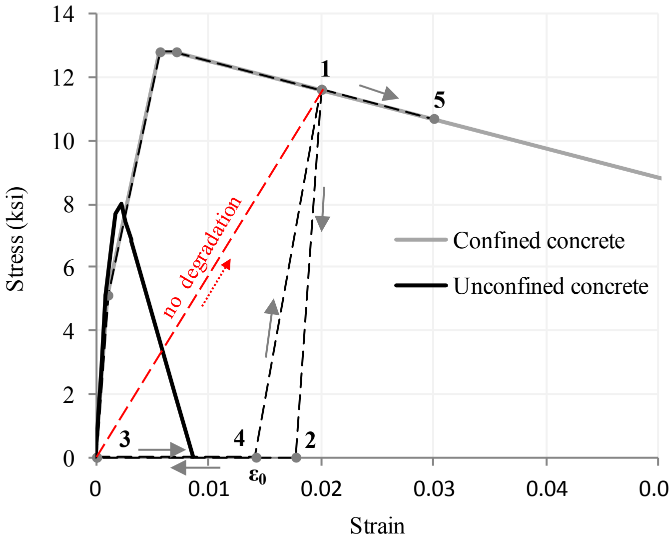

Figure 3-11 Concrete stress-strain relationships used in analytical model of test wall TW5

Typical unloading and reloading behavior of the concrete model is illustrated in Figure 3-11, on the confined concrete curve used in the analytical model for test wall TW5, through an assumed strain history consisting of loading to a compressive strain ε_1=0.02, unloading to zero strain, and reloading to a compressive strain ε_2=0.03. Key aspects of the unloading and reloading behavior illustrated in Figure 3-11 include: unloading occurs parallel to the initial elastic stiffness (path 1-2), concrete tensile strength is zero (path 2-3), and reloading occurs to the same strain ε_1 (path 3-4-1) from which unloading initiated. The reloading stiffness, and strain ε_0, are controlled through the energy degradation factors that define cyclic degradation of materials in Perform3D. In the case of no cyclic degradation (energy factor of 1.0), reloading would occur along the red dashed line (path 3-1), corresponding to the maximum energy dissipation. In the case of maximum degradation (zero energy factor) reloading and unloading lines would coincide (path 3-2-1) resulting in no cyclic energy dissipation. Experimental results for the Lehigh test walls showed that every cycle of increased amplitude caused (additional) degradation of the initial stiffness of the wall (e.g. Figure 3-25). This behavior was likely due to nonlinear behavior in the concrete and associated residual strains. Including energy degradation factors of 0.20 in the concrete material model of the Lehigh UPT walls, led to improved agreement between experimental and analytical reloading stiffness of the walls (Section 3.1.3.2), by simulating the effect of residual strains in the concrete. Note that the energy degradation factors only affect the reloading stiffness in the concrete material: reloading occurs along 3-1 for energy factors equal to 1.0, reloading occurs along 3-2-1 for energy factors equal to zero, and finally reloading occurs along 3-4-1 for energy factors of 0.2. All analyses herein were conducted using energy factors of 0.2 for the concrete material.

Recall that gap opening in this study is modeled as elongation of the wall concrete fibers that go into tension. This means that the concrete fibers on the compressed toe of the wall, upon unloading and reloading in the opposite direction, will develop tensile strains to model gap opening (Figure 3-6). So even though the assumed strain history illustrated above (0 to 0.02 to 0.00 to 0.03) did not include tensile strains, under reversed cyclic loading tensile strains will develop in the concrete. Since a no-tensile strength material is used, these positive strains would develop under zero stress (e.g. path 2-3 in Figure 3-11 would continue into the tensile strain domain under zero stress) and no increase in stress would occur until (upon reloading) the concrete strain returns to zero (gap closes). Reloading (in compression) from zero strain has already been addressed in the previous paragraph and as discussed above depends on the assumed cyclic degradation parameters.

Finally, shear behavior in the analytical models of the UPT walls described herein was implemented using an elastic uncracked shear modulus ($G_c \approx 0.4E_c$, where E_c is the modulus of elasticity of concrete) since the majority of lateral displacements in UPT walls is attributed to rocking at the critical interface and the contribution of shear deformations is expected to be small. Note however that for low aspect ratio UPT walls, the contribution of shear deformations could be more significant (Smith et al. 2012a). Given the limited data on moderate and low aspect ratio UPT walls, additional experimental and analytical studies are required to assess the effect of shear deformations on behavior of UPT walls and compare with available research on shear deformations of conventional RC walls (Massone and Wallace 2004, Beyer et al. 2011, Tran 2012, Kolozvari et al. 2014).

3.1.2.2 Modeling of unbonded post-tensioning steel

The unbonded PT bars were implemented as vertical inelastic truss elements, placed outside of the fiber section as strain compatibility is not enforced between concrete and steel over the unbonded lengths. The PT truss elements were pinned at the base, accounting for the additional unbonded length inside the foundation, and connected through rigid links to the adjacent wall nodes at the top of the wall. Bilinear force-deformation relationships that approximate the actual stress-strain relations from material characterization tests (Perez et al., 2004) were assigned to the truss elements.

Note that in order to capture the experimental behavior after complete loss of prestress occured, a tension-only material with appropriate cyclic degradation paramenters was used for the PT truss elements in the analytical model to prevent compression forces from developing in the PT steel and reflect the actual behavior (PT bar goes slack in compression). This only had an impact in the analytical responses of TW5, where the entire prestress was lost at large drifts. Unloading and reloading behavior of the PT steel material is illustrated in Figure 3-12 through an assumed strain history consisting of loading to a positive strain of 0.0065, unloading to a strain of 0.003, reloading to a strain of 0.01, unloading back to a strain of 0.003 and finally reloading to a strain of 0.012.

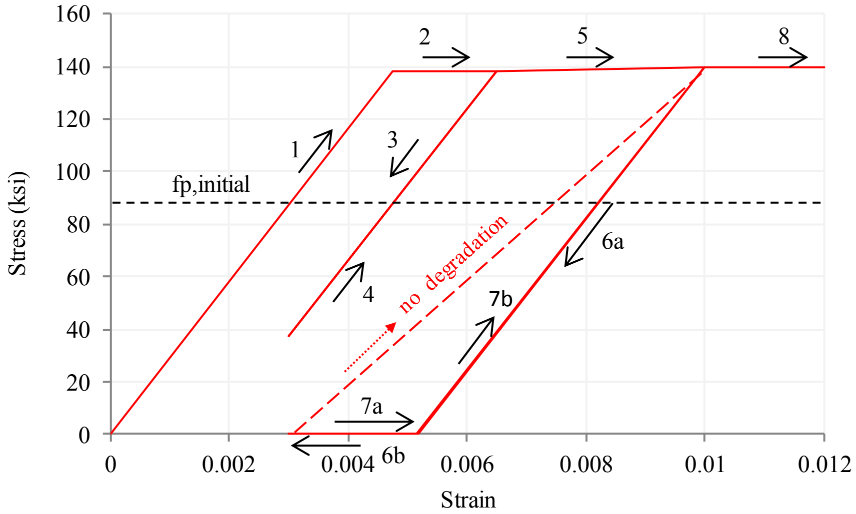

Figure 3-12 PT steel stress-strain relationship used in analytical model of test wall TW5

As shown in Figure 3-12, unloading always occurs parallel to the initial elastic stiffness (branches 3 and 6a). Reloading also occurs with the same stiffness if the entire prestress is not lost (branch 4). Upon unloading form a large inelastic strain and the entire prestress is lost (branch 6a), unloading continues along the zero stress axis (branch 6b), representing the tension-only material. Reloading always occurs to the same strain from which unloading initiated. If no cyclic degradation is included, reloading after 6b would occur along the red dashed line. In contrast, in the case of maximum degradation, reloading would occur along branches 7a and 7b, with reloading branch 7b coinciding with unloading branch 6a. This effectively means that after unloading to zero stress with a residual strain in the PT steel, no increase in PT stress occurs until that strain is reached again. This latter option was implemented in the analytical model described herein as it better reflects the connection condition of the PT steel at the top of the wall. The connection of the post-tensioning steel at the top of the wall consists of a bearing-only condition such that upon complete loss of prestress, there is no displacement compatibility between the top of the wall and the PT bearing point. That is, stress is not induced into the PT steel until, upon reloading, the wall re-engages the PT bearing point at its previous maximum residual strain. By including the maximum degradation in the PT stress-strain relationship as described above, this behavior is accurately captured in the analytical model.

3.1.2.3 Modeling of loading

Loading in the analytical models of the test walls consisted of application of gravity and prestress loads followed by a series of nonlinear static pushover analyses that simulate the displacement history that the walls were subjected to during the test.

Gravity loads include wall self-weight and superimposed axial load. The pre-stressing force was simulated as an element load (initial strain) in the inelastic truss elements that model the PT bars. In order to compare analytical responses with the experimental results, the loading histories that the walls were subjected to during the tests were implemented in Perform3D. This was achieved by running several static push-over load cases in sequence. For instance, a full reversed cycle to 1% drift consisted of applying the following three load cases in sequence: push-over to +1% drift, followed by push-over to -1% and push-over to 0% drift. Note that the first, low-amplitude, elastic cycles that the test walls were initially subjected to were not applied in the model as they mainly served to check the instrumentation in the test, and were small enough to prevent decompression from occurring at the base of the wall. Consistent with the test, the lateral load pattern that was used for the push-over analysis was based on a nodal load acting at the centerline of the wall at a height of 284 in from the base. P-Delta effects were included in all analyses. The following section presents selected analytical results from the test walls and comparisons with respective experimental results.

3.1.3 Comparisons of analytical and experimental results

3.1.3.1 Specimen TW1

Specimen TW1 included six PT bars ($A_{PT} = 7.5$ in^2) stressed to 57% of their ultimate strength ($f_{pi} = 0.57 f_{pu}$) at the end of the prestressing operation. The bottom two panels of TW1 included spiral confining reinforcement at their ends. The spiral reinforcement consisted of interlocked 4-in diameter (center-to-center) spiral coils extending horizontally over a length of 26.75 in (0.27 l_w) at each end of the precast wall panels (Figure 3-3). Specimen TW1 was tested under monotonic lateral load and constant axial load. Behavior during the test was governed by a gap opening at the wall-to-foundation interface. Concrete cover spalling initiated at a lateral drift of approximately 0.60%, while yielding of the first PT bar occurred at a drift of 1.35%. Failure in TW1 occurred due to fracture of the spiral confining reinforcement and crushing of concrete in the compression zone at the base of the wall. Detailed experimental results are provided in Perez et al. (2004, 2013).

Figure 3-13 presents comparisons between analytical and experimental results in terms of lateral load versus lateral drift response of the test wall. The repeated reductions in base shear observed on the experimental curve are associated with adjustments to the gravity load jack. Results from two analytical models are plotted in Figure 3-13. The analytical model "*unreduced t*" corresponds to the base model, implemented in accordance with modeling approaches described in Section 3.1.2.1. While this model is shown to accurately predict the initial stiffness and response up to approximately 0.8% drift, it overestimates the base shear capacity of the test wall by approximately 10%. The overestimation of base shear is likely associated with concrete cover spalling that is not accurately reflected in the analytical model. As discussed in Section 3.1.2.1, when defining the wall fiber sections of the confined ends of the wall panels in the base model, the entire wall thickness (6 in) was assigned the confined concrete properties, i.e. the (unconfined) cover concrete on either side of the spiral-confined boundary was assumed to behave as the confined core. Given that (i) the confined thickness constitutes only 67% of the wall cross-section thickness (4-in spiral coil, 6-in wall thickness, see Figure 3-3) and (ii) cover spalling initiated at 0.6%, the assumption of confined concrete properties over the entire wall thickness results in a smaller neutral axis depth and larger base shear capacity than what was observed in the test after spalling occurred.

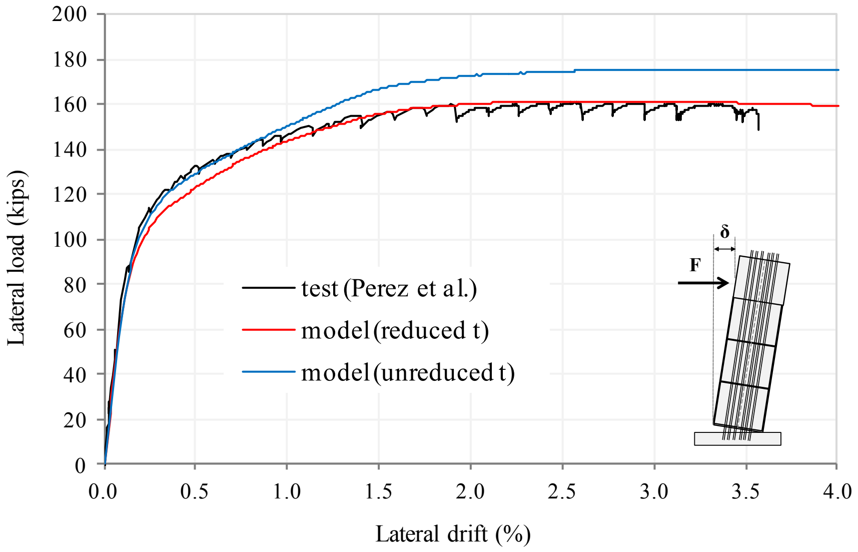

Figure 3-13 Analytical and experimental force-displacement relations for specimen TW1

In order to include the effect of concrete cover spalling in the analytical model, analyses were also run using a reduced wall thickness over the estimated neutral axis depth of the wall. The reduced thickness includes only the confined core (4 in). As expected, results from this model ("*t reduced*" in Figure 3-13) provide a better estimate of the base shear capacity of the test wall. The small discrepancies (underestimation of lateral load) at small drifts are also expected as spalling in the test did not initiate until 0.6%. Note both models use H_{cr} = 9.0 in as calculated in Section 3.1.2.1. Given the results in Figure 3-13, all subsequent analyses were conducted using reduced wall thickness over the estimated neutral axis depth of each test wall to account for the effect of concrete cover spalling.

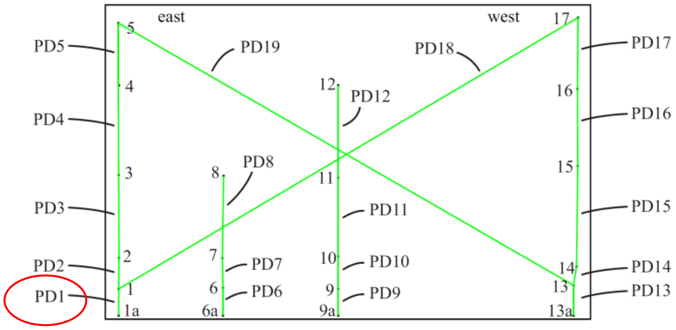

Figure 3-14 Instrumentation at base wall panel of specimen TW1 (from Perez et al. 2004)

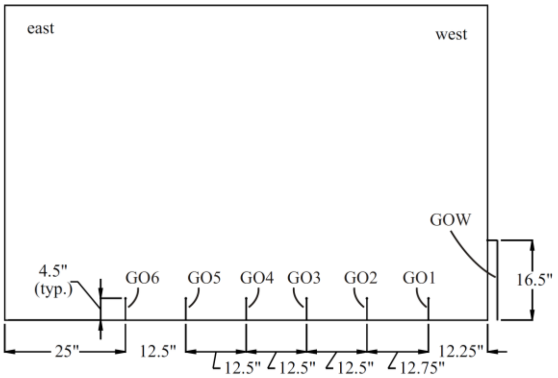

Figure 3-15 Gap opening instrumentation at base wall panel of specimen TW1 (from Perez et al. 2004)

In addition to global responses (lateral load versus lateral deformation relations), comparisons between analytical and experimental results were also conducted for local responses such as concrete strains and gap opening displacements. Figure 3-14 shows instrumentation attached to the base panel of specimen TW1 that was used to calculate concrete strains. Sensor PD1 that will be used for concrete strain comparisons was located at 2.75 in from the east edge of the wall and had a gauge length of approximately 5.5 in. Figure 3-15 shows instrumentation at the base panel of specimen TW1 that was used to measure gap opening displacements along the wall length.

Experimental concrete strains from sensor PD1 (ε_{PD1}) are compared with analytical results in Figure 3-16. Note that for consistency with the location of sensor PD1, analytical concrete strains plotted in Figure 3-16 also refer to a horizontal distance of 2.75 in from the wall edge. As noted in the previous paragraph, the sensor had a gauge length of 5.5 in, so experimental concrete strains represent average strains over that length. Note that concrete strains up to 0.06 (at 3.0%) were measured during the test. Analytical strains in Figure 3-16 are average strains over the height of the first wall element (H_{cr}), as discussed in Section 3.1.2.1. Concrete strains from two models that use different values for H_{cr} are plotted in Figure 3-16 to point out the importance of H_{cr} in strain predictions. Analytical strains from the model that uses $H_{cr} = 9.0$ in. are in good agreement with experimental results, showing that the recommended H_{cr} value is small enough to capture the magnitude of concrete strains developing at the base of the wall. Analytical results from the model that uses $H_{cr} = 22.0$ in. represent strain predictions consistent with ACI ITG-5.2 recommendations ($L_p = 0.06H_w \approx 22$ in) discussed in Section 3.1.2.1 (Table 3-2). As evidenced by the experimental results, measured concrete strains at the base of the test wall significantly exceeded ACI ITG-5.2 strain predictions (experimental strains were more than 2.5 times higher at 3.0% drift ratio). While this observation has some design implications (e.g. reexamination of the L_p value used in ACI ITG-5.2 to define strain demands and design confinement in UPT walls may be justified), gap opening displacements and base shear capacity are not as sensitive to the assumed value of H_{cr} as concrete strains are. This is discussed further in the next paragraph. Finally, it should be noted that both models in Figure 3-16 use reduced thickness to account for concrete cover spalling (model "$H_{cr} = 9$ *in*" in Figure 3-16 coincides with model "*t reduced*" in Figure 3-13).

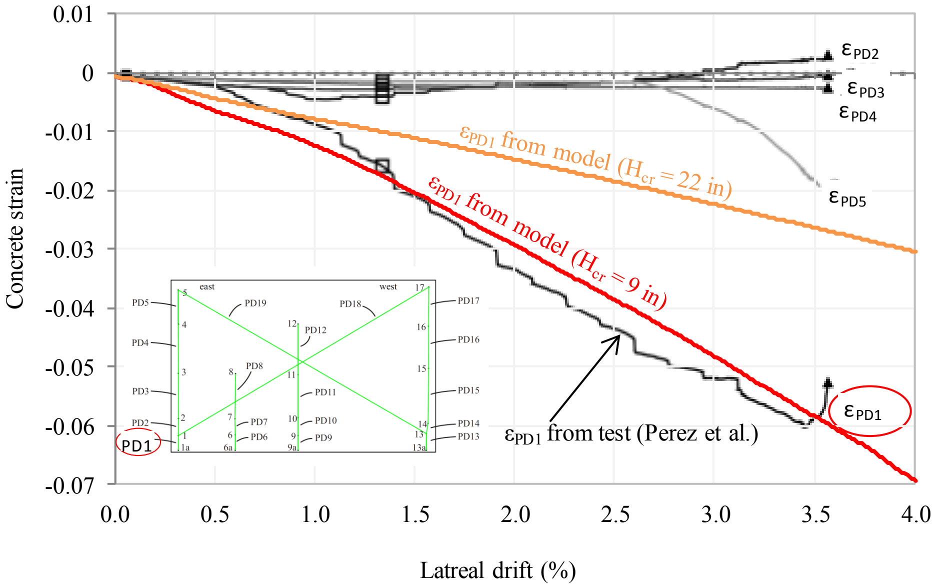

Figure 3-16 Analytical and experimental concrete strains at east end of specimen TW1

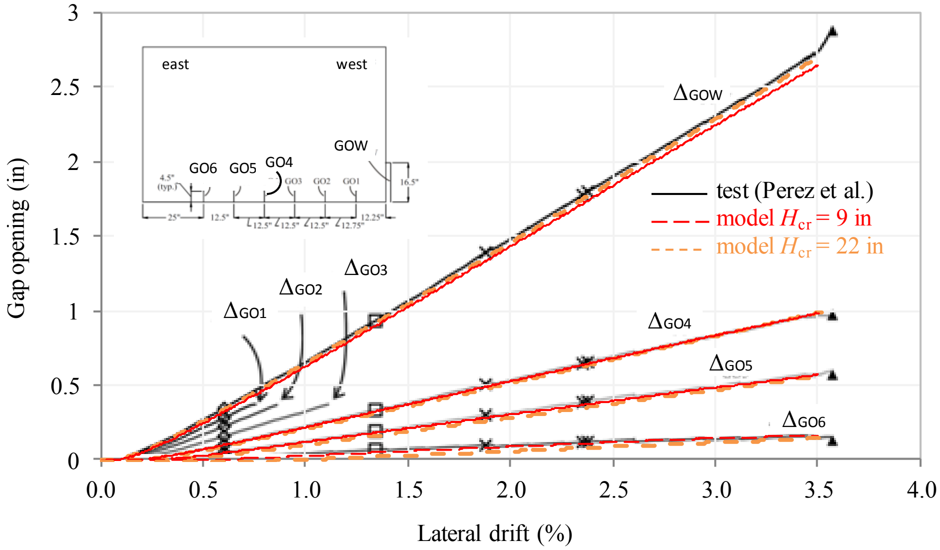

Figure 3-17 Analytical and experimental gap opening displacements along base joint of specimen TW1

Experimental gap opening displacements at the base of the wall are compared with analytical gap opening displacements in Figure 3-17. Note that the experimental gap opening displacements were measured using sensors GO (Figure 3-15). Sensor GOW had a gauge length of 16.5 in. while all remaining GO sensors had a gauge length of 4.5 in. Only measurements from GOW, GO4, GO5, and GO6 sensors are compared with analytical results as instruments GO1, GO2, GO3 ran out of range during the test. As expected, gap opening displacements are well predicted by both models (H_{cr} = 9.0 in. and H_{cr} = 22.0 in.), verifying that uplift in the analytical model, calculated by integrating strains of the extreme concrete tensile fiber over the height H_{cr}, is not sensitive to the value of H_{cr}.

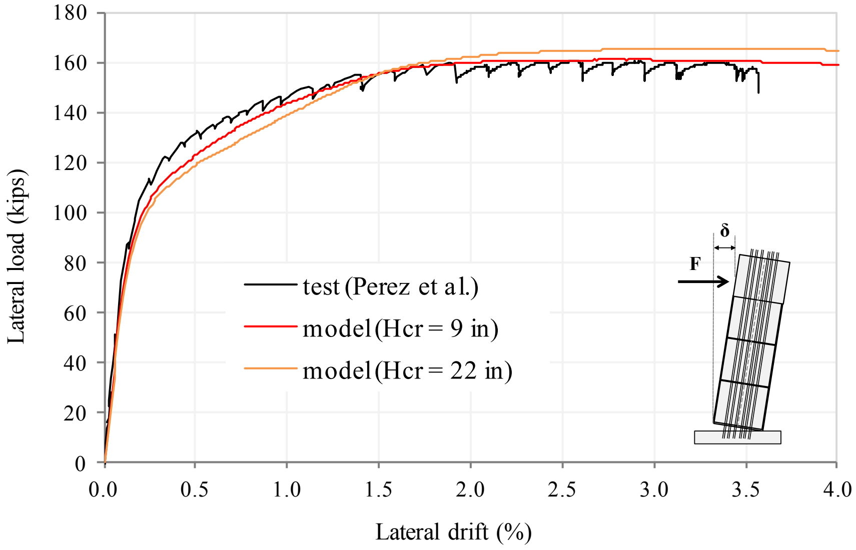

Figure 3-18 Analytical and experimental force-displacement relations for specimen TW1

Figure 3-18 shows that similar to gap opening displacements, predicted base shear capacity is not that sensitive to the value of H_{cr} either. Using a value of H_{cr} = 22.0 in. resulted in only 3.0% increase in predicted base shear capacity compared to using H_{cr} = 9.0 in. However, caution should be exercised as these differences may be more pronounced in cases where the increased concrete strains predicted with small values for H_{cr} result in degradation in the global response that would not be captured if larger values were used for H_{cr}. In the case of the spiral confined TW1 specimen, despite significantly different concrete strain predictions between models with different H_{cr} values (Figure 3-16), these strains did not result in any significant degradation to occur in the concrete or in the global lateral resistance. As will be discussed in

Section 3.1.3.5, in the case of specimen TW5, differences in predicted lateral load capacity with different values for H_{cr} were more pronounced and amounted to 10%.

Finally, it should be pointed out that although neither of the models (H_{cr} = 9.0 in. or H_{cr} = 22.0 in.) predicted the confinement failure of specimen TW1 at a drift of 3.5%, the calculated concrete strains using H_{cr} = 9.0 in (ε_c = 0.06 at 3.5% drift) are clearly more indicative of such a failure mode than calculated concrete strains using H_{cr} = 22.0 in (ε_c = 0.027 at 3.5% drift). Note that the confined concrete model used in this study (Razvi and Saatcioglu 1999) does not include an ultimate concrete strain limit (ε_{cu}) associated with fracture of the confining reinforcement; instead it assumes residual concrete strength equal to 20% of the confined concrete strength, f_{cc}', at large strains. In their analytical studies, Perez et al. (2004) used the Oh (2002) model to establish the stress-strain relationship for the spiral confined concrete. According to the Oh (2002) model, failure of the spiral confined concrete in TW1 occurs at ε_{cu} = 0.08.

3.1.3.2 Specimen TW2

Specimen TW2 was identical to TW1 but was tested under gravity and cyclic lateral loading with a loading history consisting of three cycles at each of the following drift ratios: 0.05, 0.1, 0.25, 0.5, 0.1, 1.0, 1.5, 2.0, 0.1, and 3.0%. Response of the specimen was nearly nonlinear-elastic with narrow hysteretic loops and limited energy dissipation associated with nonlinear behavior of the concrete in compression and yielding of the PT bars. Concrete cover spalling initiated at 0.65% and -0.57% drift ratios for eastward (positive) and westward (negative) loading, respectively. Yielding of the first PT bar occurred at 1.44% and -1.51% for eastward and westward loading, respectively. At a drift of -2.83% a confinement failure occurred, followed by an unstable failure consisting of sudden buckling failure of the confined region of the base panel. Detailed experimental results for specimen TW2 are provided in Perez et al. (2004, 2013).

Figure 3-19 presents comparisons between analytical and experimental results in terms of lateral load versus lateral drift response of the test wall. Note that the analytical model is identical to that presented in the previous section for specimen TW1 (H_{cr} = 9.0 in. and reduced thickness to account for concrete cover spalling). The model captures the base shear capacity, self-centering behavior, limited energy dissipation and gradual degradation in initial stiffness that occurred with each cycle of increased amplitude in the test.

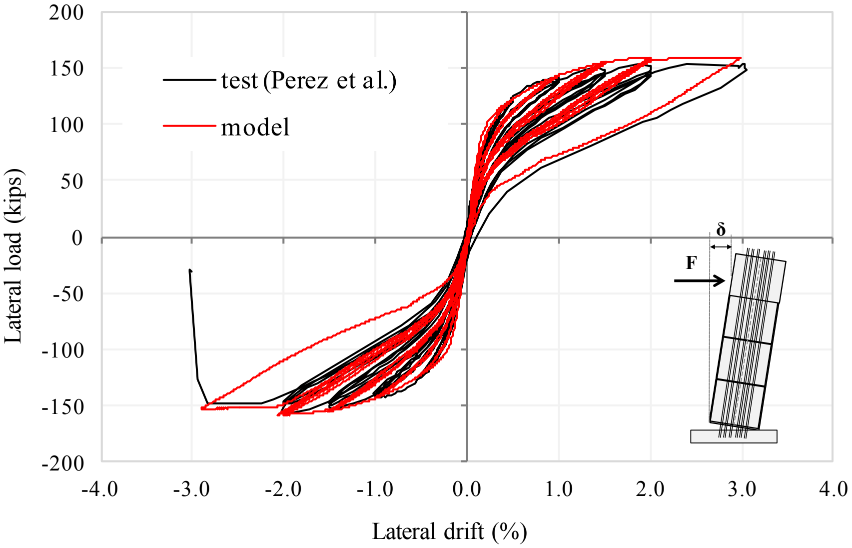

Figure 3-19 Analytical and experimental force-displacement relations for specimen TW2

As described in Section 3.1.2.1, cyclic degradation parameters were included in the concrete material of the analytical model to capture the residual strains in the concrete and the associated degradation in reloading stiffness in the global response. Figure 3-20 shows the effect of cyclic degradation on the reloading stiffness of the 2.0% cycles. Note that the 2.0% cycles shown in Figure 3-20 were preceded by the entire displacement history that the specimen was subjected to before them; only the 2.0% cycles were extracted from the experimental and analytical results for clarity. The model "with cyclic degradation" in Figure 3-20 coincides with the model in Figure 3-19. The analytical model with "no cyclic degradation" only differs from the model "with cyclic degradation" in that no degradation parameters were included in the concrete stress-strain relationship. As evidenced by the results plotted in Figure 3-20, inclusion of cyclic degradation only affected the reloading stiffness and resulted in improved agreement with the experimental results.

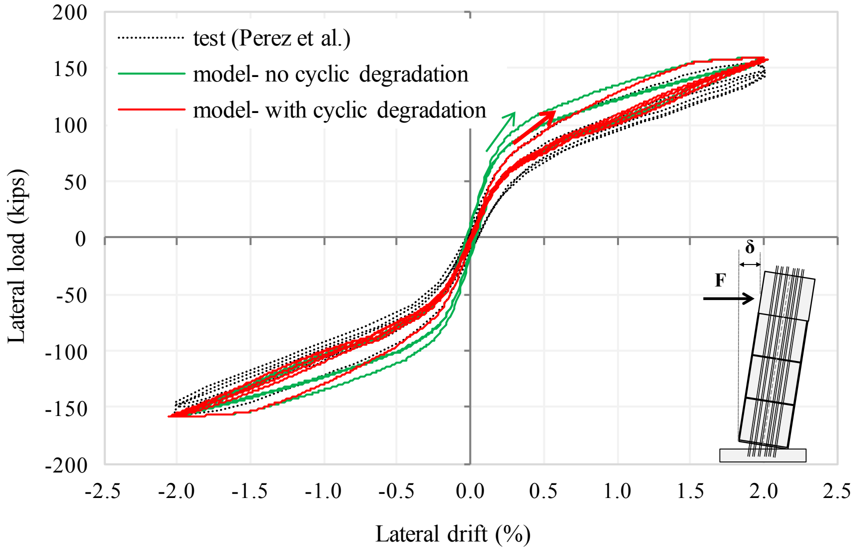

Figure 3-20 Effect of cyclic degradation on 2.0% cycles for specimen TW2

3.1.3.3 Specimen TW3

In specimen TW3 the base panel reinforcement details were modified to better control cracking and prevent the undesirable buckling failure observed in specimen TW2. These details included hoops in the confined region (Figure 3-2 versus Figure 3-3), horizontal steel extended into the confined regions, and transverse (through-thickness) hoops adjacent to the PT steel conduits to prevent the two layers of horizontal reinforcement from separating. The area, location, and initial prestress of the PT steel were identical to specimens TW1 and TW2. The wall was tested under constant axial load and the same loading history as TW2 (three cycles at each of the following drift ratios: 0.05, 0.1, 0.25, 0.5, 0.1, 1.0, 1.5, 2.0, 0.1, and 3.0%). The specimen failed during the first lateral drift cycle to 3.0% due to confinement failures (hoop fractures) at both ends of the base panel. Detailed experimental results for specimen TW3 are provided in Perez et al. (2004, 2013).

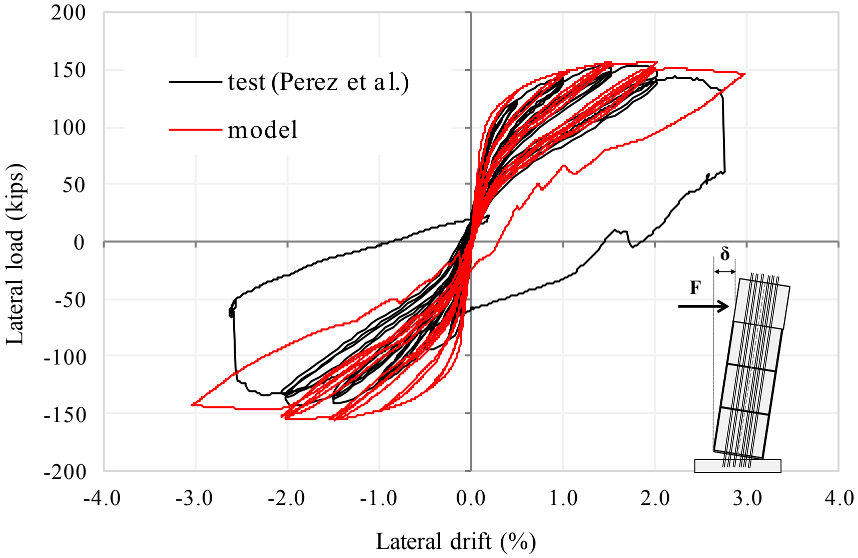

Figure 3-21 Analytical and experimental force-displacement relations for specimen TW3

Figure 3-21 compares the measured lateral load versus lateral drift response of the test wall with results from the analytical model. The model captures the self-centering behavior of the wall up to a drift ratio of 2.0% and accurately predicts the base shear capacities during the positive (eastward) half-cycles. The analytical results also show some loss of re-centering capacity upon unloading from 3.0% drift. Apparent discrepancies in the negative direction are attributed to the unsymmetrical behavior between positive and negative half-cycles observed in the experiment, and associated with premature spalling in the negative (westward) half-cycles due to poor consolidation of concrete at the west end of the base panel (Perez et al., 2013).

Figure 3-22 compares the measured axial force in one of the PT bars with the PT forces obtained from the analytical model. The model accurately predicts the variation of PT forces with lateral drift, and the prestress losses that occur under cyclic loading. The lateral drift at which yielding of the PT steel occurs (1.5%) is also accurately predicted. Finally, Figure 3-23, shows good overall agreement between measured and predicted gap-opening displacements (uplift) at the east and west ends of the wall.

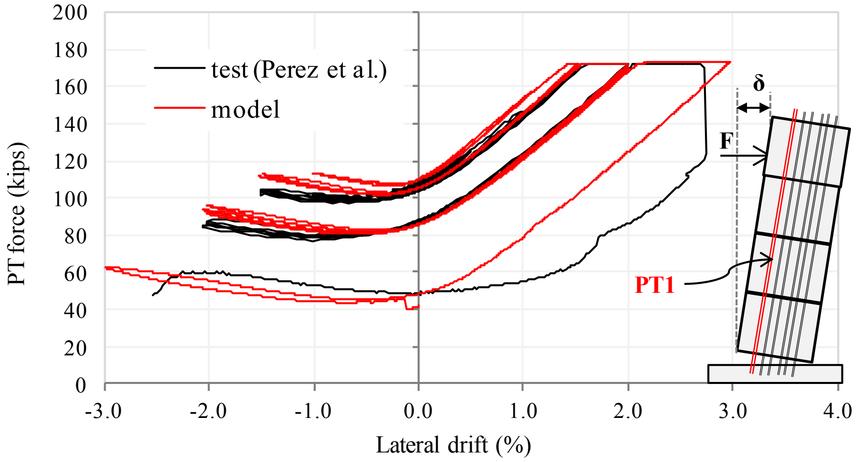

Figure 3-22 Analytical and experimental variation of forces in west PT bar of specimen TW3

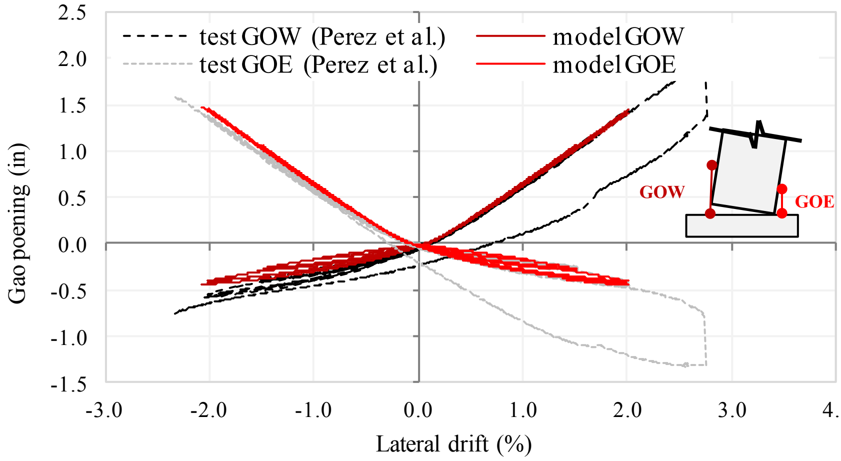

Figure 3-23 Analytical and experimental gap opening displacements at east and west ends of specimen TW3

3.1.3.4 Specimen TW4

Specimen TW4 included the same confining details (Figure 3-2) and area of PT steel as specimen TW3 but the initial prestress was reduced to half ($f_{pi} = 0.277 f_{pu}$). The loading history was also the same at that of specimens TW2 and TW3, with some additional cycles beyond 3.0% drift, until failure occurred. Concrete cover spalling initiated at 0.74% and -0.94% drift ratios for eastward (positive) and westward (negative) loading, respectively. The west PT bar did not yield during the test but it reached 93% of its yield strength. The east PT bar in the test yielded at a drift of -2.90%.

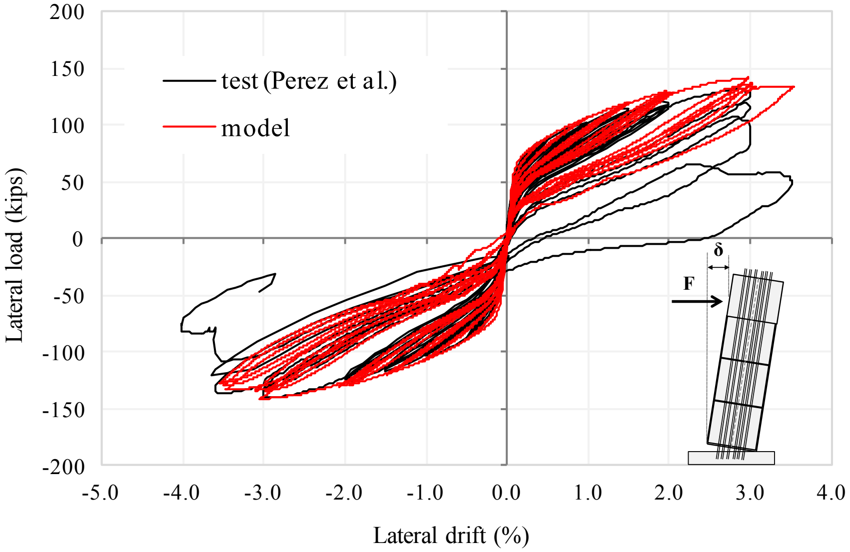

Figure 3-24 Analytical and experimental force-displacement relations for specimen TW4

Failure in specimen TW4 occurred from crushing of the confined concrete at both ends of the base panel. Unlike the sudden failures observed in TW1 through TW3, lateral load capacity in specimen TW4 was lost gradually, as hoops at various locations fractured at different instances, until a sufficient number of hoops fractured and resulted in loss of lateral load resistance and loss of self-centering capacity. Detailed experimental results for specimen TW4 are provided in Perez et al. (2004, 2013).

Figure 3-24 compares the measured lateral load versus lateral drift response of the test wall with results from the analytical model. The model accurately captures the hysteretic response of the test wall until a lateral drift of 3.0%. The model also predicts the modest strength degradation that occurred upon loading to a drift of -3.5%, but it does not capture the gradual strength degradation that occurred as the specimen was loaded to the positive 3.0% cycles. As was mentioned in the previous paragraph, this degradation was associated with hoop fractures that are not captured in the model. It is noted again that the confined concrete model used in this study (Razvi and Saatcioglu 1999) does not include an ultimate concrete strain limit (ε_{cu}) associated with fracture of the confining reinforcement; instead it assumes residual concrete strength equal to 20% of the confined concrete strength, f_{cc}', at large strains. In their analytical studies, Perez et al. (2004) used the Mander model (Mander et al. 1988a, 1988b) to establish the stress-strain relationship for the hoop confined concrete of specimens TW3-TW5. According to their calculations based on the Mander model, failure of the hoop confined concrete in TW4 occurs at $\varepsilon_{cu} = 0.0732$. Note that the predicted peak concrete strain from the analytical model described herein at the first cycle to +3.0% is 0.057. At the 2^{nd} and 3^{rd} cycles to +3.0% drift the peak concrete strains are 0.063 and 0.069, respectively, and at the subsequent cycle to +3.5%, the peak concrete strain is 0.085. Given the magnitude of these strains, and the estimated ultimate concrete strain of $\varepsilon_{cu} = 0.0732$, results from the analytical model indicate that hoop fractures could be expected between drift ratios of 3.0 and 3.5% as were observed in the test.

As evidenced by the discussion above, the ability of analytical models to capture failure of UPT walls largely relies on their ability to (i) accurately predict concrete strains at the confined toe and (ii) estimate ultimate concrete strain capacities, ε_{cu}, corresponding to fracture of the confining reinforcement. While the issue of concrete strain predictions has been addressed herein by providing recommendations for H_{cr} (Section 3.1.2.1), the issue of ultimate strain capacities, ε_{cu} has not been addressed and requires further studies. It is also noted that for UPT walls that include energy dissipating bars at the wall-to-foundation interface (not provided in the Lehigh test walls), in addition to the limit state corresponding to concrete crushing (confinement failure), the limit state associated with fracture of the energy-dissipating bars need also be considered.

3.1.3.5 Specimen TW5

Specimen TW5 included the same confining details (Figure 3-2) and initial prestress as specimen TW3 but the area of PT steel was reduced to half. The loading history was also the same at that of specimens TW3, with some additional cycles up to drifts of 6.0% drift. Behavior of specimen TW5 during the test was governed by a gap opening and closing at the wall-to-foundation interface. Concrete cover spalling at the ends of the wall initiated at 0.65% and PT yielding occurred at 1.45% drift. Despite prestress losses that resulted in complete loss of the initial prestress upon unloading from drifts larger than 4.0%, the wall maintained its self-centering behavior throughout the test and sustained lateral drifts up to 6.0% without failure. Detailed experimental results are provided in Perez et al. (2004, 2013).

Comparisons between experimental and analytical results for specimen TW5 showed excellent agreement for both global and local responses. Figure 3-25 compares the measured lateral load versus lateral drift response of the test wall with results from the analytical model (H_{cr} = 9.0 in). The model captures the self-centering behavior of the wall and accurately predicts its base shear capacity. The modest energy dissipation and the gradual degradation in initial stiffness with increasing amplitude cycles are also accurately reproduced in the analytical results. As no energy dissipating bars were provided at the base joint, the limited energy dissipation observed can be attributed to nonlinear behavior of the concrete in compression and yielding of the PT steel.

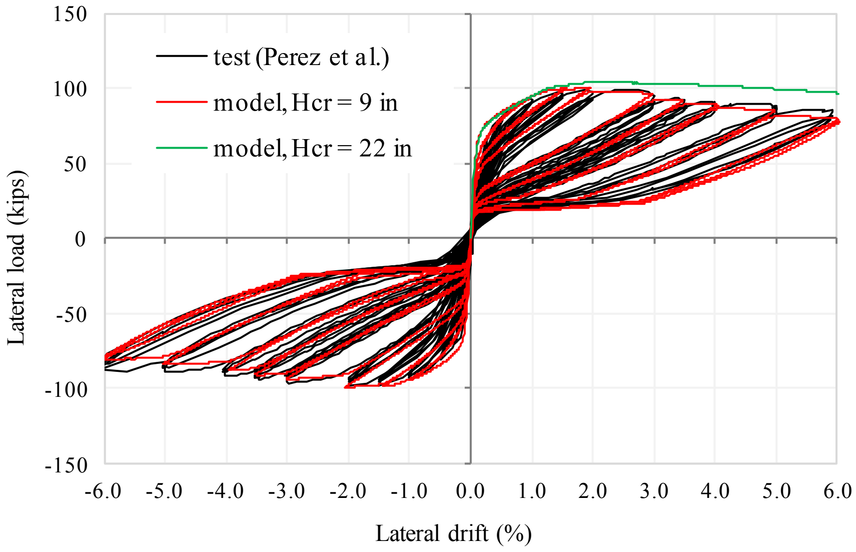

Figure 3-25 Analytical and experimental force-displacement relations for specimen TW5

Also shown in Figure 3-25, are analytical results (pushover curve) from a model that uses H_{cr} = 22.0 in. instead of H_{cr} = 9.0 in. This value for H_{cr} is consistent with ACI ITG-5.2 recommendations ($L_p = 0.06H_w \approx 22$ in) for concrete strain predictions in UPT walls as discussed in Section 3.1.2.1 (Table 3-2). As evidenced by the results in Figure 3-25, the increased value for H_{cr} resulted in approximately 10% overestimation of lateral load resistance of the specimen. As expected, differences between concrete strains in the two models (H_{cr} = 9.0 in. and H_{cr} = 22.0 in.) are more significant, with peak concrete strains in the model that uses H_{cr} = 9.0 in. approximately 2.5 times higher than peak concrete strains calculated with H_{cr} = 22.0 in.

Figure 3-26 compares the measured axial forces in the west and middle PT bars (PT1, PT2) with the PT forces obtained from the analytical model. The model accurately predicts the variation of PT forces with lateral drift, and the prestress losses under cyclic loading. Note that in order to capture the experimental behavior after complete loss of prestress occured, a tension-only material with appropriate cyclic degradation parameters was used for the PT truss elements in the analytical model to prevent compression forces from developing in the PT. This was discussed further in Section 3.1.2.2.

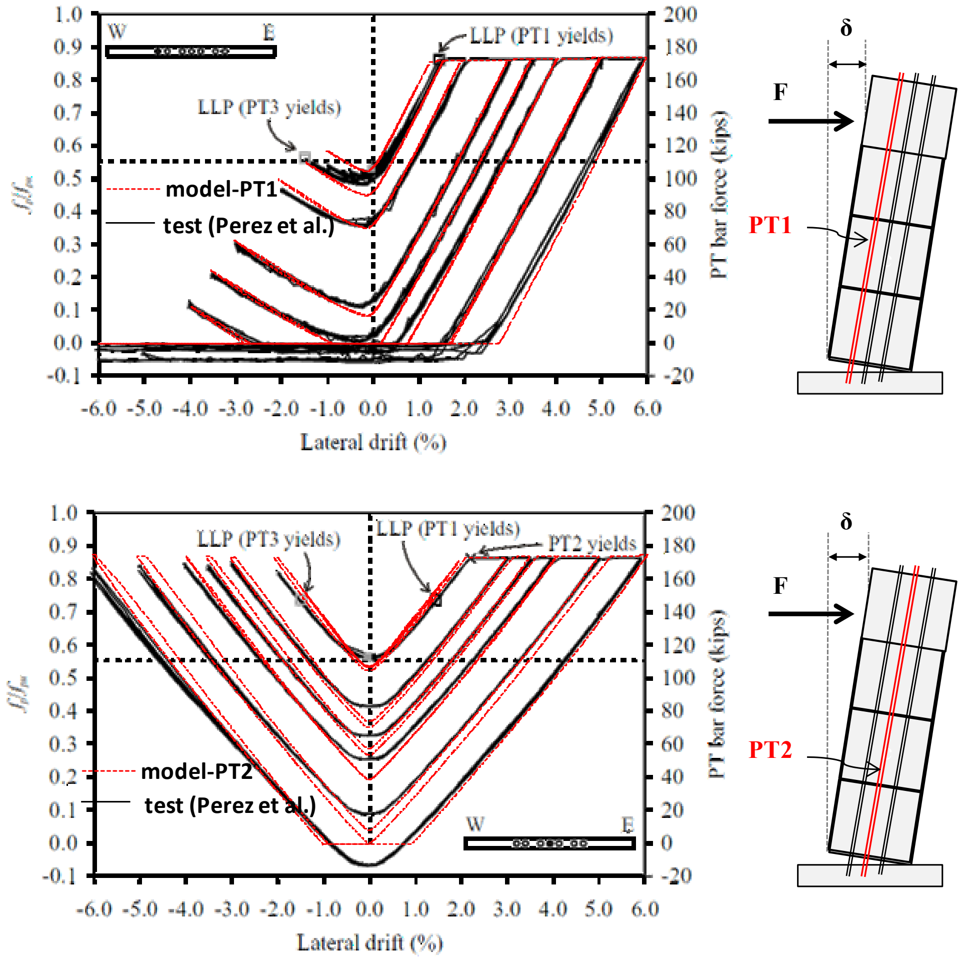

Figure 3-26 Analytical and experimental variation of forces in PT bars of specimen TW5

Figure 3-27 compares the measured gap opening displacements at the east and west ends of the wall (GOE, GOW) with uplift values obtained from the analytical model. Recall that uplift in the analytical model is captured as elongation of the extreme concrete fibers that go into tension (positive strain under zero stress, Figure 3-6). In the test, uplift at the east and west ends of the wall was measured by vertical sensors with a 24-in gauge length. The negative values from these sensors, when divided by the 24-in gauge length represent average concrete compressive strains over that height. For consistency with the experimental results, wall nodes were included at a distance of 24 in above the wall base in the analytical model, and analytical results plotted in Figure 3-27 correspond to these nodes. Comparisons of Figure 3-27 show that the model adequately captures both gap opening displacements, and average concrete strains over the bottom 24 in. Note that despite inclusion of wall nodes at a distance of 24 in from the wall base, the height of the first row of wall elements closest to the base is still equal to H_{cr} = 9.0 in, as specified in Section 3.1.2.1, and calculated strains over this height (H_{cr} = 9.0 in) are approximately 2.5 times higher than the average strain over the 24-in gauge length.

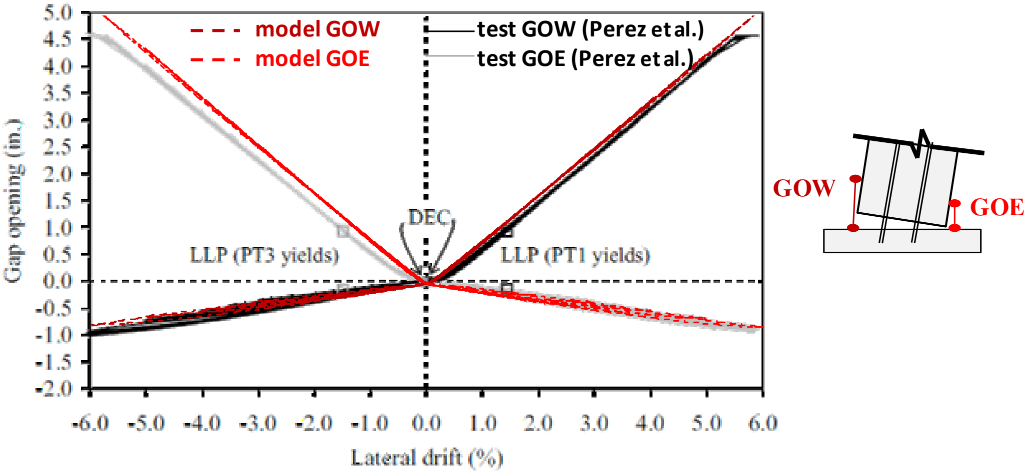

Figure 3-27 Analytical and experimental gap opening displacements at east and west ends of specimen TW5

3.2 UPT Beam model and experimental validation

Tests on UPT beam-column sub-assemblages conducted at the National Institute of Standards and Technology (NIST) by Stone et al. (1995), served as the basis for the development of the analytical model for UPT beams described herein. The following sections provide a summary of the test program that was used for the experimental validation, the development of the analytical model and comparisons between analytical and experimental force-deformation relations.

3.2.1 The NIST tests on precast concrete beam-column sub-assemblages

An experimental program to study the behavior of precast concrete beam-column connections subjected to cyclic loads was conducted at Institute of Standards and Technology (NIST) between 1987 and 1992. Phases I and II (Cheok and Lew 1991, Cheok and Lew 1993) included testing of monolithic connections and precast connections with fully bonded PT steel. Use of partially bonded tendons was examined in Phase III (Cheok and Lew 1993). Hybrid connections, that used mild reinforcing steel together with post-tensioning, were tested in Phase IV (Stone et al. 1995) of the program. Variables examined included the amount of mild steel and, the location, type and bond (fully grouted, partially grouted or unbonded) of PT steel in the beam. Specimens M-P-Z4 and O-P-Z4 of Phase IV-B of the test program were selected for the experimental validation of the UPT beam model. The two specimens differed only in the amount and properties of energy dissipating steel provided at the beam-to-column connections. A description of these two tests is provided below while more detailed information on the NIST tests can be found in Stone et al. 1995, and Stanton et al. 1997.

The 1/3-scale beam-column sub-assemblages represented interior connections cut from a prototype frame at the locations of assumed inflection points at beam mid-span and column mid-height. Accordingly, the column base of each test specimen was mounted on a hinge while the beam ends were supported on straps that allowed horizontal but not vertical displacement. The prototype frame consisted of multi-story precast concrete columns and single-bay precast beams connected with post-tensioning steel located at mid-height of the beams. Accordingly, the column of the sub-assemblage was continuous and the precast beams on either side of it were connected with post-tensioning steel running horizontally through ducts at mid-height of the beams and through the column (Figure 3-28).The post-tensioning steel was unbonded through most of its length (including the length inside the column and the critical interfaces on either side of the column) and was bonded to the concrete for its remaining length. Mild energy dissipating bars grouted inside ducts at the top and bottom of the beam also crossed the critical beam-to-column interfaces and were deliberately debonded for a short length on either side of the column to delay fracture. Fiber-reinforced grout was provided at the beam-column interfaces and steel armor angles were included at the corners of the beams to prevent concrete crushing under high compressive strains. Transverse reinforcement of the beams and column consisted of welded reinforcement grids.

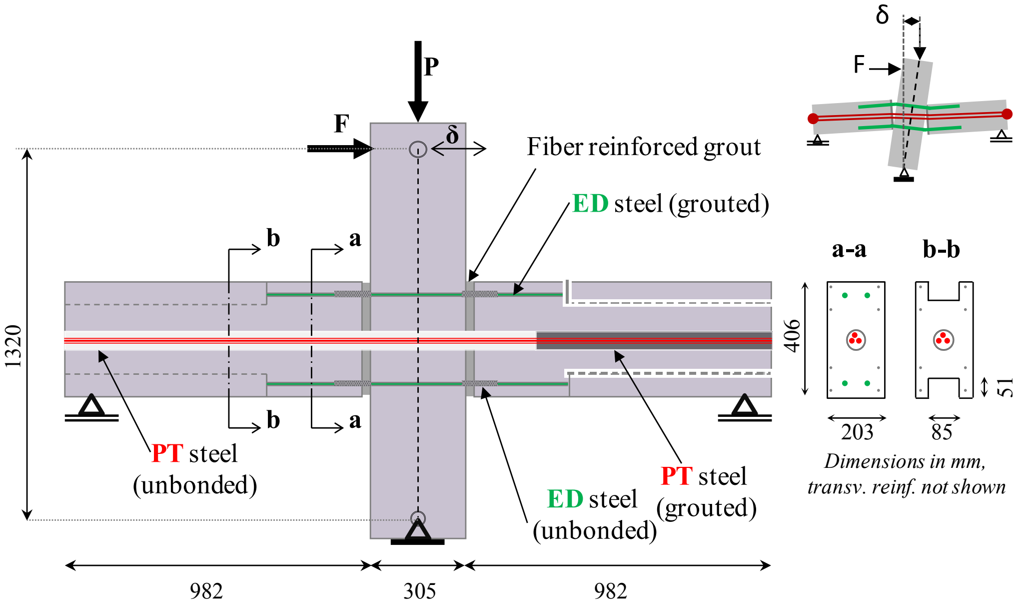

Figure 3-28 NIST beam-column sub-assemblage; test setup

Beam and column dimensions were the same in the two specimens (203x406 mm beams and 305x305 mm columns). Material properties based on component tests were f_c'=47 MPa for the concrete compressive strength, f_{py} = 1710 MPa, f_{pu} = 1868 MPa for the yield and ultimate strength of the PT steel, f_{sy} = 422 MPa, f_{su} = 673 MPa for the yield and ultimate strength of ED bars in specimen M-P-Z4, and f_{sy} = 523 MPa, f_{su} = 780 MPa for the yield and ultimate strength of

ED bars in specimen O-P-Z4. The post-tensioning steel consisted of three 13-mm, Grade 270 pre-stressing strands. The energy dissipating bars consisted of two No. 3 bars at the top and bottom of the beam in specimen M-P-Z4, and three No. 3 bars at the top and bottom of the beam in specimen O-P-Z4.

The column top of each specimen was subjected to a horizontal displacement history consisting of three cycles at several drifts ranging from 0.2% to 4.0%. Vertical loads, simulating gravity loads and maintained constant throughout the test, included an axial load on the column ($P/A_g f_c'\approx 0.40$) and a 20 kN vertical load on each beam adjacent to the column face. Initial prestress in the PT steel after losses was 45% of its ultimate tensile strength for specimen M-P-Z4 and 41% for specimen O-P-Z4.

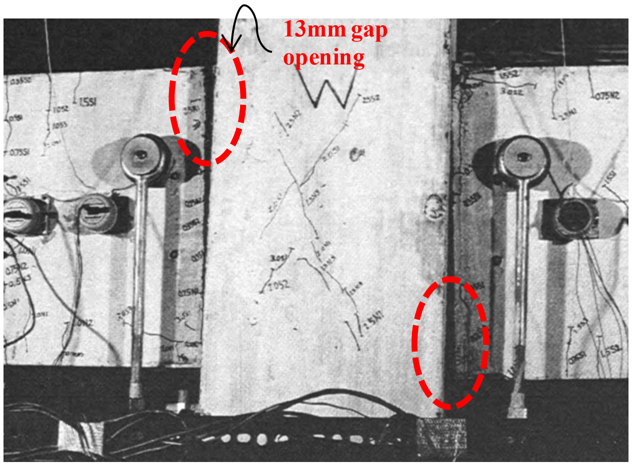

Figure 3-29 Specimen M-P-Z4 at failure (3.4% drift); from Stone et al. 1995

The behavior of the beam-column tests unit under lateral load was governed by a gap opening and closing at each beam-column interface. Minor cracks (less than 1 mm wide) developed in the beams and column at peak load and completely closed upon removal of the load. Crushing of the interface grout was also observed and concrete spalling at the beam ends began at approximately 0.75% story drift. Failure of both specimens occurred from fracture of the energy dissipating bars. In Specimen M-P-Z4 two of the bars fractured during the cycles to 2.9% story drifts and one fractured the cycle to 3.4%. The condition of the specimen at the end of the test is shown in Figure 3-29. The maximum gap opening at the beam-column interface of Specimen M-P-Z4 was 13 mm and peak PT stress was $0.85f_{pu}$. In Specimen O-P-Z4, failure occurred from fracture of eight out of the twelve energy dissipating bars (six bars per joint) at drifts of approximately 3.5 and 4.0%. The maximum gap opening at the beam-column interface was 11 mm and peak PT stress was $0.88f_{pu}$.

3.2.2 Development of analytical model of UPT beam-column sub-assemblages

Analytical models of NIST specimens M-P-Z4 and O-P-Z4 were developed in Perform3D (CSI, 2011). Figure 3-30 shows a representation of the analytical model of the beam-column test units. Similar to the wall model described in Section 3.1, main components of the model include inelastic fiber elements for the concrete members (beams, columns) and inelastic truss elements for the unbonded parts of the PT and ED steel. The longitudinal axis of the beam and column fiber elements coincides with the centerline of the beam and column, and rigid end zones were used for the portions of the beams and columns inside the joint.

Gap opening at the beam-to-column interface was modeled using a beam fiber segment with concrete-only fibers (no-tensile strength) over a critical length, L_{cr}, on either side of the column. In this way, gap opening under lateral load is simulated as elongation of the beam concrete fibers that go into tension (positive strain under zero stress). Similar to observations related to H_{cr} for UPT walls in Section 3.1, although the gap-opening displacement, calculated by integrating the concrete tensile strains over L_{cr}, is not that sensitive to the assumed value for L_{cr}, the calculated concrete compressive strains are dependent on its value. Recognizing the need for experimental validation, Stanton and Nakaki (2002) suggest using an equivalent plastic hinge length for UPT connections equal to the depth of the compression zone (or contact depth) calculated for the critical section at the design drift. This recommendation was made on the basis of St. Venant's principle which suggests that a local disturbance in stress dies out rapidly at distances greater than the member depth. Using the above recommendation, a value of $L_{cr} = c \approx 0.12h$ (where c is the estimated neutral axis depth at 2.0% beam rotation and h is the beam height) was used in this study and was found to produce results in good agreement with the experimental values.

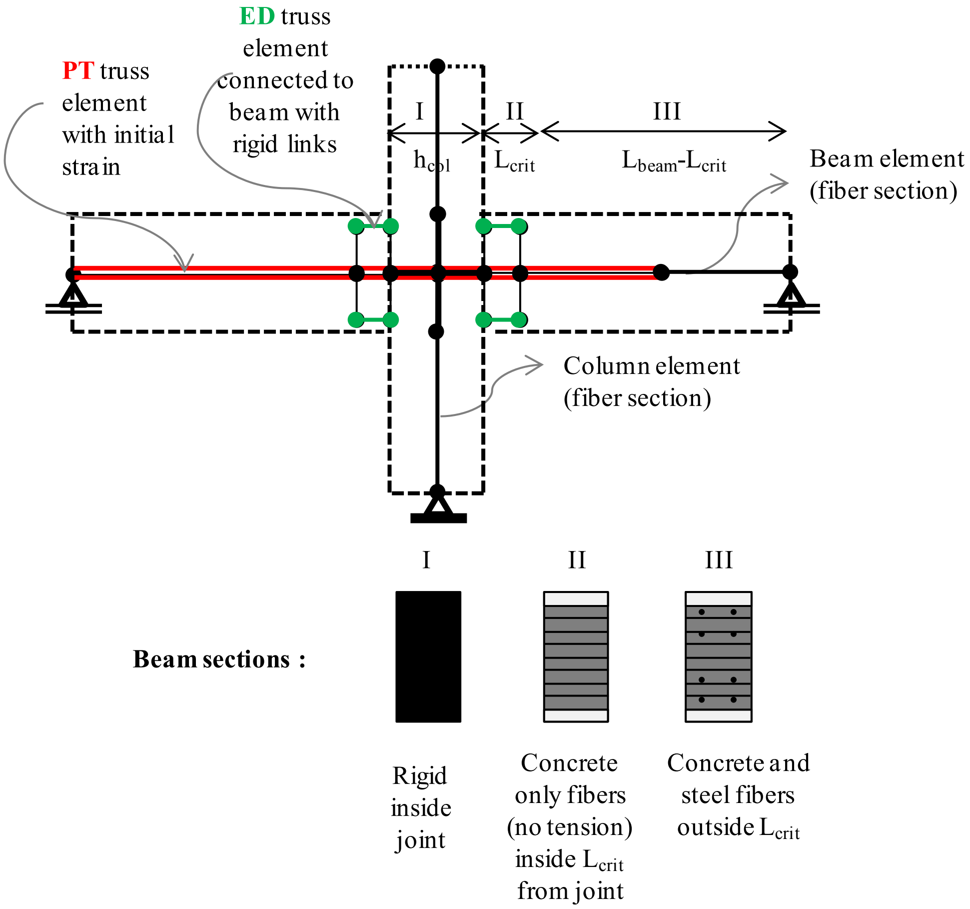

Figure 3-30 Representation of analytical model of NIST UPT beam-column sub-assemblage

Outside the length L_{cr}, any reinforcement that was bonded and adequately developed was included in the beam fiber section. The unbonded part of the PT steel was modeled as an inelastic truss element with common nodes with the beam at its end nodes. Similarly, the unbonded parts of the energy dissipating bars were modeled as truss elements with rigid links at their ends to connect them to the beam. In addition to the intentionally debonded length of the energy dissipating bars, $L_{ED,un}$, a strain penetration length, L_{sp}, on either side, was also included in the total length, $L_{ED,eff}$, of the truss elements representing the energy dissipating bars ($L_{ED,eff} = L_{s,un}+2L_{sp}$). Cheok et al. (1996) used the gap opening measurements at the beam-column interface of specimen M-P-Z4 to estimate an effective debonded length equal to 100 mm at the end of the test, which is the value used for $L_{ED,eff}$ in this study. It is noted that a very short intentionally debonded length (25 mm on either side of the column) was provided in the tests, so that in this case any additional length L_{sp} has a significant impact on calculated ED strains.

Stress-strain relationships for all materials in the model (unconfined concrete, PT and ED steel) were based on material characterization tests that were performed as part of the NIST test program (Cheok and Stone, 1994). The stress-strain relationships for the confined (by welded reinforcement grids) concrete were derived using the Saatcioglu and Razvi (1992) model. The fiber reinforced grout at the beam-column interfaces was not explicitly modeled, instead it was assumed to have the same behavior as the confined concrete.

Consistent with the test setup, a pinned boundary condition was assigned at the column base in the model and rollers are used at the beam ends. Out-of-plane degrees of freedom were fixed and P-Delta effects were included in all analyses. Loading consists of the prestressing force in the beam, simulated as an initial strain in the PT truss element, followed by application of gravity loads on the beams and column, and a series of nonlinear static pushover analyses that simulate the displacement history that the top of the column was subjected to during the test.

Monotonic pushover analyses were also performed to compare with the experimental response envelope of the test specimen.

3.2.3 Comparisons of analytical and experimental results

Figure 3-31 and Figure 3-32 compare the measured lateral load-displacement response of specimens M-P-Z4 and O-P-Z4, respectively, with results from the analytical models. Under monotonic loading, the analytical models provide a very satisfactory envelope of the experimental responses, with good predictions of the initial stiffness, peak strength, and strength loss observed at large drifts. Small discrepancies in peak strength could be associated with underestimation of the effective debonded length of the PT steel. Note that the length used in the analytical model for the truss element implementing the PT steel coincides with the deliberately debonded length specified in the test. However, as the PT steel was bonded for part of its length (Figure 3-28), strain penetration effects, similar to the ED bars, could have resulted in a larger effective debonded length for the PT steel, which is not captured in the analytical model.

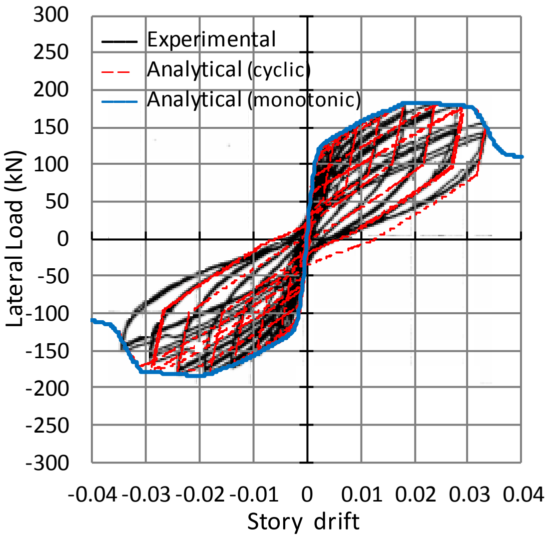

Figure 3-31 Analytical and experimental lateral load-displacement response of specimen M-P-Z4

Under cyclic lateral loading, the model adequately captures the self-centering behavior of test specimen M-P-Z4. The "fatter" hysteretic loops of specimen O-P-Z4 are also captured in the model and are associated with larger contribution to moment resistance from the energy dissipating bars (three No.3 bars in specimen O-P-Z4 as opposed to two No.3 bars in specimen M-P-Z4). The unloading and reloading stiffness of the analytical models also closely match those observed in the test, resulting in hysteretic loops of approximately equal area with the experimental ones. The slightly narrower hysteretic loops at small drifts can be attributed to possible overestimation of the effective debonded length ($L_{\mathrm{ED,eff}}$) of the energy dissipating bars as its calculation was based on estimated strain penetration lengths at the end of the test.

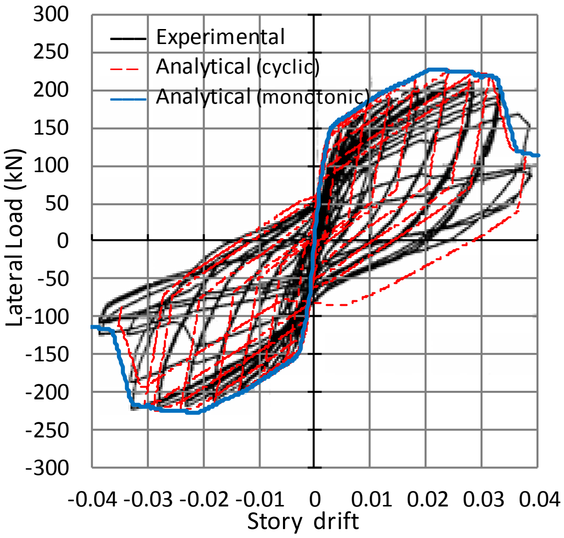

Figure 3-32 Analytical and experimental lateral load-displacement response of specimen O-P-Z4

3.3 Summary

This chapter presented the development and experimental validation of analytical models for unbonded post-tensioned precast concrete components. Analytical models of five UPT wall tests and two UPT beam-column sub-assemblages were developed and validated through comparisons of analytical results with published experimental data from the experiments. Particular emphasis was placed on modeling aspects of UPT walls and specifically on implementing the gap opening behavior, capturing peak concrete strains (through an appropriate selection for H_{cr}) and determining cyclic degradation parameters for concrete and PT steel. The good correlations between predicted and measured responses verify the viability of the proposed modeling recommendations. In Chapter 6, the modeling approaches validated through the component studies presented herein will be implemented in the analytical model of the E-Defense PT building to examine how approaches suitable for component-level analyses can be extended to predict responses at the system-level.

Chapter 4 Overview and design of four-story precast PT building

This chapter provides an overview of the full-scale, four-story, precast post-tensioned building that was tested on the E-Defense shake table in 2010. Information provided includes design details, material properties, test sequence, and instrumentation. The extent to which the unbonded post-tensioned precast walls of the test building satisfied strength and detailing provisions of ACI ITG-5.2 (2009) is also evaluated.

4.1 The 2010 E-Defense shake table tests

In December 2010, two full-scale, four-story buildings were tested under three-dimensional dynamic loading on the E-Defense shake table in Miki, Japan (Figure 4-1). The two buildings were almost identical in geometry and configuration, and were tested simultaneously, as shown in Figure 4-2 and Figure 4-3. One of the test buildings, referred to as "the RC building", incorporated conventional reinforced concrete systems (RC structural walls in one direction and RC moment frames in the orthogonal direction) whereas the other building, referred to as "the PT building" hereafter, was constructed form precast concrete members jointed together with post-tensioning steel. The PT building utilized unbonded post-tensioned precast concrete walls as the main lateral force-resisting system along one building axis, and precast bonded post-tensioned frames in the orthogonal direction. The buildings were simultaneously subjected to increasing intensity shaking, using recorded ground motions from the 1995 Kobe earthquake. Both structures were heavily instrumented and a total of 609 channels of data were collected during the tests including accelerometers, displacement transducers, and strain gauges. The tests provided a wealth of data to assess behavior of RC and UPT components under multi-directional dynamic loading and to investigate system interactions.

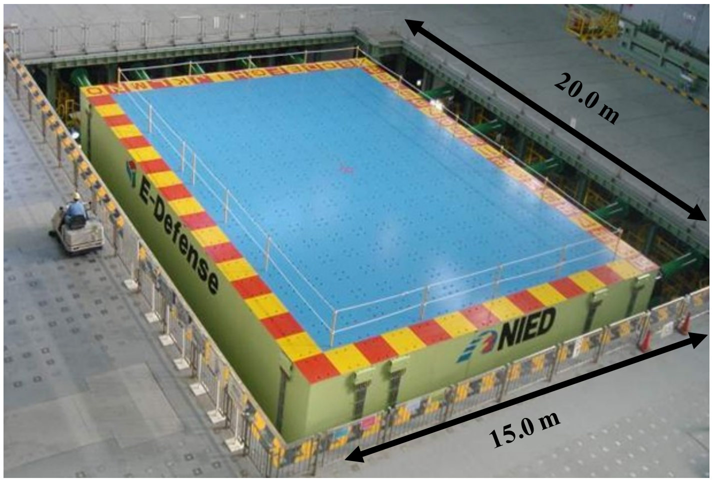

Figure 4-1 The E-Defense shake table

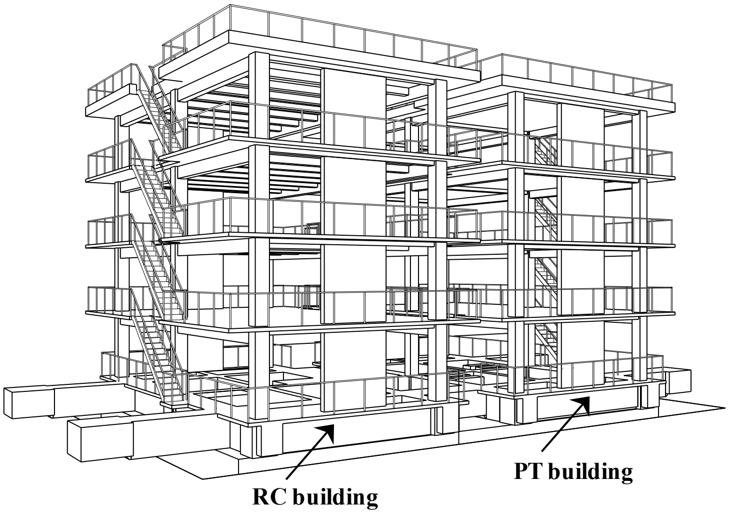

Figure 4-2 Overview of test setup on shake table

This study focuses solely on the response of the PT building and specifically on the behavior in the direction that utilized UPT walls for a lateral-force-resisting system. An overview of the test program for the PT building, including design details, material properties, test sequence, and instrumentation is provided in the following sections. Additional information can be found in Nagae et al. (2011). Experimental results in the wall direction of the PT building are presented in Chapter 5. Given that the majority of prior UPT wall tests involved two-dimensional, moderate-scale specimens, tested under quasi-static cyclic loading, the 2010 E-Defense shake table tests documented herein provide unique data to assess seismic performance of UPT walls incorporated into an entire building system. By using a full-scale physical model with sufficient complexity to represent typical connections and interactions of a real building, the tests provide insight into issues typically not addressed in component-level experimental studies.

Figure 4-3 RC and PT buildings on shake table

4.2 Description of PT test building

Figure 4-4 shows the plan layout of a typical floor of the PT building. Plan dimensions were 14.4 m in the longitudinal (x) direction and 7.2 m in the transverse direction (y). Story heights were 3.0 m at all levels, resulting in an overall height of 12.0 m.

Different lateral force resisting systems were used in the two principal directions of the PT building. In the y direction, lateral resistance was provided by UPT precast concrete walls, located at opposite sides of the building, and coupled to corner columns by UPT precast beams. Figure 4-5 shows the elevation along lines A and C of the PT building. Each UPT wall consisted of four, vertically stacked, precast concrete panels. Non-shrink grout with a thickness of 30 mm was used at joints between individual precast panels and at the interface between the base panel and the foundation. All precast wall panels were 2500 mm long and 250 mm thick. The first three wall panels were one-story tall while the fourth wall panel extended 450 mm above the roof slab so that the assembled UPT wall had a height-to-length aspect ratio (H_w/l_w) of five.

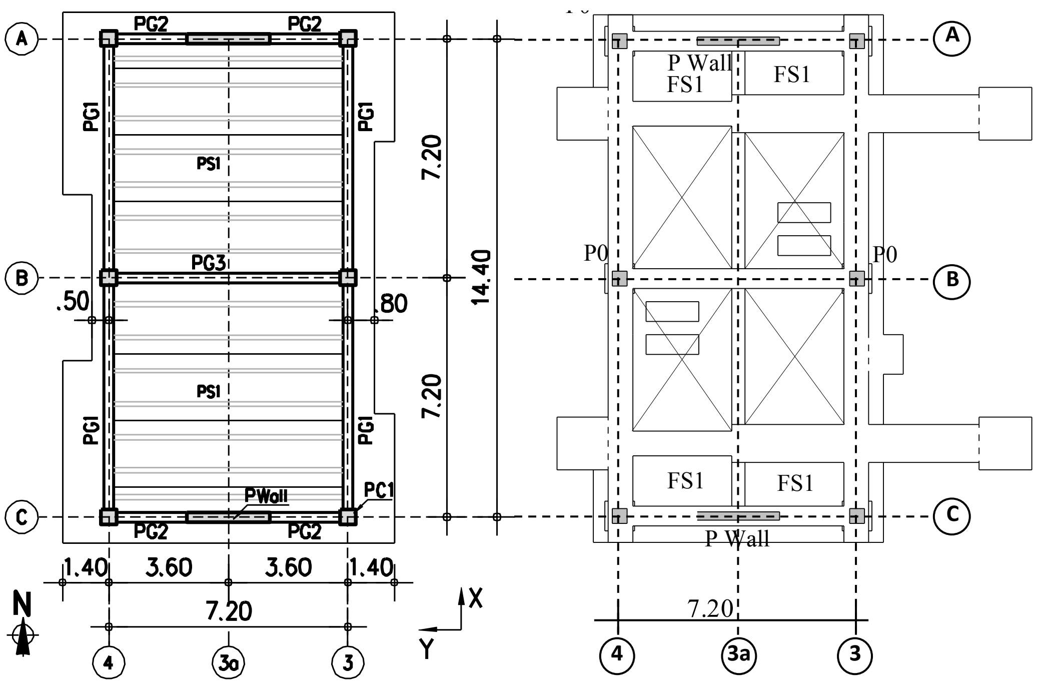

(a) (b)

Figure 4-4 Typical framing plan (a) and foundation plan (b) of PT building (dimensions in m)

The vertical post-tensioning steel was unbonded over its entire height, from an anchor at the top of the wall to an anchor at the bottom of the foundation beam. The vertical mild steel reinforcement of individual wall panels was not developed across the horizontal joints or into the foundation. At the base panel, additional mild reinforcing bars were placed across the wall-foundation interface to provide energy dissipation. These bars were unbonded over the bottom

1500 mm within the lower wall panel and were anchored within the foundation using grouted couplers.

The columns consisted of precast concrete elements (450 mm x 450 mm cross sections), two-stories tall, jointed together with post-tensioning bars placed in ducts within the columns. Threaded couplers above the third floor and above the foundation beam connected PT bars of individual precast column elements to each other and the foundation. Ducts of columns were grouted after post-tensioning. Precast UPT beams (300 mm x 300 mm cross sections) on either side of each wall coupled the wall to the corner columns at each floor level. The individual single-bay precast UPT beams on either side of the wall were connected by horizontal post-tensioning steel that ran through ducts in the beams and through the wall and columns. The beam post-tensioning steel was unbonded over its entire length between anchors at the exterior beam-column joints. The mild steel reinforcement of individual precast beams was not developed across joints and no additional mild steel reinforcement was provided across the beam-column and beam-wall interfaces. The floor system consisted of precast pre-tensioned double tees spanning across the entire building width parallel to the 2500 mm dimension of the walls. Once placed, the double tees were topped with a 100-mm thick cast in-place concrete slab. The upper 100-mm portions of the UPT beams were also cast in-place together with the slab, and the beams were prestressed after casting of the slab. In addition to the exterior frames (A and C in Figure 4-4), an interior one-bay frame consisting of an UPT beam and bonded post-tensioned columns also contributed to lateral resistance in the y direction of response (Frame B in Figure 4-4)).

In the x direction, lateral resistance was provided by two perimeter two-bay moment frames constructed with precast beam and column elements jointed together with post-tensioning steel. The individual single-bay precast beam elements were connected to the multistory precast columns by post-tensioning strands running through ducts in the beam and through the columns, and anchored at the exterior joints. Similar to the columns, the ducts of x direction beams were grouted after post-tensioning to achieve fully bonded conditions. This type of bonded post-tensioned precast concrete frame, although not common in the U.S., has been used in Japanese practice. The foundation consisted of interconnected deep concrete beams anchored to the shake table with PT bars (Figure 4-4(b)).

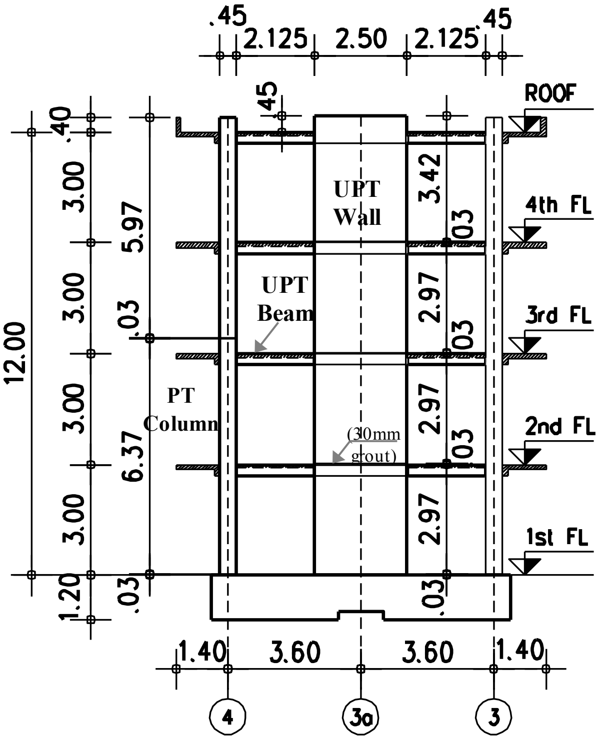

Figure 4-5 Elevation along lines A and C of PT building

Figure 4-6 shows cross-sections of the base and upper story precast wall panels. Each UPT wall was post-tensioned to the foundation by means of two strand groups, each one consisting of ten 15.2-mm-diameter strands, resulting in an overall ratio of post-tensioning steel $\rho_{PT}=A_{PT}/(l_w t_w)=0.45\%$. The strand groups were located in polyethylene ducts positioned symmetrically at a distance equal to 15% of the wall length on either side of the wall centroid and were stressed to 60% of their nominal yield stress (f_{py}). The energy-dissipating reinforcement at the base of the lowermost panel consisted of four 22-mm-diameter reinforcing bars on either side of the wall centerline, resulting in an overall ratio of energy dissipating steel $\rho_{ED}=A_{ED}/(l_w t_w)=0.50\%$. As mentioned above, these bars were deliberately debonded over the bottom 1500 mm within the lower wall panel and were anchored within the foundation using grouted couplers. The concrete at the ends of the base panel was confined by high strength (KSS785) 13-mm-diameter overlapping hoops spaced vertically at 75 mm on center and extending horizontally over a length of 540 mm at each wall panel boundary. The vertical faces of the panels were reinforced with a two-way mesh of 13-mm-diameter reinforcing bars. Supplemental 13-mm-diameter transverse (through-thickness) ties were added to prevent separation of the reinforcing mesh from the concrete core, a failure mechanism noted by Perez et al. (2004, 2013). Figure 4-7, Figure 4-8 and Figure 4-9 show the wall-to-foundation, wall-to-slab and beam-to-wall connection details, respectively.

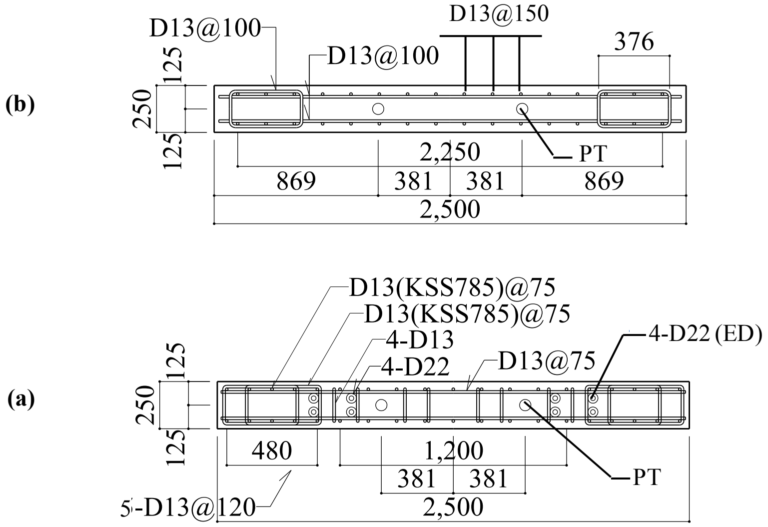

Figure 4-6 UPT wall cross sections of (a) 1st story and (b) upper wall panels (dimensions in mm)

Finally, Figure 4-10 shows the cross sections of the y-direction UPT beams (PG2 and PG3) and the cross sections of columns. The post-tensioning reinforcement of beams in Frames A and C was high-strength steel strands positioned at 130 mm from the bottom face of the 300mm deep and stressed to 60% of their nominal yield stress. The top 100 mm of the UPT beams and the slab were cast monolithically and mechanically connected through the beam stirrups. The post-tensioning reinforcement of the square columns consisted of eight 21-mm-diameter high-strength steel bars stressed to 80% of their nominal yield stress.

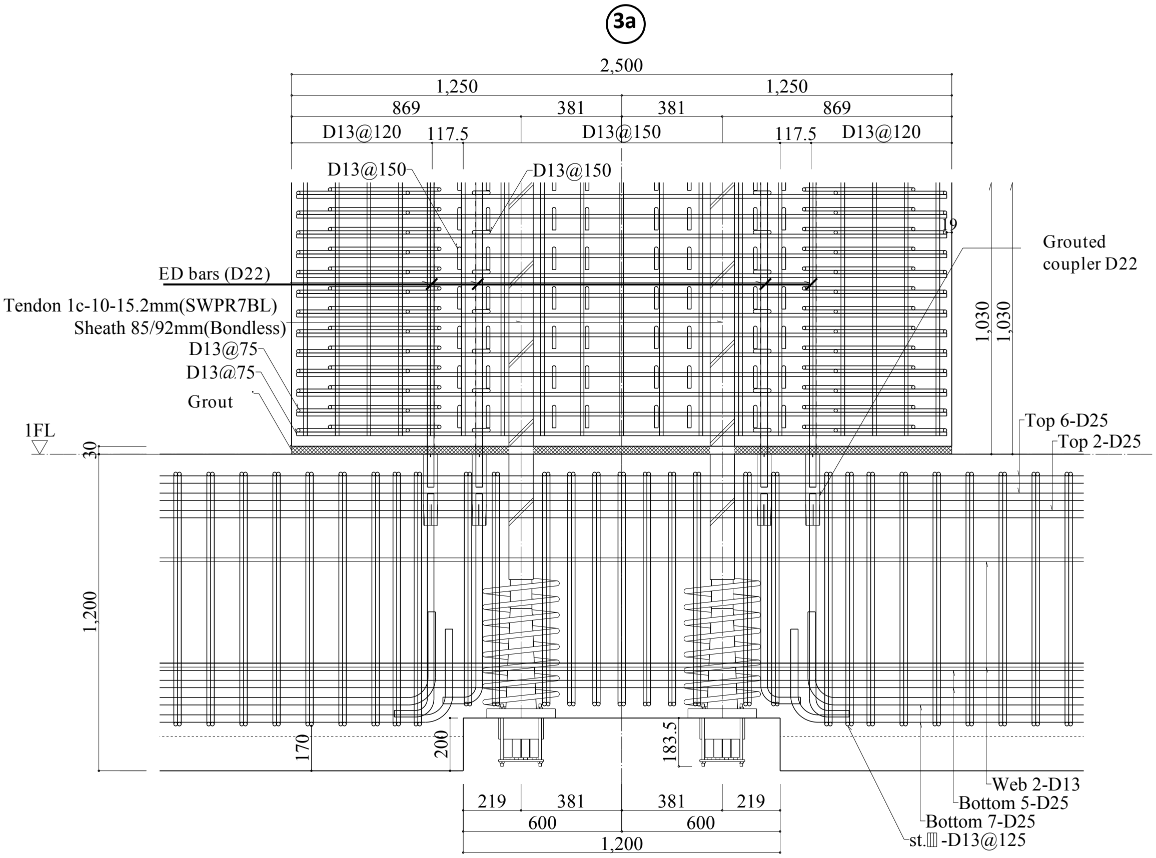

Figure 4-7 Wall-to-foundation connection detail (dimensions in mm) from Nagae et al. 2011

The lumped floor weights of the test building were 804, 806, 813 and 996 kN for the 2nd, 3rd, 4th floor and roof, respectively (Nagae et al., 2012), and include self-weight of all concrete members and superimposed dead load such as the weight of mechanical equipment that was incorporated in the building and the weight of rigid steel frames that were used for story displacement measurements. Table 4-1 shows the initial prestress of all members and the gravity load at the base of vertical members. Note that, due to the geometry of the building and orientation of the floor units, which spanned between the perimeter x-direction frames, the gravity load on the UPT walls was very low (less than $0.01f_c'A_g$).

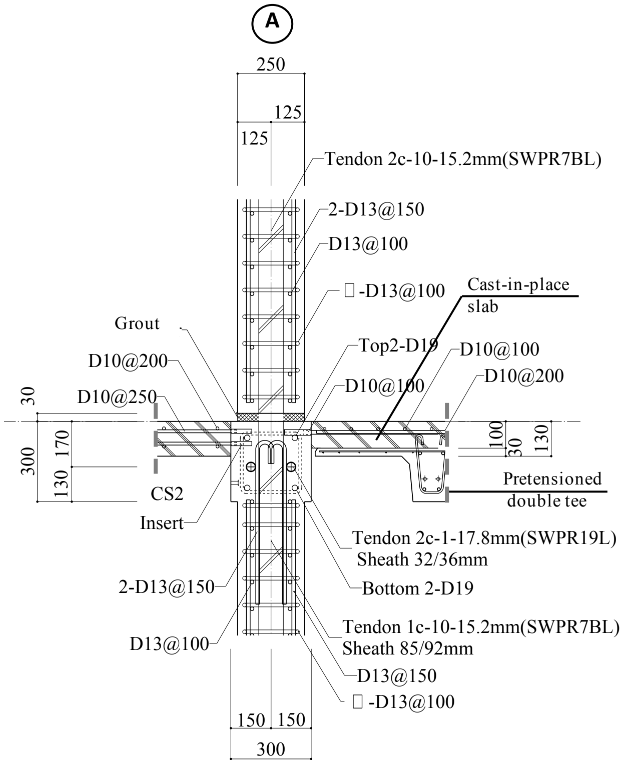

Figure 4-8 Wall-to-slab connection detail (dimensions in mm) from Nagae et al. 2011

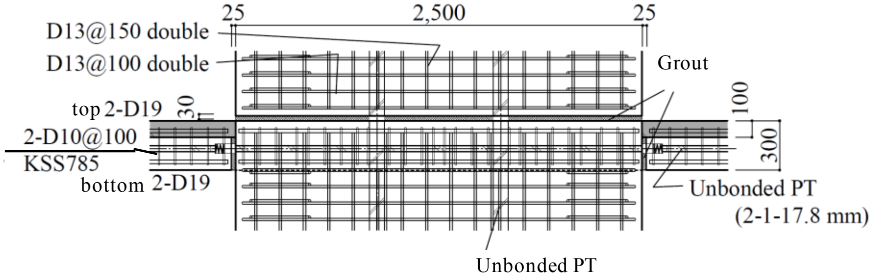

Figure 4-9 Beam-to-wall connection detail at 3rd floor (dimensions in mm) from Nagae et al. 2012

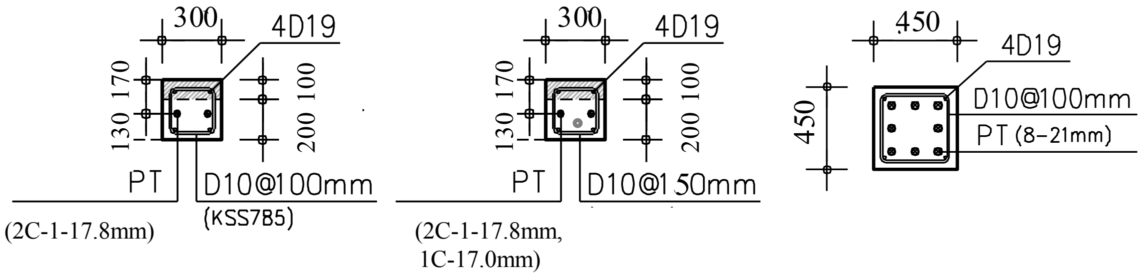

(a) PG2 beam **(b) PG3 beam** **(c) PT column**

Figure 4-10 Cross sections of y-direction UPT beams (a), (b) and PT column (c) (dimensions in mm)

Table 4-1 Initial prestress N_p and gravity load N_g

Member	N_p (kN)	N_g (kN)
Wall	2669	220
PC1 Column (Axis A)	2394	401
PC1 Column (Axis B)	2394	690
PG1 Beam (2nd, 3rd Fl)	2161	-
PG2 Beam	396	-
PG3 Beam	697	-

4.3 Materials

The specified concrete compressive strength was 60 MPa for all precast members of the PT building and 30 MPa for the cast in place slab (topping concrete). The specified compressive strength of the grout in joints between precast members (between individual precast panels, in wall-foundation joints and in the beam-to-wall, beam-to-column joints) was 60 MPa. In the north UPT wall (axis A), the first and second story precast concrete panels as wells as the grout between these panels and the grout in the wall-foundation joint contained steel fiber reinforcement. Fibers in the concrete mix were 30 mm long with a nominal strength of 1000 MPa while fibers in the grout were 10 mm long with a nominal strength of 1500 MPa.

Table 4-2 presents average compressive strengths of concrete and grout from material tests. The nominal strength of the post-tensioning strands used in the UPT walls and PG2 UPT beams was 1600 MPa while the high-strength steel bars of columns had a nominal strength of 1080. Table 4-3 presents average yield and ultimate strengths of the post-tensioning steel from material tests. Also shown in Table 4-3 are the properties of the mild steel reinforcement used in the test building. The 22-mm-diameter energy dissipating bars at the base of each UPT wall had nominal yield strength of 345 MPa (grade SD345). The vertical faces of the wall panels were reinforced with a two-way mesh of 13-mm-diameter grade SD295 reinforcing bars. Longitudinal mild reinforcement of precast beams and columns consisted of 19-mm-diameter SD345 bars. Finally, high strength transverse reinforcement with nominal yield strength of 785 MPa (grade KSSS785) was used in the UPT beams (PG2) and at the ends of the first story UPT wall panels.

Table 4-2 Concrete and grout properties

Material	f_c' (MPa)
Concrete	83.2
Concrete (fiber)	85.5
Topping concrete	40.9
Grout	135.6
Grout (fiber)	120.3

Table 4-3 Reinforcing steel properties

Material (location)	Area (mm^2)	f_y (MPa)	f_t (MPa)
15.2-mm SWPR7BL PT wire (wall, beam PG1)	140.7	1777	1969
17.8-mm SWPR19L PT wire (beam PG2, PG3)	208.4	1708	1939
21-mm SBPR1080/1230 PT bar (column PC1)	346.4	1194	1277
D22 SD345 (wall energy dissipating bars)	387	385	563
D13 SD295 (wall horizontal and vertical reinf.)	127	347	501
D13 KSS785 (wall transverse reinf.)	127	938	1107
D19 SD345 (beam PG1-PG3, column PC1 long. reinf.)	287	389	561
D10 SD295 (beam PG1, PG3, column PC1 transv. reinf.)	71	361	518
D10 KSS785 (beam PG2, transverse reinf.)	71	952	1055

4.4 Test sequence

Ground motions recorded at the JMA-Kobe and JR-Takatori stations during the 1995 Kobe earthquake (magnitude M_w=6.9) were used as input motions for the experimental program. The building was first subjected to increasing intensities of the JMA-Kobe record (10%, 25%, 50% and 100%), followed by two additional tests under the JR-Takatori record (scaled to 40% and 60%). For each record, the three components of recorded ground accelerations (NS, EW, vertical) were applied simultaneously and aligned with the transverse (y), longitudinal (x), and vertical direction of the specimen. At the beginning of the test and between records, low-amplitude white noise excitation tests were performed.

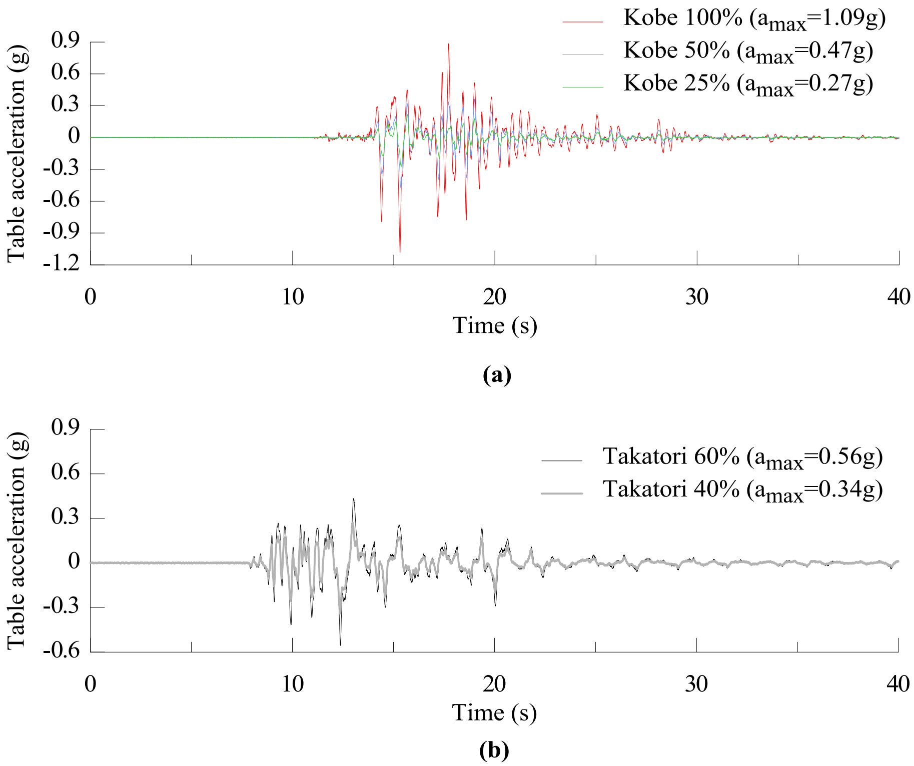

(a)

(b)

Figure 4-11 Shake-table acceleration response histories for (a) Kobe and (b) Takatori records

Figure 4-11 shows the y-direction acceleration histories for the JMA-Kobe (referred to as Kobe hereafter) and JR-Takatori (referred to as Takatori hereafter) records as observed on the shake table. Figure 4-12 and Figure 4-13 plot the 5% damped acceleration and displacement response spectra derived from the records in Figure 4-11. The input motions were selected and scaled to represent a range of earthquake levels from low-intensity frequent earthquakes to large-intensity very rare earthquakes. For reference, the design and $\mathrm{MCE_R}$ spectra (ASCE 7-10) for a site in downtown Los Angeles (S_s=2.39, S_1=0.84, site class D) are also included in Figure 4-12 and Figure 4-13. Note that the estimated fundamental period in the y direction of the PT building using test data from the white-noise base excitation at the beginning of the test was 0.27 sec (Section 5.2).

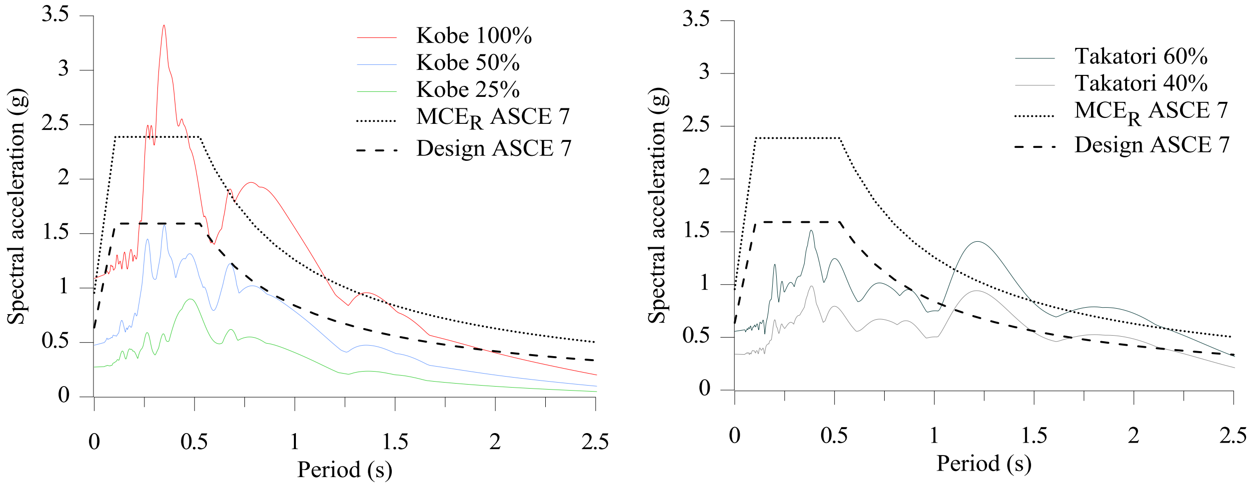

(a) **(b)**

Figure 4-12 Elastic 5.0% damped acceleration spectra for (a) Kobe and (b) Takatori records

Comparing the Kobe and Takatori records, up to periods of around 1.0 sec, spectral ordinates of the 60%-Takatori record are similar to the 50%-Kobe ordinates but for longer periods (> 1 sec), the 60%-Takatori spectra exceed the 50% Kobe spectra, and for periods longer than 1.1 sec even exceed the 100%-Kobe spectral responses. Similarly, the 40%-Takatori spectra match the 25%-Kobe spectra up to 1.0 sec but exceed both the 25% and 50%-Kobe spectral ordinates at longer periods. Based on these observations, the Takatori records impose higher demands than the Kobe records as the fundamental period elongates due to nonlinear response.

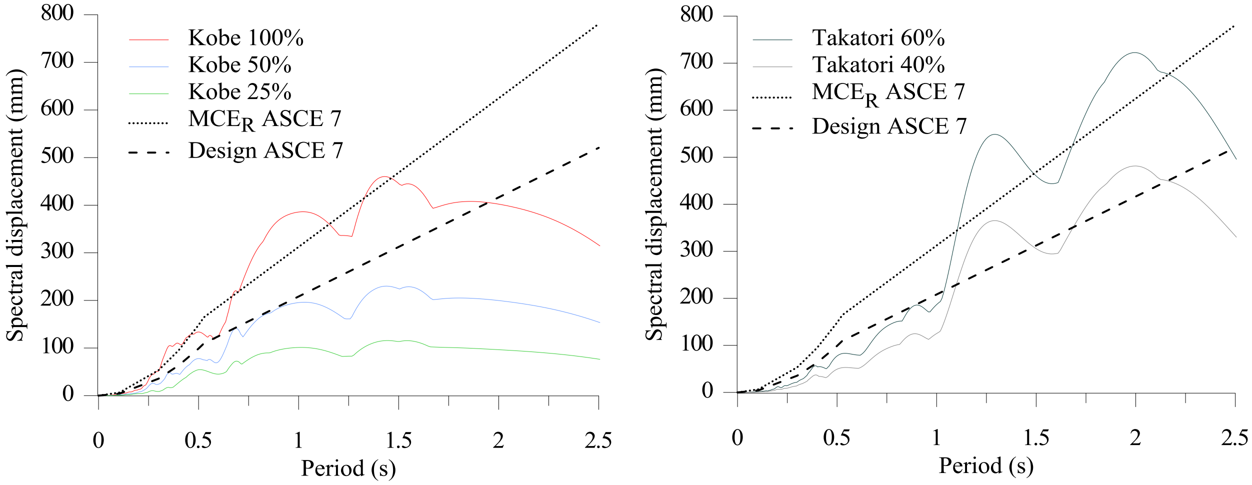

(a) **(b)**

Figure 4-13 Elastic 5.0% damped displacement spectra for (a) Kobe and (b) Takatori records

4.5 Instrumentation

The PT test building was instrumented with a large number of sensors that enabled assessment of overall structural performance and examination of local responses (NEEShub project 2011-1005). Primary data recorded during the tests included accelerations and displacements. Accelerometers were placed on the foundation and on each floor slab of the building to record accelerations in three directions. Figure 4-14 shows the locations of accelerometers A1, A2 on a plan view of a typical floor of the PT building. Also shown in the figure are the laser (D1) and wire (D2, D3) displacement transducers that recorded (relative) lateral story displacements.

Figure 4-15 shows the instrumentation used at the first story panel of the south UPT wall (axis C). The vertical LVDTs D1 and D2, attached to the edges of the panel and close to the horizontal wall centerline, allowed wall uplift and average concrete strains over their 250 mm gauge length to be computed. LVDTs D3-D6 on the interior face of the UPT wall, with a gauge length of approximately 500 mm, allowed gap-opening profiles and wall base rotations to be determined. Additional vertical displacement sensors on the exterior (SW, SE) and interior (NW, NE) faces of the south wall, with a gauge length of 1000 mm, enabled calculation of out-of-plane wall base rotations. On the exterior face, two pairs of diagonal displacement transducers measured wall-panel shear deformations over the first story while a horizontal displacement transducer at the base of the panel recorded sliding displacements. Other instrumentation in the south UPT wall included strain gauges attached to energy dissipating bars and boundary transverse reinforcement near the wall base, and load cells that measured forces in the vertical post-tensioning steel. Instrumentation at the first story panel of the north UPT wall consisted only of sensors D1-D10.

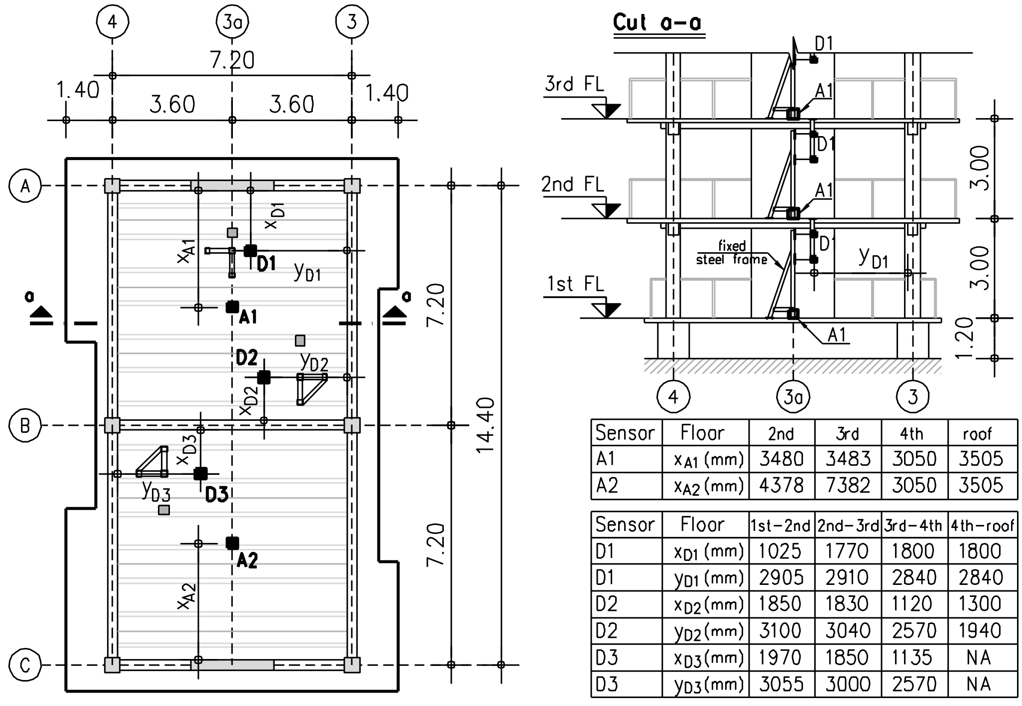

Sensor	Floor	2nd	3rd	4th	roof
A1	x_{A1} (mm)	3480	3483	3050	3505
A2	x_{A2} (mm)	4378	7382	3050	3505

Sensor	Floor	1st-2nd	2nd-3rd	3rd-4th	4th-roof
D1	x_{D1} (mm)	1025	1770	1800	1800
D1	y_{D1} (mm)	2905	2910	2840	2840
D2	x_{D2} (mm)	1850	1830	1120	1300
D2	y_{D2} (mm)	3100	3040	2570	1940
D3	x_{D3} (mm)	1970	1850	1135	NA
D3	y_{D3} (mm)	3055	3000	2570	NA

Figure 4-14 Locations of accelerometers (A1, A2) and displacement transducers (D1, D2, D3).

Beams and columns were instrumented with horizontal and vertical displacement transducers, respectively, that allowed average member end rotations to be computed and axial elongations to be estimated. Finally, displacement transducers extending vertically from the foundation beam to the second floor measured slab deflections in the proximity of the south UPT wall. The slab sensors (S1-S14) were arranged along longitudinal and transverse lines close to the south wall as shown in Figure 4-16.

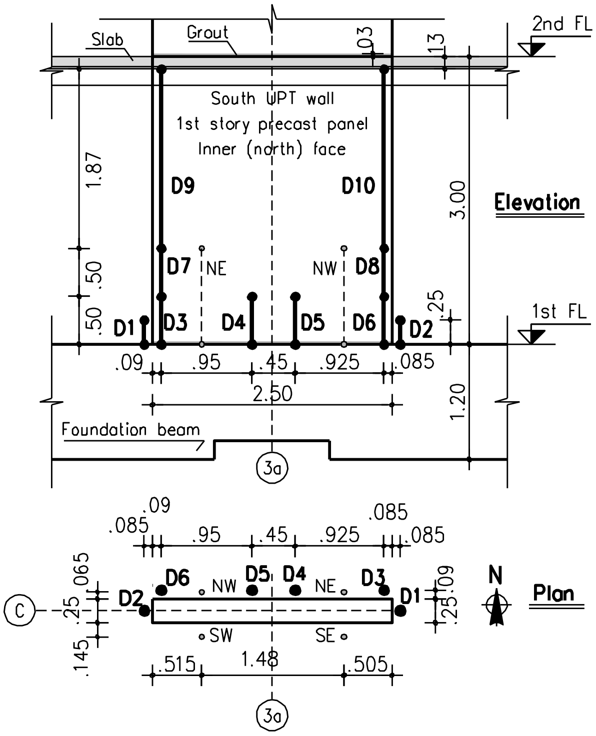

Figure 4-15 Instrumentation at first story panel of south UPT wall (dimensions in m)

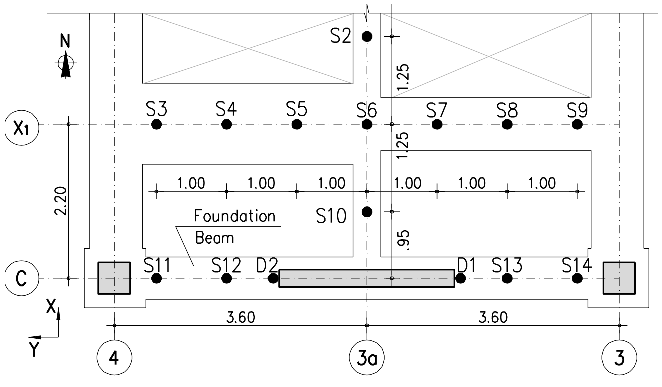

Figure 4-16 Instrumentation in second floor slab (dimensions in m)

4.6 Assessment of UPT Wall design based on ACI ITG-5.2 (2009)

While experimental research on unbonded post-tensioned structural systems has demonstrated the advantages of these systems, namely their ability to achieve large nonlinear deformations expected in strong earthquake shaking with minimal structural damage and minor residual deformations, their use in practice is still limited. In order to move UPT systems into wider practice it is necessary that experimental evidence of their seismic performance be accompanied with design and analysis tools suited for design office application.

ACI 318 permits use of precast concrete structural systems only if experimental results and analysis demonstrate that the proposed precast system has "strength and toughness" at least equal to those of a comparable monolithic (cast-in-place) reinforced concrete system (21.1.1.8). ACI ITG-5.1 (adopted since 2008 by ACI 318) defines the minimum experimental evidence required to satisfy 21.1.1.8 to permit use of UPT walls as special RC structural walls. ACI ITG-5.2, now referenced in ACI 318-11 (R21.10.3), provides design requirements for a specific type of unbonded post-tensioned precast wall system, coupled or uncoupled. These ACI Standards constitute a significant step in codifying UPT precast concrete systems and incorporating them into ACI 318.

While ACI ITG-5.2 design requirements for UPT walls have been previously validated against moderate-scale component tests under static cyclic loading (Smith and Kurama 2012b), they have yet to be benchmarked against full-scale building tests under dynamic loading. To this end, this section explores the extent to which the UPT walls of the E-Defense test building satisfied strength and detailing provisions of ACI ITG-5.2 (2009) and in subsequent discussion of experimental results in Chapter 5, reference to ACI ITG-5.2 is made where relevant. It is also noted that the Lehigh walls (Perez et al. 2013), against which the analytical models of Chapter 3 were validated, did not satisfy the requirements of ACI ITG-5.2 as moment strength at the base of these walls was provided solely by PT steel, and no energy dissipating bars were included at the wall-to-foundation rocking interface.

Finally, in addition to checking design of the E-Defense UPT walls based on ACI ITG 5.2 requirements, the design forces and wall capacities presented in this section provide a useful context for interpretation of the E-Defense experimental results presented in the following chapter.

4.6.1 Design forces

Design force demands in the y-direction of the E-Defense PT building as reported in Nagae et al. (2011) were based on a seismic base shear equal to 20% of the weight of the building to represent the design earthquake (DBE) and a seismic base shear 1.5 times higher to represent the maximum considered earthquake (MCE). In addition, the UPT concrete walls were designed to remain elastic up to a seismic base shear equal to 15% of the weight of the building (Nagae et al. 2011). While a serviceability earthquake level should be accounted for within a performance-based design approach, only the DBE and MCE levels are considered herein, consistent with the prescriptive design procedure of ACI ITG-5.2 which requires checks to be performed at the DBE (θ_{design}) and MCE (θ_{max}) levels. Based on this information, and the total weight of the building, W= 3420 kN, the design and MCE base shear forces in the y-direction of the PT building are: V_{u_DBE}= $0.2W$ = 684 kN, and V_{u_MCE}= $0.3W$ = 1026 kN.

For reference, using the elastic spectra for the site in downtown Los Angeles (S_s=2.39, S_1=0.84, site class D) shown in Figure 4-12, the design and MCE base shears would be $0.265W$ and $0.40W$ respectively, approximately 30% higher than what the E-Defense PT building was designed for. A response modification factor R= 6 was used for this calculation as permitted for

UPT walls designed according to ACI ITG-5.2 ("special" UPT walls), and an approximate fundamental period of T_A= 0.31 sec according to ASCE 7 (2010).

Using a vertical distribution of seismic forces in accordance with 12.8.3 of ASCE 7-10 (Figure 4-17), which represents an approximate first mode distribution, the base moments corresponding to V_{u_DBE}=684 kN and V_{u_MCE}=1026 kN were computed: M_{u_DBE} = 6332 kNm, M_{u_MCE} = 9497 kNm. The resultant lateral force from this first mode distribution of seismic forces acts at 77% of the height, *H*, of the building measured from the top of the foundation (H_{eff}= M_u/V_u= 0.77*H*). Design and MCE story shears and moments along the height of the building are shown in Figure 4-18.

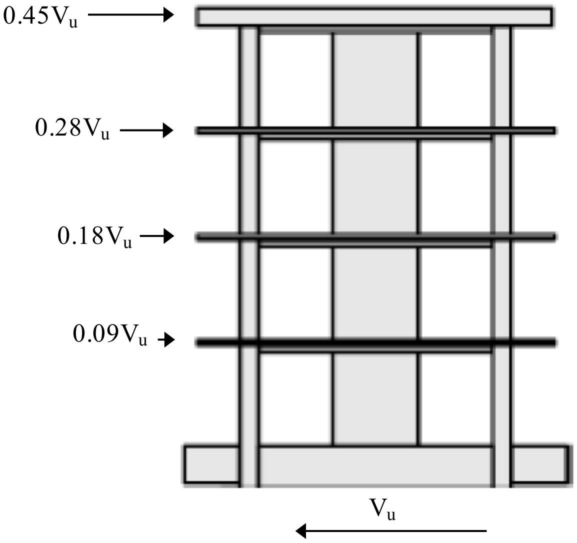

Figure 4-17 Vertical distribution of seismic forces in y-direction of PT building

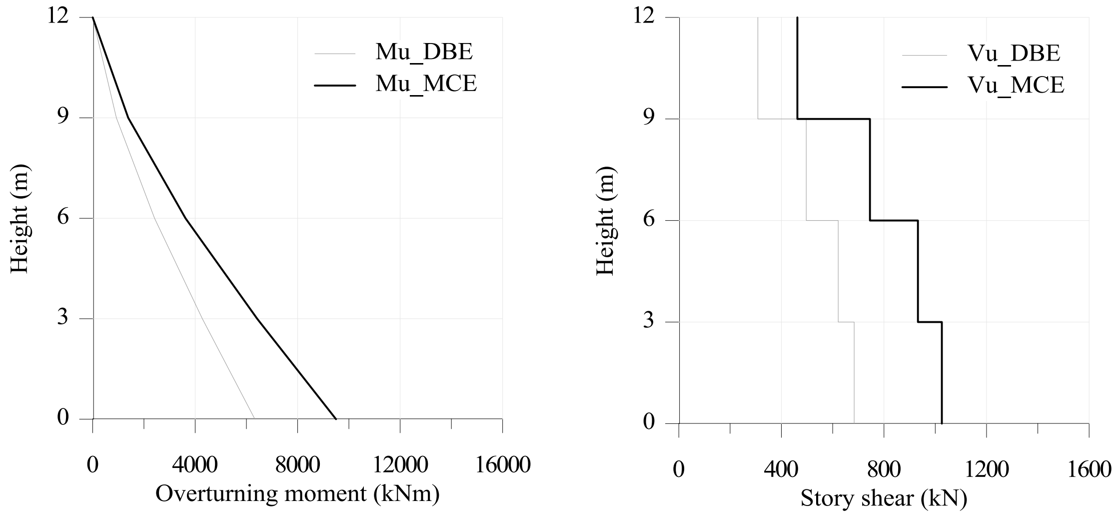

(a) **(b)**

Figure 4-18 Design and MCE (a) overturning moments and (b) story shears for y-direction of PT building

Although forces M_u, V_u in Figure 4-18 represent global system demands in the y-direction of the building, they can also be thought of as wall moment and wall shear demands since, for design purposes, the two UPT walls were assumed to resist the entire base shear and overturning moment in the y-direction of the building, neglecting (i) framing action of walls with connecting UPT beams and columns and (ii) contribution of the interior one-bay frame (Frame B in Figure 4-4). This allows global demands M_u and V_u to be directly compared to the capacities of the (two) UPT walls. The wall moment and shear capacities based on ACI ITG-5.2 and ACI 318 are presented in the following sections.

4.6.2 Flexural strength

4.6.2.1 Nominal and probable flexural strength at base

Consistent with the requirements of ACI ITG-5.2, the moment strength at the base of the UPT walls was estimated at two drift levels: (i) the design drift, θ_{design}, calculated as for a conventional special RC wall (e.g. per 12.8.6 of ASCE 7-10) and, (ii) the maximum drift, θ_{max}, which is intended to represent the drift capacity of a UPT wall and is a function of the aspect ratio of the wall: θ_{max}=0.8H_w/l_w +0.5, with 0.9%≤θ_{max}≤3.0%. The moment corresponding to the design drift, θ_{design}, represents the nominal strength M_n of the UPT wall while the moment corresponding to the maximum drift, θ_{max}, represents the probable moment strength, M_{prob}, of the UPT wall. The two (roof) drift levels for the E-Defense UPT walls are: θ_{design}=0.95% and θ_{max}=3.0%. Note that θ_{design} was computed considering isolated UPT walls (no contribution from beams and columns) and using the design seismic forces described in the previous section. A deflection amplification factor C_d=5.0 and design material strengths with $EI_{eff} = 0.50EI_{gross}$ were used for these calculations.

At each of the two drift levels, the moment strength at the base of each wall was computed based on satisfaction of applicable conditions of equilibrium and compatibility of deformations, as required by ACI ITG-5.2. The nominal and probable moments were calculated considering the contribution from the PT steel (F_{PT}), energy dissipating steel (F_S), and the wall axial load N. An iterative approach was used to calculate the neutral axis depth, c, that satisfies section equilibrium ($F_{PT} + F_S + N = F_C$). According to ACI ITG-5.2 and the work of Aaleti and Sritharan (2009), the concrete compression force F_C at θ_{max} can be calculated assuming a uniform stress of $0.92f_{cc}'$ (where f_{cc}' is the confined concrete strength), uniformly distributed over a distance of βc=0.96c from the extreme compression fiber. Although not explicitly addressed in ACI ITG-5.2, the concrete compression force F_C at θ_{design} was calculated using a uniform stress of $0.85f_c$', acting over a wall length of $\beta_1 c$=0.65c from the extreme compression fiber. This is consistent with equivalent rectangular concrete stress blocks allowed in ACI 318 for RC structural members (σ_c=0.85f_c') and high-strength concrete (β_1=0.65). The forces in the PT steel (F_{PT}) and the energy dissipating bars (F_{ED}) were calculated based on geometric considerations.

Assuming rocking (rotation) at the base of the wall occurs about the neutral axis, then for a given rotation, θ, and neutral axis depth, c, the elongations in the PT and ED steel (Δ_{PT}, Δ_s) are directly proportional to the distance of the ED and PT steel from the neutral axis. By distributing these elongations over the unbonded lengths (L_{unED}, L_{unPT}) and adding any initial strain due to prestressing ($\varepsilon_{p,i}$), the total strain, and corresponding stress, in the PT and ED bars can be determined. Consistent with the requirements of ACI ITG-5.2 for calculation of M_{prob}, the length over which the ED bars were deliberately debonded (L_{unED}=1500mm) at the base of the wall, was increased by adding an additional length equal to $\alpha_b d_b$, where d_b is the diameter of the ED bars and α_b a coefficient that accounts for strain penetration ($2.0<\alpha_b<5.5$). This had only a minor impact on calculated ED strains and forces of the UPT wall as the deliberately debonded length (1500 mm) in this case was significantly larger than recommended values for $\alpha_b d_b$.

With all forces on the wall section defined (F_{PT}, F_S, F_C, N), the flexural capacities at θ_{design} and θ_{max} can be computed by summing moments about any point of the section. Calculations of M_n and M_{prob} at the base of the wall based on the above considerations are summarized in Table 4-4 and Table 4-5, respectively. These calculations assume that the wall rocks about its base in essentially a rigid body motion, so that the wall base rotation is equal to the wall roof drift ratio, i.e. the wall base rotation for computation of M_n is assumed to be equal to θ_{design} and the wall base rotation for computation of M_{prob} is assumed to be equal to θ_{max}. Based on the calculation results summarized in Table 4-4 and Table 4-5, the nominal moment strength at the base of each UPT is M_n = 5072 kNm, and the probable moment strength is M_{prob} = 6626 kNm. Note that these values are based on actual (measured) material properties. Using design material properties, the corresponding moment strengths are $M_{n,d}$ = 4660 kNm and $M_{prob,d}$ =6253 kNm. Based on these values, the difference from design to actual material properties resulted in a moment overstrength factor of approximately 1.07. This overstrength factor is relatively small as the majority of moment strength at the base of the wall is provided by the PT steel which remains elastic in either case (design or actual material properties). On the contrary, the moment overstrength factor from M_n to M_{prob} is significant ($M_{prob}/M_n \approx 1.30$) and relates to additional elongation in the PT and ED bars as base rotation increases from θ_{design} to θ_{max}.

Table 4-4 Calculation of nominal moment M_n at base of UPT wall ($\theta=\theta_{design}=0.95\%$)

mild steel (ED)			**PT steel**			**concrete**			**axial load**		
Δ_{s1a}=	0.015	m	Δ_{PT1}=	0.012	m	fc'=	83.2	MPa			
Δ_{s1b}=	0.013	m	Δ_{PT2}=	0.005	m	β_1=	0.65				
Δ_{s2a}=	0.001	m									
Δ_{s2b}=	0.003	m									
L_{unED}=	1.5	m	L_{unPT}=	13.45	m	c=	**0.377**	m			
α_b=	0		ε_{pi}=	0.0048		β_1c=	0.245	m			
d_b=	0.022	m									
ε_{s1a}=	0.0101	$>\varepsilon_y$	ε_{PT1}=	0.0057	$= 64\%\varepsilon_{py}$						
ε_{s1b}=	0.0089	$>\varepsilon_y$	ε_{PT2}=	0.0051	$= 58\%\varepsilon_{py}$						
ε_{s2a}=	0.0009	$<\varepsilon_y$									
ε_{s2b}=	0.0021	$>\varepsilon_y$									
F_{s1a}=	312	kN	F_{PT1}=	1600	kN						
F_{s1b}=	310	kN	F_{PT2}=	1448	kN						
F_{s2a}=	146	kN									
F_{s2b}=	298	kN									
F_s=	1067	kN	F_{PT}=	3048	kN	F_C=	4335	kN	N=	220	kN
M_s=	1330	kN-m	M_{PT}=	3494	kN-m				M_N=	248	kN-m
Equilibrium check: $F_s+F_{PT}+N-F_C= 0$											
Moments about center of compression: $M_n=M_s+M_{PT}+M_N$ = **5072 kNm**											

Finally, related to calculation of M_n herein, it is noted that, as mentioned above, ACI ITG-5.2 does not provide an equivalent rectangular concrete stress block specifically for M_n. Instead, it allows the neutral axis depth computed for M_{prob} (using a uniform stress of $0.92f_{cc}'$ over a distance of βc=0.96c), to be used for M_n calculations. This essentially means that the neutral axis depth is assumed to remain constant as rotation at the base of the wall increases from θ_{design} to $\theta_{\max}$. Calculation of M_{n} based on this assumption, instead of the stress block assumed in Table 4-4, results in only a small difference in M_{n} (approximately 5.0% higher nominal moment capacity).

As mentioned in Section 4.6.1, the two UPT walls were designed to resist the entire base overturning moment in the y-direction of the building, so that the design moments $M_{\mathrm{u\_DBE}}$ and $M_{\mathrm{u,MCE}}$ can be directly compared with the wall base moment capacities M_{n} and M_{prob}, which are doubled to account for the two UPT walls in the test building:

$$2\varphi M_{\mathrm{n}} = 2(0.9)5072 = 9130\ \mathrm{kNm} > M_{\mathrm{u\_DBE}} = 6332\ \mathrm{kNm} \qquad \text{Equation 4-1}$$

$$2\varphi M_{\mathrm{prob}} = 2(0.9)6626 = 11927\ \mathrm{kNm} > M_{\mathrm{u\_MCE}} = 9497\ \mathrm{kNm} \qquad \text{Equation 4-2}$$

Table 4-5 Calculation of probable moment M_{prob} at base of UPT wall ($\theta=\theta_{\max}$=3.0%)

mild steel (ED)			PT steel			concrete			axial load		
Δ_{s1a}=	0.053	m	Δ_{PT1}=	0.043	m	fcc'=	120.8	MPa			
Δ_{s1b}=	0.047	m	Δ_{PT2}=	0.020	m	β=	0.96				
Δ_{s2a}=	0.010										
Δ_{s2b}=	0.015										
L_{unED}=	1.5	m	L_{unPT}=	13.45	m	c=	**0.208**	m			
α_b=	5.5		ε_{pi}=	0.0048		βc=	0.200	m			
d_b=	0.022	m									
ε_{s1a}=	0.0327	$>\varepsilon_y$	ε_{PT1}=	0.0080	$= 90\%\varepsilon_{py}$						
ε_{s1b}=	0.0293	$>\varepsilon_y$	ε_{PT2}=	0.0063	$= 71\%\varepsilon_{py}$						
ε_{s2a}=	0.0059	$>\varepsilon_y$									
ε_{s2b}=	0.0093	$>\varepsilon_y$									
F_{s1a}=	352	kN	F_{PT1}=	2244	kN						
F_{s1b}=	346	kN	F_{PT2}=	1766	kN						
F_{s2a}=	305	kN									
F_{s2b}=	311	kN									
F_s=	1315	kN	F_{PT}=	4010	kN	F_C=	5544	kN	N=	220	kN
M_s=	1579	kN-m	M_{PT}=	4794	kN-m				M_N=	253	kN-m
Equilibrium check: $F_s+F_{PT}+N-F_C$= 0											
Moments about center of compression: $M_{prob}=M_s+M_{PT}+M_N$ = **6626 kNm**											

4.6.2.2 Flexural design of upper joints

Discussion so far has concentrated on flexural strength requirements at the base of the UPT walls. According to ACI ITG-5.2, under the design earthquake (θ_{design}), the wall-foundation interface is the only location where nonlinear behavior is permitted, and gap openings at other horizontal joint locations should be prevented. While no detailed recommendations on design of upper joints of UPT walls are provided in ACI ITG-5.2, it is stated in Section 5.6.1 that uplift at upper joints "can be prevented through the use of capacity design principles".

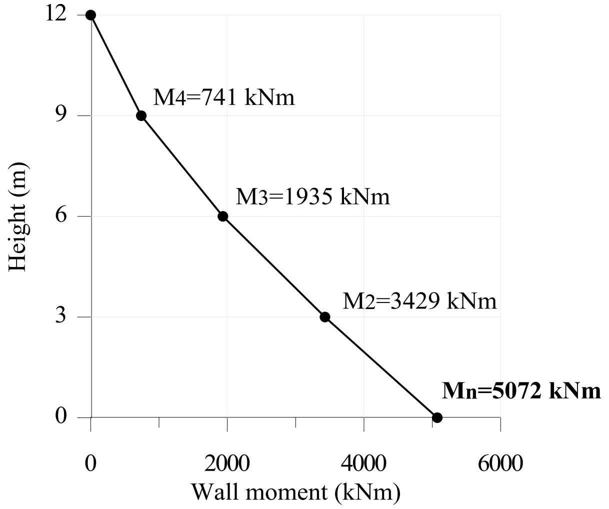

Figure 4-19 Moment along the height of the wall at development of M_n at wall base

In order to assess whether uplift occurs at the upper joints of the E-Defense UPT walls under the design earthquake, the moment demands at these locations were compared with the corresponding decompression moments. Using a capacity-design approach, moment demands at upper joints were estimated assuming that (i) the nominal moment capacity M_n =5072 kNm develops at the base of the UPT wall, and (ii) the vertical distribution of seismic forces which causes M_n to develop at the base, coincides with the design vertical distribution of forces (Figure 4-17). The resulting moment distribution along the height of the wall, at development of M_n at the base, is shown in Figure 4-19. The moment demand at the 2nd floor joint (horizontal joint between the first and second story precast panels) based on this distribution is M_2 = 3429 kNm.

It is noted that the vertical mild steel reinforcement of individual wall panels in the UPT walls of the E-Defense test building (ρ_v =0.77% for the first story panel, and ρ_v=0.65% for upper stories) did not extend across the horizontal joints between panels, so that moment resistance at upper joints was solely provided by the unbonded PT steel crossing these joints. As the post-tensioning steel was unbonded over its entire length, the forces in the PT steel at any of the horizontal joints, when M_n develops at the base, coincide with the PT forces calculated in Table 4-4, and shown in Figure 4-20. For reference, Figure 4-21 shows the forces at the base joint at development of M_{prob}. Note that calculations summarized in Table 4-4 and Table 4-5 assumed uplift was concentrated at the wall-to-foundation interface. Using the known PT forces, the decompression moment at the upper horizontal joints can be calculated, as the moment that results in compression in the concrete to be overcome at the extreme edge of the wall. This calculation is shown in Figure 4-22 for the 2nd floor joint, and resulted in a decompression moment of $M_{2,dec}$ = 1395 kNm, which is almost 2.5 times smaller than the expected moment demand at the 2nd floor joint when M_n develops at the base (M_2 = 3429 kNm). Decompression moments at the 3rd and 4th floor joints are approximately equal to $M_{2,dec}$, as PT forces are constant along the height of the wall and the contribution of axial load is very small. Given that moment demands of Figure 4-19 exceed the calculated decompression moments at the 2nd and 3rd floor joints, some uplift is expected to occur at these locations when the nominal moment capacity develops at the base of the wall.

It is worth noting that, with the exception of Smith and Kurama (2012b), uplift at upper joints of UPT walls has not been systematically addressed in prior research on UPT walls.

However, numerous analytical and experimental studies related to uplift at the wall-foundation interface have shown that, under lateral load, non-linear behavior due to gap opening at the base of UPT walls is not observed until the base moment exceeds at least two times the decompression moment. So even though gap opening theoretically initiates once precompression is overcome at the extreme edge of the wall, its impact on (reducing) the lateral stiffness of the wall is not significant until gap opening has propagated close to the centroidal axis of the wall. Restrepo et al. (2001) report that a marked change in the tangential stiffness (apparent "yield" point) of a UPT wall occurs when the neutral axis depth at the critical base section, measured from the extreme compressive fiber, migrates to approximately 25 to 50% of the wall length. Similarly, Kurama et al. (1996) and Perez et al. (2004) define an "effective linear limit state" based on a moment equal to 2.5 times the decompression moment. Priestley and Tao (1993) and El-Sheikh et al. (2000), made similar observations for gap opening at the beam-to-column interfaces of UPT precast concrete frames.

While design of upper joints of UPT walls is not specifically addressed in ACI ITG-5.2, inclusion of a simple procedure to assess whether uplift is expected to occur at locations other than the base, and whether mild reinforcement is required at horizontal joints between precast panels, would facilitate design of UPT walls using this Standard. Pending additional experimental validation, it is recommended here that mild reinforcement crossing the horizontal joints between precast panels be placed at joints where moment demands exceed $\kappa M_{\mathrm{dec,up}}$, where $M_{\mathrm{dec,up}}$ represents the decompression moment at upper stories when the nominal moment, M_{n}, develops at the base of the wall, and κ can be taken as 2.0 pending experimental validation. M_{n} was used here, as ACI ITG-5.2 requires gap opening at upper joints to be prevented at the DBE level, and does not address behavior of upper joints at the MCE level. However, for consistency with capacity design principles in ACI 318, an overstrength factor could be applied to M_n for this calculation, or, more appropriately, M_{prob} could be used in place of M_n. Calculation of moment demands at upper joints when M_n (or M_{prob}) develops at the base, can be based on the design vertical distribution of forces (as shown above for the E-Defense UPT walls, Figure 4-19) unless higher mode effects are expected to have a significant impact on moments along the wall, in which case their effect should be considered (e.g. Eberhard and Sozen 1993). If calculated moment demands at upper joints exceed $\kappa M_{dec,up}$, then, in addition to the PT steel, mild reinforcement crossing the joints should be provided at these locations. Consistent with the intent of ACI ITG-5.2 in having all inelastic demand concentrated at the critical wall-to-foundation interface of UPT walls, any reinforcement provided at upper horizontal joints should remain essentially elastic, and nonlinear behavior of the concrete at the base of upper story panels should be limited. Smith and Kurama (2012b) recommend limiting the steel strains in upper panel-to-panel joints of UPT walls to ε_{sy} (yield strain of mild reinforcement), and the concrete compressive stresses of upper panels to $0.5f_c'$. Note that a linear strain profile (plane sections remain plane) is assumed for calculation of steel and concrete strains in their approach. Moreover, in order to prevent strain concentrations in the steel, Smith and Kurama (2012b) suggest debonding a short length (10-15 cm) of the mild reinforcing bars at the horizontal joints between precast panels.

Based on the above recommendation, reinforcement at the 2nd floor joint of the E-Defense UPT walls would be required, as the expected moment demand at that location was shown to be approximately 2.5 times the decompression moment ($M_2 \approx 2.5M_{dec,2}$). As noted above, no such reinforcement was provided in the test building, where moment resistance at upper joints of the UPT walls was solely provided by the unbonded PT steel crossing the joints.

Considering limits suggested in literature for initiation of nonlinear behavior due to gap opening (generally within 2.0 to 2.5 times the decompression moment), it is expected that nonlinear behavior and uplift at the upper joints of the E-Defense UPT walls will be limited at the design drift, θ_{design}=0.95%.

While discussion so far with respect to design of upper joints of the E-Defense UPT walls has concentrated on evaluating whether uplift occurs at these joints, it is also desirable to compute flexural strength at upper joints, and compare with design and MCE (M_{u_DBE} and $M_{u,MCE}$) overturning moments of the building shown in Figure 4-18(a). Calculation of moment capacities M_n and M_{prob} of upper joints was based on the typical equivalent rectangular concrete stress block (uniform stress of $0.85f_c'$ over a distance of $\beta_1 c$=0.65c) and the known PT forces from computations of M_n and M_{prob} at the base of the wall (Table 4-4, Figure 4-20 and Table 4-5, Figure 4-21, respectively). Sample calculations for the nominal capacity of the 2nd floor joint are shown in Figure 4-23. Consistent with the design of base joints, and the expectation that gap opening at upper joints will be limited as discussed above, calculations at upper joints also assume that uplift concentrated at the base.

M_n at base joint

F_{PT1} = 1600 kN ,
F_{PT2} = 1448 kN,
N_1 = 220 kN,
F_{s1} = 623 kN ,
F_{s2} = 444 kN,
$F_{c,1}$ = 4335 kN,
M_n = 5072 kNm

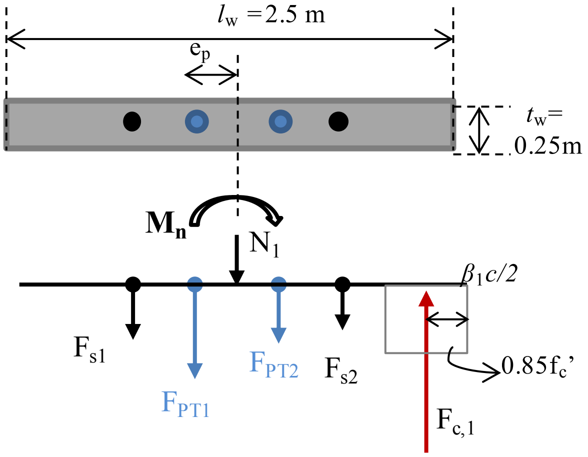

Figure 4-20 Forces at base section of UPT wall at development of M_n at base (θ=0.95%)

M_{prob} at base joint

$F_{PT1} = 2244$ kN ,
$F_{PT2} = 1766$ kN,
$N_1 = 220$ kN,
$F_{s1} = 698$ kN ,
$F_{s2} = 616$ kN,
$F_{c,1} = 5544$ kN,
$M_{prob} = 6626$ kNm

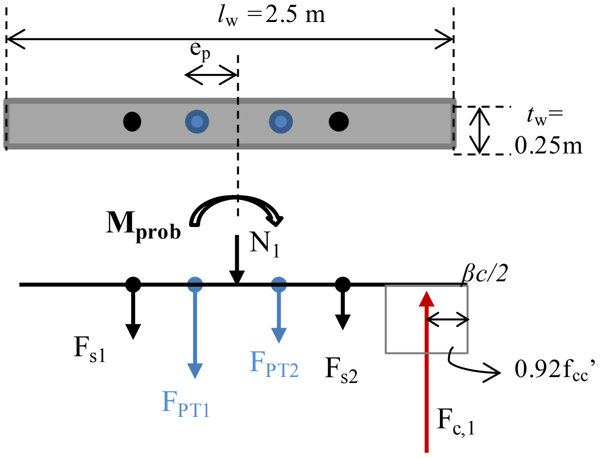

Figure 4-21 Forces at base section of UPT wall at development of M_{prob} at base (θ=3.0%)

2^{nd} floor joint

$F_{PT1} = 1600$ kN ,
$F_{PT2} = 1448$ kN,
$N_2 = 162$ kN,
$F_{c,2} = F_{PT1}+F_{PT2}+N_2 = 3210$ kN,
$M_{2,dec}=(F_{PT1}-F_{PT2})e_p+F_{c,2}l_w/6= 1395$ kNm,
$\sigma_{c2,dec}=2\ F_{c,2}/l_w t_w=10.3$ MPa

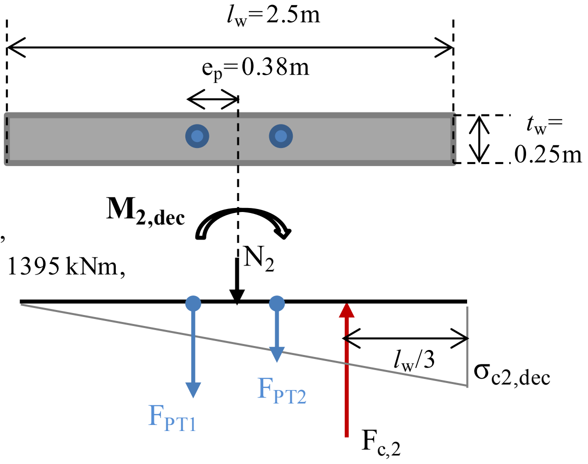

Figure 4-22 Calculation of decompression moment at 2^{nd} floor joint when M_n develops at base

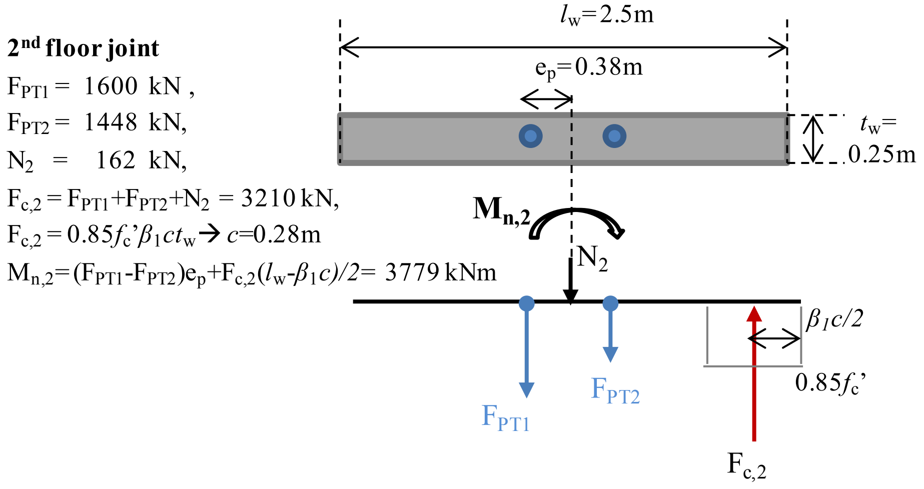

Figure 4-23 Calculation of nominal moment capacity at 2nd floor joint

It is worth pointing out that compared to design of a conventional (monolithic) RC wall, these calculations are somewhat more demanding due to the presence of the unbonded steel that "couples" behavior at each horizontal joint to behavior at remaining joints, so that a member-level analysis is required instead of a section-level analysis. For instance, if in addition to uplift at the base, significant uplift and rotation were to occur at upper joints, the increases in PT forces due to uplift at upper joints should also be reflected in the design of the base joint (e.g., increased concrete strains at the base wall panel). Moreover, even though for the same total elongation in the PT steel, the force in the PT steel is independent of the vertical distribution of uplift between the different horizontal joints (e.g. uplift concentrated at base versus uplift distributed between base joint and upper joints), local behaviors at individual joints are affected (e.g., ED and concrete strains at base). Given these added complications, it is desirable that uplift at upper joints is prevented by design so that behavior of the UPT wall under lateral load is both predictable and dependable. A simple approach on how to assess whether uplift occurs at upper joints and recommendations on design of upper joints based on prior research have been provided in this section.

4.6.2.3 Flexural demand versus flexural capacity

Combining results from calculated moment capacities at the base of the UPT walls presented in Section 4.6.2.1 and moment capacities at upper joints according to Section 4.6.2.2, Figure 4-24 compares the calculated moment capacities ($M_{n,}$ and M_{prob}) of the *two* UPT walls with the design overturning moments along the height of the building presented in Section 4.6.1 (M_{u_DBE}, M_{u_MCE}).

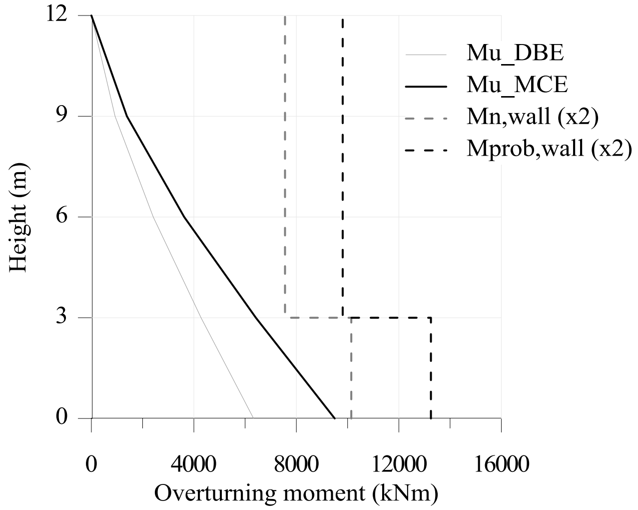

Figure 4-24 Comparisons of design and MCE overturning moments with calculated wall moment capacities

Recall that, for design purposes, the two UPT walls were assumed to resist the entire base shear and overturning moment in the y-direction of the building so that comparisons of wall capacities to design forces of the building are meaningful. Note that wall capacities indicated on Figure 4-24 are based on actual (measured) material properties and no strength reduction factors (φ) have been included to facilitate comparisons with measured experimental results presented in the next Chapter.

4.6.3 Energy dissipating bars: moment contribution and strain limits

In addition to checking flexural strength requirements at the base of the UPT wall, calculations summarized in Table 4-4 and Table 4-5 allow ACI ITG-5.2 requirements related to the energy dissipating bars to be assessed. In order to ensure a minimum amount of energy dissipation in UPT walls, ACI ITG-5.2 requires that the ED bars at the base of the wall provide at least 25% of the nominal flexural strength at the wall-foundation interface. This is satisfied for the E-Defense UPT walls as the ED bars provide 26.2% of the nominal moment capacity (Table 4-4, M_s/M_n= 1330/5072= 26.2%). Note that ACI ITG-5.2 allows the ED bars to be lumped at the wall centroid for calculation of their moment contribution (Ms), provided their eccentricity from the wall centroid is small ($e_s<0.062l_w$). Calculations summarized in Table 4-4 and Table 4-5 accounted for the exact locations of ED steel in the section: 2D22 on either side of the wall centroid at a distance of 724 mm from the centroid, and 2D22 on either side of the wall centroid at a distance of 540 mm from the wall centroid.

With respect to strains in the energy dissipating steel, ACI ITG-5.2 requires that the strain in the ED bars at M_{pr} be smaller than $0.85\varepsilon_u$, where ε_u is the strain in the energy-dissipating reinforcement at its tensile strength f_u. For ε_u=0.08, this is also satisfied for the E-Defense UPT walls (Table 4-5, $\varepsilon_{s1,a}$= 0.033<0.85(0.08)=0.068).

4.6.4 Post-tensioning steel: location, initial prestress and strain limits

ACI ITG-5.2 requires the post-tensioning steel to be located within 10% of the wall length on either side of the wall centroid. The intent of the limit is to delay yielding of the PT steel, by positioning it close to the centerline and limiting elongation due to gap opening. Moreover, it allows the two groups of PT steel, located on either side of the wall centroid, to be conveniently lumped at the centroid for design purposes. As shown in the cross-sections of Figure 4-6, the E-

Defense UPT walls did not satisfy this requirement as the PT steel was located at 15% from the wall centerline. Note that calculations of moment capacities and PT strains herein (Table 4-4 and Table 4-5) accounted for the exact locations of PT steel in the section.

In order to maintain the re-centering property of the wall, ACI ITG-5.2 requires that the post-tensioning steel does not yield under the design earthquake, so the maximum stress in the PT steel at the design drift θ_{design} should be less than the specified yield strength f_{py}. This requirement is easily satisfied for the E-Defense UPT walls as evidenced by the values in Table 4-4 ($f_{\text{p,max}} = 64\% f_{\text{py}}$). Note that even at θ_{max} (Table 4-5), the maximum stress in the PT steel is below the yield strength.

In addition to the above requirement related to yielding of the PT steel, ACI ITG-5.2 also imposes a minimum limit on the prestress force. More specifically, it requires that the force in the PT steel together with the axial load on the wall should be sufficient to cause compressive yielding in the energy-dissipating reinforcement and overcome the permanent elongations that this reinforcement develops as it yields in tension:

$$A_p f_{p,in} + 0.9N \geq A_s f_t \qquad \text{Equation 4-3}$$

$f_{\text{p,in}}$ in the above equation is the effective stress in post-tensioning tendons after allowance of all prestress losses, $A_s f_t$ is the tensile strength of all energy dissipating reinforcement and N is the self-weight of the wall plus any dead loads acting on it. This equation is an expression of the requirement that, for the wall to return to the upright position and cracks at the wall-foundation interface to close during reversed cyclic displacements, the compressive force exerted by the effective prestress force and the axial load should be large enough to overcome the maximum tensile force that can develop in the energy dissipating reinforcement. This requirement is satisfied for the E-Defense walls:

$A_p f_{p,in} + 0.9N$ = 2(1407mm^2)(960MPa)+0.9(220) = 2900 kN >

$A_s f_t$=8(387mm^2)(563MPa) = 1743 kN Equation **4-4**

Finally, ACI ITG-5.2 requires yielding of the energy dissipating reinforcement to occur before the stress in the PT steel reaches $0.95f_{py}$. This is easily satisfied for the E-Defense UPT walls as evidenced by the ED and PT strains of Table 4-4.

4.6.5 Shear strength

ACI ITG-5.2 adopts a capacity design approach and requires shear strength checks for UPT walls to be performed at the maximum drift level, θ_{max}, or equivalently, at development of M_{prob} at the base of the wall. Using an effective height equal to 77% of the height H of the building (resultant of design first mode forces), the wall base shear at development of M_{prob} was calculated as $V_{wall@Mprob} = M_{prob}/(0.77H)$ =717 kN, which when doubled for the two UPT walls in the building results in a base shear of $V_{u@Mprob}$ = 1434 kN and is 40% higher than the base shear at MCE (V_{u_MCE} = 1026 kN) that was assumed for the shear design of the UPT walls in the test building. This has no implications, as the calculated shear capacities in this case ($V_{n,}$ and $V_{n,i}$ see next paragraph) significantly exceeded shear demands, either $V_{u@Mprob}$ or V_{u_MCE}. It is of interest to note though that $V_{u@Mprob}$ is more than two times higher than the base shear that conventional RC walls would be designed for (V_{u_DBE}), indicating an added conservatism in shear design of UPT walls according to ACI ITG-5.2 when compared to shear design of conventional RC walls.

The nominal shear strength at the base of each wall based on ACI 318-11 was 3302 kN using design material properties, and V_n = 3885 kN using actual material properties. The high ratio of transverse reinforcement in the test walls ($\rho=A_{st}/(t_w s)$=0.0135, more than five times the minimum required by ACI-318) resulted in a very large calculated shear strength, close to the ACI-318 upper limit of $8\sqrt{f_c'}$(psi)A_{wall} = 3787 kN. The nominal shear strength at upper panels

($\rho=A_{st}/(t_w s)$=0.0102) was 2677 kN using design material properties and V_n = 3150 kN using actual material properties.

The nominal shear strength of the wall-foundation interface ($V_{n,i}$) based on ACI ITG-5.2 can be calculated using $\varphi V_{n,i} = \mu F_C$, where φ is the strength reduction factor for shear, μ is a coefficient of friction, and F_C is the compression force at the toe of the wall when M_{prob} develops at the base. Using the recommended in ACI ITG-5.2 values for φ and μ (φ = 0.75, μ = 0.5), and F_C = 5544 kN as calculated in Table 4-5, the nominal shear strength of the wall-foundation interface was $V_{n,i}$ = 3696 kN, again significantly exceeding the shear demand at the base of each wall. For the shear strength of the horizontal joints between the individual precast panels, ACI ITG-5.2 allows shear friction principles of ACI 318 to be used with μ = 0.6 and f_y taken as the stress in the PT steel at development of M_{prob} at the base of the wall. Based on this recommendation, and calculated F_{PT} in Table 4-5, the nominal shear strength of the horizontal joints between precast panels was $V_{n,i}$ = 2406 kN.

Figure 4-25 compares the calculated shear capacities ($V_{n,}$ and $V_{n,i}$) of the *two* UPT walls with the design story forces along the height of the building presented in Section 4.6.1 (V_{u_DBE}, V_{u_MCE}). The ACI 318 limit of $8\sqrt{f_c'(\text{psi})}A_{wall}$ is also included for reference. Recall that, for design purposes, the two UPT walls were assumed to resist the entire base shear and overturning moment in the y-direction of the building so that comparisons of wall capacities to design forces of the building are meaningful. Note that wall capacities of Figure 4-25 are based on actual (measured) material properties and no strength reduction factors (φ) have been included to facilitate comparisons with measured experimental results presented in the next Chapter. The results summarized in Figure 4-25 indicate shear demands were only 10 to 15% of shear capacities at the base wall panel, and never more than 25% of the shear capacities at upper levels.

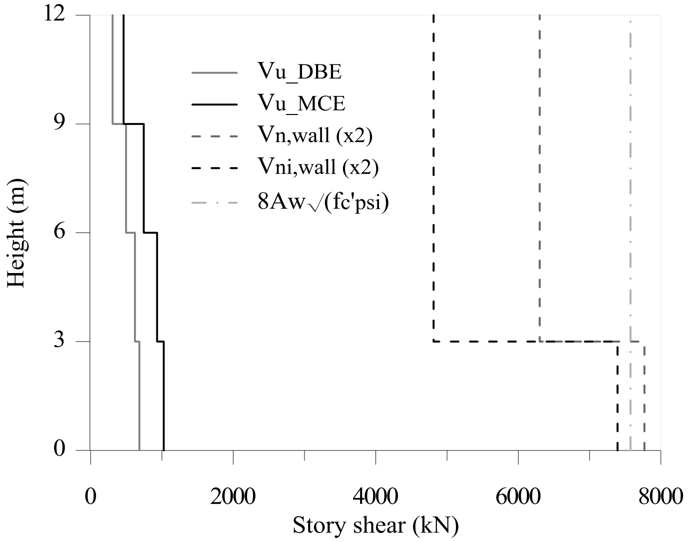

Figure 4-25 Comparisons of design and MCE story shears with calculated wall shear capacities

4.6.6 Confinement

The concrete at the ends of the base panel of the E-Defense UPT walls was confined by high strength (KSSS785, f_{yt} = 938 MPa, see Table 4-3) 13-mm-diameter overlapping hoops, spaced vertically at s = 75 mm on center, and extending horizontally over a length of 540 mm at each wall panel boundary (Figure 4-26).

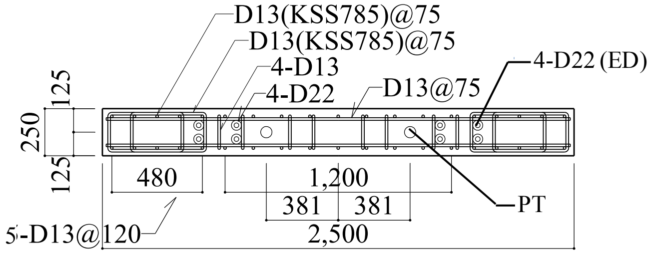

Figure 4-26 UPT wall cross section of 1st story precast wall panel (dimensions in mm)

According to ACI ITG-5.2, confinement at the ends of the base panel of a UPT wall should be selected so that the maximum usable strain at the extreme compression fiber is at least equal to $\theta_{max}c/L_p$, where c is the neutral axis depth at θ_{max} and $L_p = 0.06H_w$ (where H_w is the height of the wall). The maximum usable strain is permitted to be calculated as $\varepsilon_{cmax,u} = 0.004 + 4.6\varepsilon_{sut} \cdot (f_L'/f_{cc}')$, where ε_{sut} is the ultimate strain capacity of the transverse reinforcement, and f_L'/f_{cc}' is the ratio of the effective lateral confining stress provided by the transverse reinforcement (f_L') to the strength of the confined concrete (f_{cc}'). The effective lateral confining stress can be calculated as $f_L' = 0.35\rho_s f_{yt}$ for rectangular hoops, where $\rho_s = \rho_x+\rho_y$ is the sum of volumetric ratios of transverse reinforcement in the directions parallel to the major and minor axes of the compressed area; and f_{yt} is the yield strength of the transverse reinforcement. Given the ratio (f_L'/f_c'), ACI ITG-5.2 provides a table (reproduced here as Table 4-6) for calculation of the ratio (f_{cc}'/f_c').

Table 4-6 Ratio of core strength to concrete strength based on lateral confinement

f_L'/f_c'	0.036	0.072	0.108	0.144	0.180
f_{cc}'/f_c'	1.23	1.43	1.6	1.76	1.9

For the E-Defense UPT walls, the volumetric ratios of transverse reinforcement at each boundary are $\rho_x = 4A_s b_y/(b_x b_y s)$ and $\rho_y = 2A_s b_x/(b_x b_y s)$ in the directions parallel and perpendicular to the wall length, respectively. In these expressions, As is the area of the 13-mm bar used for the transverse reinforcement, and b_x, b_y are the dimensions of the confined core at each boundary, measured from the centerline of the outermost hoops. The total volumetric ratio of transverse reinforcement at each boundary is $\rho_s = \rho_x+\rho_y = 0.014+0.017 = 0.031$, resulting in an effective lateral confining stress equal to $f_L' = 0.35\rho_s f_{yt} \approx 10$ MPa. Noting that the (measured) concrete compressive strength of the E-Defense UPT walls was 83.2 MPa (Table 4-2), and using linear interpolation between values of Table 4-6, a ratio of $f_L'/f_{cc}' = 0.073$ was obtained. Based on the expression provided in ACI ITG-5.2, and using an ultimate strain of 0.08 (ε_{sut}) for the transverse reinforcement, the maximum usable strain was calculated as $\varepsilon_{cmax,u} = 0.004 + 4.6\varepsilon_{sut} \cdot (f_L'/f_{cc}') = 0.031$. ACI ITG-5.2 requires that the strain $\varepsilon_{cmax,u}$ exceeds the peak compressive strain developing in the wall at θ_{max}. The peak compressive strain at θ_{max} can be calculated as $\theta_{max}c/L_p$ and is equal to 0.0087 for the E-Defense walls ($\theta_{max} = 3.0\%$, $c = 208$ mm, see Table 4-5).

As the estimated strain at θ_{max} (0.0087) exceeds the calculated maximum usable strain (0.031), the ACI ITG-5.2 requirement is satisfied. Note that confinement checks above were presented for the actual (measured) material properties ($f_c' = 83.2$MPa, $f_{yt} = 938$ MPa) but they would also be satisfied if design material properties had been used instead ($f_c' = 60$ MPa, $f_{yt} = 785$ MPa). It is also worth noting that, as already mentioned briefly in Section 3.1.2.1, and further discussed in Chapter 5 with respect to measured concrete strains in the E-Defense UPT walls, the ACI ITG-5.2 expression $\theta_{max}c/L_p$ with $L_p = 0.06H_w$ was generally found to underestimate peak concrete strains in UPT walls.

Finally, with respect to confining reinforcement, ACI ITG-5.2 also requires that it extends horizontally from the extreme compression fiber a distance at least equal to $0.95c$, and not less than 305 mm, where c is the neutral axis depth. This requirement is satisfied for the E-Defense UPT walls where transverse reinforcement extended horizontally over a length of 540 mm at each wall panel boundary, exceeding the calculated neutral axis depth ($c = 208$ mm) and the 305 mm limit. With respect to spacing requirements of ACI 318, the E-Defense UPT walls satisfied all spacing requirements for special boundary elements with the exception that the 75 mm spacing exceeded the limit of $1/4t_w$, where t_w is the thickness of the wall ($s = 75$ mm $> 1/4t_w = 62.5$ mm).

4.6.7 Materials: concrete and grout

ACI ITG-5.2 requires a minimum specified compressive strength f_c' of at least 27.5 MPa (4,000 psi) for the concrete in the precast wall panels ($f_c' \geq 27.5$ MPa). The specified compressive strength of the interface grout at the wall-foundation interface, f_{cg}', is required to be at least equal to f_c' of the precast panels ($f_{cg}' \geq f_c'$). Moreover, the confined concrete strength of the precast panels, f_{cc}', cannot be taken more than 2.5 times the specified compressive strength of the grout ($f_{cc}' \leq 2.5\, f_{cg}'$). The concrete and grout of the E-Defense UPT walls satisfied these strength requirements; note that specified compressive strength for both the precast panels and the interface grout was 60 MPa.

In addition to the above strength limits, ACI ITG-5.2 also includes an upper limit on the thickness, t_g, of the grout at wall-foundation interface: it is required that the thickness of the grout be limited to 38mm (1.5 in). The 30-mm-thick grout of the test walls satisfied this limit. Finally, with respect to the grout properties, ACI ITG-5.2 requires a minimum of 0.1% by volume fibers (steel or polypropylene) to be included in the wall-foundation interface grout. While the north UPT wall (axis A in Figure 4-4) in the test included steel fiber reinforcement in the grout between the first story panel and the foundation, no fiber reinforcement was used in the interface grout of the south UPT wall (axis C in Figure 4-4). Note that although not required by ACI ITG-5.2, steel fibers were also included in the concrete mix of the first and second story precast panels of the north wall and in the grout used at the horizontal joint between these panels.

4.6.8 Summary

The assessment of the E-Defense UPT walls based on ACI ITG-5.2 presented in the previous sections showed that the walls satisfied moment and shear strength requirements at the base. Moreover, the walls also conformed to ACI ITG-5.2 requirements for minimum initial prestress force, moment contribution from energy-dissipating steel at the wall-foundation interface, strain limits in PT and ED steel, and confinement at the corners of the base panels.

Provisions not satisfied include that the post-tensioning steel in the UPT walls of the test building was located at 15% of the wall length on either side of the centroid, exceeding the ACI ITG-5.2 limit of 10%, and that the grout between the base panel of the south wall and the foundation did not contain fiber reinforcement as required by ACI ITG-5.2. Finally, although design of upper joints is not addressed in detail in ACI ITG-5.2, it was shown that, while not provided in the E-Defense test walls, mild reinforcement crossing the horizontal joint between the first and second story precast panels would have been required to prevent gap opening from occurring and thus satisfy the intent of ACI ITG-5.2 in concentrating all inelastic demand at the critical wall-to-foundation interface.

Chapter 5 Experimental results of four-story precast PT building

This chapter presents experimental results for a range of responses in the wall direction of the four-story, precast post-tensioned building that was tested on the E-Defense shake table in 2010. Results presented include global force-displacement relations, response envelopes and local responses, with an emphasis on performance of the two UPT walls in the test building. Wall local responses examined include in-plane and out-of-plane base rotations, wall uplift and concrete axial strains. Experimental results also allow the moment resistance of the UPT walls to be estimated and its contribution to the global overturning moment of the building to be quantified. Design aspects of UPT walls with reference to ACI ITG-5.2 are also discussed. In addition to wall responses, experimental results related to the UPT beams and floor slab are also presented.

The digital data from the experimental program including frame direction responses and responses of the RC building that was tested simultaneously with the PT building are available on NEEShub website (NEEShub project 2011-1005).

5.1 Global hysteretic response

The global hysteretic response in the wall (y) direction of the PT building under the sequence of earthquake records it was subjected to (25%, 50%, and 100%-Kobe, followed by 40%, 60%-Takatori records) is illustrated in Figure 5-1, in terms of global overturning moment versus roof drift relations. Results under the earlier, lower intensity, 10%-Kobe record are not discussed herein as measured responses were negligible (roof drift ratio<0.1%). Figure 5-2 plots the base shear in the y-direction of the PT building versus the roof drift ratio under the same records.

In both figures, and all subsequent discussion, westward displacements are defined as positive and "roof drift ratio" corresponds to the center of plan lateral displacement at the roof level, divided by the building height (12.0 m), unless otherwise stated. As will be discussed in Section 5.4 with respect to displacement profiles, significant torsional response was observed during testing of the building, so that lateral displacements varied across the building plan. The center of plan relative displacement at each floor level was calculated as the average of y-direction measurements from sensors D2 and D3 (Figure 5-3). As sensor D3 was not provided between the fourth floor and roof level, the relative displacement of the roof level with respect to the fourth floor at the center of plan was calculated using available measurements from sensors D2 and D1, and extrapolating to the location of the center of plan.

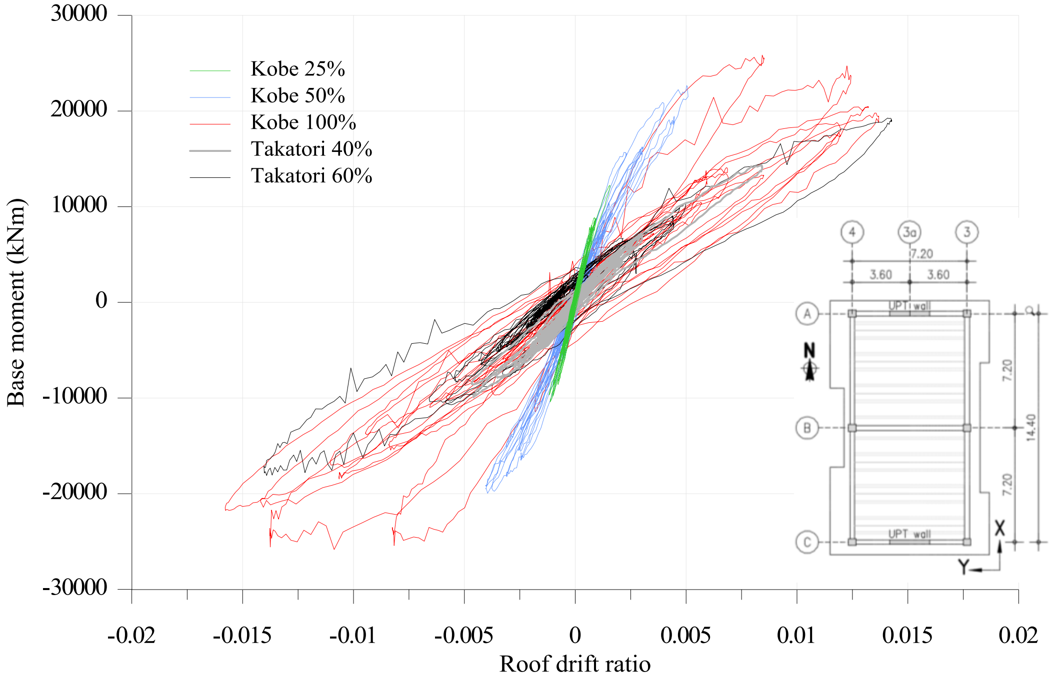

Figure 5-1 Y-direction building overturning moment versus roof drift ratio under Kobe and Takatori records

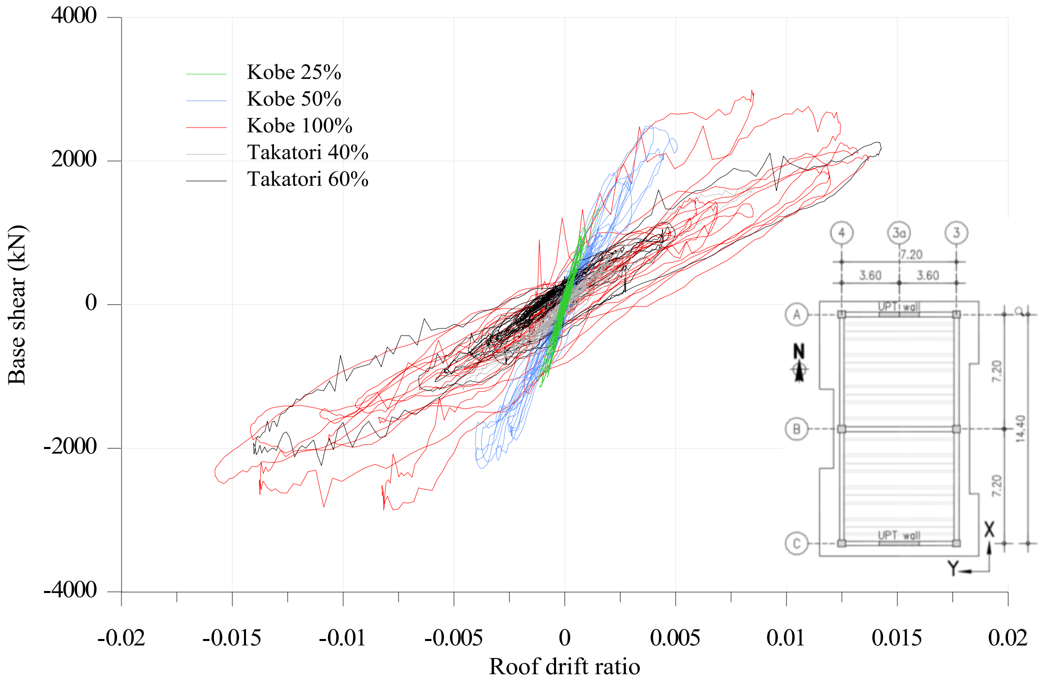

Figure 5-2 Y-direction building base shear versus roof drift ratio under Kobe and Takatori records

Base shear forces plotted in Figure 5-2 were computed as the sum of horizontal inertia forces over all floors, with inertia forces at each level calculated as the product of floor mass and associated absolute floor acceleration (average of y-direction measurements from accelerometers A1 and A2, Figure 5-3). Global overturning moments of Figure 5-1 were computed as the sum over all floors of horizontal inertia forces multiplied by the associated floor height from the base.

Figure 5-4 to Figure 5-8 plot the roof drift, base moment and base shear response histories for each record. The global hysteretic response under each record is shown for reference at the top of each figure. Response histories for the Kobe records are plotted between t = 13 s and t = 24 s, which includes the peak responses under these records, while Takatori histories are plotted between t = 8 s and t = 20 s.

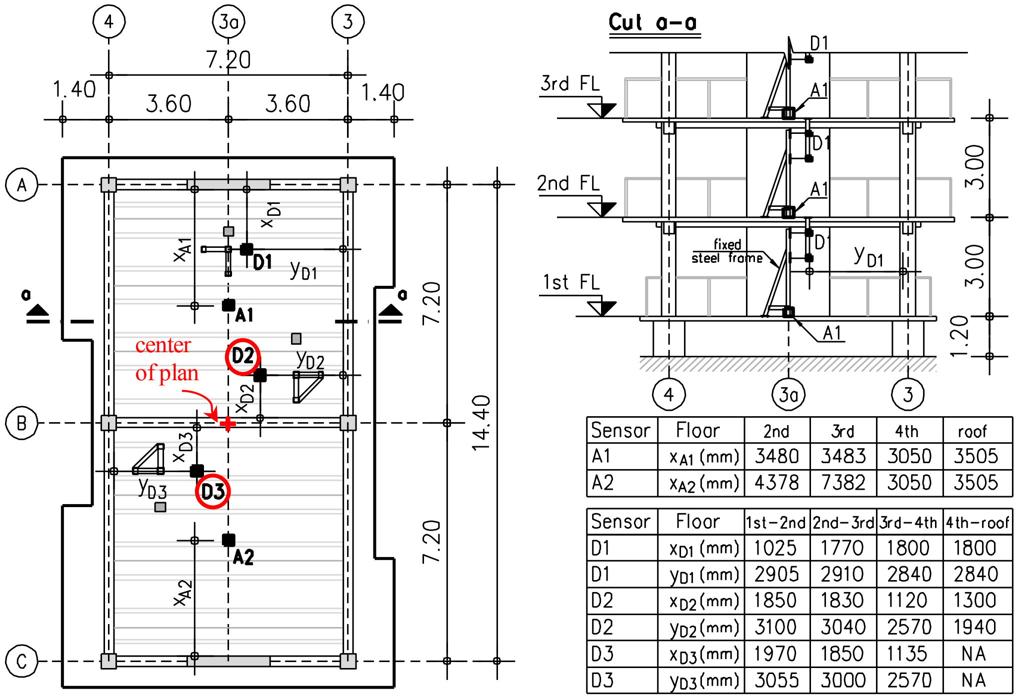

Sensor	Floor	2nd	3rd	4th	roof
A1	x_{A1} (mm)	3480	3483	3050	3505
A2	x_{A2} (mm)	4378	7382	3050	3505

Sensor	Floor	1st–2nd	2nd–3rd	3rd–4th	4th–roof
D1	x_{D1} (mm)	1025	1770	1800	1800
D1	y_{D1} (mm)	2905	2910	2840	2840
D2	x_{D2} (mm)	1850	1830	1120	1300
D2	y_{D2} (mm)	3100	3040	2570	1940
D3	x_{D3} (mm)	1970	1850	1135	NA
D3	y_{D3} (mm)	3055	3000	2570	NA

Figure 5-3 Locations of accelerometers (A1, A2) and displacement transducers (D1, D2, D3)

Response under low intensity shaking, represented by the 25%-Kobe record, was essentially linear elastic, and no damage was observed upon completion of this test. Peak roof drift ratio at the center of plan was 0.16%. Slightly nonlinear behavior was observed under the 50%-Kobe record and was mainly associated with softening (reduction in lateral stiffness) due to gap opening along the horizontal joints at the bases of the UPT walls. The narrow hysteretic loops and limited energy dissipation of the 50%-Kobe response are consistent with the characteristic nonlinear elastic response expected of unbonded post-tensioned systems before significant yielding of the energy-dissipators occurs (D22 at bases of UPT walls). Also consistent with the expected behavior of UPT systems under moderate to high intensity shaking, no visible damage to the building was observed at the end of the 50%-Kobe test and complete self-centering response was achieved. The peak roof drift ratio at the center of plan under the 50%-Kobe record was 0.51%.

Under the stronger intensity 100%-Kobe record, significant nonlinear response was observed due to yielding in tension and compression of the energy-dissipating bars at the bases of the UPT walls. Responses were largely symmetric with equal strengths obtained in the positive and negative directions. Modest strength degradation was observed after the first excursion exceeding 1.0% roof drift ratio in each direction. At peak positive roof drift (1.37%, peak F in Figure 5-6) the corresponding moment was 75% of the maximum positive moment (obtained at 0.84% roof drift ratio), while at peak negative roof drift (1.58%, peak E) the corresponding moment was 83% of its maximum value. After the first two large excursions in each direction (peaks A, B, C and D), considerable degradation of the initial stiffness also occurred. Maximum base moment and shear occurred at the same instant (t = 14.515 s, peak A) while peak roof drift ratio occurred at t = 20.115 s (peak E). Note that the peak base shear in the test ($V_{\max}$ = 2990 kN) occurred under the 100%-Kobe record and corresponded to 87% of the building weight (W = 3420 kN). This significantly exceeded the design and MCE base shears ($0.2W$ and $0.3W$, respectively) in the y-direction of the building which were presented in Section 4.6.1. This apparent overstrength is further discussed in Section 5.5 in relation to the response envelopes.

Hysteretic loops obtained during the final tests under the Takatori record scaled to 40% and 60%, displayed the same (degraded) stiffness observed at the end of the 100%-Kobe record. Peak roof drift ratio under the 40%-Takatori record was 0.84%. Peak roof drift ratios under the 60%-Takatori record were approximately 1.40% in both positive and negative direction, and were similar to the 100%-Kobe maximum drifts, without significant additional degradation in strength.

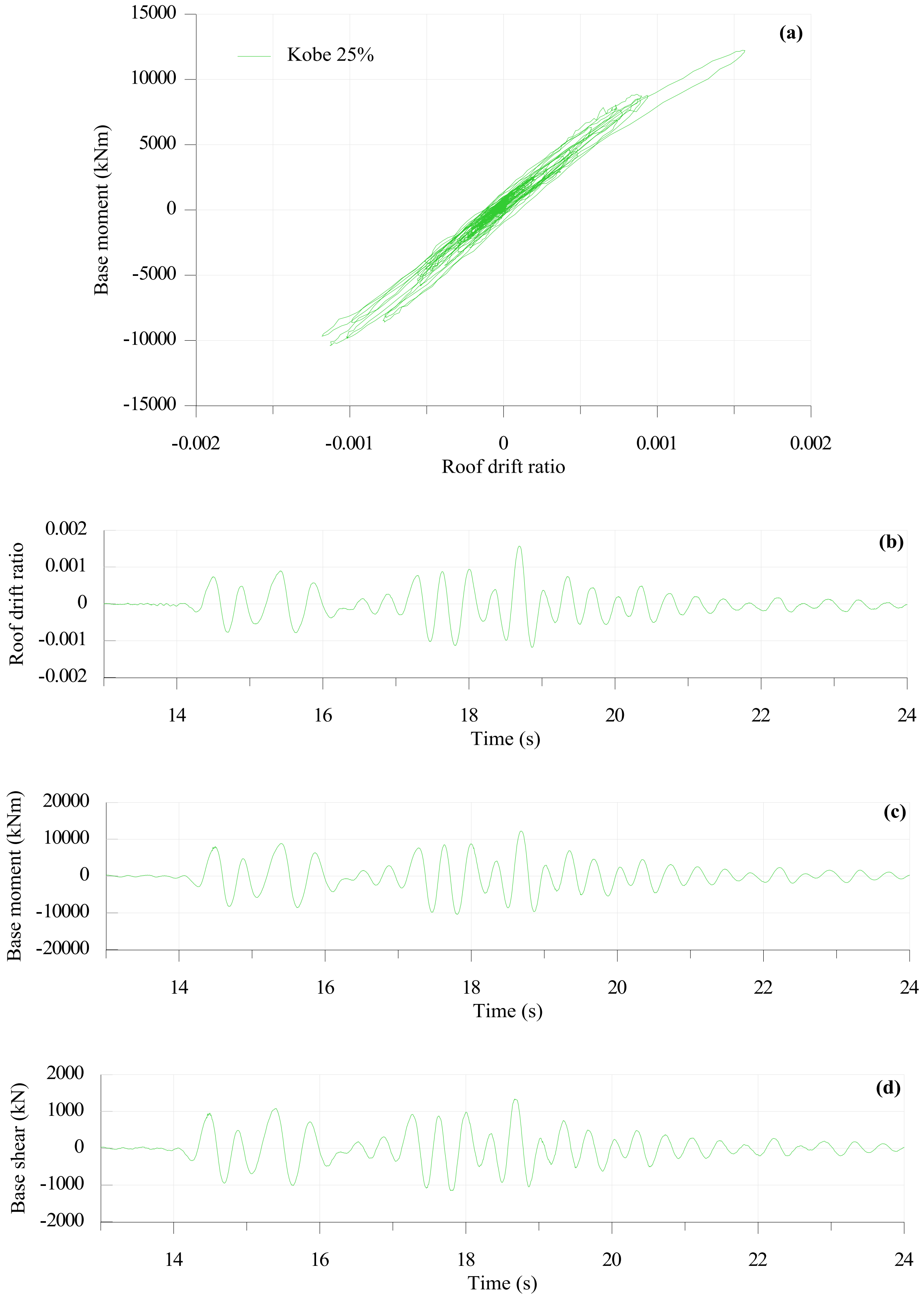

Figure 5-4 Kobe 25% record; (a) global hysteretic response and response histories of (b) roof drift ratio, (c) base moment and (d) base shear

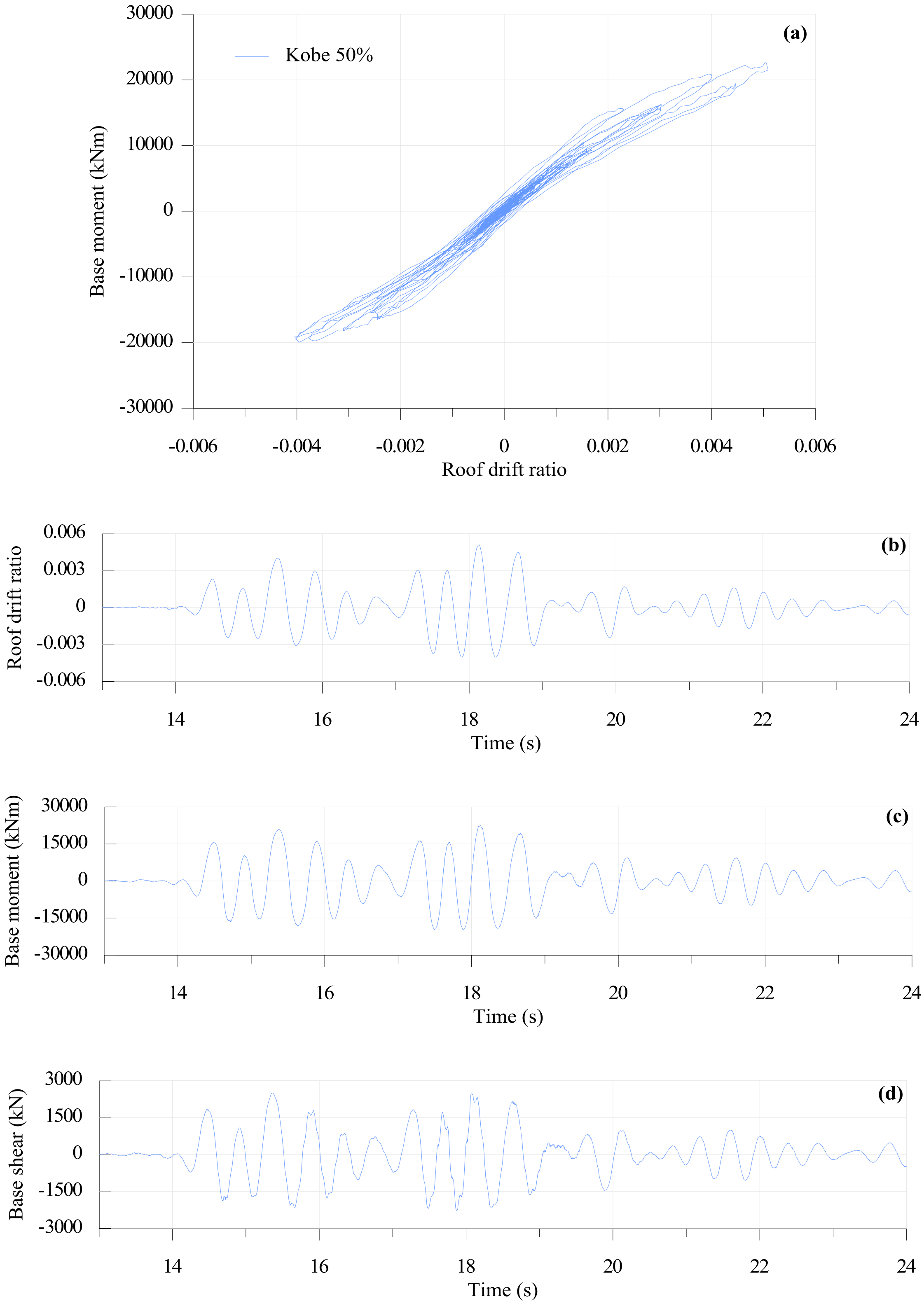

Figure 5-5 Kobe 50% record; (a) global hysteretic response and response histories of (b) roof drift ratio, (c) base moment and (d) base shear

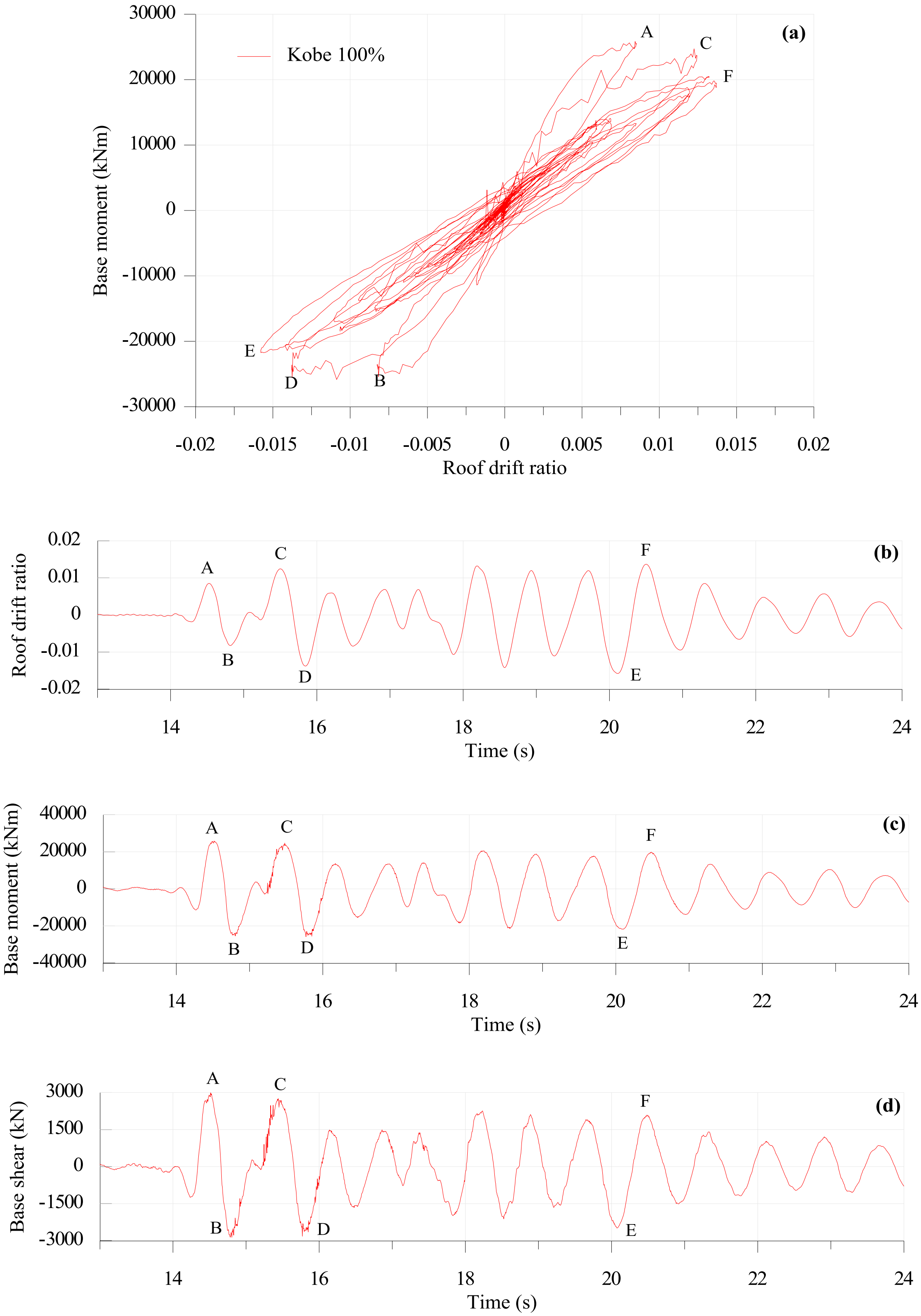

Figure 5-6 Kobe 100% record; (a) global hysteretic response and response histories of (b) roof drift ratio, (c) base moment and (d) base shear

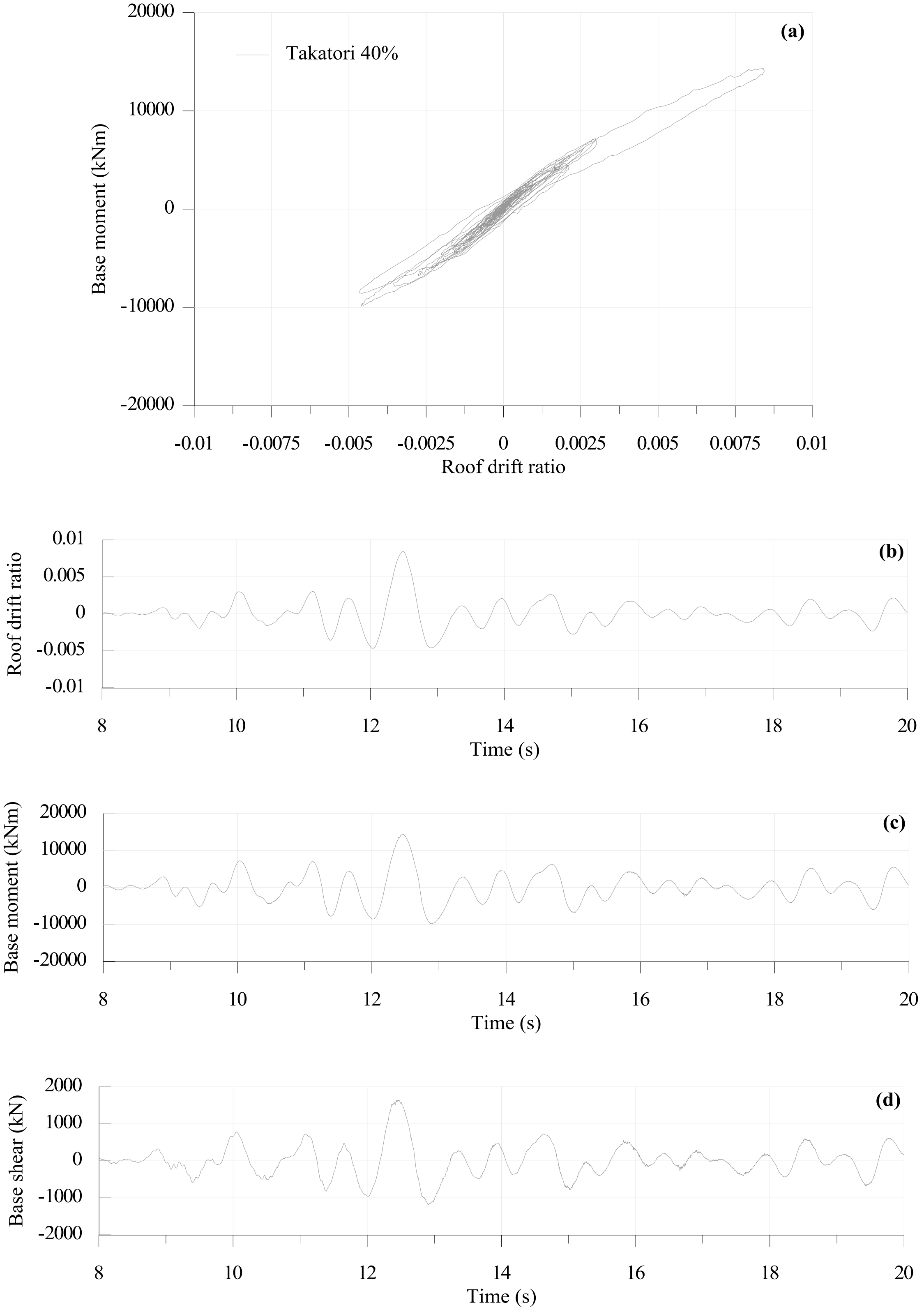

Figure 5-7 Takatori 40% record; (a) global hysteretic response and response histories of (b) roof drift ratio, (c) base moment and (d) base shear

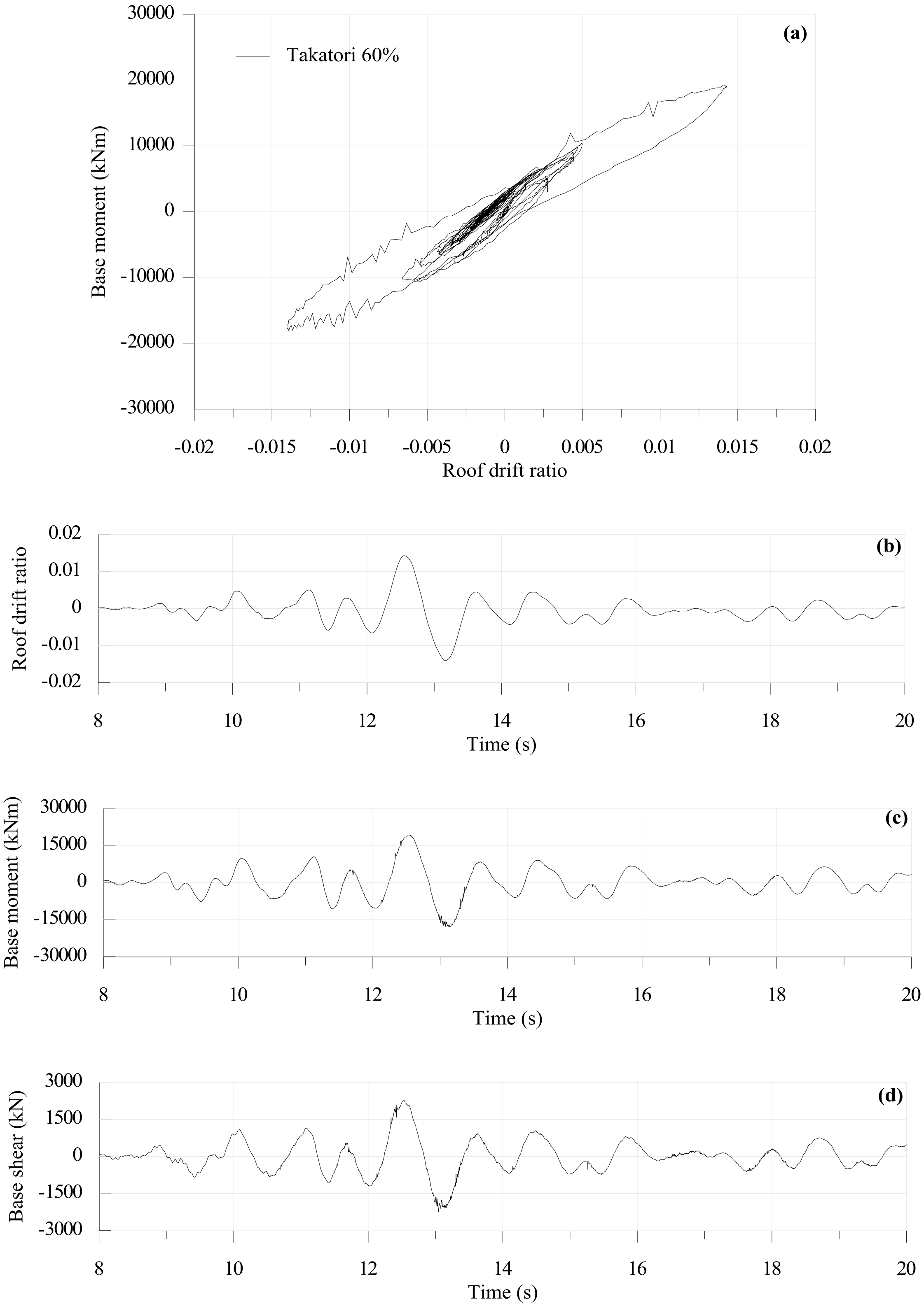

Figure 5-8 Takatori 60% record; (a) global hysteretic response and response histories of (b) roof drift ratio, (c) base moment and (d) base shear

Finally, residual displacement in the y-direction of the PT building was negligible at the end of the tests. Figure 5-9 plots the entire histories of roof drift ratio for the 100%-Kobe and 60%-Takatori records. Residual roof drift ratio at the center of plan was approximately 0.10% at the end of the 60%-Takatori record. The tests thus verify the inherent re-centering capability of UPT wall systems, even after large nonlinear displacements, provided strength contributions from PT and ED steel are appropriately selected and there is no significant loss of prestress. Note that the design of the UPT walls in the test building satisfied the re-centering criterion in ACI ITG-5.2, which as discussed in Section 4.6.4, requires the effective prestress force together with the wall axial load to exceed the maximum tensile force that can develop in the energy dissipating reinforcement. Moreover, as shown in 4.6.2.1, design of the UPT walls ensured that yielding of the PT steel was precluded under the design drift as required by ACI ITG-5.2, to prevent prestress losses and loss of the re-centering property of UPT walls.

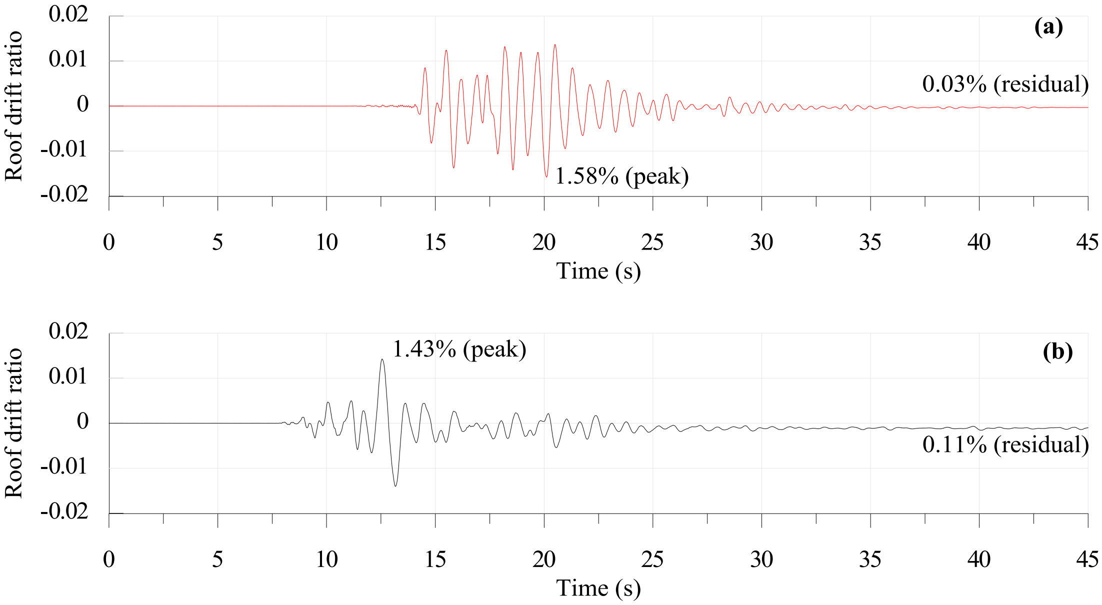

Figure 5-9 Peak and residual roof drift ratio at end of (a) 100%-Kobe and (b) 60%-Takatori records

5.2 Variation of fundamental period

As evidenced by the hysteretic responses presented in Figure 5-1, the majority of inelastic response and energy dissipation occurred during the 100%-Kobe record. This is in agreement with observed damage progression in the building, as discussed in the following section, and also consistent with the variation of fundamental period throughout the series of tests.

The fundamental period of the building was estimated using test data from low amplitude, white-noise base excitations that preceded each record. The frequency response function, $H(\omega)$, was computed for each floor and under each white-noise excitation, as the ratio of the Fourier transform (FFT) of the y-direction displacement response, to the FFT of the y-direction excitation input. The fundamental frequency in the y-direction of the PT building was identified from the peaks in the amplitude response spectrum (amplitude of response function $H(\omega)$ plotted against frequency) for each white-noise excitation. The estimated fundamental periods of the building at the beginning of each record are shown in Figure 5-10. As evidenced by the figure, gradual softening through the early stages of the test was followed by a marked change in period during the 100%-Kobe record. The gradual period elongation during the 10%, 25%, and 50%-Kobe records resulted in an overall 30% increase in period from the initial value of 0.27 sec. During the 100%-Kobe record, a considerable period shift occurred such that the calculated period from white-noise after the 100%-Kobe record was 0.50 sec, corresponding to an 88% increase from the 0.27 sec initial period. Period elongation under the 100%-Kobe record is also apparent in the roof drift histories presented in the previous section (Figure 5-6b versus Figure 5-5a). Further period lengthening under the Takatori records was limited (<10%). While more detailed system identifications algorithms are available (e.g. Moaveni et al. 2011), the approach using the frequency response function yielded results in close agreement with periods of the PT building reported elsewhere (Nagae et al. 2012).

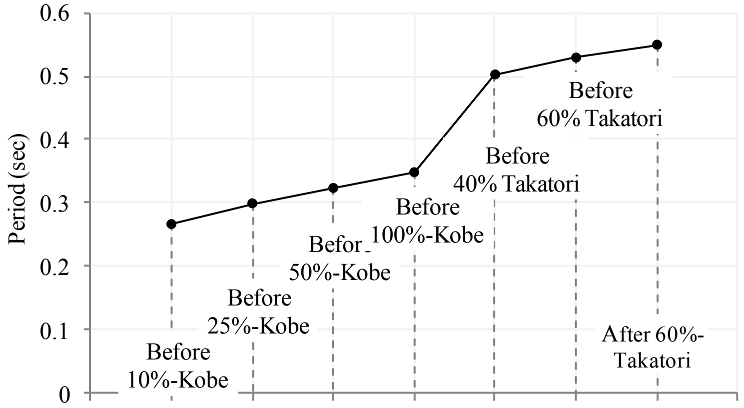

Figure 5-10 Variation of y-direction fundamental period of PT building throughout the test program

5.3 Observed damage

Figure 5-11 shows the observed damage in the y-direction of the building after the 100%-Kobe record. As previously mentioned, no visible damage was observed at the end of the lower intensity tests. Performance of the north UPT wall (axis A) was very satisfactory. Apart from the intended single crack at the base of the wall-foundation grout pad, the north UPT wall remained essentially intact and, upon completion of the tests, only minor cosmetic spalling was observed at the east end of the base panel (Figure 5-12). The fiber reinforced interface grout at the base of the north wall also remained intact as it moved upward together with the lowermost precast panel (Figure 5-13). In the south UPT wall (axis C), which did not contain fiber reinforcement, the 30-mm thick grout pad along the base joint partly crushed and spalled during the 100%-Kobe record. This caused the lowermost precast panel to separate from the grout and gap opening to develop at the base of the wall panel (as opposed to the base of the grout pad). As shown in Figure 5-14, spalling of concrete cover occurred at both corners of the south UPT wall, and extended above the foundation over a height approximately equal to the thickness of the wall (t_w = 250 mm).

Although lack of fiber reinforcement adversely affected the behavior of the south wall and led to faster degradation, damage in the south wall was still repairable and localized at the base. No cracking developed at the upper portion of the lowermost panel or in the upper story precast panels that remained essentially elastic. Moreover, as will be discussed in Section 5.6 with respect to UPT wall local responses, despite the partial crushing of the interface grout, no prestress losses occurred and no sliding was observed at the base of the south wall. This level of performance is still superior to expected performance of conventional RC walls under same intensity seismic actions (Tuna et al. 2014).

However, the marked difference in performance of the two UPT walls in the test building emphasizes the importance of ensuring that the critical joint of a UPT wall can sustain large local compressive strains in a ductile manner, without significant degradation of concrete or grout. In ACI ITG-5.2, this is achieved by transverse reinforcement at the ends of the base panel and fiber reinforcement in the interface gout, which is also required to have a specified compressive strength at least equal to the strength of the precast panels ($f_{cg}' \geq f_c'$). As discussed in Section 4.6.6, the south UPT wall of the test building did not satisfy ACI ITG-5.2 requirements, as it did not contain fiber reinforcement in the wall-to-foundation interface grout. As a result, grout crushing and concrete spalling occurred and led to degradation in the south UPT wall. In contrast, the north UPT wall, in addition to satisfying ACI ITG-5.2 requirements with respect to fiber reinforcement in the interface grout, it also included fiber reinforcement in the first and second story precast panels, which resulted in minimal concrete cover spalling and excellent performance of the north UPT wall. These differences emphasize that, by ensuring that the critical joint of a UPT wall can sustain large compressive strains, without significant degradation of concrete or grout, an essentially damage-free structural system can be obtained. Note that prior testing (Holden et al. 2003) has also verified the effectiveness of steel-fiber reinforced concrete in limiting damage at the base of UPT walls. Other means to ensure that inelastic action due to high compressive forces can develop in a ductile manner at the critical joint, include use of local armor like steel plates at the base of the wall, or placement of the grout inside a trough below the wall. Such details were successfully implemented at the base of the coupled UPT wall of the PRESSS test building (Priestley et al. 1999, Stanton and Nakaki 2002).

The UPT beams in the y-direction of the PT building generally performed as intended, with nonlinear deformation mainly concentrated at the beam-to-column and beam-to-wall connections. As shown in Figure 5-15, upon completion of the test, damage to the UPT beams ranged from grout crushing and localized damage at the interface with the walls and columns, to some concrete crushing at the bottom face, extending horizontally a short distance (typically smaller than 0.5*h*, where *h* = 300mm the beam height) from the wall or column interface.

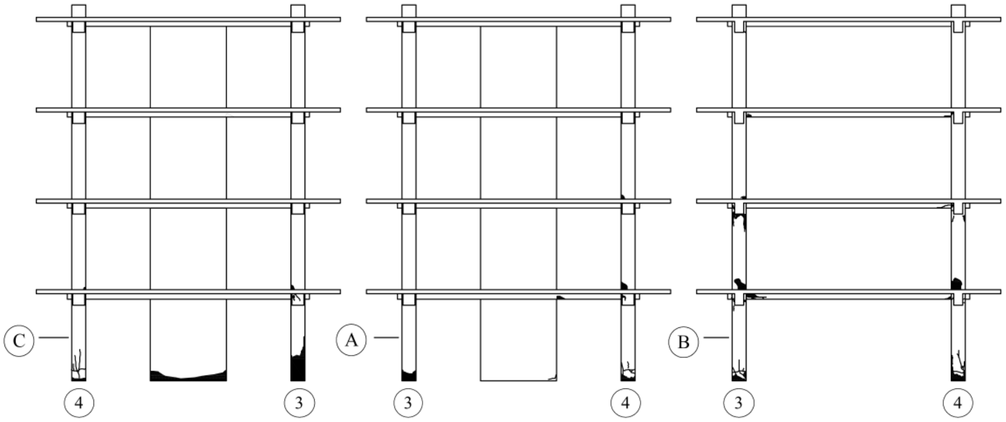

Figure 5-11 Observed damage in y-direction of PT building after the 100%-Kobe record (Nagae et al. 2012)

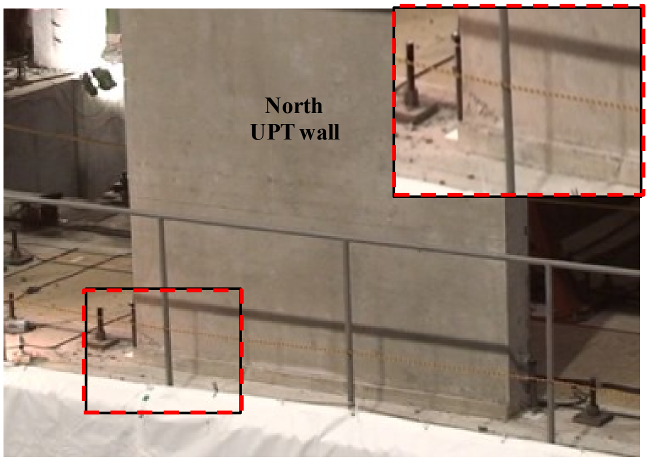

Figure 5-12 Damage at base of north UPT wall at end of tests

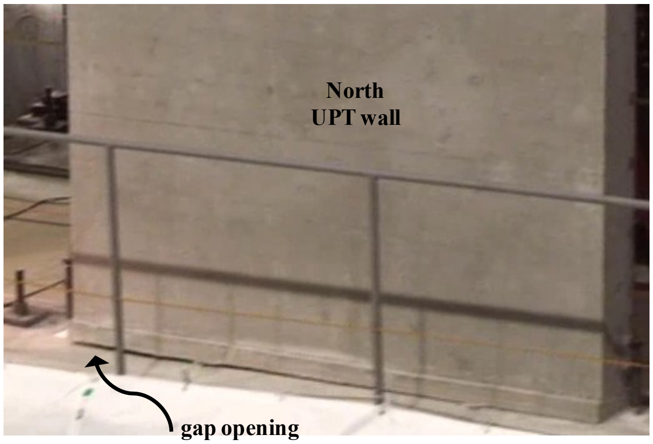

Figure 5-13 Gap opening at base of north UPT wall during 100%-Kobe record

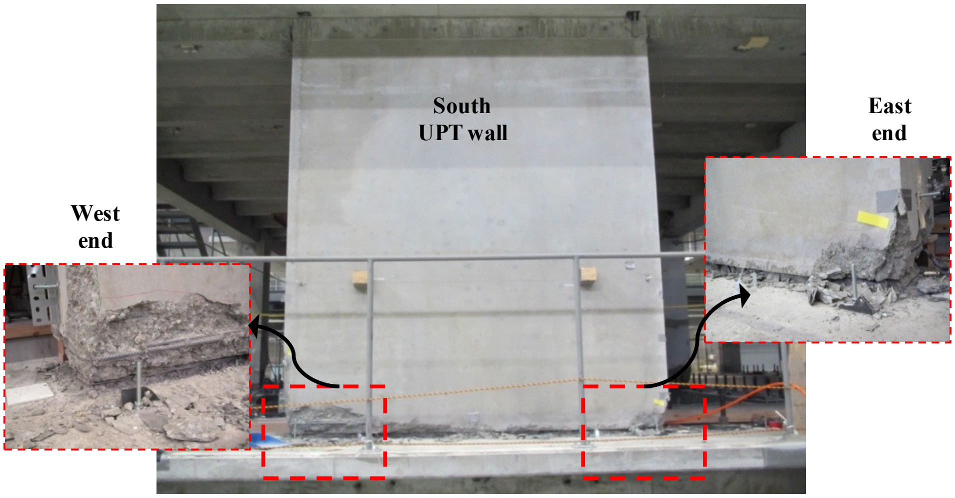

Figure 5-14 Damage at base of south UPT wall at end of tests; pictures courtesy of T. Nagae

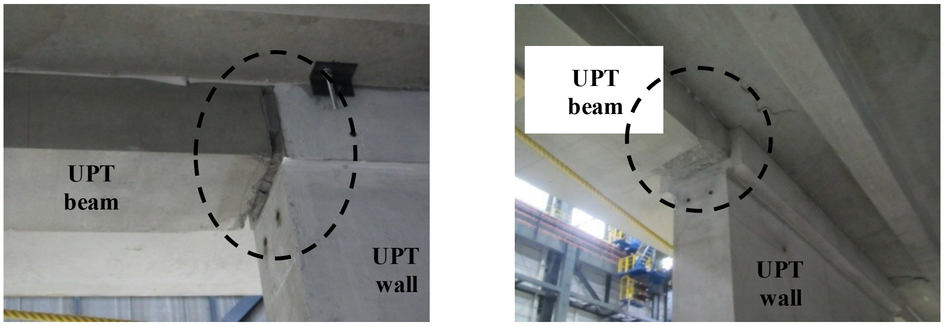

(a) (b)

Figure 5-15 Typical damage at beam-to-wall connections at end of tests; pictures courtesy of T. Nagae

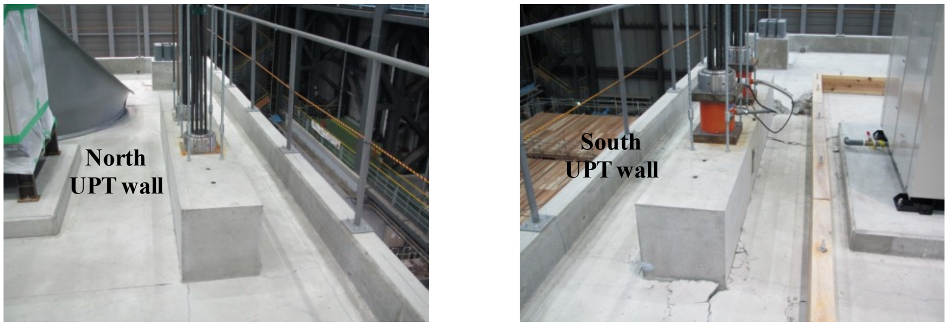

(a) (b)

Figure 5-16 Damage in slab at roof level in vicinity of (a) north and (b) south UPT wall at end of tests; pictures courtesy of T. Nagae

Figure 5-17 Damage in slab at location of UPT beams at end of tests; picture courtesy of T. Nagae

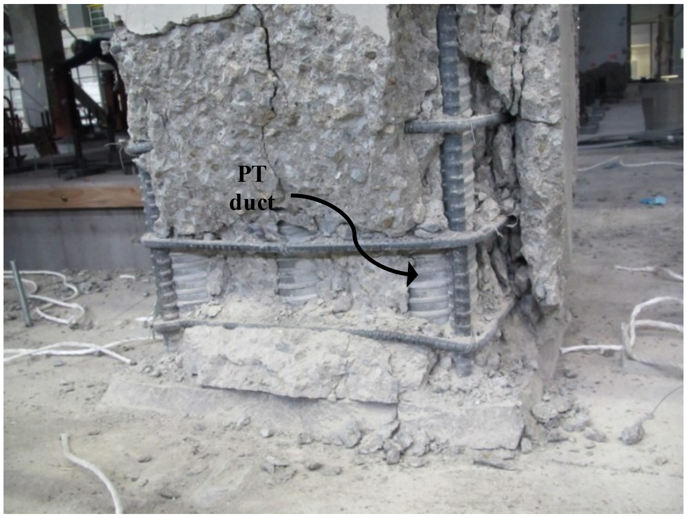

Figure 5-18 Damage at base of PT column at end of tests; picture courtesy of T. Nagae

Interaction of the slab with the UPT walls and UPT beams in the test building led to some slab damage during the tests. Figure 5-16 shows the condition of the slab in the vicinity of the UPT walls at the roof level, upon completion of all tests. Damage was more pronounced close to the south UPT wall which, as will be discussed in Section 5.6, experienced larger displacement demands and more uplift compared to the north UPT wall. Damage at the slab-to-wall connection, such as that depicted in Figure 5-16(b), can be attributed to displacement incompatibility between the UPT wall and slab. Assuming the UPT wall rocks about its base in essentially a rigid body motion, gap opening at the base of the wall causes an equal vertical displacement at the locations of slab-to-wall connections (i.e. the slab is constrained to uplift together with the wall). On the other hand, at the edge of the building the slab is constrained to the columns, which do not sustain significant vertical displacements. Note that slab displacement profiles in the vicinity of the UPT wall are presented in Section 5.7. The resulting vertical displacement and rotation of the slab-to-wall connection can cause damage to the slab, such as observed in Figure 5-16(b). In order to prevent floor damage, prior experimental research (Schoettler et al. 2009) and analytical studies (Henry, 2011) have investigated alternatives to rigid cast-in-place connections, such as isolating the floor system from uplift of the wall by means of a slotted connection. Note that in the E-Defense PT building, the 100-mm-thick slab was cast-in place together with the top part of the UPT beams on either side of the UPT walls, and was supported on precast floor units (double tees) spanning parallel to the UPT walls. The cast-in-place slab and UPT beams were mechanically connected through the beam stirrups. In the direction of the UPT beams, no slab or beam mild longitudinal reinforcement extended into the walls and moment resistance at connections of the slab-beams to the walls was provided by the unbonded post-tensioning steel that ran horizontally through the UPT beams and the wall. In the orthogonal direction, 100-mm long inserts (through the thickness of the wall) connected the slab reinforcement to the wall (Figure 4-8). While damage to the slab in the E-Defense test building was generally repairable and consisted of a few widely-spaced cracks, in keeping with the objective of an essentially damage-free building system, connections of UPT walls to the floor system require additional considerations.

While discussion so far with respect to damage to the slab has concentrated on the wall-to-floor interaction, it is worth pointing out that similar displacement incompatibilities exist between the UPT beams and the floor system. The beam-to-wall (and beam-to-column) jointed connections described above, allow gap opening to occur at the beam-to-wall (and beam-to-column) interface, resulting in axial growth of the beam. Due to the presence of the slab, this growth is restrained, creating tensile stresses and additional cracking in the slab. Beam elongation effects together with bending of the slab under excitation in the frame (x) direction likely contributed to observed floor slab cracks along the UPT beams, as shown in Figure 5-17. Note that beam elongation effects are not specific to UPT beams. Similar effects have been identified in ductile RC moment frames, where beam growth is associated with concrete cracking and shifting of the neutral axis towards the compression zone (Kim et al 2004), as opposed to the gap opening mechanism of UPT beams. In particular, the adverse effects of beam elongation on the integrity of diaphragm action of precast flooring units has been identified in the literature (Fenwick et al. 2010) and has also been observed during the February 2011 earthquake in New Zealand as reported by Kam et al. (2011). In addition to potential damage to the floor as discussed above, interaction of the UPT beams with the slab also had a significant effect on flexural strength of the UPT beams, and framing action of the UPT walls with the corner columns. These issues are discussed in detail in Chapter 6.

Finally, other damage observed to the E-Defense PT building upon completion of the tests included concrete crushing at bases of first story columns (Figure 5-18) and axis-B second-story columns. This damage was mainly associated with the frame (x) direction of response that imposed considerably larger displacement demands on the columns compared to the y-direction examined herein. Note that peak interstory drifts in the x-direction during the 100%-Kobe and 60%-Takatori records were 3.90% and 5.80%, respectively, as opposed to 1.66% and 1.55% in the y-direction (wall direction).

5.4 Displacement profiles

Figure 5-19 shows the y-direction displacement profiles along the height of the building at peak roof drift for each record. Profiles are almost linear, verifying that displacement response was largely dominated by rigid body rotation (rocking) at the bases of the UPT walls. Three lines are plotted for each record, namely north end, center, and south end. “Center” displacements correspond to average measurements from sensors D2 and D3 (Figure 5-20), assumed to represent on average displacements at the center of plan. Story displacements were not measured at the north and south ends of the building but were derived from recorded data (sensors D1, D2 and D3, Figure 5-20) and are plotted in Figure 5-19 together with the center of plan displacements. For each record, all displacement values shown are simultaneous and correspond to the instant at which the peak roof displacement occurred at the center of plan. For instance, the three displacement profiles shown for the 100%-Kobe record (north end, south end, and center) all correspond to the instant *t*=20.115s during the 100%-Kobe record, when the peak roof drift ratio at the center of plan was recorded (peak E in Figure 5-6).

Profiles of Figure 5-19 indicate a notable torsional response of the building. Displacements at the south end were consistently larger than north end displacements and differences increased with increasing level of seismic intensity. For the 25%-Kobe record, at the time of peak roof displacement at the center of plan, the roof displacement at the south end was around 20% higher and accordingly north end displacement was 20% lower than the center of plan displacement. For the 100%-Kobe and 60%-Takatori records, this difference increased to 31% and 37%, respectively.

Note that, with the exception of slab edges, the test structure was essentially symmetric in plan. At low intensities, variations of material properties and unintended mass eccentricity related to locations of non-structural elements in the building (such as mechanical equipment and fixed steel frames for displacement measurements) may have contributed to the torsional response of the building. For the 100%-Kobe and Takatori records, the earlier degradation of concrete and grout in the south wall and subsequent different behaviors at the base joints of the two UPT walls as described in Section 5.4, likely increased the torsional component of displacement and resulted in the south wall sustaining significantly larger displacement demands than the north wall. At the instant of peak roof drift at the center of plan (1.58% under the 100%-Kobe record), the south wall roof drift ratio was 2.09% while the north wall roof drift at the same time was only 1.07%. Differences are even more pronounced when peak responses at the north and south ends of the building are compared (as opposed to simultaneous values at the instant of peak response at the center of plan). This is because in addition to affecting the magnitude of responses at opposite ends of the building, torsion also causes peak responses at the north and south ends of the building to generally occur at different instances. This is further discussed with respect to wall base rotations in Section 5.6.

Finally, it is worth noting that while the purpose of including different detailing at the two UPT walls of the E-Defense PT building was to extract as much information from the test building as possible, i.e. response of fiber reinforced UPT wall/grout versus non-fiber reinforced, the test data presented above provided some insight into torsional response that can occur in real UPT wall buildings. For instance, strength or stiffness eccentricities in building plans with UPT walls of different lengths, may lead to effects similar to what was observed in the test building, i.e. torsional response due to earlier softening or degradation of one of the walls. Analytical studies are required to assess torsional effects in eccentric UPT wall buildings and compare with available studies on torsional response of conventional RC wall buildings (e.g. Priestley 2007, Beyer 2007).

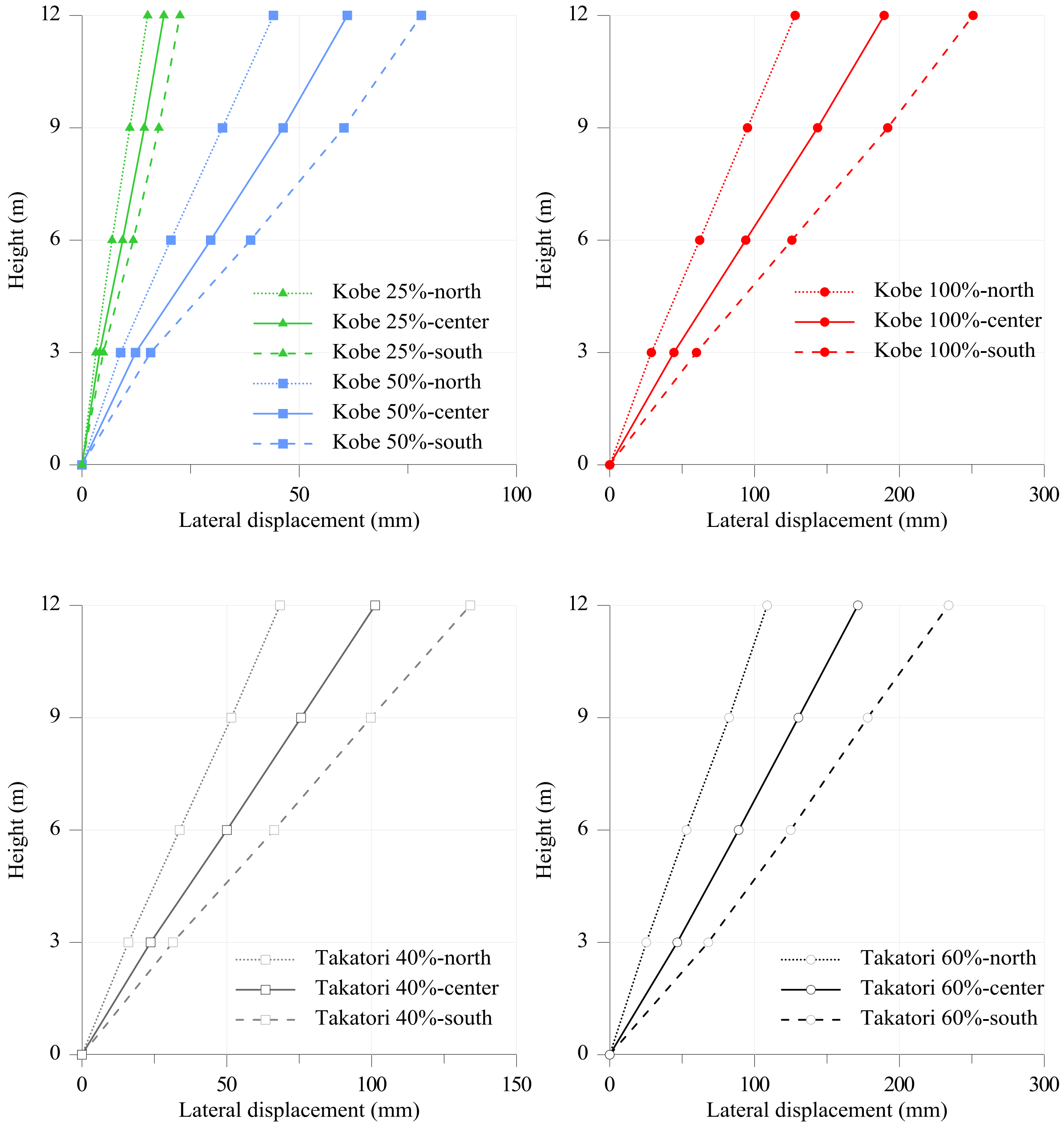

Figure 5-19 Displacement profiles at peak roof displacement

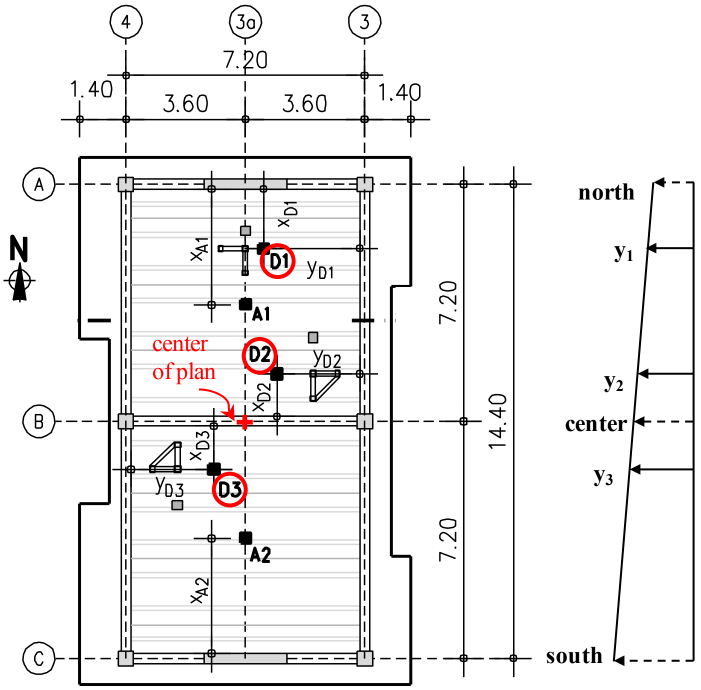

Figure 5-20 Calculation of lateral displacement at south and north ends of building

5.5 Response envelopes

This section presents envelopes over the building height of various global response quantities of the PT building in the wall direction during each test. Figure 5-21 plots the interstory drift ratio envelopes at the center of plan. Distribution of drift was almost uniform along the height of the building for all records, confirming that response was largely dominated by rocking at the bases of the UPT walls. Peak interstory drift ratio during the tests was 1.66% (at center of plan).

Figure 5-21 and Figure 5-22 show the building moment and shear envelopes in the wall direction of response for each record, along with design values for overturning moments and story shears (M_u and V_u). These design forces correspond to base shears of $0.2W$ and $0.3W$ (where W = 3420 kN is the total weight of the building) for DBE and MCE level shaking, respectively, and a vertical distribution of seismic forces according to 12.8.3 of ASCE 7-10, as discussed in Section 4.6.1. Figure 5-21 and Figure 5-22 also plot the moment (M_n and M_{prob}) and shear ($V_{n,}$ and $V_{n,i}$) capacities of the two UPT walls that were presented in Sections 4.6.2 and 4.6.5, respectively. Recall that for design purposes, the two UPT walls were assumed to resist the entire base shear and overturning moment in the y-direction of the building, and therefore design forces M_u and V_u can be directly compared to the moment and shear capacities of the two UPT walls. Calculated wall moment capacities M_n and M_{prob} exceed the design demands M_u at DBE and MCE, respectively. M_n (doubled for the two UPT walls in the building) is 60% higher than the DBE moment M_{u_DBE}, and M_{prob} is around 40% higher than M_{u_MCE}. However, the experimental moments are significantly higher than the calculated wall moment capacities. The peak overturning moment of the building during the tests was almost two times the probable moment strength at the bases of the UPT walls. This difference can be largely attributed to interaction of the walls with the UPT beams that framed into them and coupled the walls to the corner columns at each floor level. When rotations at the ends of the short length UPT beams were sufficiently large for them to develop their moment capacities, the maximum contribution from framing action occurred.

Considering the exterior frame of the PT building (frame along line A or C of Figure 4-4), Figure 5-24 illustrates a simple mechanism where, as the wall rocks against the foundation, the short length UPT beams framing into the wall on either side and at each floor level reach their moment capacities, M_b, and corresponding shear forces, V_b. Opposite sign axial loads, with a magnitude equal to the sum over all floors of these (plastic) shear forces of the framing UPT beams, develop at the base of the corner columns resulting in a tension-compression couple that adds to the overturning moment of the building. Beam shear forces are also transmitted at either end of the wall at each floor level. Due to their opposite signs, the influence of these forces on the wall axial load is small. Moment resistance at the base of the columns, although small compared to the wall moment capacities, also adds to the overturning moment. Based on this mechanism, the increase in overturning moment at each exterior frame (Frame A or C) due to coupling is $\Delta M = \mathrm{n}V_\mathrm{b}\cdot L$, where n = 4 is the number of stories, $V_\mathrm{b} = 2M_\mathrm{b}/L_\mathrm{b}$ is the beam shear force at development of M_b, $L = 7.2$ m is the centerline distance of the exterior columns (lever arm) and $L_\mathrm{b} = 2.125$ m is the clear length of the beams. For an effective height equal to 77% of the height H of the building (resultant of design first mode forces), the increase in base shear corresponding to ΔM is $\Delta V = \Delta M/0.77H$.

To appreciate the impact of beam coupling on base shear, two cases are compared: the first neglects framing action ($M_\mathrm{b} = 0$), and the second considers framing action with $M_\mathrm{b} = 0.03M_\mathrm{prob}$ (moment capacity of UPT beams equal to 3% of the wall capacity). The overturning moment capacity and associated base shear resistance for the first case is $2M_\mathrm{prob}$ and $0.42W$, respectively. For the second case, the total *increase* in overturning moment and base shear of the building due to framing action is $2\Delta M = 1.63M_\mathrm{prob}$ and $2\Delta V = 0.34W$. This translates into an approximately 80% increase in both global moment and shear resistance due to framing action compared to resistance provided by the walls alone, or equivalently a 45% contribution of framing action to global overturning moment and base shear of the building. Despite assumptions involved, these simple calculations demonstrate that: (i) contribution of framing action is expected to be significant even for a modest moment capacity of the UPT beams, (ii) an accurate evaluation of UPT beam capacities, including slab effects, is essential in any attempt to predict the lateral resistance of the test building, and (iii) an increase in wall shear demand is expected due to framing action as the total increase in base shear ($2\Delta V$) is distributed between the UPT walls and the columns.

Note that prior testing has shown that even gravity framing and coupling through slabs can have a significant effect on lateral resistance and shear demands of both UPT and RC wall building; Thomas and Sritharan (2004) report that gravity columns and framing action resulting from interaction between the seismic frames and precast floors, contributed approximately 23% of the moment resistance in the wall direction of the PRESSS test building. Similarly, with respect to the 7-story wall structure they tested on the UCSD shake table, Panagiotou et al. (2011) report that coupling through the slabs contributed 32% of the maximum base moment recorded.

In addition to the wall capacities and framing action (axial force couple at the bases of Frame A and C columns) described above, other sources adding to the lateral resistance of the test building include moment resistance at the bases of the columns and contribution of the intermediate one-bay moment frame (Frame along axis B). Analytical studies presented in a Chapter 6 quantify, by means of a nonlinear model of the building, the relative contributions of various sources to moment resistance and assess the impact of framing action on wall shear demands. The presence of the slab is also shown to have a significant impact on framing action by restraining axial growth and increasing flexural capacities of the UPT beams.

The framing action and sources noted above explain the overstrength apparent in Figure 5-21 and Figure 5-22. It is worth noting that the moment overstrength factor, defined as the ratio of maximum experimental base moment to design MCE moment, is equal to 2.72 and is close to the shear overstrength factor of 2.91 (ratio of maximum experimental base shear to design MCE shear). Also consistent with the observation of similar moment and shear overstrength factors, the ratio of experimental global overturning moment to total base shear ($H_{\mathrm{eff}}=M/V$) in the y-direction remained almost constant throughout the tests with an average value of 77% of the height of the building. For this calculation, the M/V ratio was computed for each record at all instants for which moment exceeded 90% of its peak value during the record (Panagiotou et al. 2011). Note that the calculated effective centroid of seismic actions coincides with the resultant of design lateral forces (M_u/V_u), confirming the predominantly first mode response of the building.

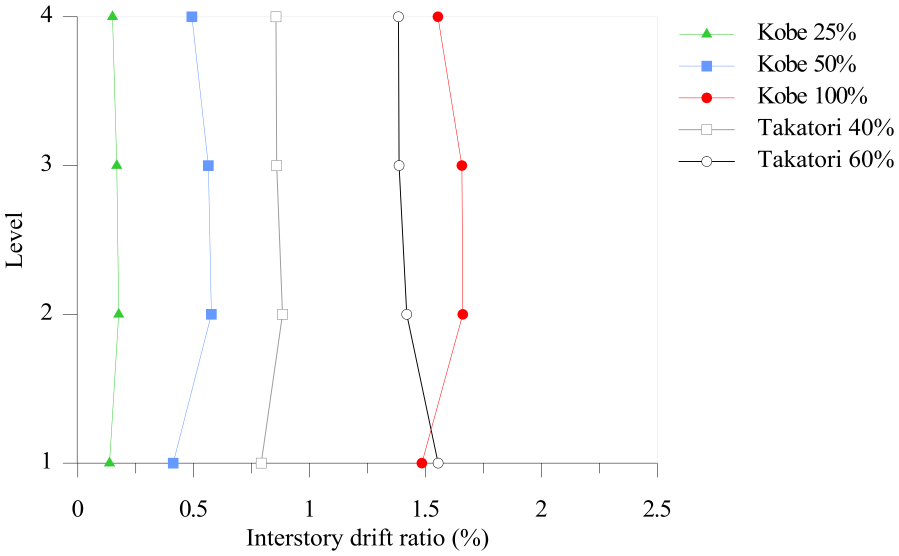

Figure 5-21 Interstory drift ratio envelopes in y-direction of PT building

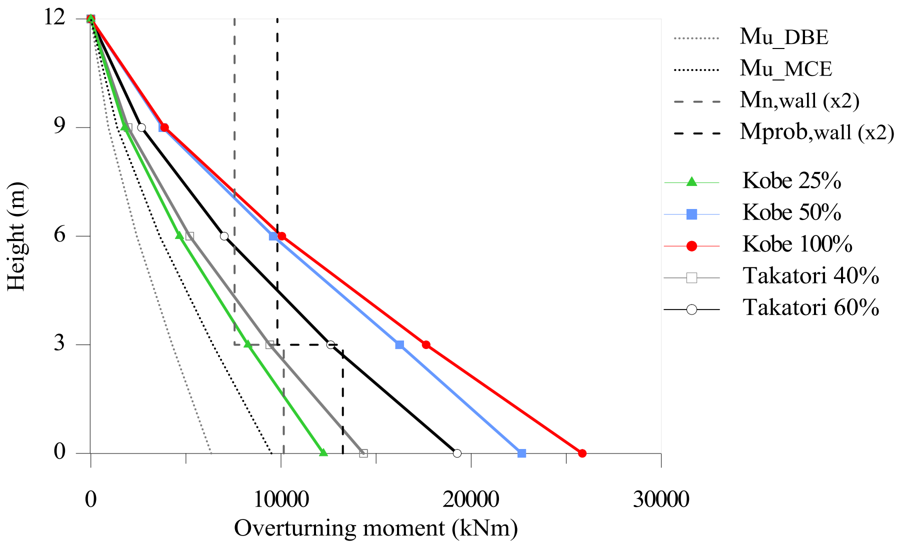

Figure 5-22 Overturning moment envelopes in y-direction of PT building

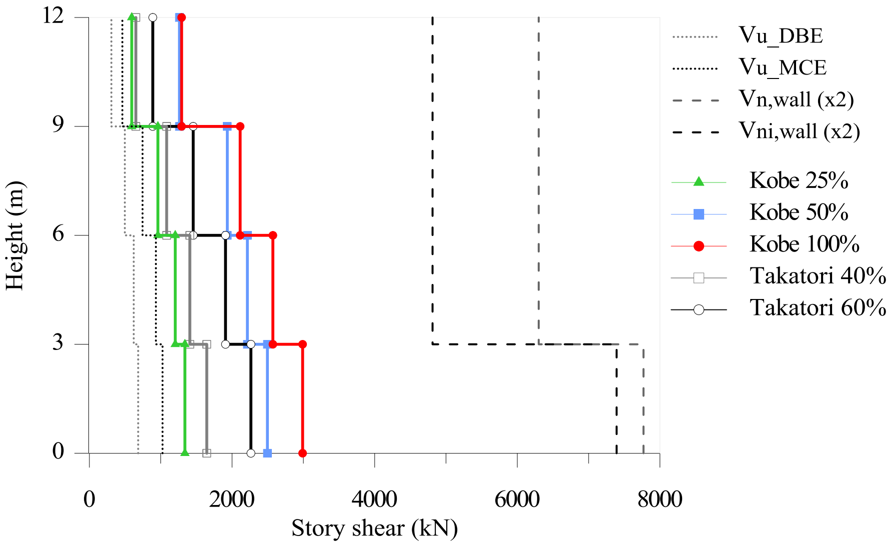

Figure 5-23 Story shear envelopes in y-direction of PT building

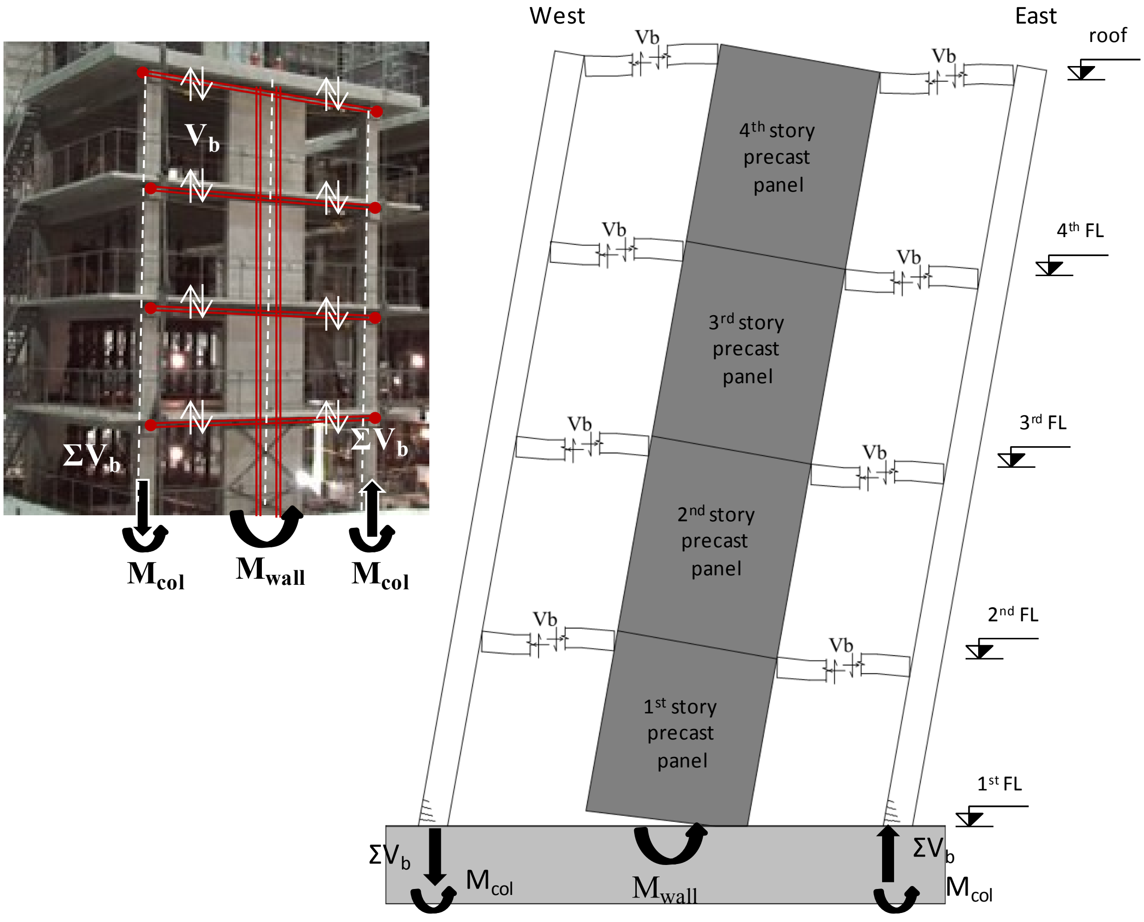

Figure 5-24 Frame A and Frame C plastic mechanism

5.6 UPT wall responses

Instrumentation of the two walls allowed rotations, uplift and compressive strains at the bases of the two UPT walls to be computed. The denser array of sensors in the south wall allowed additional response parameters, such as PT forces, out-of-plane rotations and sliding displacements to be calculated. Figure 4-15, reproduced here for reference as Figure 5-25, shows the instrumentation at the base panel of the south UPT wall. Table 5-1 presents peak values of various measured response parameters for each wall. Also shown are the peak roof drift ratios for each wall (roof lateral displacement at location of wall divided by building height). As evidenced by the tabulated values, the south wall sustained significantly larger deformations than the north wall. Note that uplift and strain values in Table 5-1 are direct measurements from the respective sensors (D1, D2, D3, D6), and thus refer to the locations of the sensors. Local wall responses summarized in Table 5-1, and extracted data (e.g., concrete strains at wall edges, wall neutral axis depth) are discussed in more detail in the following sections.

Table 5-1 Peak response parameters for south (SW) and north (NW) UPT walls

Peak response parameter	25%Kobe	50%Kobe	100%Kobe	40%Takatori	60%Takatori
SW roof drift (%)	0.19	0.65	2.09	1.12	1.95
NW roof drift (%)	0.13	0.37	1.07	0.57	1.00
SW in-plane rotation (%) [1]	0.1	0.41	1.94	0.97	1.94
NW in-plane rotation (%) [1]	0.07	0.27	1.02	0.49	0.86
SW east end uplift (mm) [2]	2.2	9.3	38.1	19.9	49.1
NW east end uplift (mm) [2]	1.6	6.0	26.3	9.1	13.5
SW west end uplift (mm) [3]	1.2	7.0	43.2	13.6	25.1
NW west end uplift (mm) [3]	0.6	4.4	23.0	6.8	30.4
SW compressive strain [4]	-0.0019	-0.0043	-0.0293	-0.009	-0.0379
NW compressive strain [4]	-0.0013	-0.0032	-0.0114	-0.0065	-0.0228
SW PT stress f_p/f_{py}	0.55	0.58	0.72	0.62	0.71
SW out-of-plane rotation (%) [5]	0.10 (0.04)	0.26 (0.04)	3.66 (0.83)	1.29 (0.51)	5.92 (4.81)
SW sliding displacement (mm)	0.38	0.89	3.13	1.45	2.44
SW transverse reinf. strain	0.00004	0.00011	0.00024	0.0001	0.00012

1 Rotations computed using data from sensors D3 and D6

2 Uplift from sensors D1 for Kobe records and sensors D3 for Takatori records

3 Uplift from sensors D2 for Kobe records and sensors D6 for Takatori records

4 Compressive strains from sensors D1 and D2 for Kobe records and sensors D3, D6 for Takatori records

5 Shown in parenthesis is the out-of-plane wall base rotation at instant of peak in-plane rotation

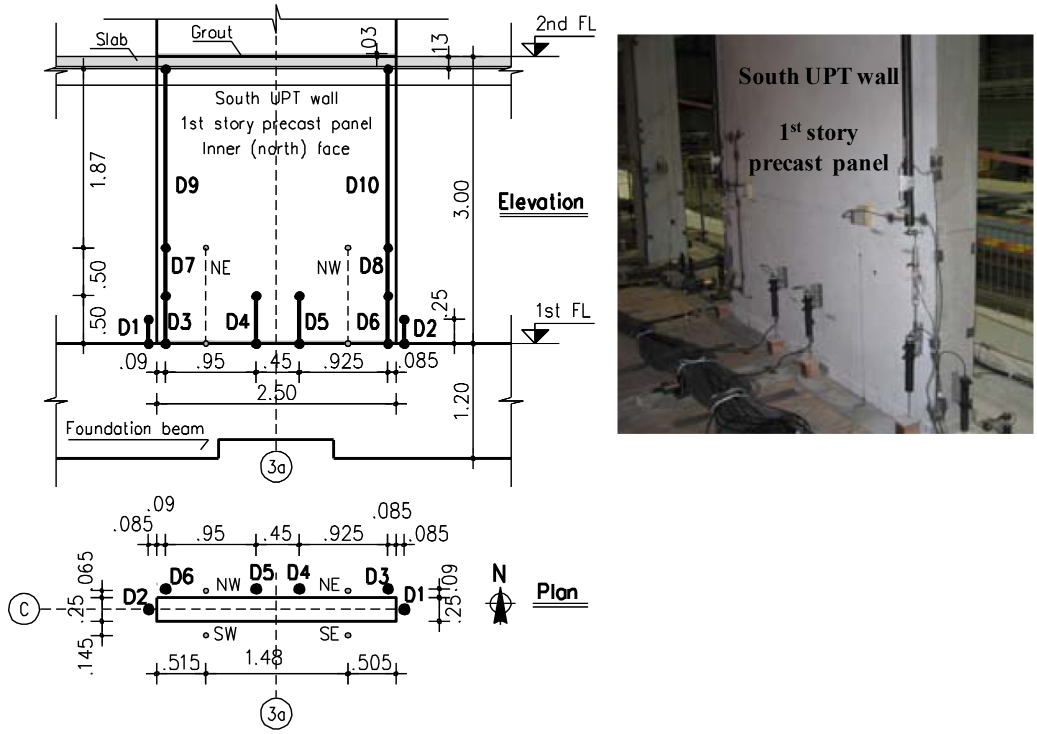

Figure 5-25 Instrumentation at first story panel of south UPT wall (dimensions in m)
(Note measurements from sensors D1, D2 not available for Takatori records)

5.6.1 Wall in-plane rotations and wall roof drift ratios

Figure 5-26 plots the base rotation histories of the north and south UPT walls under each record. Peaks values are denoted for each wall on the plots. The sign convention for plotted in-plane rotations is that westward displacements (uplift at east ends of walls) cause positive wall rotations. Rotations in Figure 5-26 were derived using measurements from sensors D3 and D6, which were located at the base of each wall, close to the wall edges (Figure 5-25). Note that sensors D3-D6 were attached to the inner face of each wall (i.e. at north face of south wall and south face of north UPT wall), so that vertical displacement measurements from these sensors are affected by out-of-plane rotations of the wall. Sensors D1, D2, located at the edges of the walls and close to the horizontal centerline, would provide a more direct calculation of wall rotations, as vertical displacements at these locations are less affected by out-of-plane rotations. However, negative measurements from D2 sensor at the west end of the south UPT wall were not reliable under the 100%-Kobe record. Moreover, measurements from D1 and D2 sensors were not available for the subsequent Takatori records. For these reasons, all rotations plotted in Figure 5-26 were derived using measured data from sensors D3 and D6. Given that reliable data from all sensors were available for the north UPT wall under the Kobe records, these were used to verify that rotation calculations with either D1, D2 or D3, D6 sensors were in close agreement. Such comparisons are shown in Figure 5-27 for the 100%-Kobe record, and confirm that rotation calculations using sensors at the inner face of the wall (D3, D6) result in almost identical rotations as calculations using sensors at the wall centerline (D1, D2) despite (i) significant out-of-plane wall rotations as discussed in the next section, and (ii) the different gauge length of the sensors (500mm versus 250mm). Finally, it is worth noting that all rotation calculations assumed a linear profile at the base of wall: e.g., $\theta=(D_3-D_6)/L_{36}$, where D_3, D_6 are the vertical measurements from sensors D3 and D6, respectively, and L_{63} is the horizontal distance between the sensors. While the "plane sections remain plane" assumption is violated at the critical joint due to the separation gap forming at that location, measured vertical displacement profiles along the length of the wall, over the gauge length of the sensors, were found to be approximately linear, especially at larger rotations. This is discussed further with respect to wall uplift in Section 5.6.3. An examination of gap opening displacements at the base of the five UPT wall specimens tested by Perez et al. (2004), also confirmed that at large base rotations the assumption of a linear profile along the length of the wall is satisfactory.

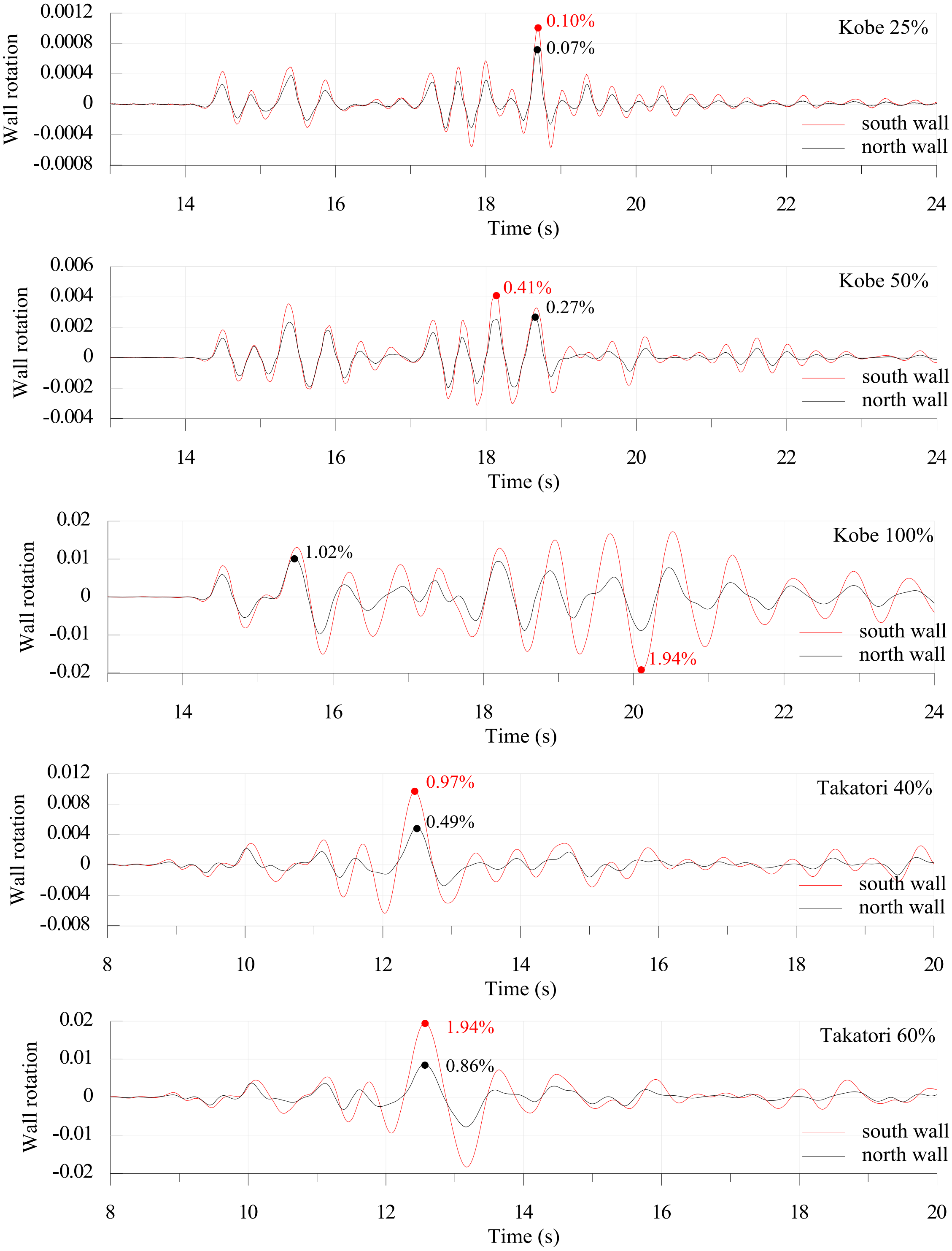

Figure 5-26 In-plane wall base rotation histories of south and north UPT walls

As evidenced by the response histories in Figure 5-26, and the differences between south and north UPT wall rotations, torsional response occurred early on in the testing sequence, with peak rotations in the south wall approximately 30% higher than north wall peak rotations during the 25%-Kobe and 50%-Kobe records. Differences between south and north wall rotations are more pronounced in the 100%-Kobe test and specifically after the first two large excursions in each direction, when crushing of the grout pad and spalling of concrete cover occurred at the base of the south UPT wall. It is also noted that peak wall rotations during the 100%-Kobe record are not simultaneous. The peak rotation of the south wall during the 100%-Kobe record occurred at t =20.1 s and was equal to 1.94%. At that instant, the rotation of the north wall was only 0.89%. The peak rotation of the north wall during the 100%-Kobe record occurred at t =15.48 s and was equal to 1.02%.

Table 5-1 summarizes peak rotation values of the two UPT walls for all records. Also tabulated are the peak wall roof drift ratios under each record. These were derived from the lateral displacement measurements at floor levels, by extrapolating to the north and south edge of the building as described in Section 5.4. Comparisons between wall base rotations and wall roof drift values reported in Table 5-1 reveal that peak wall rotations during the higher intensity records (100%-Kobe, 60%-Takatori) are close to respective peak wall roof drift ratios, confirming that the majority of wall deformations under these records originated from rocking of the walls against the foundation. Response histories of wall roof drift ratio and wall base rotation under the 100%-Kobe record shown in Figure 5-28 confirm this observation. Note that contribution of wall base rotation to peak wall roof drift under the 100%-Kobe record was 92% for the south wall, and 88% for the north wall. As evidenced by the values reported in Table 5-1, contributions of wall base rotations are smaller under the lower intensity records (25%-Kobe, 50%-Kobe). Given the essentially elastic response under these records (Figure 5-1), the smaller contribution of wall base rotation is expected, as response was likely governed by the elastic deformations of the walls.

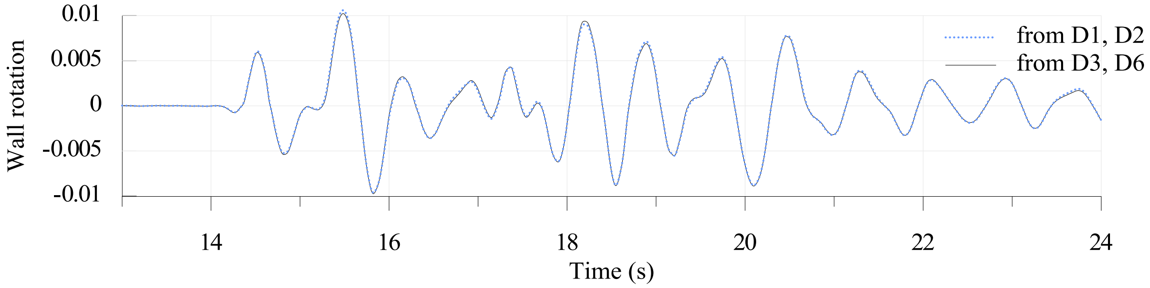

Figure 5-27 North wall rotation histories under 100%-Kobe record using alternative experimental data for rotation calculation

Finally, it is useful to compare the peak roof drift ratios during the tests to the design (θ_{design}) and maximum ($\theta_{\max}$) roof drift ratios as defined in ACI ITG-5.2. Such comparisons provide a useful context for any subsequent discussion on design implications of the tests. The ACI ITG-5.2 design and maximum roof drift ratios for the E-Defense UPT walls, as discussed in Section 4.6, were found to be equal to θ_{design}=0.95%, and $\theta_{\max}$=3.0%, respectively. Peak wall roof drift ratios during the tests were obtained under the 100%-Kobe record, and were equal to 1.07% for the north wall and 2.09% for the south wall (Table 5-1). Despite the considerable unintended torsional response of the building, both UPT walls achieved the design drift, θ_{design}, and in addition, the south wall was displaced to approximately 70% of the maximum ACI ITG-5.2 drift, $\theta_{\max}$. Moreover, peak wall base rotations during the test were very close to peak wall roof drift ratios: peak base rotations for the north and south UPT walls were 1.02% and 1.94%, respectively. Recall that calculations of nominal (M_n) and probable (M_{prob}) moments in Section 4.6.2.1, assumed that the walls rock about the base in essentially a rigid body motion, so that the wall base rotation was taken equal to the wall roof drift ratio, i.e. the wall base rotation for computation of M_{n} was assumed to be equal to θ_{design} and the wall base rotation for computation of M_{prob} was assumed to be equal to θ_{max}. Experimental results presented in this section confirm that this assumption is satisfactory.

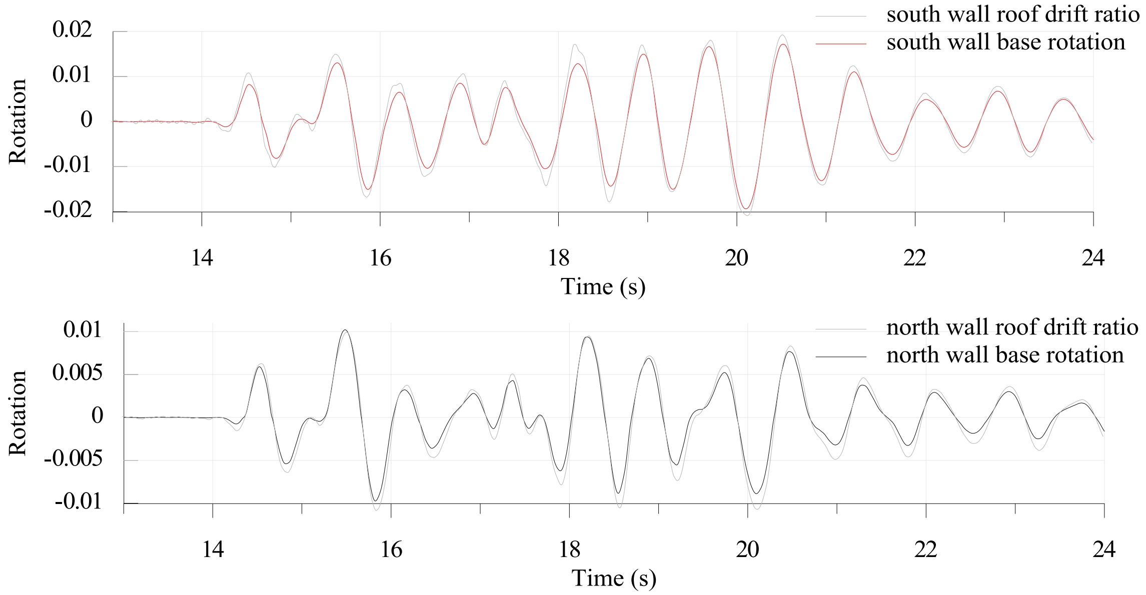

Figure 5-28 Comparisons of wall base rotation to wall roof drift ratio under 100%-Kobe record

5.6.2 Wall out-of-plane rotations

The sets of vertical displacement sensors on the outer (SW, SE) and inner (NW, NE) faces of the south wall, with a gauge length of 1000 mm (Figure 5-25), enabled calculation of wall out-of-plane rotations. Figure 5-29 plots the calculated out-of-plane wall rotation histories of the south UPT wall under each record. Peak values are denoted on the plots and are also summarized in Table 5-1. The in-plane base rotations of the south wall (previously shown in Figure 5-26), are also included in Figure 5-29 for reference. Note that similar sensors, that would enable out-of-plane wall rotation calculations for the north wall, were not provided.

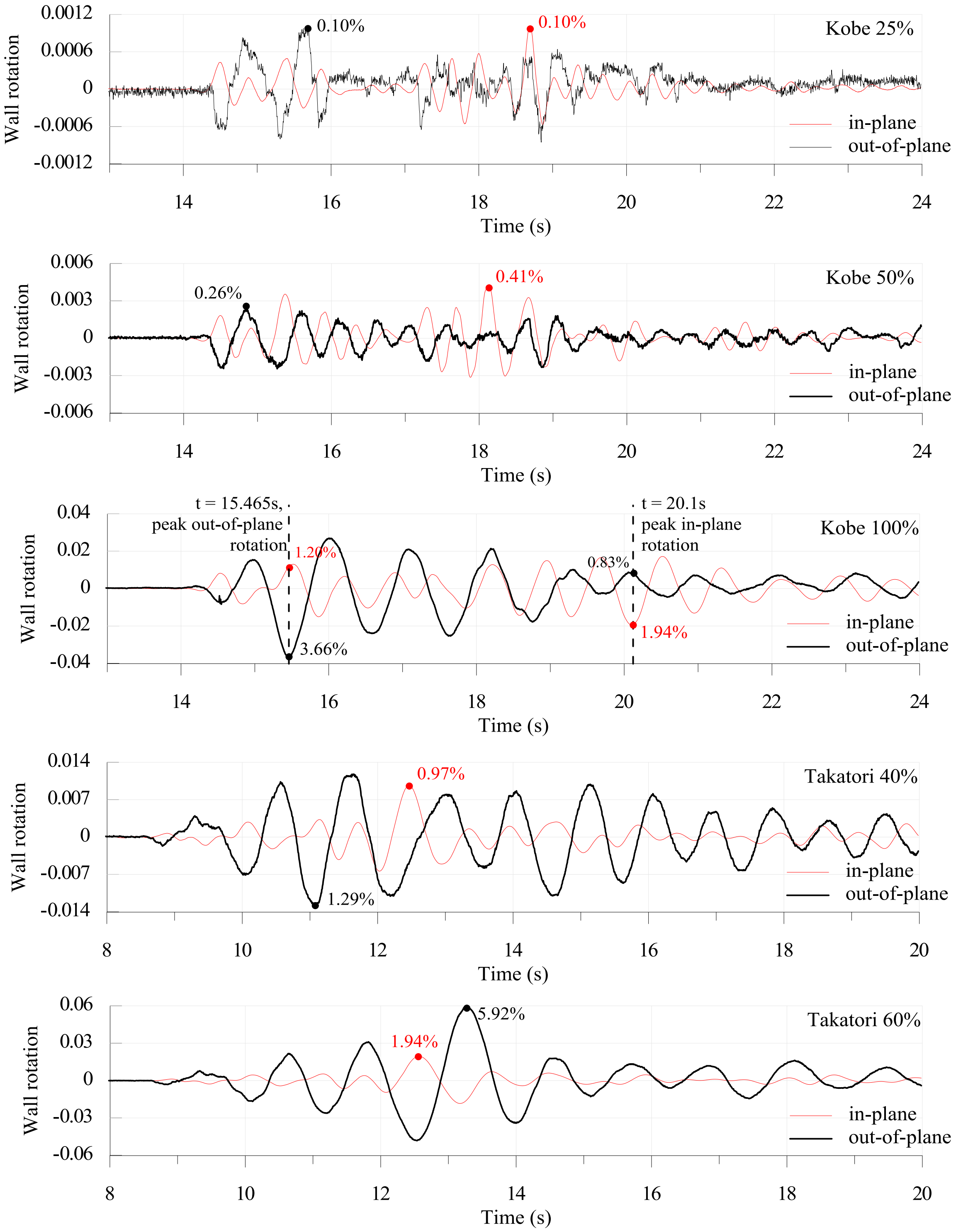

Figure 5-29 In-plane and out-of-plane wall base rotation histories of south UPT wall

The sign convention for plotted out-of-plane rotations of the south wall is that northward displacements cause positive wall out-of-plane rotations. Note that either set of sensors (SW-NW and SE-NE) can be used to compute out-of-plane rotations. Calculated rotations from the two sets of sensors were found to be in excellent agreement, with the exception of the 25%-Kobe record (where differences up to 20% were observed) and the 60%-Takatori record (where NE measurements were not reliable). Values plotted in Figure 5-29 correspond to average rotations from the two sets of sensors for all records, except for the 60%-Takatori, where the SW-NW sensors were used. Finally, using recordings from SW-SE or NW-NE sets of sensors, it was also possible to compute in-plane rotations of the south wall. These were also found in excellent agreement with previously calculated wall in-plane rotations from sensors D3-D6 (Section 5.6.1).

As evidenced by the response histories in Figure 5-29, wall out-of-plane rotations under the 100%-Kobe and 60%-Takatori records significantly exceeded in-plane rotations. Peak calculated out-of-plane rotations for these records were 3.66% and 5.92%, respectively, as opposed to 1.94% peak in-plane rotations. These values are consistent with measured story lateral displacements in the frame (x) direction of the test building; peak drift ratios of the first story (x-direction lateral displacement of second floor divided by story height) under the 100%-Kobe and 60%-Takatori records were 3.90% and 5.80%, respectively. Despite their large magnitude the out-of-plane drifts in the moment frame direction did not adversely affect the in-plane behavior of the UPT walls. Upon completion of the tests, no visible flexural cracks were observed in the walls, confirming that drifts in the moment frame direction were largely accommodated by out-of-plane rocking of the walls against the foundation. Test observations and videos from cameras providing close-up views of the UPT wall bases, confirmed that during the 100%-Kobe and 60%-Takatori records, in addition to in-plane rocking of the walls, significant out-of-plane rocking motion also occurred. Such out-of-plane rocking resulted in some localized increased compressive strains at the wall corners as will be discussed in Section 5.6.4.

Finally, it is also of interest to examine out-of-plane rotations at instants when peak in-plane wall responses occurred. Any impact of bidirectional effects is expected to be more pronounced at instants when considerable in-plane and out-of-plane wall rotations occur simultaneously. As shown in Figure 5-29, the peak in-plane rotation of the south wall during the 100%-Kobe record occurred at $t = 20.1$ s and was equal to 1.94%. At that instant, the wall out-of-plane rotation was 0.83%. Similarly, at the time of peak out-of-plane rotation during the same record ($\theta = 3.66\%$, at $t = 15.465$ s), the in-plane rotation of the wall was 1.20%. The gap opening profiles at the base of the south wall at these two instants during the 100%-Kobe record are discussed in the following section

5.6.3 Wall uplift

Figure 5-30 plots the measured uplift at the east end of each wall versus the wall base rotation for the 50% and 100%-Kobe records. Plotted values are measurements from sensors D1 (Figure 5-25) that were located at the east end of each UPT wall, close to the horizontal centerline of the wall. Given that the sensors were located some distance away (85mm) from the wall, gap opening at the wall end is somewhat smaller than the measured uplift at the location of sensor D1, and can be estimated by subtracting the wall rotation multiplied by the distance of the sensor from the wall end. By doing so, peak gap opening at the east end of the south wall was found equal to 36.7 mm (as opposed to the 38.1 mm peak value in Figure 5-30, which corresponds to the location of the sensor).

Comparing the uplift versus rotation plots of the south and north UPT walls shown in Figure 5-30, it is observed that despite the different amplitudes, associated with the larger demands on the south UPT wall, behavior of the two walls in terms of rotation-uplift relations was very similar. Under the 100%-Kobe record, peak measured uplift at the east end of the north wall was 26.3 mm, approximately 30% lower than peak uplift of the south wall (38.1 mm). Table 5-1 summarizes peak measured uplift values for all records. Note that sensors D1 and D2 were removed after the 100%-Kobe record so that uplift values for the Takatori records reported in Table 5-1 correspond to measurements from sensors D3 and D6, that were located at the inner face of each UPT wall. These measurements are affected by out-of-plane rotations so they are not representative of uplift at the centerline of the wall.

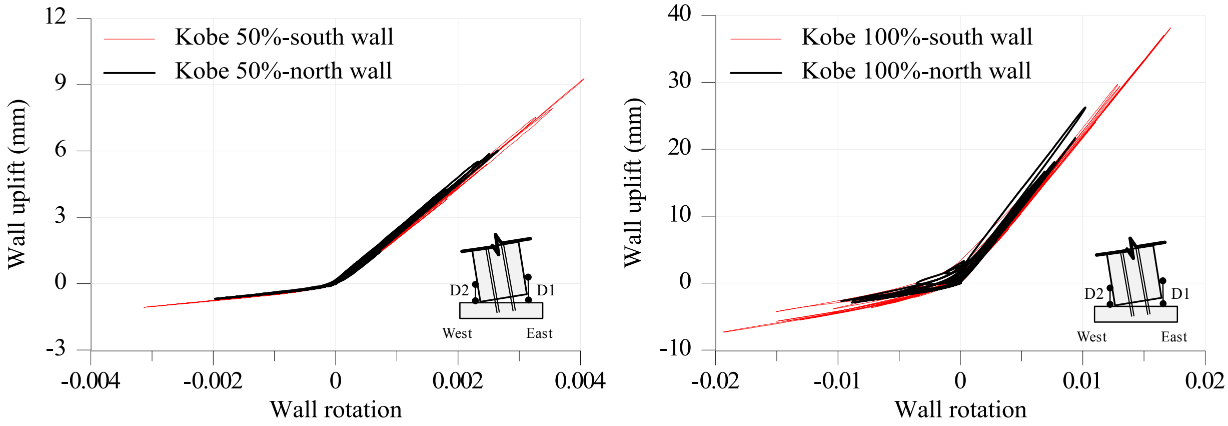

Figure 5-30 East end uplift (D1 measurements) of south and north UPT walls

Figure 5-31 shows the gap opening displacements along the base joint of the south wall at two instants during the 100%-Kobe record; the first (Figure 5-31a) corresponds to the instant of peak in-plane wall rotation (*t* = 20.1 s) and the second (Figure 5-31b) to the instant of peak out-of-plane wall rotation (*t* = 15.465 s). These instants have been previously identified on the 100%-Kobe response histories shown in Figure 5-29. In addition to the D1 and D2 measurements that represent uplift at the horizontal centerline of the wall, also plotted on each figure are the recordings from all available sensors at the base of the wall at the same instants. These include sensors SW, SE at the outer face of the wall, and sensors NW, NE, D3, D4, D5, and D6 at the inner face (Figure 5-25). Note that gauge lengths of these sensors vary from 250 mm (D1-D2), to 500 mm (D3, D4, D5, D6) and 1000 mm (SW, SE, NW, NE). While gap opening displacements (positive recordings from these sensors) are not likely to be affected by gauge lengths of sensors, concrete strains are obtained by dividing negative recordings from the sensors by their gauge length, so that caution should be exercised when interpreting negative vertical displacement measurements from sensors with different gauge lengths.

As shown in Figure 5-31(a), at the instant of peak in-plane wall rotation, differences between vertical displacement measurements at the inner and outer faces of the wall were not significant as out-of-plane wall rotation at that time was modest (0.83%). In contrast, as shown in Figure 5-31(b), differences between inner and outer face measurements at the instant of peak out-of-plane rotation (3.66%) were more pronounced and resulted in (i) the entire inner (north) face of the wall to uplift, and (ii) high, localized compressive strains to develop at the southwest corner of the wall. Note that sensor SW and the associated measurements shown in Figure 5-31, do not correspond to the corner of the wall but to the location of the SW sensor (outer face of wall, at a horizontal distance of approximately 500 mm from the corner). Concrete strains at the southwest corner of the wall are quantified in Section 5.6.4.

Results illustrated in Figure 5-31(b) are consistent with the out-of-plane rocking motion of the wall which was discussed in the previous section. Note that, in all cases, straight lines connecting the west end measurements (D2, NW, and SW) to the associated east end measurements (D1, NE, and SE) were drawn in Figure 5-31, i.e., a linear profile along the wall length is assumed. Recordings from sensors D3 to D6 provide a more accurate representation of the gap opening profile along the inner face of the wall. As evidenced by Figure 5-31(a), the gap opening profile constructed from D3 to D6 recordings is also essentially linear (profile in Figure 5-31(b) is also linear but this is associated with the entire face having uplifted). An examination of gap opening displacements at different instants during the 100%-Kobe and 50%-Kobe records revealed that wall base profiles tended to be more linear at larger wall rotations. Figure 5-32(a) shows gap opening profiles, constructed from D3-D6 recordings along the inner face of the south wall, at three instants during the 100%-Kobe history, corresponding to the first three peaks in D3 recordings. Figure 5-32(b) shows the gap opening profiles at the first three peaks in D3 recordings during the 50%-Kobe record. Uplift values and wall rotations for the 50%-Kobe record are smaller; and profiles tend to be less linear than the respective gap opening profiles under the 100%-Kobe record. Despite the observation that UPT wall base profiles are less linear at smaller rotations, for the purposes of calculating UPT wall base rotations, as discussed in Section 5.6.1, the assumption of a linear profile along the length of the wall appears to be satisfactory.

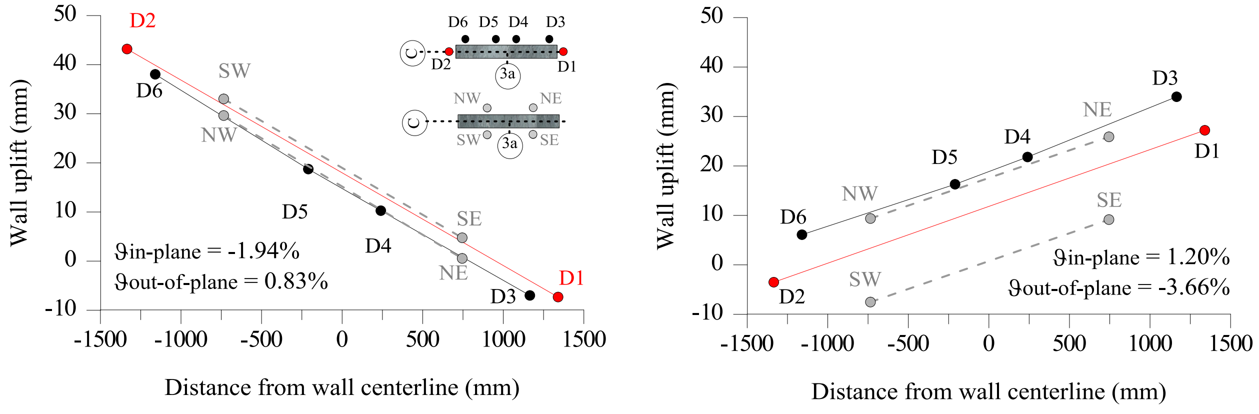

(a) **(b)**

Figure 5-31 Gap opening displacements at base of south wall for 100%-Kobe record: (a) at peak in-plane wall rotation; (b) at peak out-of-plane wall rotation

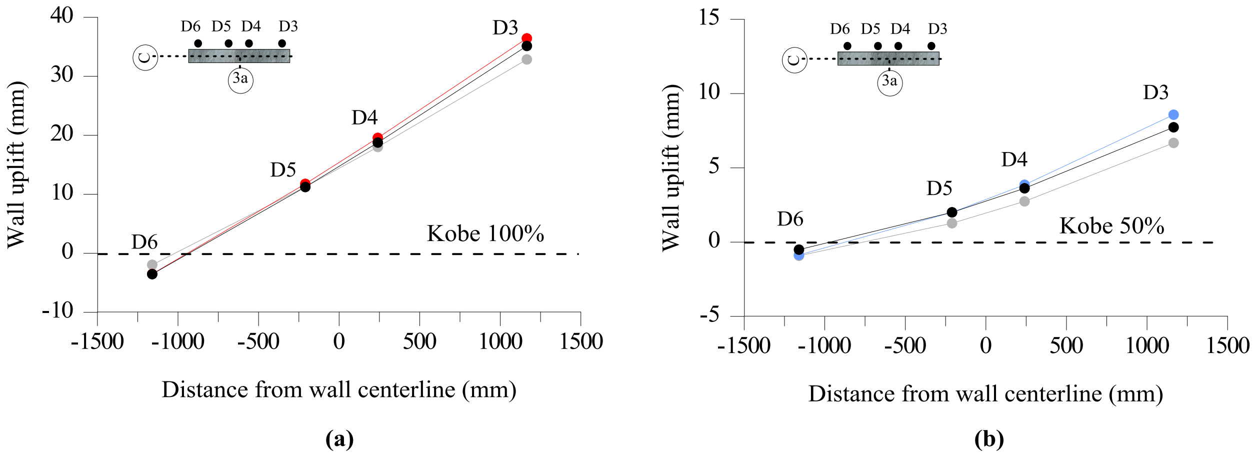

Figure 5-32 Gap opening displacements at base of south wall for (a) 100%-Kobe and (b) 50%-Kobe record

Discussion so far with respect to wall uplift has concentrated on gap opening displacements at the bases of the UPT walls, i.e. at the wall-to-foundation interface. It is also of interest to examine whether any gap opening occurred at the horizontal joints between the precast wall panels. Recall that, in discussing flexural design of upper joints of the E-Defense UPT walls in Section 4.6.2.2, the potential for uplift between the first and second story panel was identified as, at development of the nominal capacity at the base of the wall, the expected moment demand at the second floor joint exceeded the calculated decompression moment by approximately 2.5 times.

Sensors equivalent to D1 and D2, that measured uplift at the base of each wall (Figure 5-25), were not provided at the upper panel-to-panel joints. However, at the inner face of the north wall, the 2nd, 3rd and 4th story precast panels were instrumented with vertical sensors extending the entire story height (e.g., from top of 1st floor slab to bottom of 2nd floor slab for the second story panel) and at a close distance (approximately 85mm) from each wall edge (Figure 5-33). Recordings from these sensors were examined and found to be small throughout the tests (e.g., peak value from second story sensor during the 100%-Kobe record was 2.5 mm), indicating that there was no significant uplift at upper joints of the north UPT wall. Test videos from cameras providing close-up views of the joint between the first and second story panels of the north UPT wall also confirm this observation. Instrumentation similar to what was described for the north wall was not provided at the upper stories of the south UPT wall. However, the linear displacement profiles along the height of the wall presented in Section 5.4, and the large contribution (92% at peak response) of wall base rotation to wall roof drift ratio as discussed in Section 5.6.1, confirm that no significant uplift occurred at upper joints of the south UPT wall during the tests.

Figure 5-33 Instrumentation of 2nd story wall panel of north UPT wall

In Section 4.6.2.2, a simple criterion to assess whether uplift occurs at upper horizontal joints of UPT walls was presented, based on comparisons of decompression moment at upper joints ($M_{\text{dec,up}}$) to moment demands at these locations. Calculations of decompression moment and moment demands at upper joints were based on development of the flexural capacity at the base of the wall. It was suggested that uplift at upper joints is expected when moment demands there exceed $\kappa M_{\text{dec,up}}$. A value of $\kappa = 2.0$ was suggested based on prior research related to initiation of gap opening and nonlinear behavior at the base of UPT walls. It was also shown (Section 4.6.2.2) that, at development of the nominal capacity at the base of the E-Defense UPT walls, moment demands at the 2^{nd} floor joint were approximately 2.5 times the decompression moment, thus exceeding the suggested limit for $\kappa = 2.0$. Given that no significant uplift appears to have occurred at the upper joints of the E-Defense UPT walls during the test, further experimental and analytical studies are required to establish appropriate limits for κ, and more detailed design recommendations for upper joints of UPT walls. In the absence of additional experimental data, the recommendations presented in Section 4.6.2.2 will yield a conservative design.

Finally, it is worth pointing out that in all discussion related to gap opening at upper horizontal joints of the E-Defense UPT walls, the impact of the framing UPT beams has been neglected. Considering the mechanism shown in Figure 5-24, the beams on either side of the wall, transmit vertical beam shear forces to the wall. While the impact of beam shears on the axial load and moment capacity of the wall is expected to be small due to opposite signs on either side of the wall, beam shears may locally restrain gap opening at the uplifting side of the wall. Note that for eastward loading, as the west side of the wall uplifts, the reactions from the framing UPT beams on the west side of the wall act downward, and could thus prevent uplift. However, due to the connectivity of the precast members, these effects are not expected to be significant. For instance, uplift at the base of the 2^{nd} story panel is not likely to be affected by the vertical shear forces of the 2^{nd} floor UPT beams as the beams connect to the top of the 1^{st} story precast panel and reactions are only transferred to the 1^{st} story precast panel. Vertical shear forces from upper floor beams can have some impact on restraining uplift at the horizontal joint between the 1^{st} and 2^{nd} story panels, but such effects cannot be relied upon for design.

5.6.4 Wall concrete strains

This section examines the magnitude of concrete compressive strains that developed at the toes of the E-Defense UPT walls during the tests, and the variation of concrete strains with wall base rotation. Design implications and comparisons with predicted strains based on ACI ITG-5.2 are also discussed. Realistic estimates of peak concrete strains in UPT walls are essential in designing the transverse reinforcement at the base wall panel and ensuring that inelastic action due to high compressive forces at the base joint can develop in a ductile manner, without significant degradation in the concrete.

Concrete compressive strains at the wall toes of each UPT wall were computed using vertical displacement measurements from sensors D1 and D2 (Figure 5-25). As previously mentioned, measurements from D2 sensor at the west end of the south UPT wall were not reliable under the 100%-Kobe record. For the purposes of calculating wall rotations in Section 5.6.1, vertical measurements from sensors D3 and D6 at the inner face of the walls were used instead of D1 and D2, and it was shown that these provide reliable estimates of wall base rotations. For the purposes of calculating concrete strains at the wall toes, it was desirable to use measurements from sensors D1 and D2, as these are located close to the horizontal centerline of the wall and are not significantly affected by out-of-plane rotations. Calculated in this way strains result in meaningful concrete strain versus (in-plane) rotation plots, and can be directly compared with predicted strains based on ACI ITG-5.2, which does not consider demands from wall out-of-plane rotations.

Using vertical displacement measurements from sensor D1 at the east end of the south wall and the calculated south wall base rotations presented in Section 5.6.1, it was possible to estimate the vertical displacements at the location of sensor D2 during the 100%-Kobe record.

The estimated D2 vertical displacements are plotted in Figure 5-34(a) together with the measured D1 and D2 displacements. As evidenced by the figure, estimated D2 displacements are in good agreement with measured D2 values, at all instants when the latter were reliable. Using the negative measured D1 and estimated D2 values, adjusted to account for the small distance (85mm) of the sensors from the wall edges, and dividing by the 250 mm gauge length of the sensors, the concrete strains at the east and west ends of the south wall were computed and are shown in Figure 5-34(b). Peak concrete strains at the east and west ends of the south UPT wall during the 100%-Kobe record were 0.023 and 0.025, respectively. The histories of in-plane and out-of-plane wall rotations are also shown for reference in Figure 5-34(c). Figure 5-35 plots the calculated wall concrete strains at the base of the south wall against the (in-plane) rotation of the wall. As observed from the figure, beyond wall rotations of approximately 1.0%, concrete strains were higher at the west end of the wall. This is also consistent with damage observations, as shown in Figure 5-14, where concrete spalling was more severe at the west end of the wall. At a wall base rotation of 1.5%, the concrete strains at the west end were approximately 20% higher than east end strains at the same rotation.

Figure 5-36 and Figure 5-37 present for the north UPT wall, the same results that were presented in Figure 5-34 and Figure 5-35 for the south wall. Note that all D1 and D2 measurements were reliable for the north wall under the 100%-Kobe record. Peak concrete strains at the east and west ends of the north UPT wall during the 100%-Kobe record were 0.0085 and 0.008, respectively. These values are 37% and 32% of the peak strains calculated for the east and west end of the south wall, respectively.

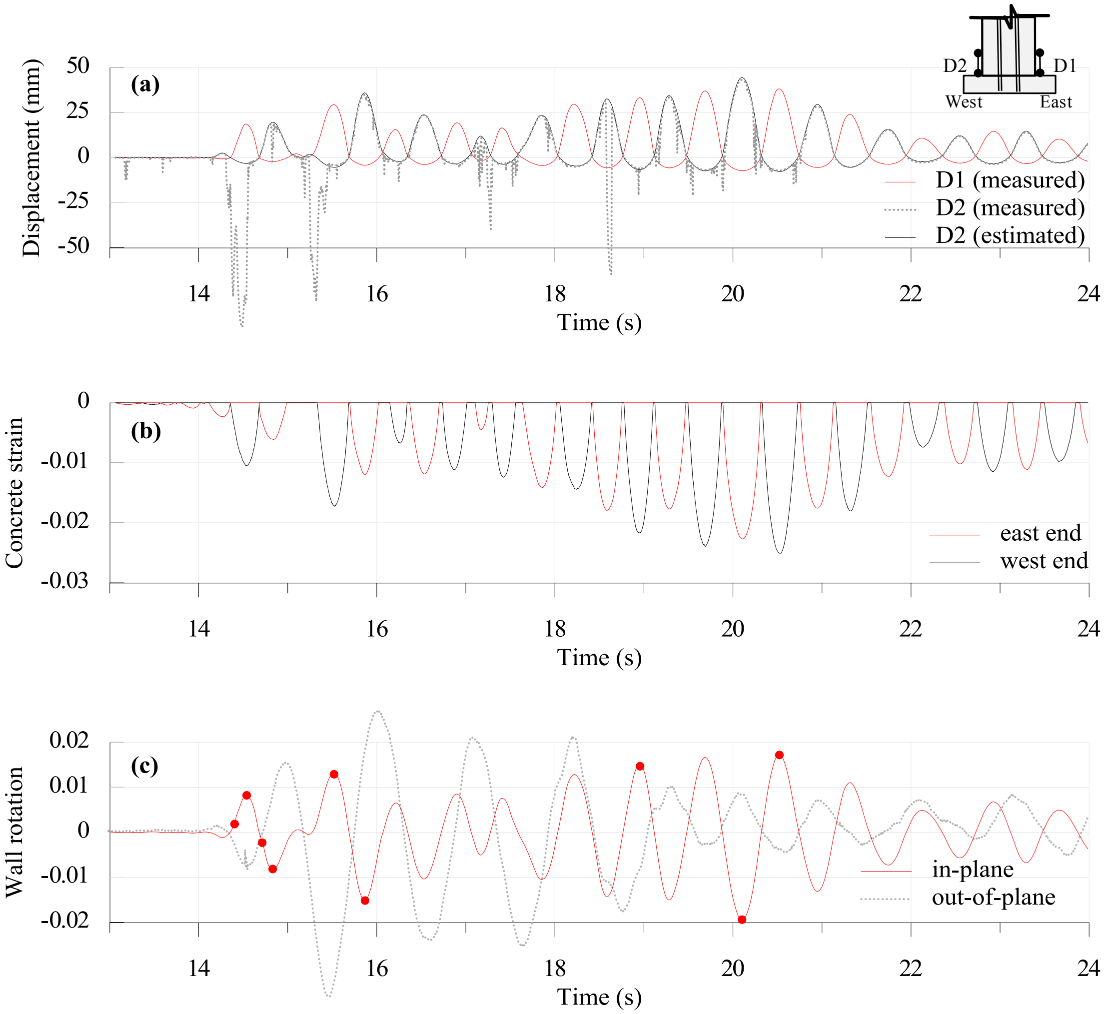

Figure 5-34 South wall response histories under 100%-Kobe record: (a) vertical displacement measurements D1, D2, (b) concrete strains at east and west ends, and (c) wall base rotations

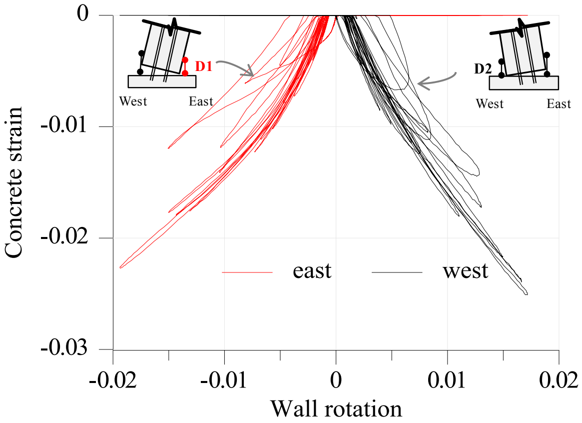

Figure 5-35 Concrete strains at base of south wall plotted against wall rotations for 100%-Kobe record

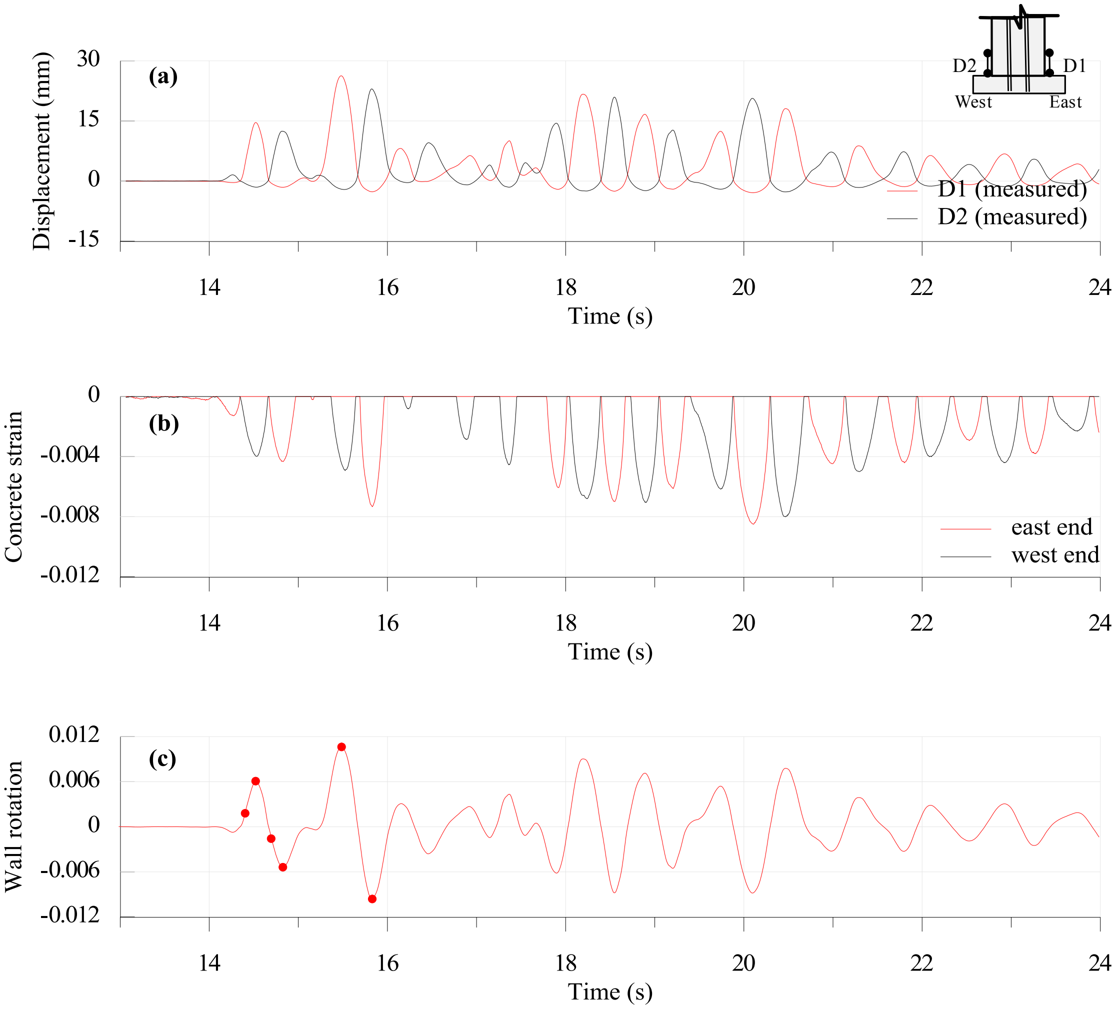

Figure 5-36 North wall response histories under 100%-Kobe record: (a) vertical displacement measurements D1, D2, (b) concrete strains at east and west ends, and (c) wall base rotations

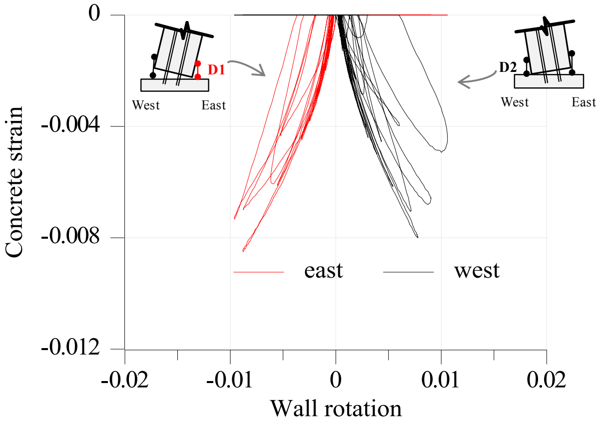

Figure 5-37 Concrete strains at base of north wall plotted against wall rotations for 100%-Kobe record

Section 4.6.6 discussed concrete confinement requirements for UPT walls according to ACI ITG-5.2. Design of confining reinforcement in ACI ITG-5.2 is based on an estimate of the peak concrete strain at $\theta_{\max}$: $\varepsilon_{c,\max} = \theta_{\max}c/L_p$, where c is the neutral axis depth and $L_p = 0.06H_w$, where H_w is the wall height. This expression predicts a peak strain of 0.0087 at $\theta_{\max} = 3.0\%$ for the E-Defense UPT walls. Comparing this strain with the peak measured strains of the north and south UPT walls during the 100%-Kobe record, it can be observed that (i) the north wall developed similar strains (peak strain 0.0085) but at significantly smaller base rotations (peak rotation 1.02%) and (ii) the south wall developed significantly higher concrete strains (approximately 2.5 times higher). While recognizing that the large strains in the south UPT wall during the experiment could also be related to grout crushing, which generally would have been avoided (or limited) had the grout included fiber reinforcement (as required by ACI ITG-5.2), the under-predictions of concrete strains by the ACI ITG-5.2 equation ($\theta_{\max}c/L_p$, with $L_p = 0.06H_w$) warrant a re-examination of the expression for L_p used in defining concrete strains in UPT walls. Note that similar observations have been made for the Lehigh test walls discussed in Sections 3.1.2.1 and 3.1.3.1. Pending additional experimental validation, it is recommended herein that $H_{cr} \leq (1.5t_w, c)$ be used instead of the plastic hinge length $L_p = 0.06H_w$ for estimating concrete strain demands in UPT walls. Selection of appropriate limits for H_{cr} was discussed in Section 3.1.2.1. Using H_{cr} in place of L_p, the estimated peak concrete strain for the E-Defense UPT walls (H_{cr} = c = 208mm) would be 0.03 at $\theta_{\max} = 3.0\%$. Finally, related to the issue of confining reinforcement, it is noted that strain measurements were available for the fourth hoop up from the base of the south wall from a single strain gauge that was glued on the exterior hoop at the east end of the south UPT wall and at a height of 320 mm from the base of the wall. Peak recorded strain values from this strain gauge (0.00024), summarized in Table 5-1, were significantly lower than the yield strain of the high strength 13-mm-diameter hoop ($\varepsilon_{yt} = 0.0047$), verifying that inelastic demand was limited to a short distance from the base of the wall (<320 mm).

Discussion so far with respect to concrete strains has concentrated on strain demands at the ends of the wall, close to the horizontal wall centerline (sensors D1 and D2 in Figure 5-25). As was suggested in Section 5.6.3, out-of-plane rotations of the wall likely resulted in some localized higher strains at the corners of the walls. These increases are quantified in the discussion that follows. At the instant of peak out-of-plane rotation in the south wall (t = 15.465 s, θ_{out} = 3.66%, Figure 5-34c) the concrete strain at the west end of the south wall, close to the horizontal centerline, was 0.0152 - which is the value plotted in Figure 5-34(b) at t = 15.465 s. Considering the out-of-plane rotation of 3.66%, the strain at the southwest corner of the wall at the same instant can be estimated as $0.0152 + 3.66\%(t_w/2)/L_{gauge}$, where t_w = 250 mm is the wall thickness and L_{gauge} = 250 mm is the gauge length of sensor D2 that was used to calculate the concrete strain of 0.0152 at the wall centerline. This results in a peak concrete strain of 0.034 at the southwest corner of the wall, which is approximately 2.2 times higher than the concrete strain at the west end at the same instant (0.0152 at t = 15.465 s) and 1.35 times higher than the peak concrete strain at the west end of the south wall during the 100%-Kobe record (0.025 at t = 20.525 s). In a similar way, the concrete strains at the southwest (and northwest) corners of the wall can be estimated at each instant during the 100%-Kobe record. Results from these calculations, in terms of histories of concrete strains at southwest and northwest corners of the south wall, are illustrated in Figure 5-38(a). As expected, differences between strains at the wall corners and strains close to the horizontal centerline of the wall are more pronounced at instants when both in-plane and out-of-plane rotations are large. Note that based on the sign convention used herein, positive in-plane wall rotations cause compression at the west end of the wall and tension (uplift) at the east end; while positive out-of-plane rotations cause compression at the inner (north) face of the wall and tension at the outer (south) face of the wall.

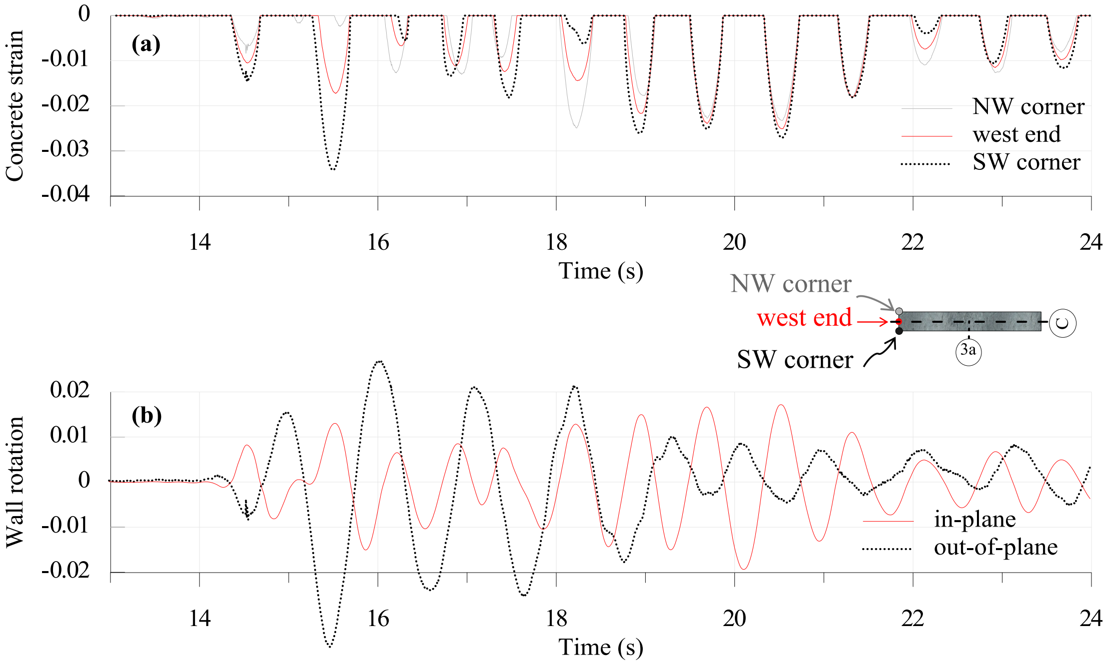

Figure 5-38 South wall response histories under 100%-Kobe record: (a) concrete strains at wall corners and (b) wall base rotations

Finally, given that selection of limits for H_{cr} in Section 3.1.2.1 was based on the assumption that inelastic deformations in UPT walls are limited to a short distance from the foundation, it was also of interest to examine the magnitude of concrete strains above the base in the E-Defense UPT walls. To this end, concrete strains were calculated using measurements from sensors D7 and D8 (Figure 5-25). Note that these sensors were attached to the inner (north) face of the south UPT wall, at a vertical distance of 500 mm above the base and had a gauge length of approximately 500 mm. Figure 5-39 compares, for the 100%-Kobe record, concrete strains derived from sensor D8 to concrete strains from sensor D6, which was located right below it (Figure 5-25). Comparisons between concrete strains from sensors D7, D8 and concrete strains from sensors D3, D6 (Figure 5-25) are meaningful as both sets of sensors (i) were located at the inner face, (ii) had a gauge length of 500 mm and (iii) were located at the same horizontal distance from the wall edges. Sensors D3, D6 provide estimates of average concrete strains over the bottom 500 mm from the base, while sensors D7, D8 provide estimates of average concrete strains over the wall height between 500 mm and 1000 mm from the base. As evidenced by Figure 5-39, concrete compressive strains from sensor D8 are significantly smaller than concrete strains from sensor D6: peak concrete strain from D6 is approximately 0.015, while peak strains from sensor D8 are smaller than 0.001. These observations, which are also consistent with observed damage in the south UPT wall (Figure 5-14), verify that inelastic concrete strains were concenterated over a short vertical distance from the base of the wall, smaller that two times the thickness of the wall ($2t_w$ = 500 mm).

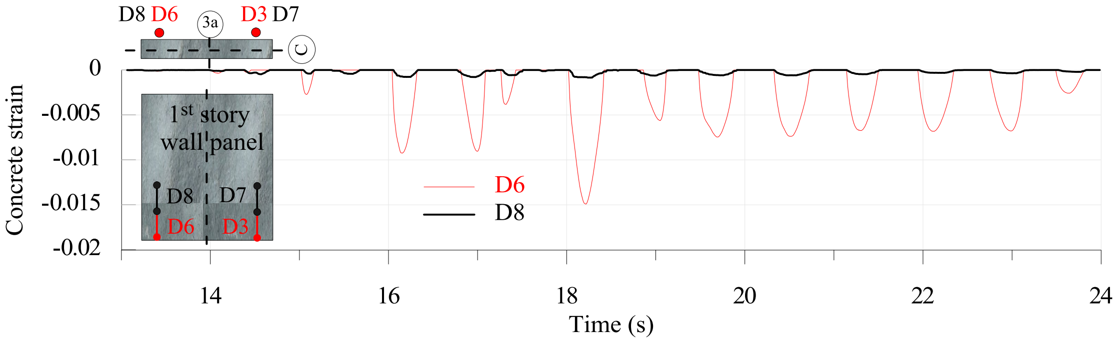

Figure 5-39 Concrete strain response histories at inner face of south wall under 100%-Kobe record

5.6.5 PT forces

Instrumentation of the south UPT wall included load cells that measured forces in the vertical post-tensioning steel of the wall. Figure 5-40 shows the variation of PT stresses in each of the two tendons of the south wall during the 50%-Kobe, 100%-Kobe, 40%-Takatori and 60%-Takatori records. Stresses were normalized with respect to the yield stress of the post-tensioning steel (f_{py}=1777 MPa) and plotted against the south wall rotations for each record. The dashed horizontal line corresponds to the initial prestress. At the maximum wall rotation during the tests (1.94% for both the 100%-Kobe and 60%-Takatori records), the PT stress increased by 32% but remained below the yield stress, so that at the end of the test, denoted by the symbol (•) on the plots, no prestress losses occurred. Table 5-1 summarizes peak PT stresses of the south UPT walls for all records. With respect to the 60%-Takatori plot, the apparent increase in PT stresses at (and close to) zero rotations compared to the initial prestress, is the result of large wall out-of-plane rotations that caused some elongation of the PT steel despite the small in-plane wall rotations.

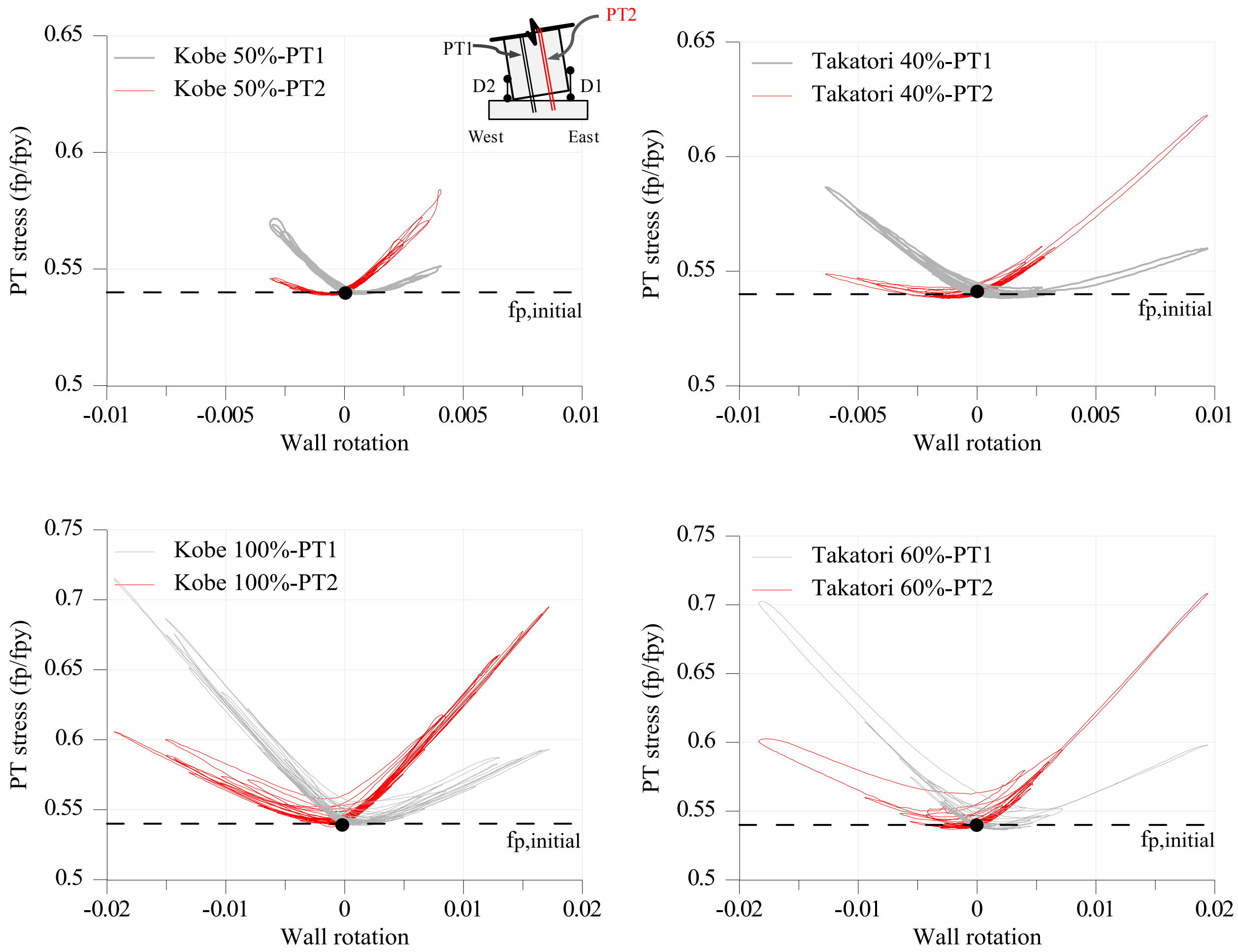

Figure 5-40 Variation of PT stresses in south UPT wall

As discussed in Section 4.6.4, the post-tensioning steel in the test walls was located at 15% of the wall length on either side of the centroid, exceeding the ACI ITG-5.2 limit of 10%. The intent of the limit is to delay yielding of the PT steel, by limiting elongation due to gap opening. Moreover, it allows the two groups of PT steel on either side of the wall centroid to be conveniently lumped at the centroid for design purposes. Based on the performance of the test walls, an increase of the ACI ITG-5.2 limit may be justified provided the exact locations of PT steel are accounted for in the design. This would allow applicability of ACI ITG-5.2 to a wider range of UPT wall configurations, and even extension to non-planar walls pending experimental validation. As evidenced by the test, yielding of the PT steel can be effectively controlled through appropriate selection of initial prestress and consideration of the exact location of the PT steel in the design process.

5.6.6 Wall neutral axis depth

The neutral axis depth, or contact depth, at the base of each UPT wall during the 100%-Kobe record was estimated using the vertical displacement measurements at wall ends (D1, D2) and the calculated wall base rotations (shown in Figure 5-34 and Figure 5-36 for the south and north wall, respectively). The neutral axis depth values are used in the following section to estimate wall base moments.

Neutral axis depth calculations were based on the assumptions of linear profile at the base of the wall and rotation occurring about the neutral axis. As discussed in Section 5.6.3, the assumption of a linear profile at the base of the wall was generally found to be satisfactory, especially at larger wall base rotations. At smaller rotations, and for non-planar profiles, the linear profile assumption likely underestimates the actual neutral axis depth (Figure 5-32).

Figure 5-41 shows the variation of neutral axis depth with wall base rotation in the south and north UPT walls during the 100%-Kobe record (grey points in figure). Using selected data points from the 100%-Kobe response history, the "envelopes" represented by the dashed lines in Figure 5-41 were obtained. The discrete data points from the 100%-Kobe history that were used to construct the "envelopes" of Figure 5-41 are denoted by the symbol (●) on the rotation histories of the south and north wall shown in Figure 5-34(c) and Figure 5-36(c), respectively. These points include in each direction: instant when rotation of 0.2% was first reached during the 100%-Kobe response history, first two peaks during the 100%-Kobe response history and additional points for the south wall to include instants of peak rotation in each direction.

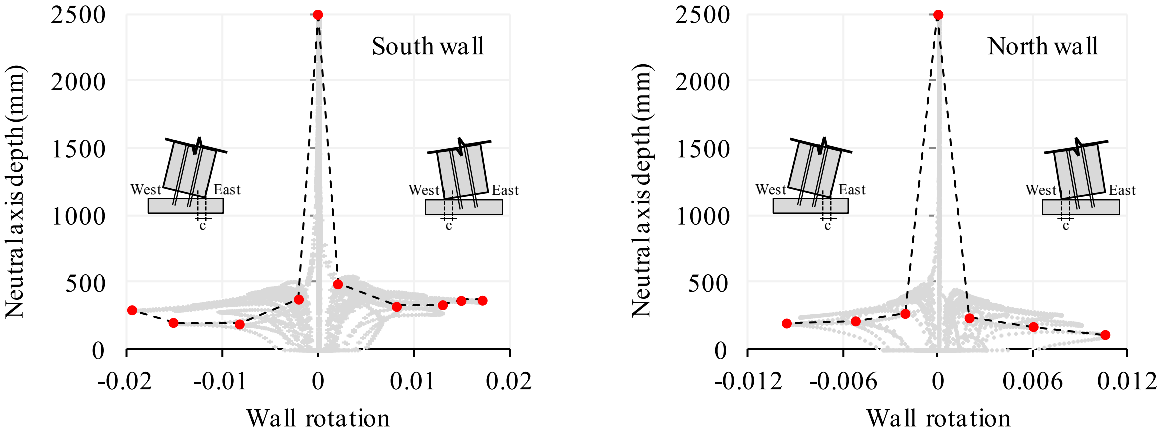

Figure 5-41 Variation of wall neutral axis depth with wall base rotation

Comparing the neutral axis depth values of the south and north UPT walls, it can be observed that larger values were generally obtained for the south wall. The increased neutral axis depth in the south wall is likely associated with grout crushing and concrete spalling that occurred at the base of the south wall during the 100%-Kobe record (Section 5.3). Note that when calculating the probable flexural strength (M_{prob}) of the E-Defense UPT walls in Section 4.6.2.1, the neutral axis depth at $\theta_{\max}$ was found equal to c = 208 mm. ACI ITG-5.2 assumes the neutral axis depth to remain constant as rotation at the base of the wall increases from θ_{design} to θ_{max}, that is, for design purposes, the neutral axis depth can be assumed constant and equal to 208 mm from $\theta_{\text{design}} = 0.95\%$ to $\theta_{\text{max}} = 3.0\%$. Results presented in Figure 5-41 show that the south wall neutral axis depth exceeded the design neutral axis depth $c = 208$ mm by up to 75%. North wall neutral axis depth values shown in Figure 5-41 are in closer agreement with the design neutral axis depth. Finally, it should be noted that neutral axis depth values illustrated in Figure 5-41 should be thought of as average values since, due to out-of-plane wall rotations, concrete strains varied along the thickness of the wall (Figure 5-38).

5.6.7 Wall base moments

Instrumentation of the test building (e.g., accelerometers on the floor slabs) allowed global force responses, such as total base shear and global overturning moment, to be calculated in each principal direction of building response. These results have been presented in Sections Chapter 5 and 5.5 for the wall direction of building response. Instrumentation attached to the walls also allowed direct measurements of wall deformation responses, such as gap opening displacements and wall base rotations. However, wall force responses, such as wall base moments, can only be indirectly extracted from the experimental measurements.

In this section, previously reported experimental data (e.g. wall rotations, wall neutral axis depth, PT forces) are used to estimate wall moments at the bases of the two UPT walls of the test building. These are referred to as "the experimental wall moments" hereafter. The objectives of these calculations are: (i) to compare experimental moments of the south and north UPT walls, (ii) to compare experimental wall moments to the nominal and probable wall moment capacities calculated in Section 4.6.2.1 and (iii) to isolate wall responses from the global response of the building and assess the contribution of wall moments to the measured global overturning moment of the building.

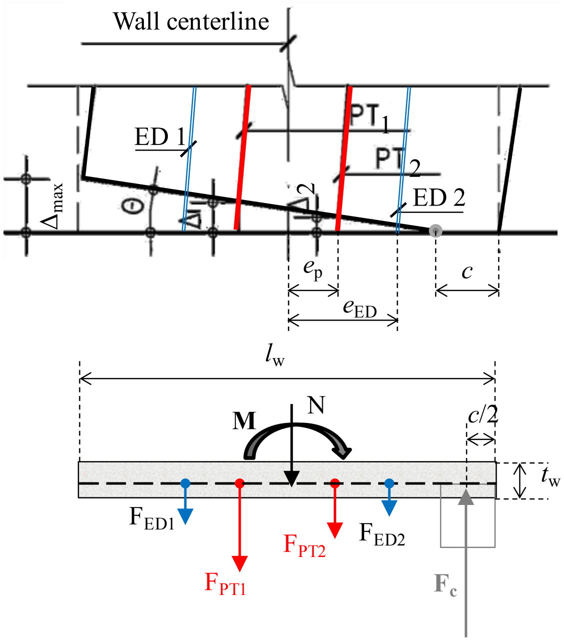

$$F_{PT1} + F_{PT2} + F_{ED1} + F_{ED2} + N = F_c$$

$$M = (F_{PT1} - F_{PT2})\, e_p + (F_{ED1} - F_{ED2})\, e_{ED} - F_c\, (l_w - c)/2$$

Figure 5-42 Calculation of UPT wall base moment

Using the wall base rotations and neutral axis depth estimates presented in the previous sections (5.6.1 and 5.6.6), the elongation of the post tensioning steel and energy dissipating bars due to uplift at the base of each wall was calculated. For instance, with reference to Figure 5-42, for a given wall base rotation θ and neutral axis depth c, the elongation in PT_1 was calculated as $\Delta_1 = \theta\ (l_w/2\text{-}c\text{+}e_p)$, where e_p is the distance of the PT bar from the wall centerline. In a similar way, elongations in both PT and ED (energy dissipating) bars were computed. By distributing these elongations over the unbonded lengths and adding any initial strain due to the prestress, the total strain and corresponding forces in the PT and ED steel were estimated. Note that for the south UPT wall, for which PT force measurements were available, the experimental values were used instead of the estimated PT forces (differences between experimental and estimated PT forces were in all cases smaller than 4.0%). With all forces on the wall base section defined, equilibrium equations were used to calculate the wall base moment as shown in Figure 5-42. Note that the concrete compressive force F_c, which balances the axial load and sum of forces in the PT and ED steel, was assumed to act at $c/2$ from the extreme compression fiber. Given the approximations related to calculation of the neutral axis depth c itself, as described in Section 5.6.6 (e.g., linear profile assumption, effect of out-of-plane rotations), this assumption is deemed satisfactory for the purposes considered herein.

Following the procedure described above for discrete instants during the 100% Kobe response history, the wall response envelopes shown in Figure 5-43 were obtained. These represent the envelopes of experimental wall base moments. Consistent with the observation of higher concrete strains (Section 5.6.4) and larger neutral axis depth (Section 5.6.6) at the base of the south UPT wall compared to the north wall, results in Figure 5-43 show that base moments were smaller in the south UPT wall (approximately 18% at 1.0% wall roof drift ratio). Despite the assumptions involved in calculating the experimental wall moments, results in Figure 5-43 indicate that the different degrading behaviors at the base joints of the two UPT walls during the test ultimately resulted in strength eccentricity in the building that explains the observed torsional response (Section 5.4).

The nominal and probable moment capacities of the E-Defense UPT walls according to ACI ITG-5.2 were calculated in Section 4.6.2.1. The nominal moment strength at $\theta_{design} = 0.95\%$ was found equal to $M_n = 5072$ kNm, and the probable moment strength at $\theta_{max} = 3.0\%$ was equal to $M_{prob} = 6626$ kNm. Comparing these values with results in Figure 5-43 it can be observed that the nominal moment, M_n, is in good agreement with the experimental moment of the north wall at a roof drift ratio of 1.0%. The south wall experimental moment at 1.0% roof drift ratio is 13% lower than the calculated nominal moment. This is associated with grout crushing and concrete cover spalling that occurred at the base of the south UPT wall, and is not reflected in M_n calculations.

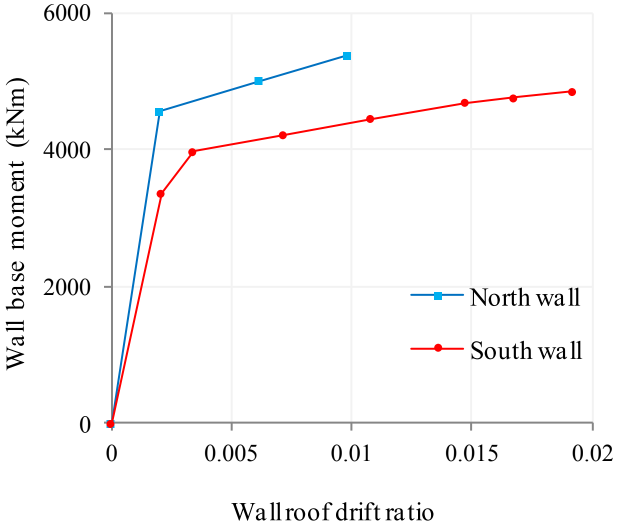

Figure 5-43 Estimates of north and south wall base moments

Finally, it is also of interest to compare the sum of the experimental wall moments to the peak measured global overturning moment of the building in the wall direction of response. Recall that the two UPT walls in the building were designed to resist the entire base shear and overturning moment in the wall direction of response. The peak global overturning moment (25,850 kNm) was obtained during the 100%-Kobe record and corresponds to peak A in Figure 5-6. At that instant the south wall roof drift ratio was 1.45% while the north wall roof drift was 1.00% (Figure 5-28). The sum of experimental wall moments at these drifts corresponds to only 40% of the peak global overturning moment, indicating that in addition to the wall, other sources also added to the lateral resistance of the building. In Section 5.5, these sources were identified as the framing action resulting from coupling of the walls to the corner columns through the UPT beams, the moment resistance at the bases of columns, and the contribution of the intermediate one-bay moment frame. Analytical studies presented in a Chapter 6 quantify, by means of a nonlinear model of the building, the relative contributions of these sources to global moment resistance of the building in the wall direction of response.

5.7 Slab deflections

The displacement transducers that extended vertically from the foundation beam (first floor) to the second floor were used to measure slab deflections. The sensors (S1-S14) were arranged close to the south wall along longitudinal and transverse lines as shown in Figure 5-44.

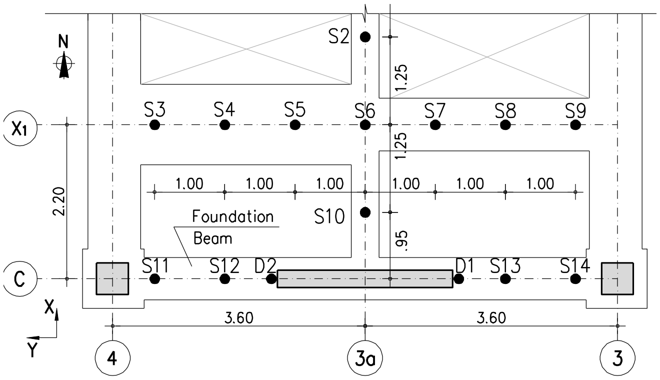

Figure 5-44 Instrumentation in second floor slab (dimensions in m)

Figure 5-45(a) plots the slab displacement profiles along axis C (sensors S11-S14) and X1 (sensors S3-S9) at the instant of peak in-plane rotation at the base of the south wall for the 100%-Kobe record (*t* = 20.1 s). This instant coincided with the time of peak wall uplift recorded by sensor D2 at the base of the wall. Assuming that uplift at the base of the wall caused an equal vertical displacement of the wall-to-slab connection at the second floor, measurements from wall sensors D2 and D1 were included in the slab displacement profile along axis C.

The slab profile along axis C shows a large displacement gradient between the wall-to-slab connection, where the slab was constrained to uplift with the wall and the edge of the building where the slab was constrained to the columns, which did not sustain significant vertical displacements. Similarly, in the orthogonal direction, the large vertical displacement of the slab close to the uplifting end of the wall reduced rapidly away from the wall so that at a distance approximately equal to the wall length (axis X1), slab displacements were negligible. Due to displacement response in the moment frame direction of response, slab displacements along axis X1 at different instants were not negligible. Figure 5-45(b) plots the slab displacement profiles along axis C (sensors S11-S14) and X1 (sensors S3-S9) at the instant of peak out-of-plane rotation at the base of the south wall for the 100%-Kobe record (*t* = 15.465 s).

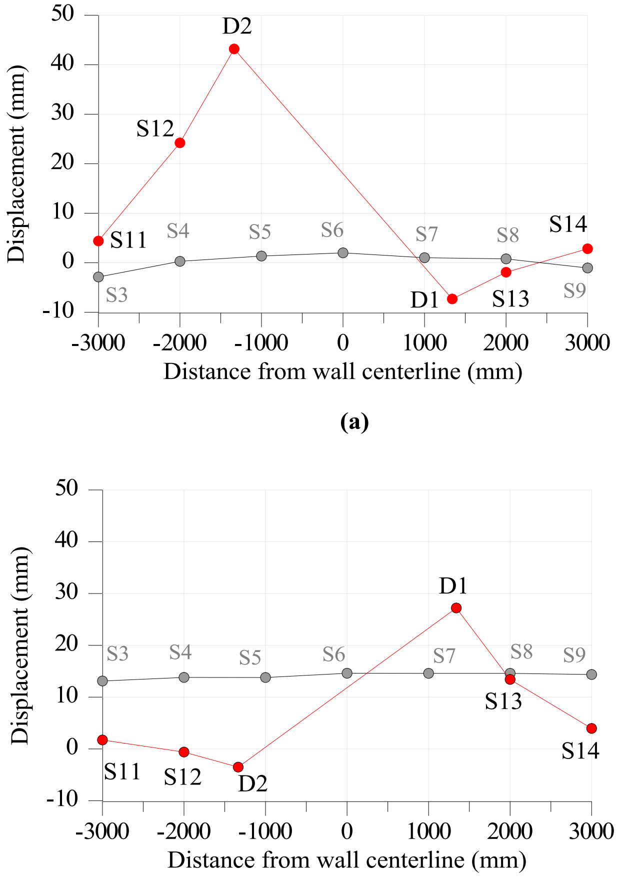

(a)

(b)

Figure 5-45 Second floor slab displacement profiles for 100%-Kobe record: (a) at peak in-plane wall rotation; (b) at peak out-of-plane wall rotation

5.8 Beam responses

The top and bottom faces of the east UPT beams of Frame C (south frame) were instrumented with horizontal displacement transducers at their ends with a gauge length of 750 mm. These sensors allowed rotations, axial growth and neutral axis depth to be estimated for all instrumented beams. Calculations assumed a linear deformation profile along the height of the beam and accounted for the exact locations of the sensors reported in Nagae et al. 2011. Results are presented here for the east end of the third floor UPT beam of Frame C, under the 100%-Kobe record.

Figure 5-46 presents the calculated axial growth at beam mid-height, plotted against the calculated beam rotations. These results allow calculation of axial growth, or gap opening, at any location along the 300 mm height of the beam. For instance, at -3.0% beam rotation (tension at bottom), the gap opening at the bottom of the beam at the beam-to-column interface was approximately 3mm+0.03(150mm) = 7.5 mm. The relatively small axial growth values and unsymmetrical behavior (smaller gap opening for positive rotations) indicate that beam boundary conditions and the presence of the slab likely restrained gap opening from occurring at beam ends. Results of calculated beam neutral axis depths presented in Figure 5-47, confirm the observation that behavior of UPT beam was affected by the presence of the slab and also show an unsymmetrical behavior. While for negative beam rotations (tension at bottom), the neutral axis was approximately at the center of the 100-mm cast-in-place slab, for positive rotations (tension at top), a large portion of the beam was under compression ($c \approx 0.3h$) indicating that axial restraint from the slab likely induced compressive axial forces to develop in the UPT beams. Such interactions between the UPT beams and the slab, and their impacts on beam flexural capacities will be further discussed in Chapter 6.

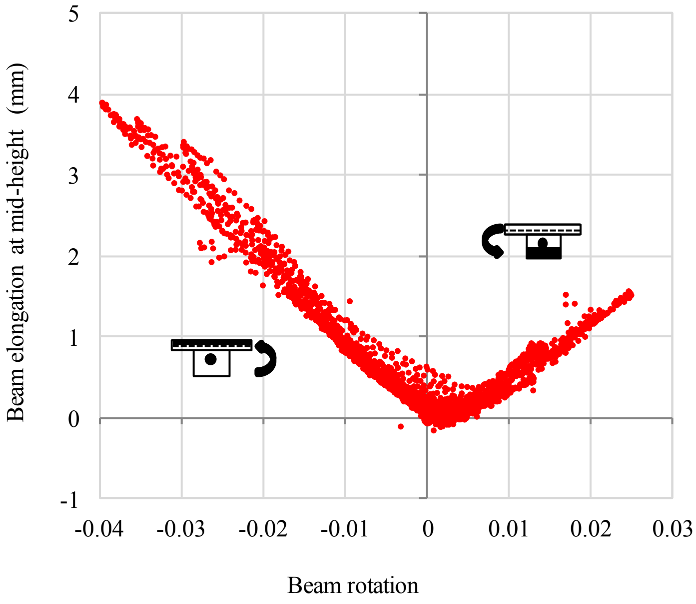

Figure 5-46 Beam elongation at east end of 3rd floor UPT beam of Frame C under 100%-Kobe record

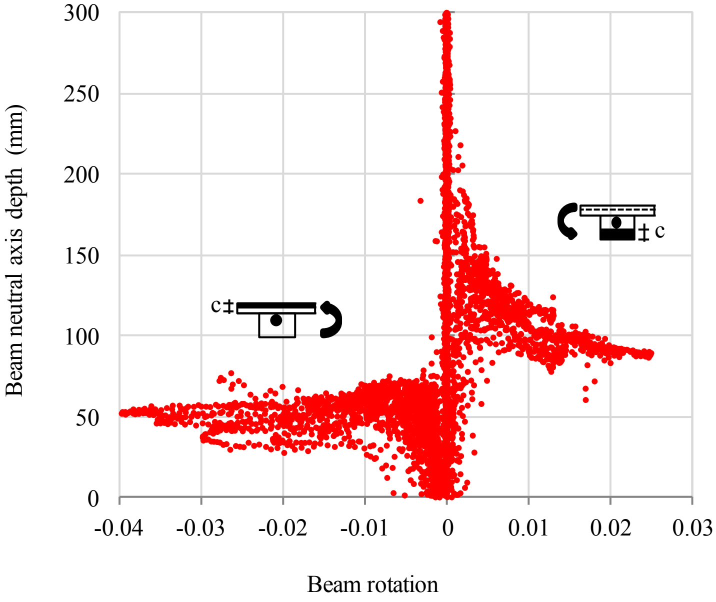

Figure 5-47 Beam neutral axis depth at east end of 3rd floor UPT beam of Frame C under 100%-Kobe record

5.9 Summary and design implications

Performance of the test building in the wall direction was very satisfactory. Response for the 25% and 50%-Kobe records was essentially elastic, with no visible damage; during the higher intensity 100%-Kobe and subsequent Takatori records, damage to the UPT walls was limited to grout crushing and concrete spalling at the base of the south wall. Apart from this localized and repairable damage, no cracking developed at the upper portion of the walls. The UPT beams also behaved as intended, with only localized concrete spalling adjacent to the joints. The bonded post-tensioned columns suffered more damage; however, this was very likely associated with the moment frame direction of response, not examined in this work.

Overall response of the test building in the wall direction was dominated by gap opening at the bases of the UPT walls (rocking), with displacement profiles along the height of the building being almost linear. The peak roof drift ratio during the tests was equal to 1.58% at the center of plan, while residual drift at the end of the tests was minor (on the order of 0.1%). Calculated peak displacements for the south and north UPT walls differed from the center of plan displacement due to torsional response. Peak wall roof drift ratios were equal to 1.07% for the north wall, and 2.09% for the south wall. Both UPT walls achieved the ACI ITG-5.2 design drift, $\theta_{\mathrm{design}} = 0.95\%$, and in addition, the south wall was displaced to approximately 70% of the maximum ACI ITG-5.2 drift, $\theta_{\max} = 3.0\%$. Despite their large magnitude, out-of-plane drifts in the moment frame direction, did not adversely affect the in-plane behavior of the UPT walls, as they were largely accommodated by out-of-plane rocking of the walls against the foundation.

The experimental program documented herein provided a wealth of data for validation of ACI ITG-5.2 design provisions. A detailed assessment of the E-Defense UPT wall design based on ACI ITG-5.2 design requirements was presented in Section 4.6. Based on the performance of the two UPT walls during the tests presented in this chapter, the following paragraphs present design implications that were identified.

The post-tensioning steel in the E-Defense UPT walls was located at 15% of the wall length on either side of the wall centroid, exceeding the ACI ITG-5.2 limit of 10%. Based on the performance of the walls in the test (south wall reached 1.94% base rotation without yielding of PT steel, no prestress losses and no residual deformations), a relaxation of the 10% limit may be justified. This would allow applicability of ACI ITG-5.2 to a wider range of UPT wall configurations, and even extension to non-planar walls pending experimental validation. As evidenced by the test, yielding of the PT steel can be effectively controlled through appropriate selection of initial prestress and consideration of exact locations of PT steel in the design process.

Peak measured concrete compressive strains at the ends of the north and south UPT walls during the tests were 0.0085 and 0.025, respectively; with corresponding peak base rotations of 1.02% and 1.94%, respectively. For the purposes of designing the confining reinforcement at the wall toes, ACI ITG-5.2 assumes, constant strain over an equivalent plastic hinge length $L_p = 0.06H_w$ (where H_w is the wall height), so that $\varepsilon_{c,max} = \theta_{max}c/L_p$, where c is the estimated neutral axis depth at θ_{max}. This assumption resulted in an estimated strain of $\varepsilon_{c,max} = 0.0087$ at $\theta_{max} = 3.0\%$ for the E-Defense walls. Noting that the north wall developed similar strains at a wall rotation of only 1.02%, and that peak strain in the south wall was almost three times the estimated by ACI ITG-5.2 $\varepsilon_{c,max}$, a reexamination of the expression for the equivalent plastic hinge length for UPT walls L_p is warranted. It was suggested herein that, instead of L_p, which appears more appropriate for conventional RC walls, a height $H_{cr} \leq (1.5t_w, c)$ be used for estimating strain demands on UPT walls. H_{cr} represents the height above the base over which nonlinear behavior of the concrete in compression is expected to extend. Recommended limits for H_{cr} were based on review of prior experimental results of UPT walls, and were also shown to provide good estimates of peak strains for the E-Defense walls (0.03 strain at $\theta_{\mathrm{max}} = 3.0\%$).

The marked difference in performance of the two UPT walls in the test building emphasizes that behavior of UPT walls is largely dependent on the ability of the critical base joint to sustain large local compressive strains in a ductile manner, without significant degradation of concrete or grout. Lack of fiber reinforcement in the grout at the wall-foundation interface of the south UPT wall adversely affected the performance of the wall and validated the appropriateness of the ACI ITG-5.2 requirement for a minimum amount of fiber reinforcement in the grout. In contrast, inclusion of fiber reinforcement in the concrete mix of the north wall panels (in addition to the interface grout), although not required by ACI ITG-5.2, resulted in excellent performance and only minor cosmetic damage in the north UPT wall.

Chapter 6 Analytical studies of four-story precast PT building

Building on the information presented in the previous chapters, the development and experimental verification of a nonlinear analytical model in the wall direction of the four-story, precast post-tensioned building that was tested on the E-Defense shake table is presented herein. The modeling approaches implemented for different components are described, and comparisons between analytical and experimental results are presented for a range of global and local responses including story lateral displacements, story shear forces and moments, and gap opening due to rocking at the wall base. In addition to validating the proposed computational model, the analyses allow investigations of system interactions such as framing action resulting from coupling of the UPT walls to the corner columns through the UPT beams, and interactions of the UPT beams with the floor system. Together with the experimental results, the analyses provide valuable insight into the dynamic responses and interactions of a full-scale, three-dimensional UPT building.

6.1 Model development

As experimental investigations on dynamic behavior and interactions of UPT systems are limited to-date, the 2010 E-Defense shake-table tests on the four-story, precast post-tensioned building that were documented in the previous chapters, provide unique data against which analytical models for UPT systems can be benchmarked. In addition to validating the proposed computational model, the analyses provide insight into system interaction issues that are typically not addressed in component-level analytical and experimental studies.

This section describes the development of a nonlinear analytical model of the test building. Although the building was subjected to simultaneous multidirectional shaking (x, y, z), this study focuses solely on the response in the direction that utilized UPT systems (y-direction in Figure 6-1). To this end, an analytical model that includes the frames along axes A, B and C (Figure 6-1) of the building was developed, and subjected to the y-direction accelerations observed on the shake-table during the test (Figure 4-11). Limitations of the analytical model include its inability to capture bidirectional effects and torsional response. These limitations are discussed in Section 6.1.6.

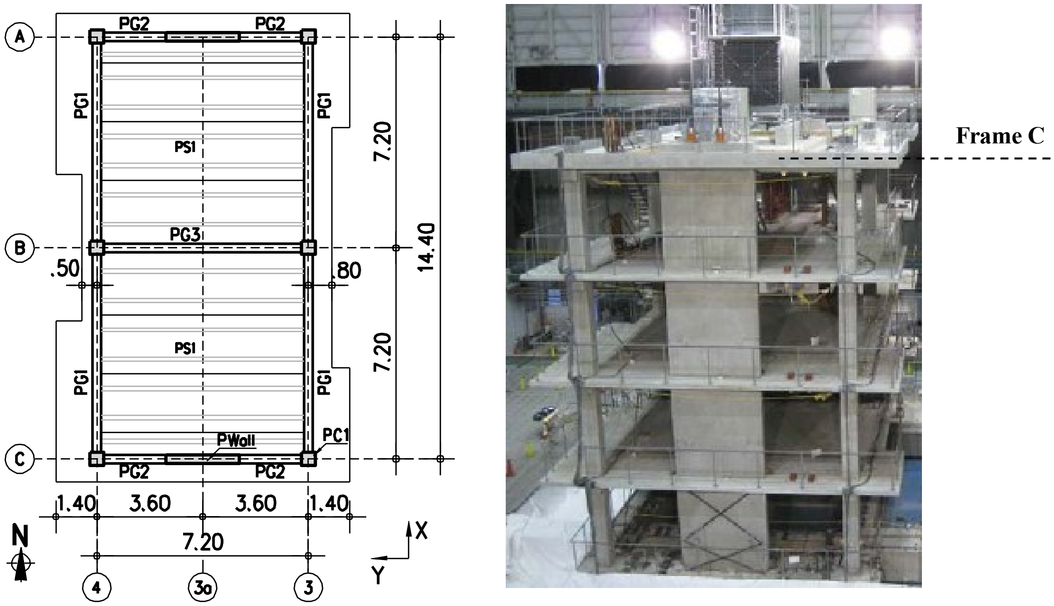

(a) **(b)**

Figure 6-1 (a) Typical framing plan of PT building; (b) view of Frame C of PT building on shake table

All analyses were conducted using the commercially available software Perform3D (CSI, 2011a), as use of a commercial program was deemed necessary to promote systems use in practice. The following subsections present a summary of modeling approaches implemented for different components.

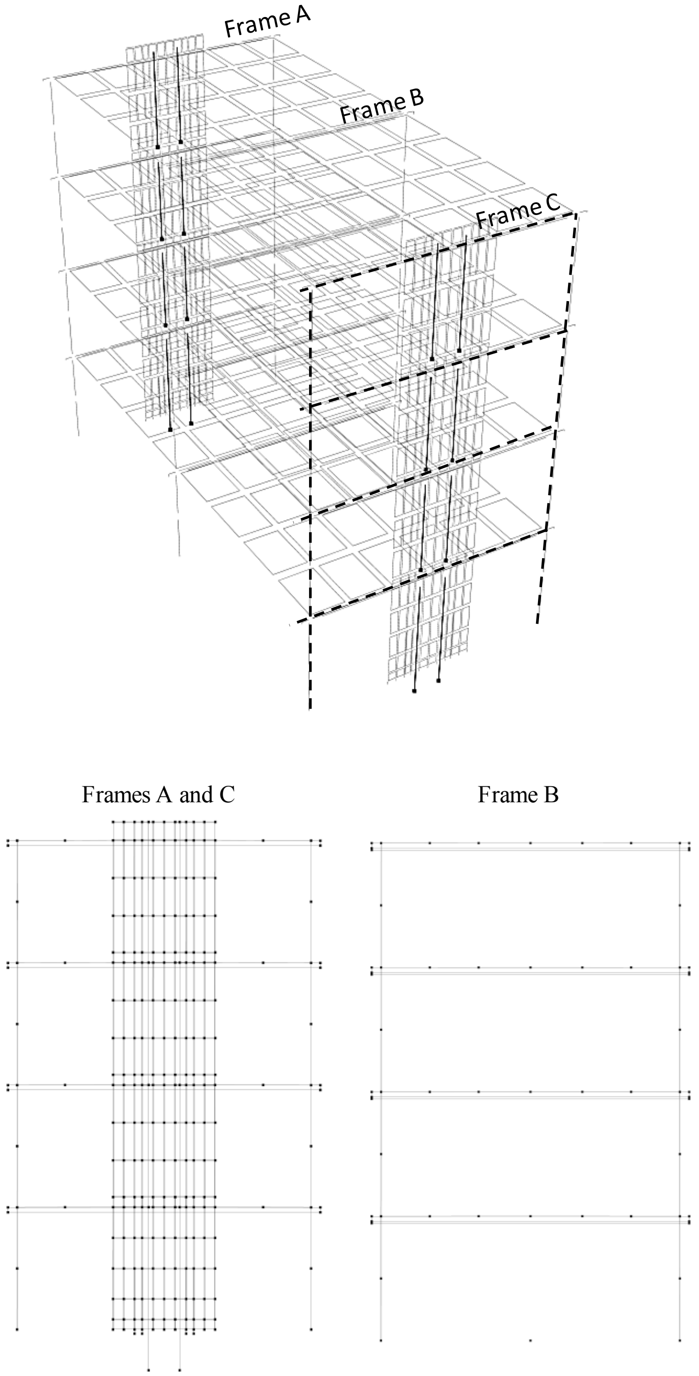

Figure 6-2 3D view of analytical model in Perform3D and 2D views of Frames A, B and C

6.1.1 UPT wall modeling

The UPT walls were modeled using a combination of inelastic shear wall elements and truss elements. As discussed in Section 3.1.2.1, shear wall elements in Perform3D are 4-node macro-elements organized in two layers acting in parallel: an axial-bending layer and a shear layer. The axial-bending properties parallel to the element axis are captured by fiber sections consisting of concrete and steel fibers described by uniaxial stress-strain relationships. The shear layer is defined by a shear material, described by a stress-strain relationship, and is based on the assumption of constant shear stress in the element.

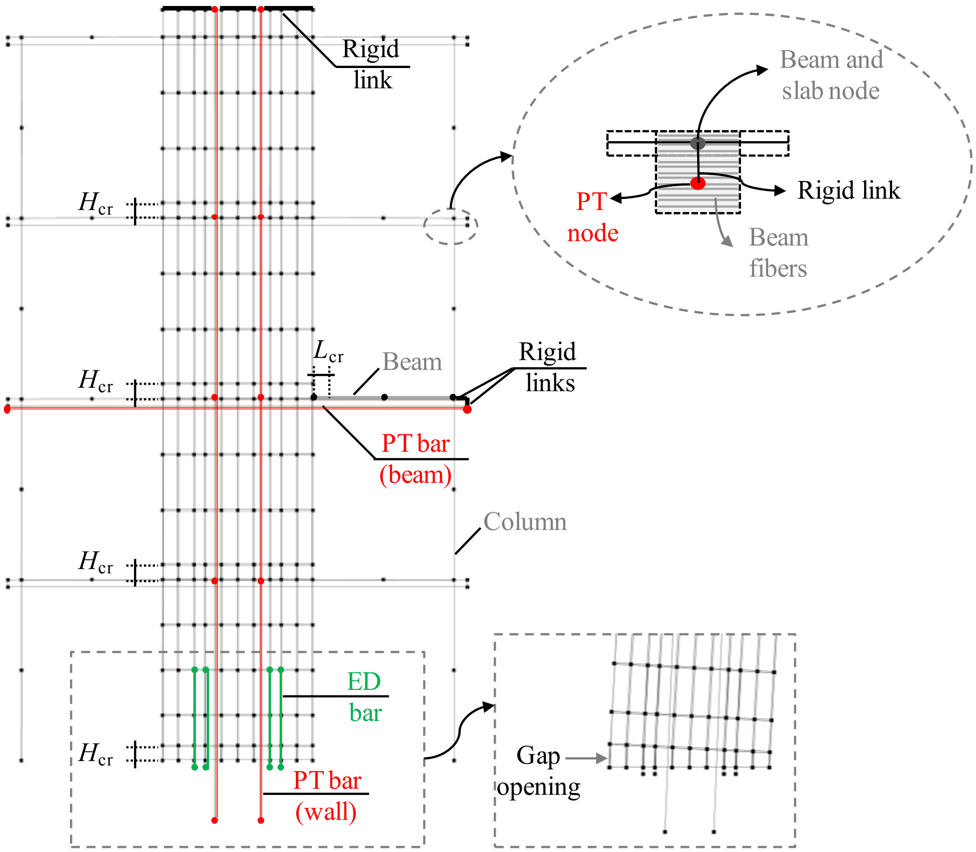

Figure 6-3 Frame A (and Frame C) of analytical model

Gap opening at the base of the UPT walls was modeled using shear wall elements with concrete-only fibers (no-tensile strength) over a critical height, $H_{cr} = t_w = 250$ mm from the base (Figure 6-3), where t_w is the wall thickness. In this way, gap opening and associated softening behavior of the wall under lateral load, was simulated as elongation of the wall concrete fibers that go into tension, developing positive strain under zero stress. Selection of H_{cr} was based on observed damage at the base of the south UPT wall, where concrete spalling extended vertically for a distance approximately equal to the thickness of the wall. Moreover, the selected value for H_{cr} coincides with the gauge length of the vertical sensors provided at the wall ends (D1, D2 in Figure 5-25), thus facilitating comparisons of analytical and experimental wall local responses such as concrete strains and wall uplift.

As noted in Section 3.1.2.1, although the gap-opening displacements, calculated by integrating the concrete tensile strains over H_{cr}, are not that sensitive to the assumed value for H_{cr}, the calculated concrete compressive strains are dependent on the value of H_{cr}. Granted that in the present model H_{cr} was test-specific, as it was based on observed damage and available instrumentation of the E-Defense test walls, it is also of interest to compare with the recommended values for H_{cr} discussed in Chapter 3 (Section 3.1.2.1). Based on examination of prior experimental results of UPT walls, it was recommended that $H_{cr} \leq (1.5t_w, c)$ be used for estimating strain demands on UPT walls, where t_w is the wall thickness and c is the estimated neutral axis depth at the maximum drift ratio, θ_{max}. The neutral axis depth at the maximum drift as defined in ACI ITG-5.2 ($\theta_{max} = 3.00\%$ for the E-Defense UPT walls) was calculated in Section 4.6.2.1, and was found equal to $c = 208$ mm, so that the limit $H_{cr} \leq (1.5t_w, c)$ yields $H_{cr} \leq 208$ mm. This is 17% lower than the 250 mm height that was used in the model described here. It is noted that analyses were also run with $H_{cr} = 208$ mm, and resulted in modest changes in local responses (13% increase in peak concrete compressive strain at the end of the wall) and essentially identical global responses with the model that uses $H_{cr} = 250$ mm. Noting that in either case, no significant degradation occurred in the confined concrete in the analytical model, the negligible impact on the global response is expected.

The wall fiber sections over the height H_{cr} consist of concrete only fibers with no tensile strength. The mild bonded reinforcement of the precast wall panel (D13@120mm in Figure 6-4a) was not included in the base fiber sections as it did not cross the wall-foundation interface and did not provide moment strength at the base of the wall. Above the height H_{cr}, any reinforcement that was bonded and adequately developed was included in the wall fiber sections.

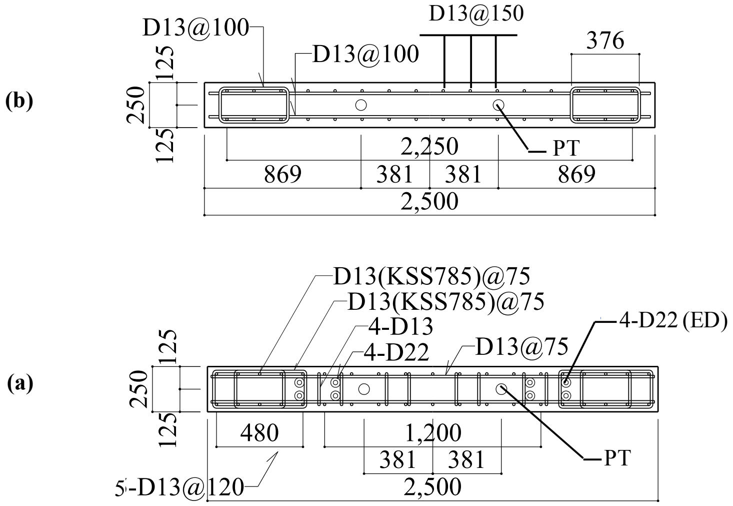

Figure 6-4 UPT Wall cross sections of (a) 1st story and (b) upper panels (dimensions in mm)

The effect of transverse reinforcement (high strength D13@75mm) was accounted for by using concrete fibers with different stress-strain relationships to model the well-confined ends of the base panel compared to the unconfined concrete within the middle portion (web) of the panel. The unconfined concrete stress-strain relationship was based on material characterization tests performed on concrete cylinders prior to the shake-table test (Nagae et al. 2011), while the confined concrete relationship was defined based on the Razvi and Saatcioglu (1999) confinement model for high-strength concrete (Figure 6-5).

Unloading and reloading behavior of the concrete model is illustrated on the confined concrete curve of Figure 6-5 through an assumed strain history consisting of loading to a compressive strain ε_1, unloading to zero strain and reloading to ε_2. Key aspects include: unloading occurs parallel to the initial elastic stiffness, concrete tensile strength is zero, and reloading occurs to the same strain ε_1 from which unloading initiated. Strain ε_0, and reloading stiffness are controlled through the energy degradation factors that define cyclic degradation of materials in Perform3D. Energy degradation factors of 0.20 were used based on calibration studies presented in Chapter 3.

It is noted that the vertical mild steel reinforcement ($\rho_v = 0.77\%$ for the first story precast wall panel, and ρ_v=0.65% for upper stories) of individual wall panels in the test building did not extend across the horizontal joints between panels, so that moment resistance at upper joints was solely provided by the unbonded PT steel crossing the joints. This behavior was implemented in the analytical model by introducing a series of wall elements with concrete-only fibers (no-tensile strength) over a height H_{cr} at the base of each panel, similar to modeling of gap opening at the base section (Figure 6-3). This allowed gap opening to occur at upper joints, provided moment demands at those locations overcame the initial precompression due to post-tensioning (plus any additional PT force due to uplift having occurred at the base of the wall). Given that assessment of upper joints presented in 4.6.2.2 indicated that at development of the wall nominal capacity, the decompression moment at the second floor is likely to be exceeded, it is of interest to examine predicted uplift values at these locations from the analytical model. This will be discussed in Section 6.2.2.

The different confining reinforcement details of the upper story panels compared to the base precast wall panel (Figure 6-4) were accounted for by using a different confined concrete stress-strain relationship in the fiber sections of upper panels. The confined concrete relationship for upper panels was also defined based on the Razvi and Saatcioglu (1999) model. Note that the calculated strength of the confined concrete was f_{cc}'=120.8 MPa for the base panel and f_{cc}'=96.7 MPa for the upper panels (f_c'=83.2 MPa in both cases).

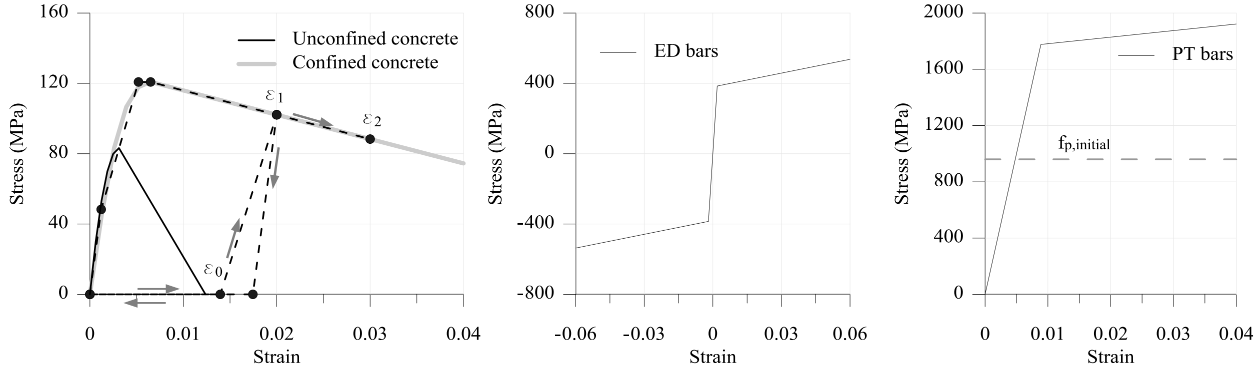

Figure 6-5 Material stress-strain relationships for E-Defense UPT wall model

Shear behavior of the wall panels was modeled using an elastic uncracked shear modulus ($G_c \approx 0.4E_c$, where E_c is the modulus of elasticity of concrete) as the majority of lateral displacements in UPT walls is attributed to rocking at the critical interface and the contribution of shear deformations is generally expected to be small. This observation was verified by the experimental results of the E-Defense UPT walls presented in the previous chapter. It was shown that at peak response the contribution of wall base rotation to wall roof drift was 92%, confirming that contribution of both flexural and shear deformations was small. Note that, contribution of shear deformations can be more significant for lower aspect ratio UPT walls, Based on experimental results from a 0.4-scale, low aspect ratio (M/Vl_w = 1.5) UPT wall with perforations tested under reversed cyclic loading, Smith et al. (2012a) report that the contribution of shear deformations to the total wall drift was approximately 19% at θ_{max} = 2.30%. Discrepancies between analytical results using a fiber model (Smith et al. 2012a) of the aforementioned UPT wall specimen and experimental results, were attributed to the inability of the model to capture the nonlinear shear deformations of the wall panels. Given the limited data on moderate and low aspect ratio UPT walls, additional experimental and analytical studies are required to assess the effect of nonlinear shear deformations on behavior of UPT walls and compare with available research on shear deformations of conventional RC walls (Massone and Wallace 2004, Beyer et al. 2011, Tran 2012, Kolozvari et al. 2014). For the model described here, use of an elastic uncracked shear stiffness is warranted by the large aspect ratio of the E-Defense UPT walls (H_w/l_w = 5.0) and the high shear capacity over shear demand ratio as discussed in 4.6.5, and was also confirmed by the measured experimental responses presented in the previous chapter.

The unbonded PT steel and unbonded length of the energy dissipating (ED) bars were implemented as vertical inelastic truss elements, placed outside of the fiber section as strain compatibility is not enforced between concrete and steel over the unbonded lengths. Nonlinear force-deformation relationships that approximate the actual stress-strain relations from material characterization tests were assigned to the truss elements (Figure 6-5). The tops of the ED truss elements were connected to the wall nodes above the base at a distance equal to the deliberately debonded length of the ED bars (1500 mm). The bottom nodes were pinned below the wall base at a distance that accounts for an additional debonded length due to strain penetration according to ACI ITG-5.2. The PT truss elements were pinned at the base, accounting for the additional unbonded length inside the foundation, and connected through rigid links to the adjacent wall nodes at the top of the wall (Figure 6-5). While the PT truss elements were only constrained to the vertical displacement of the wall at their top nodes (through the rigid links), additional PT nodes were used at each floor level for the truss elements. These additional PT nodes were kinematically constrained to have the same horizontal displacement as the adjacent wall nodes at each floor level and ensure that the displaced shape of the truss elements is compatible with the displaced shape of the wall (Perez et al. 2004). The pre-stressing force was simulated as an element load (initial strain) in the PT bars.

As shown in Figure 6-1, the analytical model includes the frames along axes A, B and C. The UPT wall model described above was implemented for both walls in the building, i.e., identical behaviors were assumed in the analytical model for the north (Frame A) and south (Frame C) UPT walls. However, the two test walls in the building differed in that the north wall included fiber reinforcement in the wall-foundation interface grout and the grout between the first and second story panels, as well as in the concrete mix of the first and second story precast wall panels. In contrast, no fiber reinforcement was included in the grout or concrete mix of the south UPT wall. These differences are not reflected in the analytical model. The interface grout at the wall-foundation interface and at the horizontal joints between precast panels was not explicitly implemented in the analytical model. Instead, the 30-mm thick grout was included in the height of the wall panels in the model, and was assumed to behave as the wall panel section above it. Note that this is consistent with the intent of ACI ITG-5.2, that requires the specified compressive strength of the grout to be at least equal to the specified compressive strength of the concrete. Moreover, ACI ITG-5.2 requires a minimum amount of fiber reinforcement to be included in the interface grout between the base wall panel and the foundation to ensure that the grout behaves in a ductile manner and wall behavior is not adversely affected by degradation or crushing of the interface grout. In cases where these ACI ITG-5.2 requirements are satisfied, then for modeling purposes, it is reasonable to assume that the grout behaves similar to the concrete wall panel and need not be explicitly modeled.

As discussed in Section 4.6.6, the north UPT wall satisfied ACI ITG-5.2 with respect to grout properties, and performance of the wall during the tests, as documented in Section 5.3, verified the efficiency of ACI ITG-5.2 requirements in maintaining the grout intact as the wall (and grout) rock against the foundation. In contrast, performance of the south wall was adversely affected by the lack of fiber reinforcement in the wall-to-foundation interface grout and behavior of the wall was largely governed by degradation and crushing occurring in the grout layer. Based on these observations, the model described here is more appropriate for the north UPT wall in the test, and cannot predict the degradation associated with grout crushing that was observed in the south wall during test.

Finally, in addition to the fiber reinforcement in the grout, the north wall also included fiber reinforcement in the concrete mix of the first and second story precast wall panels. While not required by ACI ITG-5.2, inclusion of fiber reinforcement in the base precast wall panel resulted in negligible damage to the wall toes of the north UPT wall. In contrast, concrete cover spalling occurred at both ends of the south wall and extended horizontally approximately one to two times the thickness of the wall. Material characterization tests performed on concrete cylinders prior to the shake-table test (Nagae et al. 2011) show similar compressive strengths for the fiber reinforced concrete used in the precast panels of the north wall and the high-strength concrete used for all other precast elements in the PT building (Table 4-2). Despite the similar compressive strengths, the fiber reinforced concrete is likely to be more ductile in compression and prior experimental research on fiber reinforced cement composites has verified their increased ductilities in compression (e.g. Parra-Montesinos et al. 2006). In the analytical model of the E-Defense PT building described here, although the fiber reinforcement was not explicitly accounted for in the stress-strain relationships used for the confined and unconfined concrete, it is noted that in defining the wall fiber sections of the confined ends of the wall panels, the entire wall thickness (250 mm) was assigned the confined concrete properties, i.e. the (unconfined) cover concrete on either side of the well-confined boundary was assumed to behave as the confined core. Based on observed damage to the walls described above, the wall model implemented here is again more representative of the north UPT wall in the test, where the fiber reinforcement prevented concrete cover spalling from occurring despite peak measured concrete strains in the order of 0.009 (Figure 5-37).

6.1.2 UPT beam modeling

Similar to the UPT walls, where deformations were primarily concentrated at the wall-foundation interface, the UPT beams were intended to act essentially as rigid bodies under lateral loading with rotations concentrated at the beam-to-column and beam-to-wall connections. In the absence of axial restraint, the concentrated rotations cause gap openings to form at the critical interfaces, and elongation of the PT steel. The PT force (initial prestress plus additional force due to gap opening) forms a couple with the compression force in the concrete to resist the applied load. This behavior is shown schematically in Figure 6-6 for the beam-to-column connection.

The experimental validations using the NIST beam-column tests presented in Chapter 3 (Section 3.2) showed that the behavior of a UPT beam as that shown in Figure 6-6 can be adequately captured with a model consisting of beam fiber sections and inelastic truss elements with initial strain. Using this approach, the E-Defense UPT beams were modeled using a combination of inelastic beam fiber sections and horizontal inelastic truss elements (Figure 6-3). Differences between the E-Defense UPT beams and the NIST test beams such as eccentric placement of PT steel, no energy dissipating bars, different concrete strengths between the precast and cast-in place parts of the beam, were straightforward to implement in the analytical model of the E-Defense UPT beams. However, modeling of the E-Defense UPT beams poses additional challenges, largely related to boundary conditions and interaction with the floor system. This is discussed further later in the section.

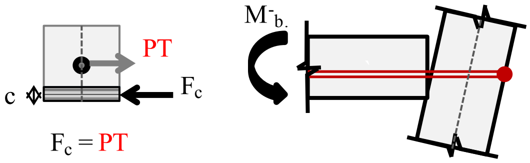

Figure 6-6 Gap opening at beam-column joint (unrestrained extension)

Based on recommendations provided in Section 3.2.2, gap opening at critical interfaces of the E-Defense UPT beams was modeled using a beam fiber segment with concrete-only fibers (no-tensile strength) over a critical length, L_{cr}, at each beam end. Outside the length L_{cr}, any beam reinforcement that was bonded and adequately developed was included in the beam fiber section. L_{cr} represents the beam length over which nonlinear behavior of the concrete in compression is expected to extend. It is noted that upon completion of the test, damage to the E-Defense UPT beams ranged from grout crushing and localized damage at the interface with the walls and columns, to some concrete crushing at the bottom face extending horizontally a short distance (typically smaller than $0.5h$) from the column interface. Some cracking in the slab at the locations of UPT beams was also observed, and was likely related to deformation incompatibility between the beam and slab (beam elongation effects) as discussed in Section 5.3. A value of $L_{cr} = 0.4h$ was used in the analytical model of the E-Defense building for all UPT beams. Note that in Chapter 3 it was recommended that, in the absence of experimental evidence, $L_{cr} \leq c$, where c is the beam neutral axis. As discussed in Section 5.8, the presence of the slab likely affected the behavior of UPT beams and experimental results showed that the beam neutral axis depth for negative moment (tension at top) ranged between 0.3-$0.4h$. This increased neutral axis depth is believed to be the result of interaction of the beams with the floor system.

Note that while in the NIST beam-column sub-assemblages the beam ends were free to move horizontally and no slab was present, the E-Defense UPT beams were connected to the wall and columns at their ends and, in addition, the presence of the slab partially restrained gap opening from occurring at the beam ends. This restraint induced axial compressive forces that increased beam moment capacities, and beam neutral axis depth under negative bending (tension at top). In order to capture these interactions of the UPT beams with the floor system, the slab was explicitly modeled. The slab modeling and slab-beam interaction mechanism are discussed further in the following section. Note that the connectivity and eccentricities between the different components in the model (beam, slab, PT steel) is essential in obtaining realistic results. While beam and slab elements had common nodes, defined at mid-height of the 100-mm cast-in-place slab, as shown in Figure 6-3, beam fibers were offset to account for the eccentric connection between the beam and slab. Similarly, the horizontal inelastic truss elements that modeled the unbonded PT steel in the beams were eccentrically located with respect to the beam to represent their actual locations in the section (Figure 4-10). Vertical rigid links at the locations of the PT steel anchorages at the external faces of columns connected the end nodes of the PT truss elements to the adjacent beam element nodes (Figure 6-3). The initial prestress was implemented as an initial strain in the truss elements implementing the PT steel. Note that all material relationships (PT steel, f_c' of beam and f_c' of topping concrete) were based on material characterization tests performed prior to the shake-table test (Nagae et al. 2011). The stress-strain relationship for the confined core of the beam was defined based on the Razvi and Saatcioglu (1999) model.

In order to ensure a moment-resisting connection between the UPT beams and the wall, the beam elements at each floor level were connected to the wall by horizontal beam elements imbedded in the wall and extending the full length of the wall. Elastic beam elements with large bending stiffness were used for the imbedded beams. It is noted that if embedded beams are not used, the beam-to-wall connection will behave as pinned since shear wall elements in Perform3D have no in-plane rotational stiffness at their nodes (CSI, 2011b). Finally, rigid end zones were used for the portions of the beams inside the beam-column joint (i.e. panel zone shear deformations were ignored).

6.1.3 Slab modeling

In analysis of buildings, concrete floor diaphragms are typically considered to be infinitely rigid in-plane. This assumption was not appropriate for the model described herein as a rigid diaphragm would not allow the horizontal PT truss elements to precompress the UPT beams under the initial prestress or to elongate under lateral load. Similarly, a rigid diaphragm would completely restrain gap opening (elongation of beam fibers at the level of the rigid diaphragm) from occurring, causing unrealistically large compressive axial forces to develop in the UPT beams in order to satisfy compatibility.

With the intent of capturing the interaction between the UPT beams and the slab, and the effect of the in-plane action of the floor system in limiting beam axial growth, the slab was explicitly modeled using elastic shell elements with an effective membrane thickness equal to 25% of the gross section thickness ($EA_{\text{eff}} = 0.25E_cA_g$). An effective thicness was used as the restraint provided by the slab is likely to reduce once cracking and deterioration of the slab occur (Lau and Fenwick 2002, Kim et al. 2004). Sensitivity of model results to effective membrane stiffness is examined in Section 6.4. Bending effects of the slab were neglected in this study.

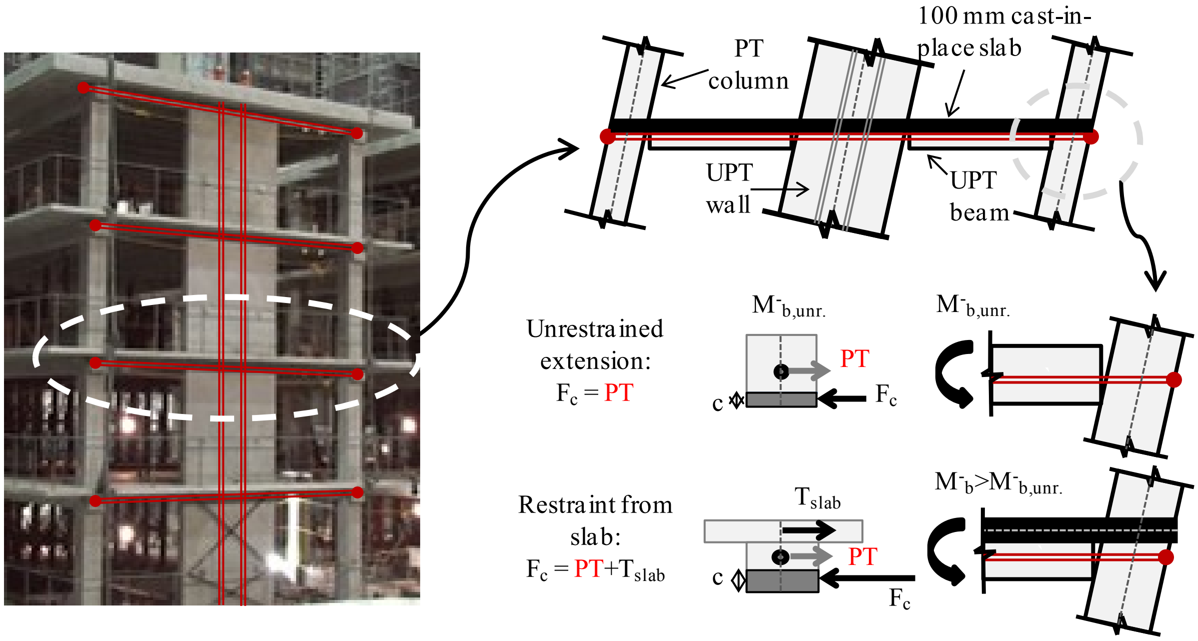

Figure 6-7 Effect of axial restraint from slab on UPT beam negative moment capacity

Figure 6-7 shows schematically the effect of axial restraint for negative bending at the beam-to-column connection. In the analytical model, the restraint is provided by the in-plane action of the slab elements as follows: gap openings at the ends of the UPT beams, implemented in the model as extension of the beam concrete fibers over L_{cr} at the critical interfaces, cause the overall length of the beams at the vertical location of the slab elements (mid-depth of cast-in-place slab) to increase, and consequently tensile forces to develop in the slab. Depending on their magnitude, these forces can have a significant impact on the negative moment capacity of the beams as illustrated in Figure 6-7 for negative bending at the beam-column joint. In the case of unrestrained extension, the concrete compressive force at the bottom of the beam need only balance the tensile force in the PT steel. With the restraint from the slab, represented as an effective tensile force acting at mid-depth of the slab, the concrete compressive force, neutral axis depth and moment strength of the beam are increased. The magnitude of these effects are expected to be dependent on the assumed in-plane (membrane) thickness for the elastic slab elements.

Despite limitations associated with the assumption of elastic response based on a constant effective thickness, this approach was able to capture key aspects of the interaction between the UPT beams and the slab (Section 6.2.3.2). Sensitivity of local beam responses to the effective membrane stiffness is examined in Section 6.4.

6.1.4 Column modeling

The prestressed concrete columns of the test building contained PT bars inside ducts that were grouted after the bars had been stressed. The behavior of the columns was modeled using inelastic fiber column sections consisting of concrete and steel fibers. The area of the bonded PT steel was included in the fiber section with an appropriate stress-strain relationship based on material characterization tests. However, the initial strain in the PT bars, $\varepsilon_{p,i}$, could not be explicitly accounted for because the fiber section assumes equal strains between any steel fiber and the surrounding concrete ($\varepsilon_p = \varepsilon_c$). This assumption is appropriate for a non-prestressed concrete member, assuming there is no bond slip between concrete and reinforcement. In a prestressed member however, the concrete and bonded PT steel do not have the same strain. At the time the two materials are first bonded together, there is a large tensile strain in the PT steel (initial strain $\varepsilon_{p,i}$) and a small compressive strain in the concrete (elastic shortening $\varepsilon_{c,i}$), resulting in a strain difference of $\Delta\varepsilon = \varepsilon_{p,i}-\varepsilon_{c,i}$. As the member is loaded, this strain difference remains constant because any additional strain due to the load is identical in both the bonded PT steel and the surrounding concrete (Collins and Mitchell, 1997). As a result, the strain in the prestressed reinforcement at any stage is $\varepsilon_p = \varepsilon_{c+}\Delta\varepsilon$.

The assumption of equal strains between the PT and surrounding concrete ($\Delta\varepsilon = 0$), enforced within fiber sections in Perform3D, results in a section where concrete cracking occurs earlier than in the actual prestressed section, and PT yielding is delayed, i.e., the effects of the initial prestress are neglected. In order to improve initial behavior of the column model, elastic bar elements with initial strain were used in parallel with the column elements. These parallel bars were assigned small axial stiffness (note that the PT steel is included in the fiber section with its actual axial stiffness) and an initial strain resulting in a tensile force equal to the actual initial prestress force. An equal compressive force developed in the column, simulating the effect of the initial prestress in precompressing the concrete section and delaying concrete cracking. However, caution should be exercised as the approach overestimates yield curvature and ultimate moment capacity of the section (equivalent to applying an external axial load). While for the range of demands in the present study the approach was satisfactory, modeling of concrete elements with bonded prestressed reinforcement using fiber sections should be generally avoided, unless the difference in strain between PT steel and surrounding concrete can be explicitly accounted for at the fiber section level, an option not available in Perform3D.

6.1.5 Mass, damping and loading

The seismic masses reported in Section 4.2 were distributed to the slab nodes in the analytical model at each floor level. Gravity loads were applied as point loads on wall and column nodes and prestress forces as initial strains on truss elements implementing the PT steel. P-Delta effects were included in all analyses. Rayleigh damping was used with damping ratios of 2.5% at $0.2T_1$ and $1.5T_1$, where $T_1 = 0.27$ s is the calculated (elastic) fundamental period in the wall direction of response. Analyses were run in sequence: after application of gravity and prestress forces, the sequence of Kobe records (25%, 50%, 100%) was run. Response under subsequent Takatori records is not examined here.

6.1.6 Limitations of analytical model

The analytical model described here considers response and excitation only in the wall direction of the test building (y-direction in Figure 6-1). As a result of neglecting bidirectional effects, some discrepancies between analytical and experimental results are expected, most notably with respect to behavior of the columns in the model. Note that peak interstory drift in the x-direction during the 100%-Kobe was 3.90% as opposed to 1.66% in the y-direction (at center of plan). With respect to the UPT walls, drift in the moment frame (x) direction did not adversely affect the in-plane performance of the walls as was discussed in Section 5.6.2. With the exception of localized high concrete strains at the wall corners (Section 5.6.4) that are not captured in the model, neglecting bidirectional effects is not expected to have a significant effect on analytically derived wall responses (PT forces, wall moment capacities). However, behavior of the PT columns in the y (wall) direction examined herein, was likely affected by the large displacements demands in the x (moment frame) direction. It is noted that under the 100%-Kobe record, concrete crushing was observed at the bases of the PT columns, and was mainly associated with the moment frame direction response. As the analytical model described here does not capture these bidirectional effects, it is likely to underestimate degradation in columns and possibly overestimate their moment capacities. As will be shown in Section 6.3, contribution of column base moments to global overturning moment in the y-direction of the building was relatively small (approximately 10%), but contribution of the axial force couple at the bases of Frame A and C columns played a significant role in the lateral resistance of the building. Assuming that the axial load bearing capacity of the columns was not compromised due to bidirectional effects, column behavior in the model is expected to provide sufficiently accurate global results.

As discussed in Section 5.4, significant torsional response was observed during the experiment. Torsion was mainly attributed to different behaviors at the base joints of the two UPT walls due to lack of fiber reinforcement in the wall-foundation interface grout and concrete mix of the south wall. As a result, the south wall in the experiment sustained earlier degradation and larger displacement demands than the north wall. During the 100%-Kobe record, the peak roof drift ratio at the center of plan was 1.58%. As a result of torsional rotation, at that instant the south wall roof drift ratio was 2.09% and the north wall roof drift ratio was 1.07%. While this behavior is not reflected in the analytical model, where the grout is not explicitly modeled and identical behaviors are assumed for the south and north UPT walls, comparisons between displacement responses from this symmetric model and (average) experimental responses at the center of plan of the test building are meaningful. Nonlinear response history analyses of RC wall buildings with strength and stiffness eccentricities reported by Priestley et al. (2007) and Beyer (2007), show that torsional response does not affect the center-of-mass displacement. Based on this observation, and assuming that the center of mass was close to the geometric center of the building plan, consistent comparisons between analytical and experimental global responses at the center of plan can be made. Note that with the exception of slab edges and asymmetrically placed non-structural elements in the building (such as mechanical equipment and fixed steel frames for displacement measurements), the building was essentially symmetric, so that the assumption that the center of mass was located close to the center of plan is satisfactory for the purposes considered here.

Despite the limitations explained above, mainly associated with bidirectional and torsional effects, the analytical model was able to provide good estimates of the global hysteretic responses observed in the y-direction of the test building such as story lateral displacements, story shear forces and moments. Local responses such as base uplift versus wall rotation relations for the walls, and axial growth versus beam rotation relations for the beams were also found in close agreement with experimental local responses. These results are presented in the following section.

6.2 Comparisons of analytical and experimental results

This section provides comparisons of analytical and experimental global responses under the three Kobe records. More detailed results, including local responses and system interactions, are presented for the 100%-Kobe record under which the majority of inelastic response occurred.

6.2.1 Global Hysteretic Responses

Figure 6-8 to Figure 6-10 compare base moment versus roof drift relations determined from the analysis with those extracted from the experimental data in the wall direction of response of the test building. Also shown are the analytical and experimental response histories of base moment, base shear, and roof drift ratio. Experimental roof drift ratios correspond to the geometric center of the building plan. As discussed previously in Section 6.1.6, comparisons between results from the symmetric analytical model and experimentally measured drifts at the center of plan are conditioned on the assumptions that torsional response in the test did not affect the center of mass displacement, and the center of mass was close to the geometric center of the building plan.

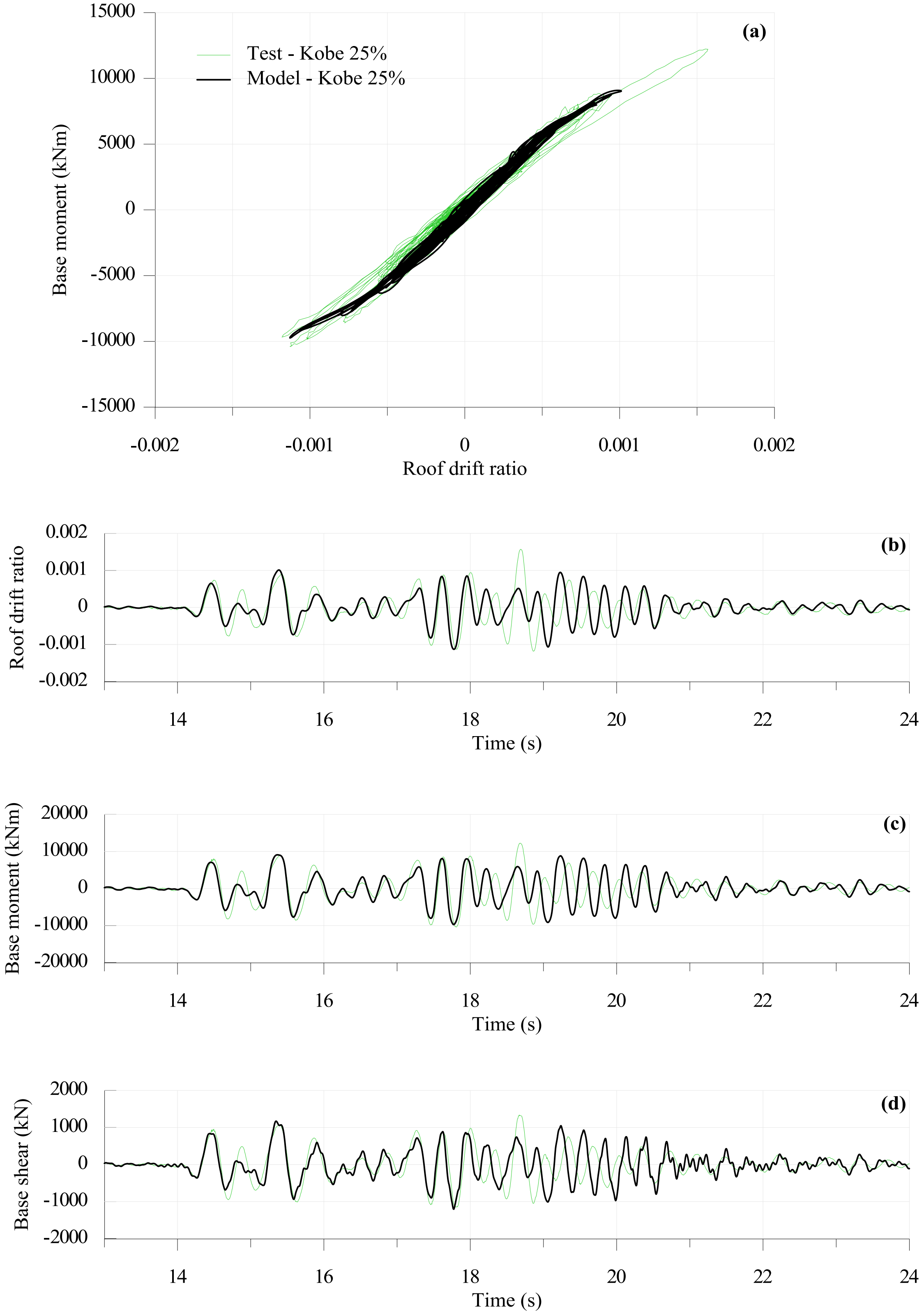

Figure 6-8 Analytical and experimental results for 25%-Kobe record; (a) global hysteretic response and response histories of (b) roof drift ratio, (c) base moment and (d) base shear

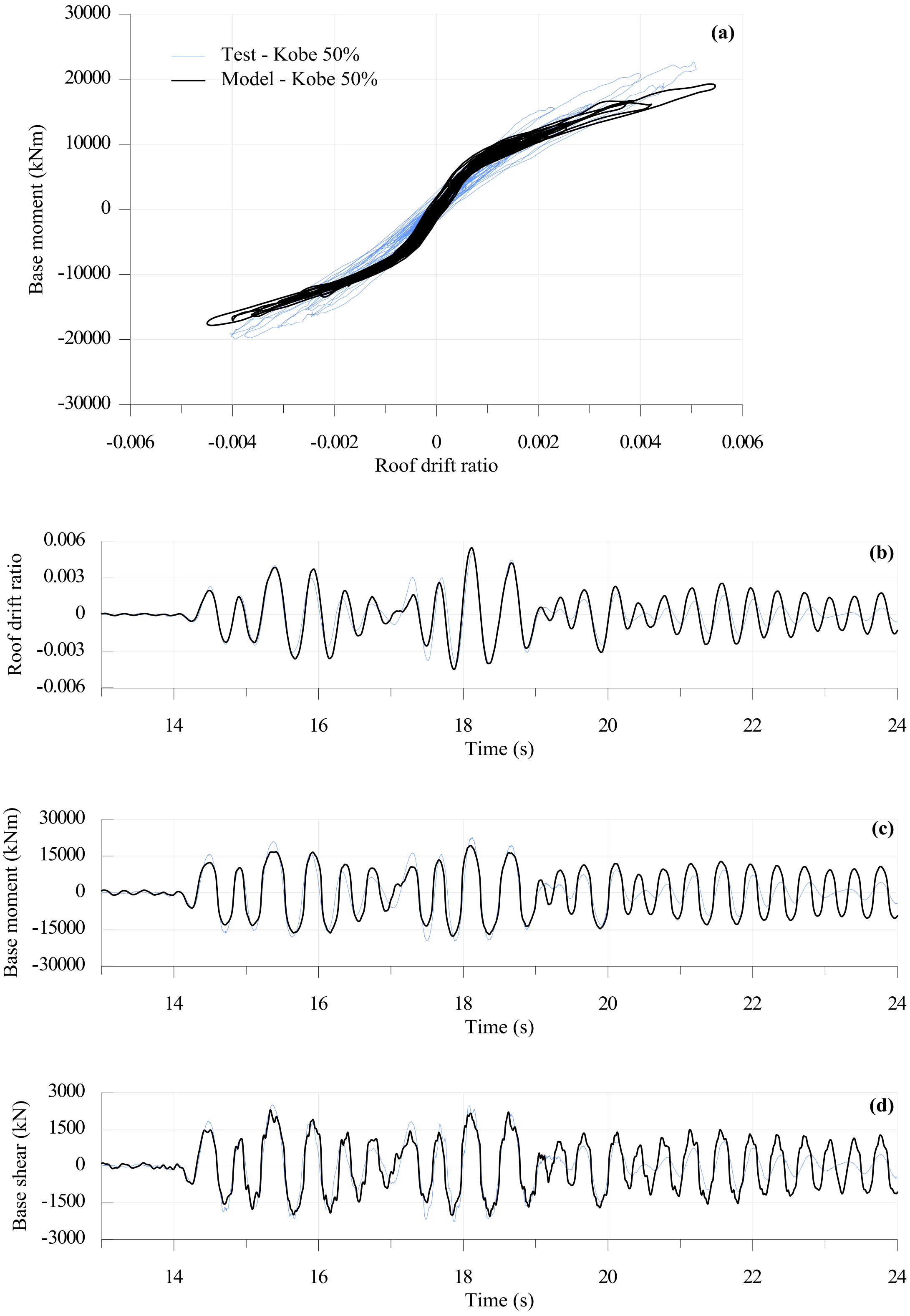

Figure 6-9 Analytical and experimental results for 50%-Kobe record; (a) global hysteretic response and response histories of (b) roof drift ratio, (c) base moment and (d) base shear

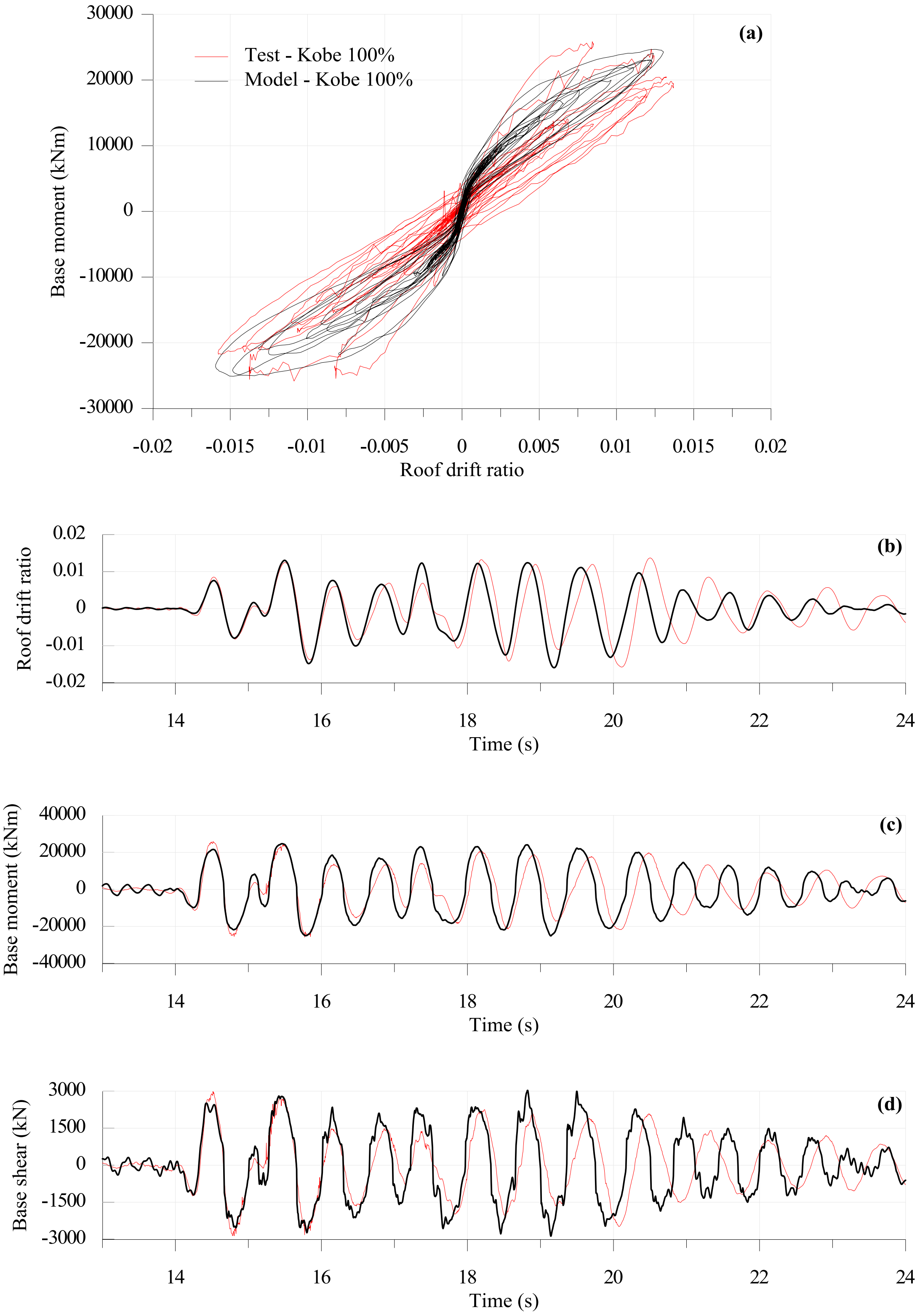

Figure 6-10 Analytical and experimental results for 100%-Kobe record; (a) global hysteretic response and response histories of (b) roof drift ratio, (c) base moment and (d) base shear

Comparisons of Figure 6-8 show that the analytical model adequately captures the initial stiffness and essentially linear elastic response of the building under the 25%-Kobe record. It is also noted that the (elastic) fundamental period calculated from the model matches the initial period in the wall direction of the building that was calculated from the white-noise base excitation at the beginning of the tests (T_1 = 0.27 s in both cases). Analytical response histories under the 25%-Kobe record are in good agreement with experimental responses up to approximately t = 18 s. Between t = 18 s and t = 20 s significant discrepancies are observed, with experimental and analytical responses being out-of-phase at some instants. The model also fails to predict the peak excursion in the positive direction.

Under the 50%-Kobe record (Figure 6-9), peak displacements are well predicted in both directions of loading but analytical responses damp out slower than the experimental respones. Moreover, earlier softening is observed in the analytical hysteretic response. The earlier softening, also apparent in the beginning of the 100%-Kobe analytical response (Figure 6-10), can be attributed to the effective stiffness value assumed for the slab. This is further discussed with respect to framing action in Section 6.4. Finally, even though peak displacements are well predicted for the 100% Kobe record, the model tends to recover the initial stiffness at small drifts and thus exhibits a more pronounced flag-shaped hysteretic response compared to the test results. A possible explanation is related to bidirectional effects not captured in the model, which only considers excitation and response in the wall direction of the building. The period elongation apparent at the end of the experimental response histories under the 100%-Kobe record is also not reflected in the analytical results. Such period elongation could be related to degradation at the base joint of the south UPT wall. As explained at the end of Section 6.1.1, with respect to modeling of the grout and the fiber reinforced concrete, behavior of the UPT walls in the analytical model is more representative of the north UPT wall in the test, so that degradation related to crushing of the grout in the south wall during the 100%-Kobe record is not captured in the analytical results.

6.2.2 Response envelopes

Figure 6-11 to Figure 6-13 compare analytical and experimental envelopes of various global response quantities of the building during the 100%-Kobe record. Although the model was shown to accurately predict peak roof drift ratios under this record, results of Figure 6-11 reveal some discrepancies between analytical and experimental vertical distribution of drift. Most notably, the model underestimates the first story peak drift ratio by 24%. Experimental results reported in Section 5.6.1 showed that the main contributor to measured peak roof displacement during the 100%-Kobe record, was base uplift and resulting wall rotation. More specifically, contribution of wall base rotation to peak wall roof drift was 92% for the south wall, and 88% for the north wall. The large contribution of wall base rotation resulted in almost uniform vertical distribution of drift as evidenced by the experimental envelope of Figure 6-11. In the analytical model, contribution of wall base rotation amounted to roughly 70%, with remaining deformation largely provided by gap opening at the second level (horizontal joint between first and second story panels). This is reflected in the analytical envelope of Figure 6-11 by the increase from first to second level drift ratio.

As mentioned in Section 6.1.1, the possibility of uplift at upper joints was implemented in the analytical model by introducing a series of wall elements with concrete-only fibers (no-tensile strength) over a height H_{cr} at the base of each panel. So similar to the base section, gap opening at upper joints was represented as elongation of the concrete fibers that go into tension over the height H_{cr} (positive strain under zero stress). Theoretically, uplift at upper joints initiates once moment there exceeds the initial precompression due to post-tensioning in addition to any change in PT forces due to uplift at the base. Calculations presented in Section 4.6.2.2 identified the potential for uplift at the second floor joint when the nominal wall moment capacity develops at the base. Interestingly, the model predicts that uplift occurs at the base of the second story precast panel, with a peak value of 9 mm during the 100%-Kobe record. However, experimental results for the 100%-Kobe record showed no significant uplift at upper joints as discussed in Section 5.6.3. Possible explanations include the effect of the framing UPT beams and slab in locally restraining wall gap opening, and the possible tensile resistance provided by the grout to concrete interface at the horizontal joints.

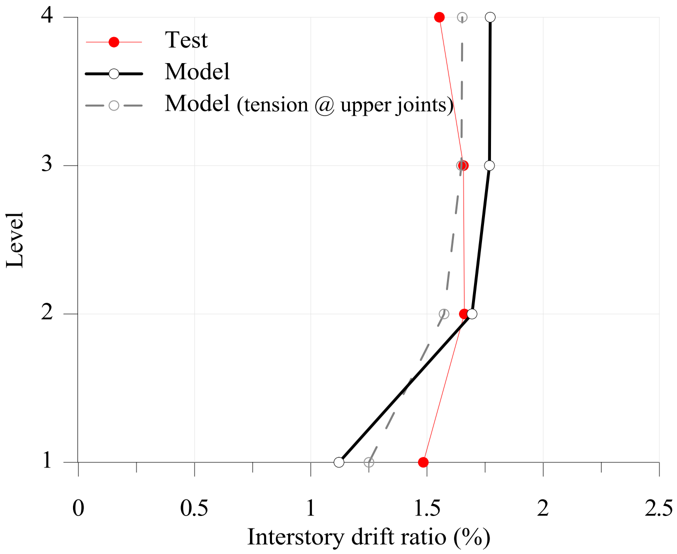

Figure 6-11 Analytical and experimental interstory drift ratio envelopes for 100%-Kobe record

In order to examine the effect of introducing some tensile capacity at the base sections of upper panels, the model was modified to include uniformly distributed mild steel reinforcement (with ρ_v=0.65%) at these sections. These modifications resulted in small changes (less than 5.0% reduction) in predicted peak roof drift ratios, but more significant changes in vertical distribution of drift, mainly associated with reduction of uplift at the second story joint, as shown by the dashed line in Figure 6-11. It is worth noting that design of the UPT walls of the test building based on ACI ITG-5.2, which requires all inelastic deformations to be concentrated at the base, would have required mild reinforcement to be provided across the second story joint as design moment at that level exceeded the decompression moment (Section 4.6.2.2).

Finally, despite discrepancies between analytical and experimental vertical distribution of drift, moment and shear envelopes along the height of the building were well predicted for the 100%-Kobe record (Figure 6-12, Figure 6-13). Note that although accurate predictions of distribution of uplift between the horizontal joints of the wall (e.g. all uplift concentrated at base as opposed to uplift occurring at both the base and upper joints) are critical for concrete strain predictions, design of confinement, and design of the energy dissipating reinforcement at the base of the wall, PT forces in the wall are not particularly sensitive to vertical distribution of drift since the PT steel is unbonded along the entire height of the wall. This essentially means that for the same total elongation in the PT steel (or, approximately, for the same wall roof drift), the force in the PT steel is independent of the vertical distribution of uplift between the different horizontal joints. Given that (i) the peak roof drift ratio was well predicted by the analytical model, and (ii) PT forces in the wall account for 75% of the wall moment capacity at the base (with remaining 25% provided by the energy dissipating bars) and 100% of the wall moment capacity at upper joints, the model is expected to provide reasonably accurate predictions of wall moments. Note that the analytical and experimental envelopes of Figure 6-12 and Figure 6-13 are global moment and shear envelopes in the y-direction of the test building. That is, in addition to wall moments and shears, they include all contributions to lateral resistance of the building. The decomposition of global resistance to its different contributions is presented in Section 6.3.

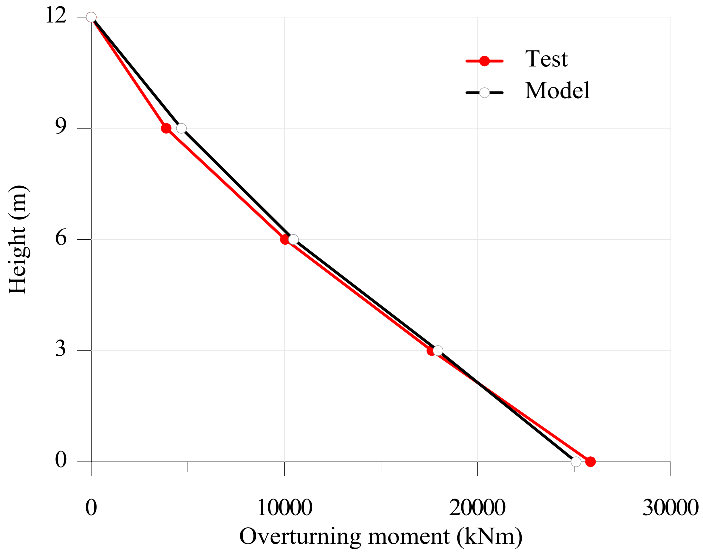

Figure 6-12 Analytical and experimental overturning moment envelopes for 100%-Kobe record

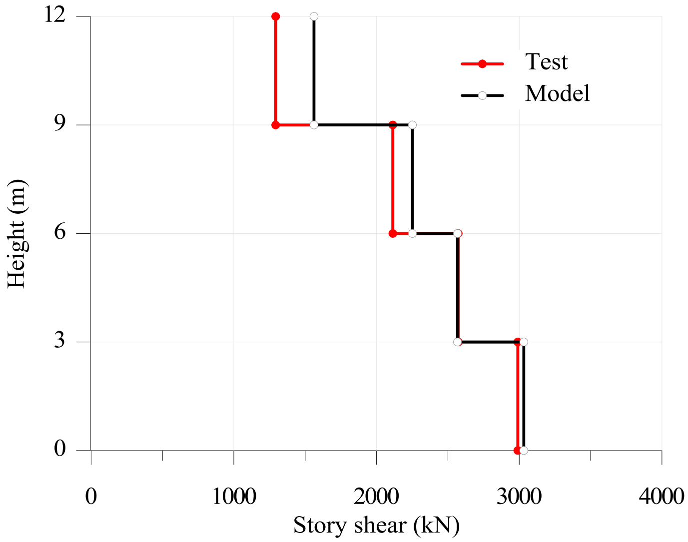

Figure 6-13 Analytical and experimental story shear envelopes for 100%-Kobe record

6.2.3 Local responses

Due to torsional response of the test building, which is not captured in the model, direct comparisons between analytical and experimental wall response histories are not meaningful. Recall that, in addition to affecting the magnitude of responses at opposite ends of the building, torsion also caused peak responses to occur at different instances. For example, as was shown in

Figure 5-26, peak wall rotations at the bases of the south and north wall were not simultaneous under the 100%-Kobe record. Similar to wall responses, UPT beam local response histories (e.g. beam rotation, axial growth) are expected to vary between the south and north frame UPT beams. Note that only south frame (Frame C) UPT beams were instrumented.

Although measured response histories of local wall and beam responses are not directly comparable to analytical response histories, it was possible to use experimental data to validate the local behavior of components in the model, such as the base uplift versus wall rotation relation for the walls and the axial growth versus beam rotation relation for the beams. Such comparisons are shown in Sections 6.2.3.1 and 6.2.3.2 for the 100%-Kobe record. Despite differences in magnitude, associated with torsional response that is not reflected in the analytical model, these comparisons show that the overall behavior of the UPT walls and UPT beams is adequately captured in the analytical model.

6.2.3.1 UPT wall local responses

Figure 6-14 compares the base uplift versus wall base rotation relations obtained from the analytical model with those extracted from experimental data for the two UPT walls. For consistency with analytical uplift values, which refer to the east and west ends of the wall, vertical displacement measurements from sensors D1 and D2 were adjusted to account for the short distance that the sensors were located away from the wall edges (Figure 5-25). Recall that west end (D2) measurements for the south UPT wall were not reliable. For that reason, plotted experimental uplift values for the west end of the south UPT wall were obtained using the "estimated D2" values shown in Figure 5-34(a) and calculated as discussed in Section 5.6.4.

Results in Figure 6-14 show that, for a given wall base rotation the analytically predicted gap opening displacements are in good agreement with experimental uplift values. Discrepancies in the range of rotations and uplift values between analytical and experimental responses are associated with (i) torsional response, and (ii) underestimation of wall base rotations and base uplift in the analytical model due to contribution from uplift at the upper joints.

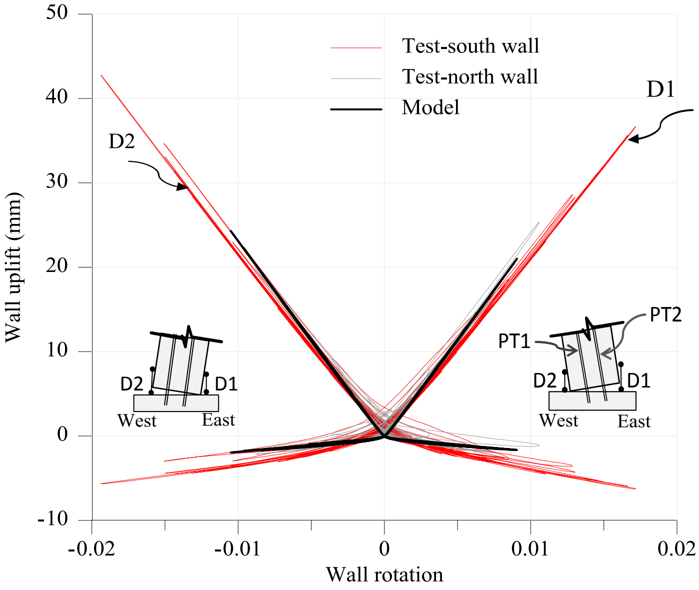

Figure 6-14 Analytical and experimental uplift at east and west ends of UPT walls under 100%-Kobe record

Note that, when divided by the associated 250 mm gauge length, the negative uplift values in Figure 6-14 represent concrete compressive strains at the ends of the walls (Figure 6-15). Recall that H_{cr} = 250 mm was used for the height of the first wall fiber elements in the analytical model, to allow direct comparisons with experimental data (Section 6.1.1). Comparisons of analytical and experimental results in Figure 6-15 show that analytical concrete strains at a given rotation are in better agreement with experimental strains of the north UPT wall. This is expected given that in Section 6.1.1, it was recognized that modeling assumptions with respect to the interface grout and fiber reinforced concrete, which were adopted in the analytical model for both UPT walls, were in effect more appropriate for the north UPT wall in the test. That is, predicted concrete strains at a given wall rotation from the model, are expected to represent the behavior at the base of the north UPT wall at the same rotation. Results in Figure

6-15 verify this observation and confirm the ability of the model to accurately capture local behaviors of the north UPT wall.

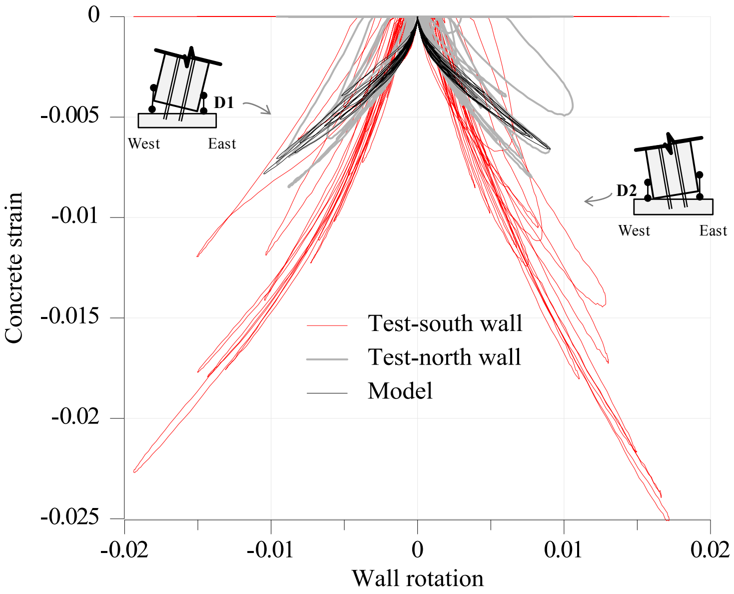

Figure 6-15 Analytical and experimental concrete strains at east and west ends of UPT walls under 100%-Kobe record

Figure 6-16 shows comparisons between analytical and experimental PT forces. Experimental PT forces are shown only for the south UPT wall since north wall PT forces were not measured during the tests. Note that PT forces are in both cases plotted against the wall roof drift ratio as opposed to wall base rotation. This was selected because in the analytical model, uplift at upper joints contributed to elongation in the PT steel, so that a plot of wall base rotation versus PT forces would be misleading. For consistency, experimental PT forces are also plotted against the (experimental) wall roof drift ratio; although in this case, elongation of the PT steel was largely associated with uplift at the base. As noted in 6.2.2, these discrepancies (contribution to PT elongation from uplift at upper joints versus elongation originating solely from base uplift), are not expected to affect predicted PT forces, provided that the total elongation is the same (or, approximately, comparisons refer to the same wall roof drift ratio).

Differences between analytical and experimental PT forces in Figure 6-16 are more likely associated with the analytical model being more representative of the north UPT wall, as discussed with reference to Figure 6-15. While PT forces were not measured in the north UPT wall, comparisons between the south and north wall neutral axis depths presented in Section 5.6.6, showed that the neutral axis depth was larger in the south wall, so that at a given rotation, PT forces in the south wall are expected to be smaller than north wall PT forces at the same rotation. Noting that the model is more representative of the north wall, and that experimental results in Figure 6-16 refer to the south wall, the small overestimation of PT forces from the analytical model is expected. It is also worth noting that despite these discrepancies, PT forces calculated from the analytical model at a given drift are still within 5-10% from measured PT forces in the south wall and are thus considered satisfactory predictions.

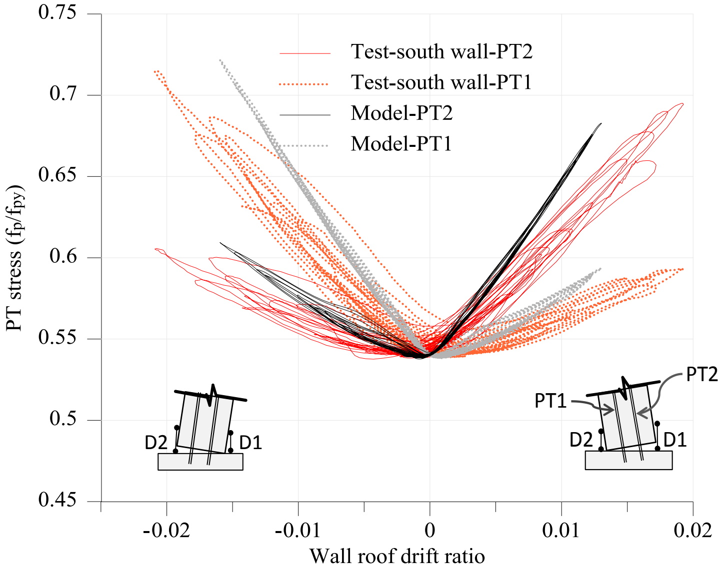

Figure 6-16 Analytical and experimental PT forces under 100%-Kobe record

6.2.3.2 UPT beam local responses

Figure 6-17 compares the beam axial growth versus beam rotation relations obtained from the analytical model with those extracted from experimental data. Both analytical and experimental results refer to the east end of the third floor UPT beam of Frame C (south frame). Experimental beam responses were obtained using measurements from horizontal displacement transducers that were attached to the top and bottom faces of the UPT beam at its ends, as discussed in Section 5.8. Plotted beam elongation values refer to beam mid-height.

Note that the beams in the analytical model use fiber sections. As discussed in 6.1.2, a value of $L_{\mathrm{cr}} = 0.4h = 120$ mm was used for the length of the first beam fiber segment closer to the beam-to-column and beam-to-wall interfaces. Beam end rotations from the model were calculated by extracting the positive and negative strains at the extreme fibers of the first beam fiber segment ($L_{\mathrm{cr}} = 120$ mm), integrating these strains over the length L_{cr} to obtain top and bottom displacements, and dividing the difference between the top and bottom displacement by the beam height, $h = 300$ mm, to obtain beam end rotations. Beam axial growth (over L_{cr}) at mid-height of the beam was computed as the average of the calculated top and bottom displacements. It is noted that the sensors that were used to calculate experimental beam rotations and beam growth values, had a gauge length of 750 mm, so that experimental values are average rotations and average elongations over the 750-mm gauge length. For consistency with the experimental values, calculations of beam rotations and beam growth values from the analytical model were repeated accounting for deformations within the additional 630 mm beyond the length $L_{\mathrm{cr}} = 120$ mm of the first fiber segment. Rotation values were found identical to values computed using only the deformations within L_{cr}. Axial growth calculations were more affected but were still within 10% of the values computed using only the deformations within L_{cr}. This is consistent with the expectation that UPT beam deformations mainly concentrate close to the beam-to-column (and beam-to-wall) interface. Analytical results plotted in Figure 6-17 correspond to calculations using beam deformations over the 750-mm length.

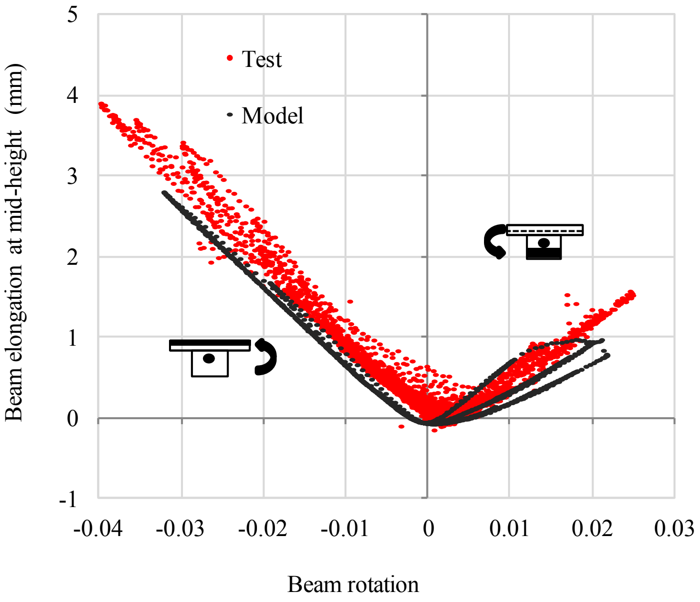

Figure 6-17 Analytical and experiment beam elongation at east end of 3rd floor UPT beam of Frame C under 100%-Kobe record

Results in Figure 6-17 show that the beam axial growth at a given rotation is adequately predicted in the analytical model. Given that plotted axial growth values refer to beam mid-height, then in combination with beam rotation values, they allow calculation of axial growth, or gap opening, at any location along the 300 mm height of the beam. For instance at -3.0% beam rotation (compression at top), the experimental gap opening at the bottom of the beam at the beam-to-column interface was approximately 3mm+0.03(150mm) = 7.5mm and is well predicted by the model. The model also captures the unsymmetrical behavior for positive and negative rotations (smaller gap opening for negative rotations) indicating that the effect of the slab in restraining gap opening from occurring at beam ends is adequately reflected in the analytical results. This is further discussed in Section 6.4, where sensitivity of beam local responses to the assumed effective stiffness of the slab is also examined.

Figure 6-18 compares the beam neutral axis depth versus beam rotation relations obtained from the analytical model with those extracted from experimental data. Similar to the analytical beam rotations and beam axial growth values plotted in Figure 6-18, analytical results plotted in Figure 6-18 correspond to calculations using beam deformations over a beam length of 750 mm from the column interface, for consistency with the 750-mm gauge length of the beam sensors that were used to compute the experimental data shown in Figure 6-18.

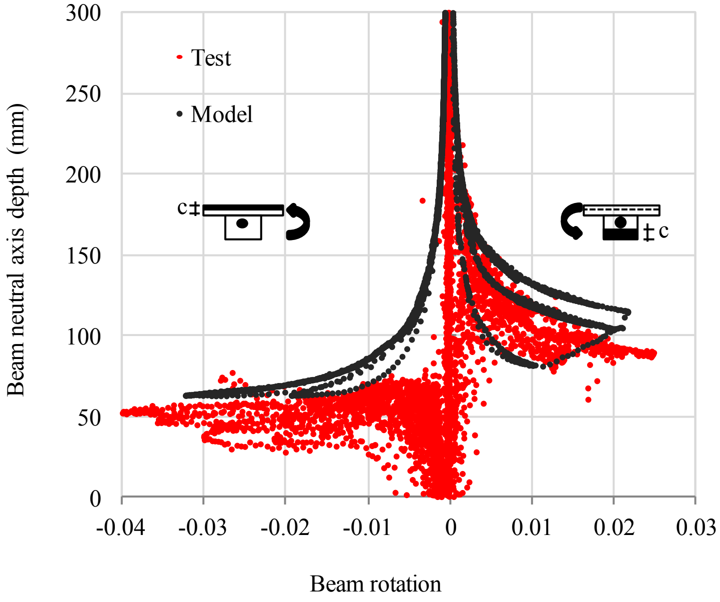

Figure 6-18 Analytical and experiment beam neutral axis depth at east end of 3rd floor UPT beam of Frame C under 100%-Kobe record

Results in Figure 6-18 show that the beam neutral axis depth is well predicted for both positive and negative rotations. As suggested in Section 5.8, the large neutral axis depth (c ≈ $0.3h$) at positive rotations (tension at top) was likely due to induced axial compressive forces in the beams due to interactions with the slab. The good correlations between analytical and experiment results indicate that the axial restraint from the slab and induced axial forces, are adequately represented in the analytical model. Section 6.4, examines sensitivity of calculated beam neutral axis depth to the effective membrane stiffness of the slab.

6.3 Decomposition of base moment resistance

In this section, the various contributions to the total base moment resistance of the test building in the wall direction of response are quantified. The objectives are to isolate the wall response, in terms of wall moment resistance, from the global responses, and assess the effect of framing action resulting from coupling of the walls to the corner columns through the UPT beams and floors. As discussed in Section 5.5, framing action was suspected to have contributed significantly to the lateral load resistance of the test building.

Using the analytical results for the 100% Kobe record, Figure 6-19 plots the distribution of base moment between the exterior two-bay frame consisting of the UPT wall, UPT beams and corner columns (Frame A), and the interior one-bay frame (Frame B). Due to symmetry in the analytical model, response of Frame C is identical to Frame A. The contributions from the three frames add up to the total base moment resistance of the building previously plotted in Figure 6-10(a). As evidenced by Figure 6-19, the interior frame exhibits a nonlinear elastic response, attributed to the beam-column connections which relied solely on unbonded PT steel for moment resistance. Contribution of this interior frame to global response is relatively small, accounting for 10% of the total base moment resistance at the instant of peak strength. The remaining 90% was provided by the two exterior frames which also accounted for the majority of hysteretic energy dissipation in the building through yielding of the mild ED bars at the bases of the UPT walls. As shown in Figure 6-19, Frame A exhibits a flag-shaped hysteretic response, characteristic of UPT systems with additional energy dissipation.

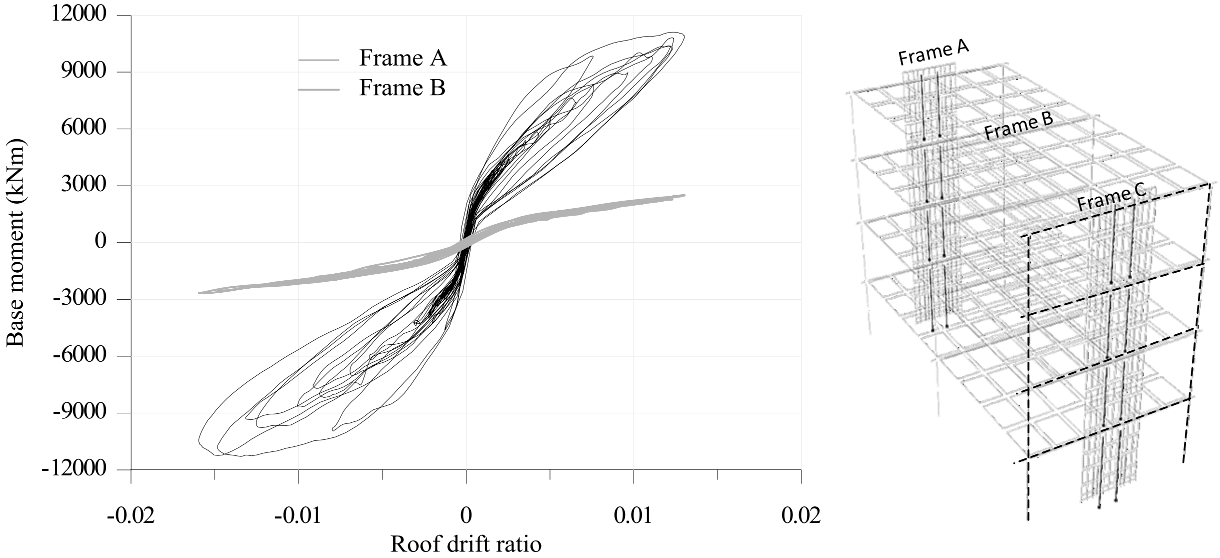

Figure 6-19 Decomposition of 100%-Kobe analytical overturning moment between Frames A, B, C

Further decomposition of Frame A resistance into its components (Figure 6-20), namely the wall moment, column moments, and moment from the force couple produced by the axial loads at the column bases, shows a significant contribution of the force couple. The moment resistance from the force couple, referred to as framing action herein, is directly related to the end moments and corresponding shear forces of the UPT beams as the magnitude of the (seismic) axial load at the base of each column equals the sum over all floors of the shear forces of the framing UPT beams. Beam shear forces are also transmitted at either end of the wall at each floor level. Due to their opposite signs, the influence of these forces on the wall axial load is small.

Combining results from Figure 6-19 and Figure 6-20 the building's total moment resistance at the instant of peak strength during the 100%-Kobe record, can be decomposed into the following contributions: 22.5% from the moment capacity at the base of each UPT wall, 17.5% from framing action at each exterior frame, 5.0% from the column moments at each exterior frame and, finally, 10% contribution from the interior one-bay frame. It is noted that bi-directional loading and torsional effects that were not accounted for in the model described here, would likely have an impact on the calculated relative contributions (e.g. variations in axial loads, moment capacities of columns, and different responses of the two walls).

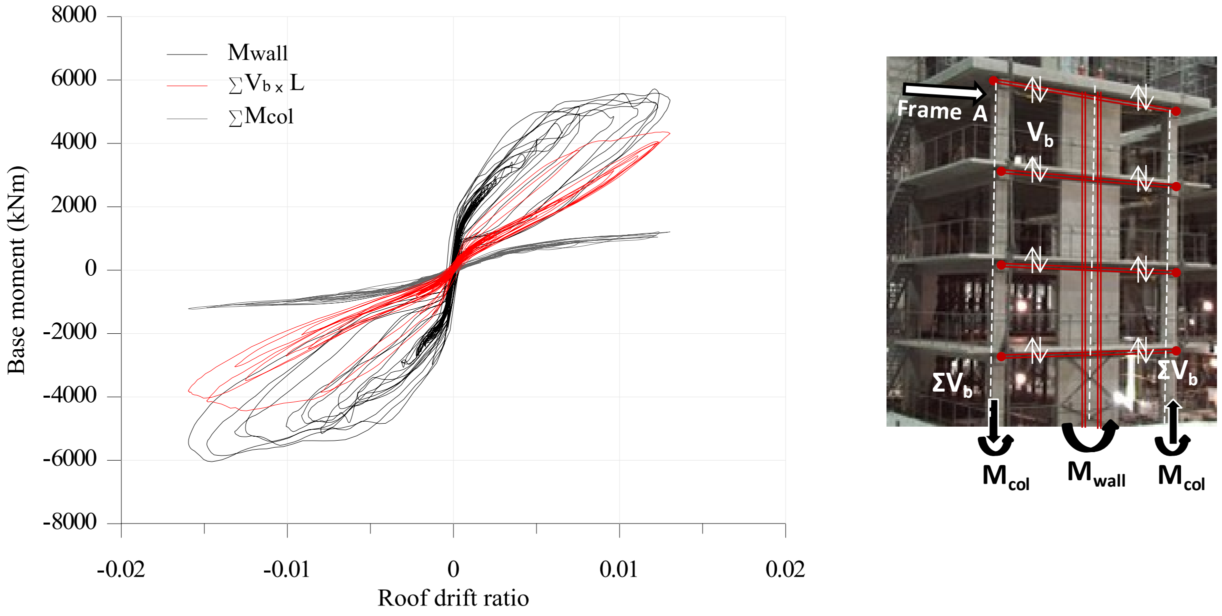

Figure 6-20 Decomposition of 100%-Kobe analytical overturning moment of Frame A into contributions from: wall moment (M_{wall}), column moments (ΣM_{col}) and framing action ($\Sigma V_b x L$)

While experimental data to validate these relative contributions are not available, and torsion and bidirectional effects were neglected in the model, these analytically derived individual contributions add up to global responses that relate favorably to the experimentally measured ones (e.g., Figure 6-10). Moreover, wall base moments from the analytical model can be directly compared to the estimated experimental wall moments that were presented in Section 5.6.7. Note that these experimental moments were estimated using data recorded by instrumentation attached to the walls (e.g. wall uplift, PT forces). Figure 6-21 compares the wall base moments derived from the analytical model under the 100%-Kobe record, with the estimated experimental wall moments of the north and south UPT walls. Consistent with observations previously made in Section 6.2.3.1, analytical results are in good agreement with experimental results for the north UPT wall in the test as the reduced moment capacity of the south UPT wall, associated with grout crushing and concrete cover spalling, is not reflected in the analytical model.

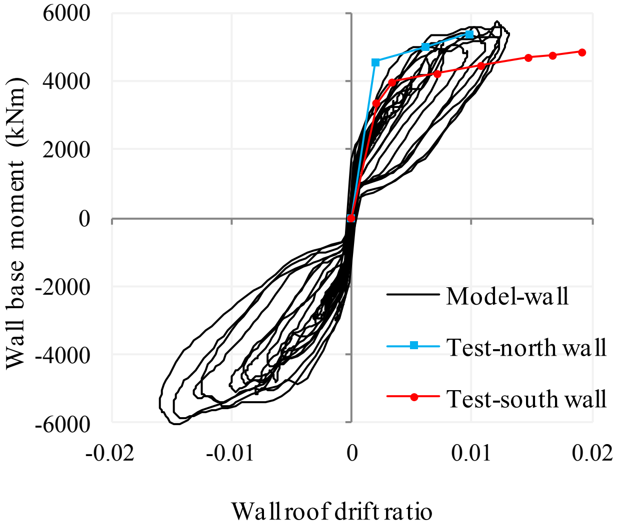

Figure 6-21 Comparisons of analytical wall moments under 100%-Kobe record to experimental wall moments of south and north UPT walls

6.4 Framing action and slab effects

As emphasized in the previous section, framing action in the context considered herein, is solely dependent on beam moments and corresponding shears, so an accurate calculation of beam moment capacities is critical in assessing framing action. In effect, if the beam capacities are known, an estimate of the maximum contribution of framing action involves a simple mechanism in which the UPT beams develop these known moment capacities at their ends.

Experimental beam local responses presented in Section 5.8 suggested that interactions of the UPT beams with the slab likely affected the measured beam responses. In discussing the modeling approach for the UPT beams and the slab in Sections 6.1.2 and 6.1.3, respectively, the beam-slab interaction mechanism and its implementation in the analytical model were presented. It was suggested that slab effects are likely to increase moment capacities and framing action by restraining gap opening from occurring at beam ends, and it was shown that, in the analytical model, the restraint is provided by the in-plane action of the slab elements. Analytical results, including beam local responses presented in Section 6.2.3.2, from the model that uses an effective membrane thickness of 25 mm, were found to be in good agreement with experimental responses. Based on results from this model, in Section 6.3 the contribution of framing action to global base moment resistance in the y-direction of the building was quantified to be 35%. This section examines the sensitivity of analytical results to the effective membrane stiffness used for the slab elements in the analytical model. The impact of the in-plane stiffness of the slab on both global lateral resistance of the building and beam local responses is examined.

In order to study these impacts, static pushover analyses using different effective membrane thickness values for the slab elements were run and compared against the 100%-Kobe experimental response (Figure 6-22). Note that the model with $t_{\mathrm{slab}} = 25$ mm coincides with the analytical model for which results have been presented in the previous sections so that the corresponding response of Figure 6-22 represents an envelope of the dynamic response shown in Figure 6-10(a). All pushover analyses were run using a displacement pattern consistent with the first mode shape of the building in the wall direction of response.

Results plotted in Figure 6-22 show that at small drifts (<0.2%), slab effects had no impact on global responses as beam rotations and beam axial growth were not sufficiently large to activate the restraint by the slab. For drift ratios between 0.2% and 1.2%, increasing the effective slab thickness increased beam moment capacities by up to 2.5 times and overall moment resistance of the building by up to 35% (at a drift ratio of 1.0%). At larger drifts, increases in effective slab thickness did not result in further increase of moment resistance, showing that the analytical model captures an upper bound of the increase in beam moment capacities from axial restraint provided by the slab. While this appears counterintuitive, considering that the model uses elastic slab elements with no limit on the effective tensile force that can develop in them, it is easily explained. At large drifts, the induced axial forces cause crushing of the concrete in compression at the bottom of the beams, which increases the neutral axis depth and limits beam moment capacities. This behavior is captured in the analytical model through the axial-flexural interaction at the inelastic beam fiber sections, but the magnitude of the induced axial forces is dependent on the assumed effective stiffness for the slab.

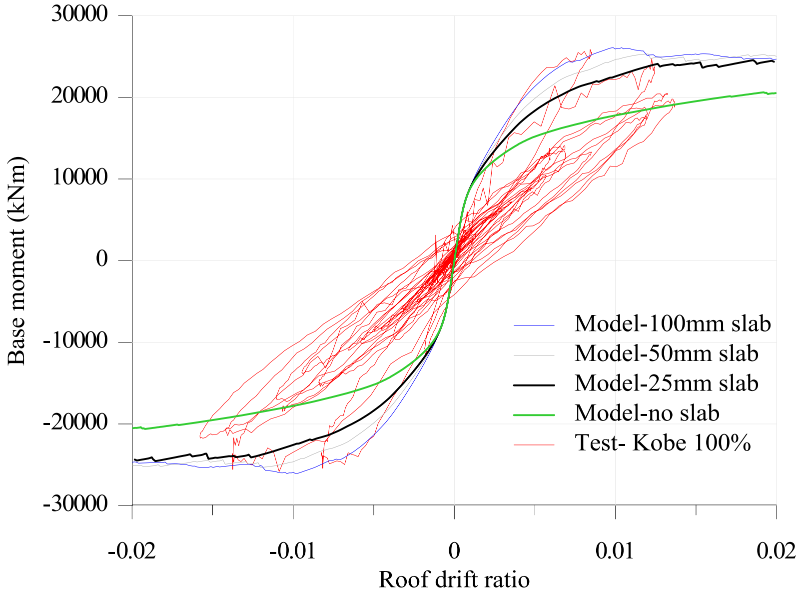

Figure 6-22 Effect of slab membrane stiffness on global moment resistance

Although direct measurements of the axial forces that developed in the beams during the experiment are not available to validate the slab model, it was possible to estimate the depth of the compression zone in the beams (neutral axis depth) and the beam elongation, using displacement measurements from the horizontal sensors that were attached to the beams at their ends (Section 5.8). These responses provide an indication of the magnitude of induced axial forces and restraint provided by the slab, and can be directly compared to analytical results. Such comparisons under the 100%-Kobe record were already shown in Section 6.2.3.2 for the model that uses an effective slab thickness of 25 mm and are repeated here for reference in Figure 6-23(b) and Figure 6-24(b). Figure 6-23(a) and Figure 6-24(a) present the same comparisons for the analytical model that uses gross membrane thickness (100mm slab) and the case of unrestrained extension (no slab).

Results of Figure 6-23 show that for negative beam rotations (tension at bottom), the neutral axis was approximately at the center of the 100-mm cast-in-place slab and was reasonably well predicted by all models. As expected, slab effects were more pronounced for positive beam rotations (tension at top). Use of gross membrane thickness caused artificially large axial forces to develop in the slab, producing a large compression zone at the bottom of the beam which exceeded experimental values. In contrast, neglecting altogether the restraint provided by the slab underestimated the beam neutral axis depth. As shown in Figure 6-23 (b), use of an effective slab thickness of 25 mm resulted in better agreement with the experimental results. Moreover, as shown in Figure 6-24, calculated beam axial growth from the same model also compared more favorably with axial growth values derived from the experimental data. Use of gross membrane thickness artificially restrained beam growth, and even resulted in compression at beam mid-height under positive rotations. In contrast, as evidenced by Figure 6-24(a), neglecting the in-plane stiffness of the slab resulted in overestimation of beam axial growth. More importantly, neglecting the in-plane stiffness of the slab resulted in significant underestimation of beam moment capacities and overall lateral resistance of the building in the wall direction (Figure 6-22).

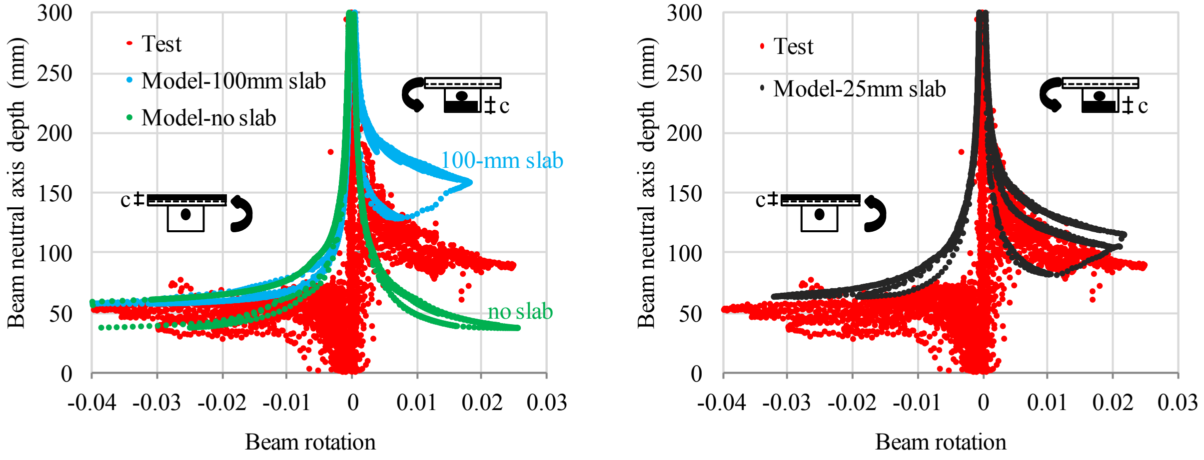

(a) **(b)**

Figure 6-23 Effect of slab membrane stiffness on beam neutral axis depth under 100%-Kobe record

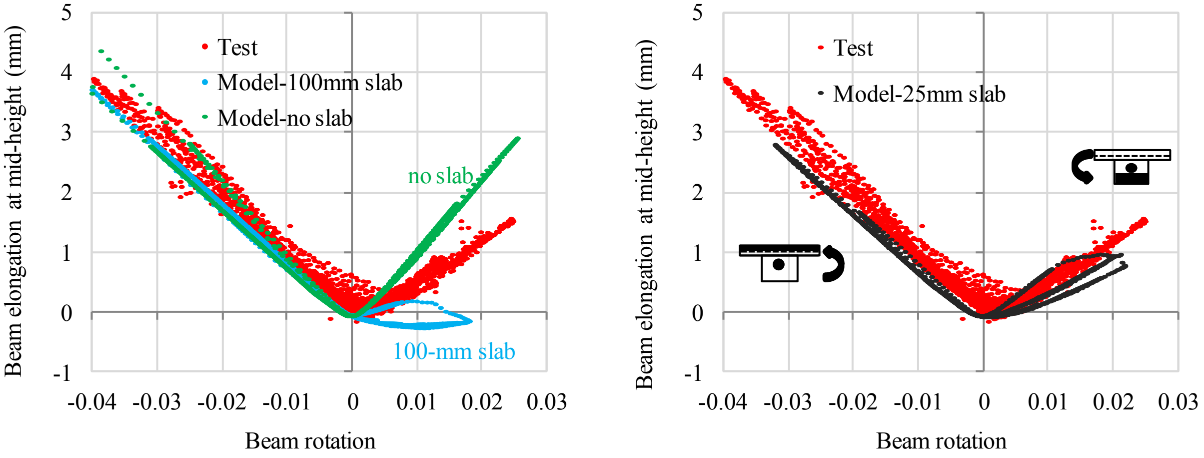

(a) **(b)**

Figure 6-24 Effect of slab membrane stiffness on beam elongation under 100%-Kobe record

While the assumption of elastic behavior with a constant membrane thickness constitutes an approximation of the actual deformability of the floor system, results in Figure 6-23 and Figure 6-24 show that, with an appropriate selection of the effective in-plane stiffness of the slab, the approach was able to capture the overall level of restraint provided by the slab during the test. However, as shown in Figure 6-22 for monotonic loading and Figure 6-9 and Figure 6-10 for dynamic loading, use of an effective stiffness also resulted in earlier softening than was observed in the test. While this limitation could be overcome with a more refined, inelastic model for the slab, this option was not explored as it would require further assumptions (e.g. degree of composite action of cast-in-place slab with pre-tensioned double tees) and calibrations beyond the scope of this study.

Although discussion so far has concentrated on (i) the impact of slab effects on beam behavior and (ii) the impact of framing action on overall moment resistance of the test building, it is also important to note design implications of such effects. With slab effects almost doubling beam flexural strength, their importance for capacity designed members and actions (beam shear design, column flexural and shear design, joint design) is obvious. It is also of interest to examine the effect of framing action on wall moment and wall shear demands.

Figure 6-25 examines, by means of pushover analyses in models with different degree of framing action (represented by the effective membrane thickness of the slab), the effect on wall base moment and wall base shear. Also included for reference is the case of the cantilever UPT wall ("wall-only model"); this differs from the "no slab" model which accounts for framing action of walls with beams and columns but neglects slab effects. The "wall-only model" is relevant since as discussed in 4.6.1, for design purposes, the two UPT walls in the building were designed to resist the entire base shear and overturning moment in the wall direction of response, neglecting contribution of framing action.

Results presented in Figure 6-25(a) show that the moment at the base of the wall at a given drift is independent of the degree of framing action, and is in this case accurately predicted by a simple cantilever model of the UPT wall (wall-only model). It is noted that if beams were to frame into the wall only on one side, the wall axial load and base moment would be influenced by framing action. Figure 6-25(b) shows that, as expected, the wall base shear increased with increasing degree of framing action. At 1.5% roof drift ratio, the wall base shear predicted by a model using an effective slab thickness of 25 mm is approximately 30% higher than the base shear of the cantilever wall at the same drift. While these increases did not adversely affect the behavior of the UPT walls in the E-Defense test building in any way (note that wall shear capacities presented in Section 4.6.5 exceeded 2,000 kN at all levels), results of Figure 6-25(b) indicate that the effects of framing action should be evaluated when defining wall shear demands.

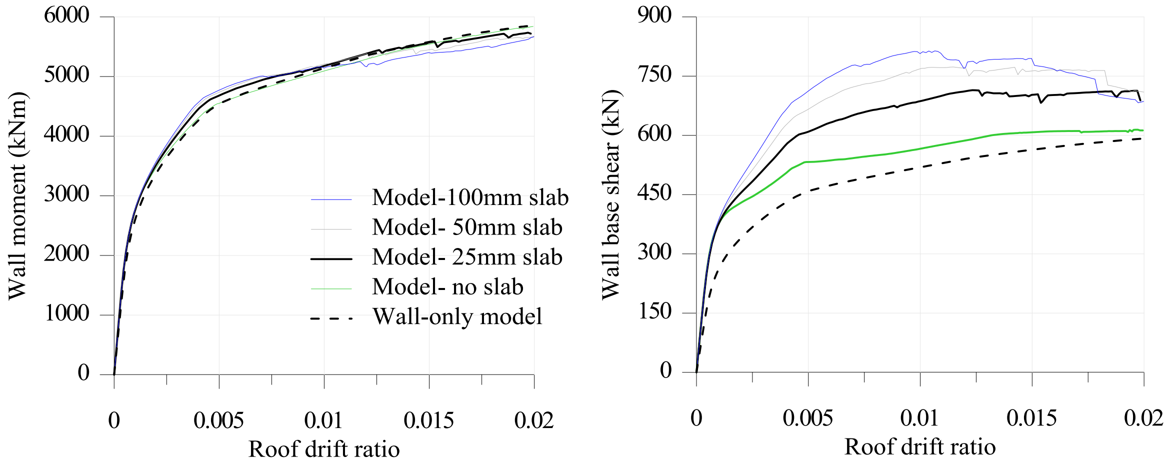

(a) **(b)**

Figure 6-25 Effect of framing action on: (a) wall base moment; (b) wall base shear

Finally, using results from pushover analyses in (i) the model that uses an effective slab thickness of 25 mm and (ii) the wall-only model (cantilever wall), Figure 6-26 compares the distribution of wall moments and wall shears along the height of the wall between the two models. In both models, wall moments and shears were extracted at a reference roof drift ratio of

1.5%. As noted above, a larger force is required (approximately 30% higher) to displace the wall to that drift when framing action is considered. As shown in Figure 6-26(a), although framing action did not affect the wall base moment (at 1.5% drift), wall moments along the height of the wall were affected by the reactions- shear forces and moments- of the framing UPT beams. Framing action had an even more significant impact on wall shear forces along the height of the wall. Results in Figure 6-26(b) show that increases in wall shear forces in excess of 50% were obtained due to framing action.

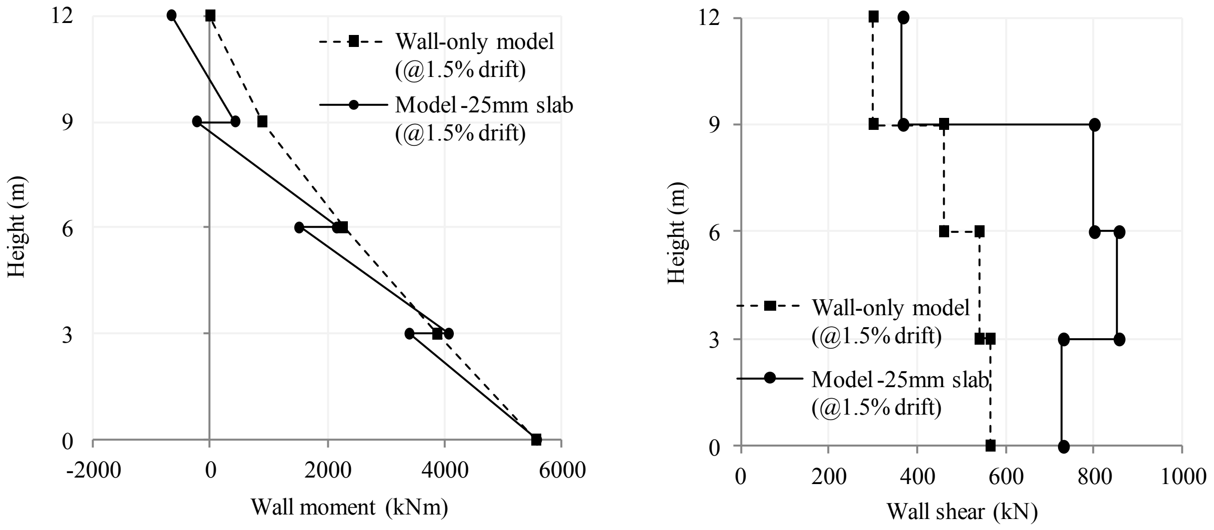

(a) **(b)**

Figure 6-26 Effect of framing action on: (a) wall moments; (b) wall shear forces along the height of the wall

While discussion of design implications of framing action so far has concentrated on force demands (e.g., increases in wall shear forces), it is also worth pointing out that framing action and slab effects need to be considered to obtain a realistic estimate of displacement demands in the E-Defense PT building. As was shown in Figure 6-9 and Figure 6-10, the model that uses an effective slab thickness of 25 mm provided very good predictions of measured peak roof drift ratios under the 50%-Kobe and 100%-Kobe records. Note that if slab effects are neglected ("no slab" model in Figure 6-22 and Figure 6-25), the lateral resistance of the building would be significantly underestimated as evidenced by the pushover curve of Figure 6-22, and accordingly, the displacement demands under dynamic loading would be overestimated. More specifically, the model that neglects slab effects predicts approximately 65% higher peak displacements under the 50%-Kobe record than what was observed in the test, and approximately 40% higher peak displacements under the 100%-Kobe record.

Results presented in this section indicate that framing action and beam axial growth effects had a significant impact on responses of the E-Defense PT building (e.g., on beam flexural strengths, wall shear demands, displacement demands). Prior experimental research on both UPT and RC wall buildings has also shown gravity framing and coupling through slabs to have a significant effect on global lateral resistance and wall shear demands (Thomas and Sritharan 2004, Panagiotou et al. 2011). Similarly, axial growth effects are not limited to UPT concrete beams; similar effects occur in conventional (monolithic) RC beams. While in UPT beams the growth is associated with the gap opening at beam ends, in conventional RC beams axial growth is related to concrete cracking and steel yielding, which cause the neutral axis to shift towards the compression side, and beam length at its centerline to increase. Prior analytical and experimental research on frame structures (MacRae and Gunasekaran 2006, Kim et al. 2004, Lau and Fenwick 2002, Kabeyasawa et al. 2000, Fenwick et al. 2005, 2010) has shown that restraint of such elongation, through the presence of a slab or the beam boundary conditions, can have a significant impact on beam flexural strength and column demands.

The studies presented in this section provided additional insight into framing action and axial growth effects and indicated that, although typically ignored in design and analysis of buildings, these effects can have a significant impact on responses and need to be evaluated to successfully implement capacity design principles and obtain realistic estimates of force and displacement demands.

6.5 Summary

Building on the information presented in Chapters 4 and 5, a nonlinear model of the wall direction of the four-story post-tensioned precast concrete building that was tested on the E-Defense shake table was developed. Experimental results in this direction were used to assess the ability of the analytical model to capture the dynamic responses and interactions of unbonded post-tensioned (UPT) structural systems.

The analytical model of the test building used a combination of inelastic fiber sections (for walls, beams and columns), inelastic truss elements (for unbonded PT steel, unbonded lengths of energy dissipating bars) and elastic slab (membrane) elements. The analytical results were found to provide good simulations of observed global responses, with satisfactory correlations between predicted and measured roof displacements, overturning moments and story shears. Peak values of global roof drift, overturning moment, and base shear from the model were all within 5.0% of the measured peak values during the test. While roof drift ratios were well predicted, some discrepancies were observed in the vertical distribution of drift along the height of the building. These were largely associated with overestimation of wall uplift at the second level joint in the analytical model.

Decomposition of base moment resistance of the building into its components showed that coupling of the walls to the corner columns, through the UPT beams and slab, contributed significantly to lateral resistance of the building. Using results from the analytical model, the relative contributions to the building's overturning moment were quantified as follows: wall base moments provided 45% of the building's moment resistance, the interior one-bay frame contributed 10%, moments at the bases of the four corner columns provided another 10%, and the remaining 35% was provided by force couples forming at the column bases of the exterior frames, referred to as framing action herein.

Contribution of framing action in the building was accentuated by interactions of UPT beams with the floor system. By restraining beam axial growth, the slab induced axial compressive forces in the beams that increased beam flexural capacities and framing action. These effects were captured in the analytical model by interactions between the axial-flexural behavior of beam fiber sections and the in-plane action of slab elements. The in-plane stiffness of the elastic slab elements in the analytical model was shown to have a significant impact on both global behavior and local beam responses, such as beam elongation and neutral axis depth. Despite limitations of using elastic slab elements, it was found that an effective slab membrane stiffness equal to 25% of gross stiffness produced analytical results in satisfactory agreement with experimental results for a range of global and local responses.

In addition to experimental verification of the proposed computational model, the analytical studies presented provided insight into design implications of system interactions, such as increases in beam flexural strength due to axial restraint provided by the slab and increases in wall shear forces due to framing action.

Chapter 7 Summary and conclusions

The work presented herein is aimed at further advancing knowledge on unbonded post-tensioned (UPT) concrete structural systems and promoting their wider use by (i) providing experimental evidence of their seismic performance, including data to address system interactions and (ii) validating design methodologies and analysis tools that are ultimately required to move these systems into practice.

7.1 Test significance

The experimental program documented herein provided unique data on seismic response of UPT precast concrete walls incorporated into an entire building system. The experiment was conducted in 2010 at the E-Defense shake table facility in Japan and included dynamic testing of a full-scale, four-story precast concrete building using recorded ground motions from the 1995 Kobe earthquake. The building utilized unbonded post-tensioned concrete walls in one direction of response and bonded post-tensioned concrete frames in the orthogonal direction. Performance of the test building in the wall direction, exhibiting minimal damage and no residual deformations, confirmed that UPT walls are a viable alternative to conventional RC structural walls.

By using a full-scale physical model with sufficient complexity to represent typical connections and interactions of a real building, while subjected to realistic loading histories expected during earthquake shaking, the tests provided valuable insight into issues typically not addressed in component-level experimental studies, such as the role of the floor diaphragm, influence of component interactions, and contributions of three dimensional responses and torsion.

7.2 UPT wall performance

Overall response of the test building in the wall direction was dominated by gap opening at the bases of the UPT walls (rocking), with displacement profiles along the height of the building being almost linear. The peak roof drift ratio during the tests was equal to 1.58% at the center of plan, while residual drift at the end of the tests was minor (on the order of 0.1%). Calculated peak displacements for the south and north UPT walls differed from the center of plan displacement due to torsional response. Peak wall roof drift ratios were equal to 1.07% for the north wall, and 2.09% for the south wall. Both UPT walls achieved the ACI ITG-5.2 design drift, θ_{design} = 0.95%, and in addition, the south wall was displaced to approximately 70% of the maximum ACI ITG-5.2 drift, $\theta_{\max}$ = 3.0%. Despite their large magnitude, out-of-plane drifts in the moment frame direction, did not adversely affect the in-plane behavior of the UPT walls, as they were largely accommodated by out-of-plane rocking of the walls against the foundation. Interaction of the UPT walls with the framing UPT beams and the floor system, played a significant role in the global resistance of the building in the wall direction. This is further discussed in Section 7.5.

Lack of fiber reinforcement in the grout at the base of the south UPT wall adversely affected the performance of the base joint. During the 100%-Kobe record, the grout crushed and partly fell out while concrete spalling also occurred at the compressive corners of the lower precast panel, extending above the foundation over a height approximately equal to the thickness of the wall. In the north UPT wall, which contained steel fiber reinforcement, the grout pad remained intact as it moved upward together with the wall panel, and only minor cosmetic spalling occurred at a corner of the lower precast panel. Due to differences in performance of the base joints of the two UPT walls, significant torsional response was observed in the building during the tests. The torsional component of displacement increased with increasing seismic intensity resulting in peak displacements at the south wall approximately twice the peak displacements of the north wall, as noted above.

Although lack of fiber reinforcement adversely affected the behavior of the south wall and led to faster degradation, damage in the south wall was still repairable and localized at the base. No cracking developed at the upper portion of wall, and despite the partial crushing of the interface grout, no prestress losses occurred and no sliding was observed at the base of the south wall. This level of performance is still superior to expected performance of conventional RC walls under same intensity seismic actions.

7.3 Design implications

ACI ITG-5.2 is currently the only codified (ACI 318-11, R21.10.3) design Standard for UPT walls in the United States. While it has been previously validated against moderate-scale component tests under static cyclic loading, it has not yet been benchmarked against full-scale building tests under dynamic loading. The experimental program documented herein provided a wealth of data for validation of ACI ITG-5.2 design provisions. A detailed assessment of the E-Defense UPT wall design, indicated that the walls met the majority of ACI ITG-5.2 design requirements including moment and shear strength requirements at the base, moment contribution from energy-dissipating steel, minimum initial prestress, strain limits in PT and ED steel, and confinement at the corners of the base wall panels. Provisions not satisfied include: location of PT steel in the wall section, properties of the wall-foundation interface grout of the south UPT wall, and design of the second floor panel-to-panel horizontal joints. Based on the performance of the two UPT walls during the tests, the following design implications were identified:

- The post-tensioning steel in the E-Defense UPT walls was located at 15% of the wall length on either side of the wall centroid, exceeding the ACI ITG-5.2 limit of 10%. Based on the performance of the walls in the test (south wall reached 1.94% base rotation without yielding of PT steel, no prestress losses and no residual deformations), a relaxation of the 10% limit may be justified. This would allow applicability of ACI ITG-5.2 to a wider range of UPT wall configurations, and even extension to non-planar walls pending experimental validation. As evidenced by the test, yielding of the PT steel can be effectively controlled through appropriate selection of initial prestress and consideration of exact locations of PT steel in the design process.
- Peak measured concrete compressive strains at the ends of the north and south UPT walls during the 100%-Kobe record were 0.0085 and 0.025, respectively; with corresponding peak base rotations of 1.02% and 1.94%, respectively. For the purposes of designing the confining reinforcement at the wall toes, ACI ITG-5.2 assumes, constant strain over an equivalent plastic hinge length $L_p = 0.06H_w$ (where H_w is the wall height), so that $\varepsilon_{c,max} = \theta_{max}c/L_p$, where c is the estimated neutral axis depth at θ_{max}. This assumption resulted in an estimated strain of $\varepsilon_{c,max} = 0.0087$ at $\theta_{max} = 3.0\%$ for the E-Defense walls. Noting that the north wall developed similar strains at a wall base rotation of only 1.02%, and that peak strain in the south wall was almost three times that estimated by ACI ITG-5.2, a reexamination of the expression for the equivalent plastic hinge length for UPT walls L_p is warranted. It was suggested herein that, instead of L_p, which appears more appropriate for conventional RC walls, a height $H_{cr} \leq (1.5t_w, c)$ be used for estimating strain demands on UPT walls. H_{cr}

represents the height above the base over which nonlinear behavior of the concrete in compression is expected to extend. Recommended limits for H_{cr} were based on review of prior experimental results of UPT walls, and were also shown to provide good estimates of peak strains for the E-Defense walls (0.03 strain at $\theta_{max} = 3.0\%$).

- The marked difference in performance of the two UPT walls in the test building as described in the previous section emphasizes that behavior of UPT walls is largely dependent on the ability of the critical base joint to sustain large local compressive strains in a ductile manner, without significant degradation of concrete or grout. Lack of fiber reinforcement in the grout at the wall-foundation interface of the south UPT wall adversely affected the performance of the wall and validated the appropriateness of the ACI ITG-5.2 requirement for a minimum amount of fiber reinforcement in the grout. In contrast, inclusion of fiber reinforcement in the concrete mix of the north wall panels (in addition to the interface grout), although not required by ACI ITG-5.2, resulted in excellent performance and only minor cosmetic damage in the north UPT wall. In keeping with the objective of an essentially damage-free structural system, incorporating high performance materials in UPT walls deserves further exploration.
- Finally, although design of upper joints is not addressed in detail in ACI ITG-5.2, the intent of the Standard is that all inelastic demand be concentrated at the critical wall-to-foundation interface, and gap opening at upper panel-to-panel horizontal joints be prevented through capacity design principles. A simple approach for assessing whether uplift is expected at upper joints was presented and recommendations on flexural design of upper joints of UPT walls were discussed. It is noted that while both design calculations and analytical results predicted uplift at the horizontal joint between the first and second story precast panels of the E-Defense UPT walls, no significant gap opening at upper joints was observed during the

tests. Given these discrepancies, further studies are required to establish design and modeling recommendations for upper joints of UPT walls. This is especially true for taller walls where design of upper joints can be critical due to increased moment demands above the base, as a result of higher mode effects.

7.4 Analytical tools

As experimental investigations on dynamic behavior and interactions of UPT systems are limited to-date, the 2010 E-Defense tests provided unique data against which analytical models for UPT systems can be benchmarked. To this end, a nonlinear analytical model of the wall direction of the E-Defense PT building was developed and subjected to the accelerations observed on the shake table in that direction. The analytical model used a combination of inelastic fiber sections (for walls, beams and columns), inelastic truss elements (for unbonded PT steel, unbonded lengths of energy dissipating bars) and elastic slab elements. Behavior of individual components of the model (UPT walls, UPT beams) under static loading was first validated by comparisons with prior static cyclic tests of cantilevered UPT walls and UPT beam-column sub-assemblages. These separate component-level analytical studies validated the ability of the proposed models to capture the force-deformation characteristics of individual UPT components under static cyclic loading.

The ability of the model to capture the dynamic responses and system interactions of the test building was then assessed through comparisons of analytical and experimental results for a range of global and local responses, including story lateral displacements, story shear forces and moments, and gap opening displacements due to rocking at the wall base. It was shown that the in-plane stiffness of the elastic slab elements in the analytical model had a significant impact on predicted global lateral resistance of the building and local beam responses. These impacts were largely associated with restraint of beam axial growth provided by the slab, and were captured in the analytical model by the interaction between the axial-flexural behavior of beam fiber sections and the in-plane action of slab elements. Despite limitations of using elastic slab elements, it was found that an effective slab membrane stiffness equal to 25% of gross stiffness produced analytical results in satisfactory agreement with experimental results for a range of global and local responses; peak values of global roof drift, overturning moment, and base shear from the model were all within 5.0% of the measured peak values during the test. Wall local responses such as base uplift, concrete strains and PT forces from the analytical model correlated well with measured responses for the north UPT wall, as the degradation associated with crushing of the grout that occurred at the base of the south wall was not reflected in the analytical model. Finally, good correlations were also observed between analytical and experimental beam local responses such as beam elongation and beam neutral axis depth.

7.5 System interactions

In addition to validating the proposed computational model, the analyses allowed investigations of system interactions such as framing action resulting from coupling of the UPT walls to the corner columns through the UPT beams and floor system, and assessment of slab effects and axial growth on UPT beam flexural capacities. Design implications of these interactions were also identified.

Decomposition of base moment resistance of the building into its components showed that coupling of the walls to the corner columns, through the UPT beams and slab, contributed significantly to lateral resistance of the building. Using results from the analytical model, the relative contributions to the building's overturning moment were quantified as follows: wall base moments provided 45% of the building's moment resistance, the interior one-bay frame contributed 10%, moments at the bases of the four corner columns provided another 10%, and the remaining 35% was provided by force couples forming at the column bases of the exterior frames, referred to as framing action herein. Given its large contribution to lateral resistance, framing action needs to be considered to obtain realistic estimates of displacement demands and wall shear demands of the E-Defense test building; increases in wall shear demands due to framing action amounted to approximately 30%. The increase in shear demand was not a factor for the E-Defense building, as the wall nominal shear capacity was very high.

It is noted here that while ACI ITG-5.2 recognizes the potential for increased wall shear demands due to contributions of gravity framing supported on wall ends, "these contributions shall not be assumed to contribute to the strength of the shear wall system" (Section 4.6). Given observations from the E-Defense tests as well as prior experimental research on both UPT and conventional RC wall buildings, it is recommended that the effects of framing action on wall shear demands be evaluated, even when neglected for design purposes (e.g. for design drift calculations). Contribution of framing action in the E-Defense building was accentuated by interactions of the UPT beams with the floor system. By restraining beam axial growth, the slab induced axial compressive forces in the beams that increased beam flexural capacities by almost two times. In addition to increasing contribution of framing action, the increased beam flexural strengths have obvious implications on capacity designed members and actions.

These results show that although typically ignored in design and analysis of buildings, framing action and beam axial growth effects can have a significant impact on responses and need to be considered to successfully implement capacity design principles and obtain realistic estimates of force and displacement demands.

7.6 On-going and future studies

The analytical model of the E-Defense PT building that was described herein included the frames along axes A, B and C in the wall (y) direction of the building, and was subjected to the y-direction accelerations observed on the shake-table during the test. Limitations of the analytical model include its inability to capture bidirectional effects and torsional response. Limitations associated with use of elastic slab elements with an effective (constant) membrane thickness have also been identified (e.g. earlier softening than what was observed in the test). Possible improvements to the analytical model of the E-Defense PT building that was presented herein include: (i) implementation of inelastic elements for the slab, and (ii) inclusion of the x-direction bonded PT beams in the model and simultaneous application of the x- and y-direction accelerations observed on the shake table.

Future studies related to design and analysis of UPT concrete systems will focus on extension of design and analysis tools presented herein to walls of different proportions and configurations. Of particular interest are: (i) applications to low aspect ratio UPT walls for which contributions of shear deformations could be significant and require further analytical and experimental investigations, (ii) application to tall buildings and assessment of sensitivity of UPT wall systems to higher mode effects, (iii) extension to non-planar walls, such as U or C-shaped UPT walls, which are not covered by ACI ITG-5.2 and require special considerations e.g., eccentricity of PT steel with respect to the geometric centroid of the section can induce moment/drift upon application of prestress.

Future studies with respect to performance and responses of the E-Defense PT building will focus on detailed comparisons with equivalent responses of the RC building that was tested simultaneously on the shake table. Responses of interest include wall local responses, such as concrete strains and wall axial growth (gap opening versus cracking/yielding), global responses such as floor accelerations, and finally, a comparative assessment of system interactions effects in both buildings (framing action, slab effects). Such comparisons would allow (i) differences in seismic performance of the two systems, when subjected to seismic actions of the same intensity, to be quantified, and (ii) an assessment of whether these differences are considered in the design process. Note that, for UPT walls designed in accordance with ACI ITG-5.2, design forces and design drifts are the same as for equivalent RC special structural walls (same response modification factor R and displacement amplification factor C_{d}).

Finally in keeping with the objective of promoting wider use of UPT concrete structural systems in practice, and demonstrating that they are an economically viable alternative to conventional RC systems, a series of comparative case studies of seismic performance and life-cycle costs of UPT and equivalent RC wall buildings will be compiled using the methodology of FEMA P-58. Preliminary results from these studies have been presented in Gavridou et al. 2014 and Zimmerman et al. 2015.

References

1. Aaleti, S. and Sritharan S. (2009). "A simplified analysis method for characterizing unbonded post-tensioned precast wall systems." *Engineering Structures*, 31, 2966-2975.
2. American Concrete Institute (ACI) Committee 318 (2011). "*Building code requirements for structural concrete (ACI 318-11) and commentary.*" ACI, Farmington Hills, MI.
3. ACI Innovation Task Group 5 (2007). "*Acceptance criteria for special unbonded post-tensioned precast structural walls based on validation testing (ITG 5.1-07)*." ACI, Farmington Hills, MI.
4. ACI Innovation Task Group 5 (2009). "*Requirements for design of a special unbonded post-tensioned precast shear wall satisfying ACI ITG-5.1 (ITG 5.2-09)*." ACI, Farmington Hills, MI.
5. ACI 374.1 (2005). "*Acceptance criteria for moment frames based on structural testing and commentary*." ACI, Farmington Hills, MI.
6. American Society of Civil Engineers/Structural Engineering Institute (ASCE/SEI) Committee 7 (2010). "*Minimum design loads for buildings and other structures (ASCE/SEI 7-10).*" Reston, VI.
7. Beyer, K. (2007). "Seismic design of torsionally eccentric buildings with RC U-shaped walls." *PhD thesis*, ROSE School, IUSS, Pavia.
8. Beyer K., Dazio A., and Priestley, M. J. N. (2011). "Shear Deformations of Slender Reinforced Concrete Walls under Seismic Loading." *ACI Struct. J.*, 108(2), 167-177.

9. Bradley B.A., Dhakal R.P., Mander, J.B. and Li, L. (2008). "Experimental multi-level seismic performance assessment of 3D RC frame designed for damage avoidance." *Earthquake Eng. Struct. Dyn.*, 37(1), 1–20.
10. Buchanan, A.H. , Bull, D., Dhakal, R., MacRae, G., Palermo, A., and Pampanin S. (2011). "Base isolation and damage-resistant technologies for improved seismic performance of buildings." *Research Report 2011-02*, University of Canterbury, New Zealand.
11. Cheok G.S. and Lew H.S. (1991). "Performance of precast concrete beam-to-column connections subjected to cyclic loading." *PCI J.*, 36(3), 56-67.
12. Cheok G.S. and Lew H.S. (1993). "Model precast concrete beam-to-column connections subjected to cyclic loading." *PCI J.*, 38(4), 80-92.
13. Cheok G.S. and Stone W.C. (1994). "Performance of 1/3-scale model precast concrete beam-column connections subjected to cyclic inelastic loads- Report No. 4" *Report NISTIR 5436*, National Institute of Standards and Technology, Gaithersburg, MD.
14. Cheok G.S., Stone W.C, and Nakaki S.D. (1996). "Simplified design procedure for hybrid precast concrete connections" *Report NISTIR 5765*, National Institute of Standards and Technology, Gaithersburg, MD.
15. Christopoulos, C., Pampanin, S., and Priestley, M.J.N. (2003). "Performance-based seismic response of frame structures including residual deformations. Part I: Single-Degree-of-Freedom Systems." *Journal of Earthquake Engineering*, 7(1), 97-118.
16. Christopoulos, C., Pampanin, S., and Priestley, M.J.N. (2004). "Seismic design and response of buildings including residual deformations". *Proceedings of the 13th World Conference on Earthquake Engineering*, Vancouver, B.C., Canada.

17. CSI Perform-3D V5 (2011a). "Nonlinear analysis and performance assessment for 3D structures." *Computer and Structures, Inc*, Berkeley, CA.

18. CSI Perform-3D V5 (2011b). "Components and elements for Perform-3D and PERFORM-COLLAPSE." *Computer and Structures, Inc*, Berkeley, CA.

19. Collins, M. P., Mithell, D. (1997). "Prestressed concrete structures." *Response publications*, Canada

20. Eatherton, M.R., Ma, X., Krawinkler, H., Mar, D., Billington, S., Hajjar, J.F., and Deierlein, G.G. (2014). "Design concepts for controlled rocking of self-centering steel-braced frames." *J. Struct. Eng.*, 10.1061/(ASCE)ST.1943-541X.0001047, 04014082.

21. Ebernhard, M. O., and Sozen, M. A. (1993). "A behavior-based method to determine design shear in earthquake-resistant walls." *J. Struct. Eng.*, 119(2), 619–640.

22. El-Sheikh, M., Pessiki, S., Sause, R., and Lu, L. W. (2000). "Moment rotation behavior of unbonded post-tensioned precast concrete beam-column connections." *ACI Struct. J.*, 97(1), 122-131.

23. FEMA P-58 (2012). Seismic Performance Assessment of Buildings. *Federal Emergency Management Agency*, Washington, D.C.

24. Gavridou, S., Melek, M., Wallace, J. W. (2014). "Conventional and unbonded post-tensioned lateral force resisting systems– A comparative assessment of expected performance and losses." *Proc. 10th National Conf. in Earthquake Eng.*, Earthquake Eng. Research Institute, Anchorage, AK.

25. Fenwick, R., Bull, D. K., and Gardiner, D. (2010). "Assessment of hollow-core floors for seismic performance." *Research report 2010-02*, Dept. of Civil and Natural Resources Eng., University of Canterbury, Christchurch, NZ.

26. Fenwick, R.C., Davidson B. J. and Lau, D.B.N. (2005). "Interaction between ductile RC perimeter frames and floor slabs containing precast units." *2005 NZSEE Conference*

27. Henry, R.S., Brooke, N.J., Sritharan, S. and Ingham, J.M. (2012). "Defining concrete compressive strain in unbonded post-tensioned walls." *ACI Struct. J.*, 109(1), 101-112.

28. Henry, R. S. (2011). "Self-centering precast concrete walls for buildings in regions with low to high seismicity." *PhD thesis*, University of Auckland, Auckland.

29. Holden, T., Restrepo, J., and Mander, J.B. (2003). "Seismic performance of precast reinforced and prestressed concrete walls." *J. Struct. Eng.*, 129(3), 286-296.

30. Kam WY, Pampanin S, Elwood K. (2011). "Seismic performance of reinforced concrete buildings in the 22 February Christchurch (Lyttelton) earthquake." *Bulletin of the New Zealand Society for Earth. Eng.,* 44 (4), 239-278.

31. Kabeyasawa, T., Sanada Y., and Maeda M. (2000). "Effect of beam axial deformation on column shear in reinforced concrete frames." *Proceedings of the 12th World Conference on Earthquake Engineering*, Auckland, New Zealand.

32. Kawashima, K., MacRae G., Hoshikuma, J., and Nagaya, K. (1998). "Residual displacement response spectrum and its application." *J. Struct. Eng.*, 124(5), 523-530.

33. Kim, J., Stanton, J.F., and MacRae, G.A. (2004). "Effect of beam growth on reinforced concrete frames." *J. Struct. Eng.*, 130(9), 1333-1342.

34. Kolozvari, K., Orakcal, K., and Wallace, J. W. (2014). "Modeling of cyclic shear-flexure interaction in reinforced concrete structural walls. Part I: Theory." *J. Struct. Eng.*, 10.1061/(ASCE)ST.1943-541X.0001059, 04014135.

35. Kurama, Y. C., Pessiki, S., Sause, R., Lu, L.-W., and El-Sheikh, M. (1996) "Analytical modeling and lateral load behavior of unbonded post-tensioned precast concrete walls."

Center for Advanced Technology for Large Structural Systems (ATLSS), *Report No. EQ-96-02*, Lehigh University, Bethlehem, PA.

36. Kurama, Y. C. (2001). "Simplified seismic design approach for friction-damped unbonded post-tensioned precast walls.", *ACI Struct. J.*, 98(5), 705-716.
37. LATBSDC (2008). "An alternative procedure for seismic analysis and design of tall buildings located in the Los Angeles region.", *Los Angeles Tall Buildings Structural Design Council*, Los Angeles, CA.
38. Lau, D. and Fenwick, R. (2002). "The influence of precast prestressed flooring components on the seismic performance of reinforced concrete perimeter frames", *SESOC J.*, 14(2), 17-26.
39. MacRae, G.A. and Kawashima, K. (1997). "Post-Earthquake Residual Displacements of Bilinear Oscillators". *Earthquake Engineering and Structural Dynamics*.", Vol. 26, 701-716.
40. MacRae, G.A. and Gunasekaran, U. (2006). "A concept for consideration of slab effects on building seismic performance" *2006 NZSEEE Conference*.
41. Mander, J. Priestley, M., and Park, R. (1988a). "Theoretical stress-strain model for confined concrete." *J. Struct. Eng.*, 114(8), 1804-1826.
42. Mander, J., Priestley, M., and Park, R. (1988b). "Observed stress-strain behavior of confined concrete." *J. Struct. Eng.*, 114(8), 1827-1849.
43. Marriott, D., Pampanin, S., Bull, D., and Palermo, A. (2008). "Dynamic testing of precast, post-tensioned rocking wall systems with alternative dissipating solutions." *Bulletin of the New Zealand Society for Earthquake Engineering*, 41(2), 90-103.

44. Marriott, D. Pampanin, S., Palermo, A. (2009). "Quasi-static and pseudo-dynamic testing of unbonded post-tensioned rocking bridge piers with external replaceable dissipaters." *Earthquake Engineering & Structural Dynamics*, 38(3), 331-354.

45. Massone L.M. and Wallace J.W (2004). "Load-deformation response of slender reinforced concrete walls." *ACI Struct. J.* 101(4), 103-113.

46. Moaveni, B., He, X., Conte, J. P., Restrepo, J. I., and Panagiotou, M. (2011). "System identification study of a 7-story full-scale building slice tested on the UCSD-NEES shake table." *J. Struct. Eng*., 137(6), 705–717.

47. Nagae, T., Tahara, K., Taizo, M., Shiohara, H., Kabeyasawa, T., Kono, S., Nishiyama, M., Wallace, J.W., Ghannoum, W.M., Moehle, J.P., Sause, R., Keller, W., and Tuna, Z. (2011). "Design and instrumentation of the 2010 E-Defense four-story reinforced concrete and post-tensioned concrete buildings." *PEER Report 2011/104*, Berkeley, CA.

48. Nagae T., Tahara K., Fukuyama K., Matsumori T., Shiohara H., Kabeyasawa T., Kono S, Nishiyama M., Moehle J.P, Wallace J.W., Sause R, and Ghannoum W.M. (2012). "Test results of Four-Story Reinforced Concrete and Post-Tensioned Concrete Buildings: The 2010 E-Defense Shaking Table Test." *Proceedings of the 15th World Conference on Earthquake Engineering*, Lisbon, Portugal.

49. Nakaki, S. D., Stanton, J. F., and Sritharan, S. (1999). "An overview of the PRESSS five-story precast test building." *PCI J.,* 44(2), 26-39.

50. Nazari, M., Aaleti, S., and Sritharan S. (2014). "Shake table testing of unbonded post-tensioned precast concrete walls." *Proc. 10th National Conf. in Earthquake Eng.*, Earthquake Eng. Research Institute, Anchorage, AK.

51. NEEShub project 2011-1005, https://nees.org/warehouse/report/project/1005

52. New Zealand Standards, NZS (2006). Appendix B: Special provisions for the seismic design of ductile jointed precast concrete structural systems, NZS 3101:2006, *Concrete standards New Zealand*, Wellington, NZ.

53. NZCS (2010). *PRESSS Design Handbook*. Wellington New Zealand, New Zealand Concrete Society.

54. Oh, B. (2002). "A Plasticity Model for Confined Concrete Under Uniaxial Loading". *Ph.D. Dissertation*, Department of Civil and Environmental Engineering, Lehigh University, Bethlehem, PA.

55. Okada, T., Kabeyasawa, T., Nakano, T., Maeda, M., Nakamura, T. (2000) "Improvement of seismic performance of reinforced concrete school buildings in Japan - Part 1: Damage survey and performance evaluation after the 1995 Hyogo-Ken Nambu earthquake". *Proceedings of the 12th world conference on earthquake engineering*, Auckland, New Zealand.

56. Palermo, A. Pampmanin S., Buchanan, A. (2006). "Experimental investigations on LVL seismic resistant wall and frame subassemblies." *First European Conference on Earthquake Engineering and Seismology*, Geneva, Switzerland

57. Pampanin, S., Christopoulos, C., Priestley, M.J.N. (2003). "Performance-based seismic response of frame structures including residual deformations. Part II: Multi-Degree-of-Freedom Systems." *Journal of Earthquake Engineering*, 7(1), 119-147.

58. Pampanin, S., Priestley, M.J.N. and Sritharan, S. (2001). "Analytical Modeling of the Seismic Behavior of Precast Concrete Frames Designed with Ductile Connections." *Journal of Earthquake Engineering*, 5(3), 329-367.

59. Panagiotou, M., Restrepo, J.I., and Conte, J.P. (2011). "Shake-table test of a full-scale 7-story building slice. Phase I: Rectangular wall." *J. Struct. Eng.*, 137(6), 691–704.

60. Parra-Montesinos, G.J., Canbolat, B.A., and Jeyaraman, G. (2006). "Relaxation of confinement reinforcement requirements in structural walls through the use of fiber reinforced cement composites." *8th National Conference on Earthquake Engineering*, San Francisco, CA.

61. PEER/ATC-72-1. (2010). Modeling and acceptance criteria for seismic design and analysis of tall buildings. *Applied Technology Council*, Redwood City, CA.

62. Pennucci, D, Calvi, G.M. and Sullivan, T. (2009). "Displacement-based design of precast walls with additional dampers." *J. Earthquake Eng.*, 13(S1), 40-65.

63. Perez, F.J., Pessiki, S., and Sause, R. (2004). Experimental and analytical lateral load response of unbonded post-tensioned precast concrete walls, Center for Advanced Technology for Large Structural Systems (ATLSS), *Report No. 04-11*, Lehigh University, Bethlehem, Pa.

64. Perez, F.J., Pessiki, S., and Sause, R. (2013). "Experimental lateral load response of unbonded post-tensioned precast concrete walls." *ACI Struct. J.*, 110(6), 1045-1053.

65. Perez, F.J., Sause, R., and Pessiki, S. (2007). "Analytical and experimental lateral load behavior of unbonded post-tensioned precast concrete walls." *J. Struct. Eng.*, Special Issue: Precast-Prestressed Concrete Structures under Natural and Human-Made Hazards, 133(11), 1531-1540.

66. Pettinga, D., Christopoulos, C., Pampanin, S., and Priestley,M.J.N. (2007). "Effectiveness of simple approaches in mitigating residual deformations in buildings." *Earthquake Engineering & Structural Dynamics*, 36(12), 1763–1783.

67. Powell, G.H. (2007). "Detailed Example of a Tall Shear Wall Building Using CSI's Perform 3D Nonlinear Dynamic Analysis." *Computers and Structures Inc*., Berkeley, CA.
68. Priestly, M.J.N., Sritharan, S., Conley, J., and Pampanin, S. (1999). "Preliminary results and conclusions from the PRESSS five-story precast concrete test building." *PCI J.*, 44(6), 42–67
69. Priestley, M.J.N. and Tao, J. (1993). "Seismic response of precast prestressed concrete frames with partially debonded tendons." *PCI J*., 38(1), 58-69.
70. Priestley, M.J.N., Calvi, G. M., and Kowalski M. J. (2007). "Displacement-based seismic design of structures." *IUSS Press*, Pavia.
71. Rahman, A. and Restrepo, J. I. (2000). "Earthquake resistant precast concrete buildings: seismic performance of cantilever walls prestressed using unbonded tendons." *Research Report 2000-5*, Dept. of Civil Engineering, University of Canterbury, Christchurch, New Zealand.
72. Razvi, S., and Saatcioglu, M. (1999). "Confinement model for high-strength concrete." *J. Struct. Eng*., 125(3), 281-289.
73. Restrepo, J.I. and Rahman, A. (2007). "Seismic performance of self-centering structural walls incorporating energy dissipators." *J. Struct. Eng.*, 133(11), 1560-1570.
74. Restrepo, J.I., Mander, J., and Holden, T.J. (2001). "New generation of structural systems for earthquake resistance." *NZSEE 2001 Conference*.
75. Ruiz-García, J. and Miranda, E. (2006). "Residual displacement ratios for assessment of existing structures." *Earthquake Engineering & Structural Dynamics*, 35(3), 315–336.
76. Ruiz- García, J. and Miranda, E. (2010). "Probabilistic estimation of residual drift demands for seismic assessment of multi-story framed buildings." *Engineering structures*, 32(1), 11-20.

77. Saatcioglu, M., Razvi, S. (1992). "Strength and ductility of confined concrete." *J. Struct. Eng*, 118(6), 1590-1606.

78. Schoettler, M. J., Belleri, A., Zhang, D., Restrepo J.I. and Robert B. Fleischman, R.B. (2009). "Preliminary results of the shake-table testing for the development of a diaphragm seismic design methodology." *PCI Journal*, Winter 2009, 100-124

79. Smith, B., Kurama, Y., McGinnis, M. (2012a). "Hybrid precast wall systems for seismic regions." *Structural Engineering Research Report #NDSE-2012-01*, University of Notre Dame, IN.

80. Smith, B., Kurama, Y. (2012b). "Seismic Design Guidelines for Special Hybrid Precast Concrete Shear Walls." *Structural Engineering Research Report #NDSE-2012-02*, University of Notre Dame, IN.

81. Stanton, J.F., and Nakaki, S. D. (2002). Design guidelines for precast concrete seismic structural systems. *PRESSS Report No. 01/03-09, UW Report No. SM 02-02*, University of Washington, Seattle, WA.

82. Stanton J.F., Stone W.C, and Cheok G.S. (1997). "A hybrid reinforced precast frame for seismic regions". *PCI J.*, 42(2), 20-32.

83. Stone, W.C., Cheok, G.S., and Stanton, J.F. (1995). "Performance of hybrid moment-resisting precast beam-column concrete connections subjected to cyclic loading." *ACI Struct. J.*, 92(2), 229–249.

84. Thomas, D. J. and Sritharan, S. (2004). "An evaluation of seismic design guidelines proposed for precast jointed wall systems." *ISU-ERI-Ames Report ERI-04643*, Department of Civil and Construction and Environmental Engineering, Iowa State University, Ames, Iowa.

85. Toranzo, L. A. (2002). "The use of rocking walls in confined masonry structures: a performance-based approach." *Ph.D. Thesis*, University of Canterbury, Christchurch, New Zealand.

86. Tran T. A. (2012). "Experimental and Analytical Studies of Moderate Aspect Ratio Reinforced Concrete Structural Walls." *Ph.D. Dissertation*, Department of Civil and Environmental Engineering, University of California, Los Angeles.

87. Tuna, Z., Gavridou, S., Wallace, J.W., Nagae, T., and Matsumori, T. (2014). "2010 E-Defense four-story reinforced concrete and post-tensioned buildings - comparative study of experimental and analytical results." *Proc. 10th National Conf. in Earthquake Eng.*, Earthquake Eng. Research Institute, Anchorage, AK.

88. Tuna, Z. (2012). "Seismic performance, modeling, and failure assessment of reinforced concrete shear wall buildings." *Ph.D. Dissertation*, University of California, Los Angeles.

89. Zimmerman, R., Gavridou, S., Rivera, J., Wallace, J.W. (2015). "Application of rocking/re-centering walls to long-period buildings." *2015 ASCE/SEI Structures Congress*, Portland, OR.